UNIVERSITE MATIERE BRETAGNE MOLECULES LOIRE ET MATERIAUX

UNIVERSITÉ DE RENNES 1

THESE DE DOCTORAT DE

L'UNIVERSITE DE RENNES 1
COMUE UNIVERSITE BRETAGNE LOIRE

ECOLE DOCTORALE N° 596
Matière Molécules et Matériaux
Spécialité : Sciences de matériaux

Par

Shuo CHEN

Préparation et caractérisation de semi-conducteurs à base de séléniures pour applications photoélectriques

Thèse présentée et soutenue à Campus de Yuquan, Université de Zhejiang en Chine, le 20 Novembre 2018
Unité de recherche : UMR 6226 Institut des Sciences Chimiques de Rennes
Thèse N° :

Rapporteurs avant soutenance :

Junjie ZHANG, Professeur, China Jiliang University
Hongbing ZHAN, Professeur, Fuzhou University

Composition du Jury :

Antoine MAIGNAN, DR CNRS, ENSICAEN / Président
Junjie ZHANG, Professeur, China Jiliang University
Hongbing ZHAN, Professeur, Fuzhou University
Xusheng QIAO, Professeur, Zhejiang University

Directeur de thèse
Xianghua ZHANG, DR CNRS, Université de Rennes 1

Co-directeur de thèse
Xianping FAN, Professeur, Zhejiang University

ACKNOWLEDGEMENT

The research works presented here are accomplished in the Laboratoire de Verres et Céramiques of Université de Rennes 1 in France and School of Materials Science & Engineering of Zhejiang University in China.

Firstly, I would like to express my gratitude to my PhD supervisor Prof. Xianghua ZHANG for his patience and knowledgeability that directed me in the field of semiconductors and thin film solar cells through the research experience. The sincere thanks are also given to my co-supervisor, Prof. Xianping FAN, for directing me in the field of semiconductor nanomaterials synthesizing and for recommending me to Université de Rennes 1.

I would like to thank the members of jury for accepting to judge the thesis. My sincere thanks are given to Prof. Hongbing ZHAN and Prof. Junjie ZHANG for their acceptance to be the reporters of my thesis. I also want to thank Prof. Antoine MAIGNAN, Prof. Xianping Fan and Prof. Xusheng Qiao for participating in my PhD defense. Meanwhile, I wish to express my sincere acknowledgement to Prof. Xavier Rocquefelte and Prof. Laurent Le Brizoual as my CSI members to judge my annual reports.

I would like to give my sincere thanks to Mr. Michel Cathelinaud of Université de Rennes 1 for his kindness and for the valuable discussion and cooperation in the preparation of Sb_2Se_3-based thin film solar cells. Thanks will be given to Prof. Yang XU of Zhejiang University for his guidance in the fabrication of photodetectors. I wish to thank all the people who helped me in completion of this thesis project. I would give my thanks to Prof. Xusheng Qiao for his valuable advices in my research work. My gratitude also goes to Ms. Hongli Ma for her helps both for my work and life. My thanks are addressed particularly to Prof. Xianghua Zhang and Prof. Xianping Fan, for their wise advices, their imagination, as well as their encouragement throughout this work.

I wish to thank all my colleagues both in the Laboratoire de Verres et Céramiques of Université de Rennes 1 in France and Laboratory of Luminescent Functional Materails of Zhejiang University in China.

My Chinese fellows, Guangxing LIANG, Zhuanghao ZHENG, Qing JIAO, Renguang Ye, Anping YANG, Yanghai XU, Yimin WU and Muzhi CAI also gave me a lot of help and made my life in France colorful.

My final thanks are addressed to my family, who never doubted me and always supported me.

SOMMAIRE

Abbreviations

ODE	=	octadecene
HDA	=	hexadecylamine
OA	=	oleic acid
TOPO	=	trioctylphosphine oxide
XRD	=	X-ray diffraction
SEM	=	Scanning electron microscope
TEM	=	Transmission electron microscope
HRTEM	=	High Resolution TEM
SAED	=	Selected Area Electron Diffraction
STEM	=	Scanning TEM
EDS	=	Energy Dispersive Spectrometer
XPS	=	X-ray photoelectron spectroscopy
Eg	=	energy band gap
1D	=	one-dimensional
2D	=	two-dimensional
3D	=	three-dimensional
R_{res}	=	responsivity
NEP	=	noise equivalent power
D*	=	detectivity
EQE	=	external quantum efficiency
τ_{res}	=	response time
τ_{rec}	=	recovery time
RF	=	Radio Frequency
DC	=	Direct Current
PVD	=	physical vapor deposition
CVD	=	chemical vapor deposition

PEC	=	photo-electro-chemical
J_{SC}	=	short circuit current density
V_{OC}	=	open circuit voltage
FF	=	fill factor
PCE	=	power conversion efficiency

RÉSUMÉ DÉTAILLÉE EN FRANÇAIS

1. Introduction

Depuis plus d'un demi-siècle, les semi-conducteurs sont au cœur des technologies modernes pour des applications multiples. A titre d'exemples, l'énergie et l'environnement sont deux défis majeurs auxquels est confronté le monde d'aujourd'hui. Les semi-conducteurs font partis des matériaux clés pour développer des solutions durables.

En fonction de leur composition chimique, les semi-conducteurs peuvent être divisés en semi-conducteurs élémentaires, inorganiques et organiques. Dans toute la famille des semi-conducteurs, les séléniures métalliques jouent un rôle très important. Ils possèdent généralement une largeur de bandgap comprise entre 0,3 eV et 3,0 eV, couvrant un large domaine spectral de l'ultraviolet jusqu'à l'infrarouge. Ils sont intensément étudiés pour un grand nombre d'applications tels que cellules solaires, dispositifs thermoélectriques, éclairage, détecteurs infrarouges, lasers, matériaux optiques non linéaires, matériaux photo-catalytiques.

Actuellement, les semi-conducteurs à base de séléniures existent principalement sous trois formes: massifs, nanomatériaux et couches minces. Les procédés de fabrication sont généralement complexes et les propriétés des matériaux obtenus dépendent étroitement des paramètres tels que la structure cristalline, la taille, la structuration de surface. Les séléniures massifs sont généralement préparés un frittage à haute température de poudres. Les nanomatériaux sont principalement préparés en solution. Lorsque la taille de semi-conducteurs est à l'échelle du nanomètre, de nouvelles propriétés intéressantes peuvent apparaitre pour rendre ces matériaux encore plus attractifs. Enfin, les couches minces sont actuellement au centre de la recherche avec de nombreuses réalisations scientifiques et technologiques.

Cette thèse porte sur deux séléniures relativement peu étudiés, le Sb_2Se_3 et le In_2Se_3, qui possèdent cependant d'excellentes propriétés. Le Sb_2Se_3 est un semi-conducteur du groupe V-VI ayant une structure en feuillet et il possède un bandgap direct d'environ 1,0 ~ 1,2 eV avec un coefficient d'absorption très élevé, d'environ 10^5 cm^{-1}, dans le domaine visible. Toutes ces propriétés lui confèrent un grand potentiel d'applications notamment pour la conversion photoélectrique. Même si la recherche sur le Sb_2Se_3 a permis d'obtenir des résultats très importants, les applications réelles sont encore limitées, en grande partie dû à sa conductivité électrique intrinsèquement très faible (10^{-6} $\Omega^{-1}m^{-1}$). Par conséquent, la présente étude vise à

proposer des solutions pour résoudre ce problème majeur et pour démontrer le potentiel d'applications.

Le In_2Se_3 est un semi-conducteur important avec aussi d'excellentes propriétés optiques et électriques. Actuellement, la synthèse de matériaux de haute qualité et cristallographiquement purs est un problème majeur. Dans cette étude, nous allons utiliser la technique d'injection à chaud pour obtenir des nano-fleures γ-In_2Se_3 de grande qualité, formées de feuillets à deux dimensions. Nous allons également, pour la première fois, fabriquer une photodiode à hétérojonction pour démontrer l'intérêt de ce matériau pour la détection optique.

Enfin, nous espérons que les précédés de préparation, la méthodologie pour le contrôle de propriétés ainsi que les performances démontrées des dispositifs obtenus dans ce travail, contribueront à l'accélération de recherche et développement de semi-conducteurs à base de séléniures.

2. Amélioration de la conductivité et fabrication de photo-détecteurs à base de Sb_2Se_3

Ces dernières années, de nouvelles méthodes de synthèse, hydrothermal, solvothermal, méthode tensioactif-assistée par exemples, ont été développées pour synthétiser des Sb_2Se_3 en phase liquide. En raison de sa structure cristalline unique, ce matériau est généralement formé de chaines unidimensionnelles de $(Sb_4Se_6)_n$ assemblées le long des directions x et y par la force Van Der Waals, ce qui donne une grande variété de nanomatériaux de Sb_2Se_3 unidimensionnels tels que les nano-fils , nano-tiges, nano-rubans, nano-tubes, avec des propriétés parfois uniques.

Un de problèmes associés à Sb_2Se_3 est sa très faible conductivité intrinsèque (10^{-6} $\Omega^{-1}m^{-1}$), ce qui constitue un handicap réel pour des applications. Bien qu'il existe déjà des travaux sur l'amélioration de sa conductivité, une étude plus systématique est encore nécessaire pour une meilleure compréhension et un meilleur contrôle de ses propriétés électriques et électroniques.

Dans ce travail, deux techniques seront utilisées pour améliorer la conductivité des matériaux à base de Sb_2Se_3. La première consiste à préparer des nano-tiges composites contenant une structure à hétérojonction Sb_2Se_3/$AgSbSe_2$, La deuxième technique est basée sur son dopage par Sn notamment. L'intérêt de ces matériaux sera démontré par la fabrication et les caractérisations d'un photo-détecteur à haute performance à base de ces matériaux.

2.1 Synthèse et caractérisation de nano-tiges de Sb_2Se_3

Les nano-tiges de Sb_2Se_3 ont été préparées par un procédé chimique colloïdal associé à une injection à chaud. Le procédé est basé sur la technique de Schlenk line sous atmosphère d'argon. Le précurseur de Se est d'abord dissout à chaud et refroidi jusqu'à la température ambiante avant d'être rapidement injecté dans la solution de précurseur de Sb, chauffée à la température de réaction. Après 10 minutes de réaction, le chauffage est arrêté et la solution est ensuite refroidie à la température ambiante. Le produit obtenu est lavé, rincé et séché pour obtenir les nano-tiges de Sb_2Se_3. Ce procédé de préparation est schématiquement illustré sur la Figure 1.

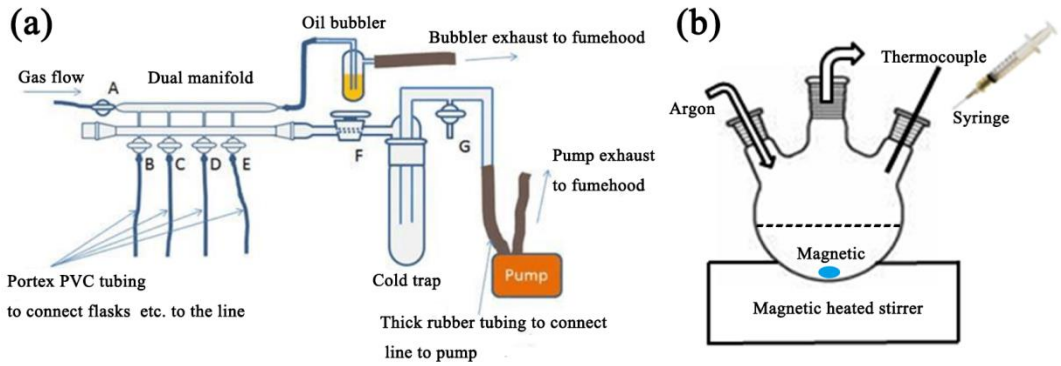

Figure 1. *(a) Schematic illustration of the Schlenk line technology and (b) synthesis method of hot-injection.*

La Figure 2 montre les diagrammes XRD des nano-tiges de Sb_2Se_3 synthétisées à différentes températures de réaction (160 °C, 200 °C, 240 °C et 280 °C). Tous les spectres montrent des pics de diffraction intenses et fins, indiquant que les Sb_2Se_3 obtenus possèdent une cristallinité élevée et une taille de grains relativement importante. Des pics de diffraction attribués à une trace d'impureté de Sb_2O_3 sont présents dans le produit obtenu avec une réaction à 160 °C, température trop basse pour permettre une réaction complète. Pour les trois autres produits, tous les pics de diffraction sont attribuables à Sb_2Se_3 orthorhombique (carte JCPDS n° 15-0861), sans la présence d'une deuxième phase, démontrant la pureté du produit.

La morphologie et la structure des nano-tiges ont été étudiées. Figures 2b et 2c sont des images MEB et MET de nano-tiges de Sb_2Se_3, obtenues par réaction 240 °C pendant 10 min. Ces nano-tiges présentent une surface lisse, une distribution de taille uniforme. La Figure 2d est une micrographie électronique en transmission à haute résolution (HRTEM), un diagramme de diffraction d'électrons d'une zone sélectionnée (SAED) et le transformée de

Fourier d'une seule nano-tige, indiquant clairement sa forte cristallinité. Les distances inter-planaires ont été mesurées et sont respectivement de 0,392 nm et 0,526 nm pour les plans (001) et (120), en accord avec la structure orthorhombique de Sb_2Se_3. L'image HRTEM montre également une croissance préférentielle des nano-tiges le long de la direction [001]. Le spectre EDS présenté sur la Figure 2c confirme le rapport stœchiométrique Sb/Se=2/3.

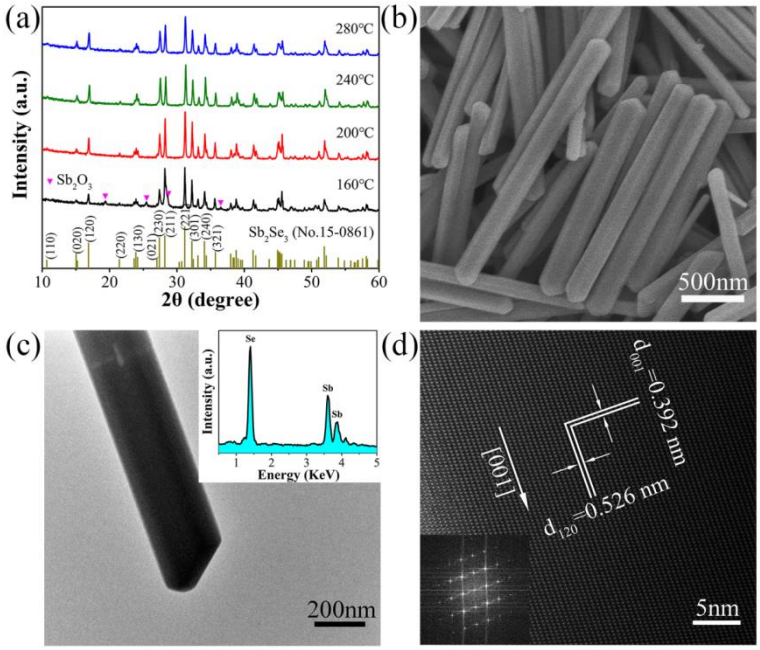

Figure 2. *(a) XRD patterns of the Sb_2Se_3 nanorods synthesized at different temperatures (160 ℃, 200 ℃, 240 ℃ and 280 ℃); The 240 ℃ sample is studied in detail : (b) SEM image; (c) TEM image and corresponding EDS spectrum (inset); (d) HRTEM image, the bottom inset is a selected-area FFT.*

2.2 Préparation et caractérisation d'un détecteur optique à base de couches minces de Sb_2Se_3

Afin d'étudier les propriétés photoconductrices des nano-tiges de Sb_2Se_3, nous avons construit un photo-détecteur prototype à base de couches minces. La Figure 3 est une vue schématique du dispositif: les nano-tiges sont dispersées dans du chloroforme à l'aide de l'ultrason, puis déposées sur des électrodes en Au.

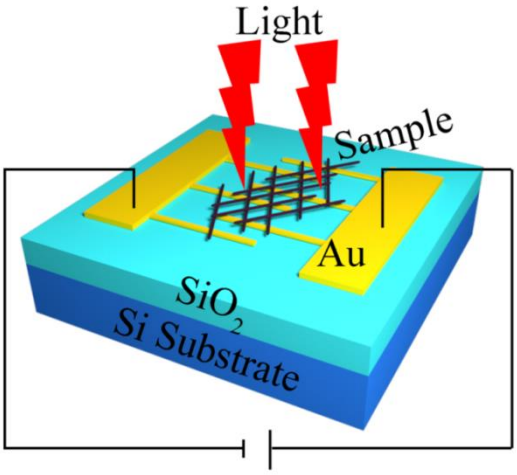

Figure 3. *Schematic illustration of the photodetector based on the Sb_2Se_3 nanorod film.*

La photoconductivité se réfère au phénomène de changement de la conductivité électrique d'un matériau sous illumination et c'est une propriété importante d'un semi-conducteur. La Figure 4a est une courbe I(courant)-V(voltage) d'un photo-détecteur à couches minces de Sb_2Se_3. On peut constater que le courant d'obscurité est faible, en accord avec la faible conductivité intrinsèque de ce matériau. Ce dispositif présente une forte sensibilité à la lumière sous différentes intensités lumineuses et l'intensité du photocourant augmente significativement avec l'augmentation de l'intensité lumineuse. Afin d'étudier plus en détail les caractéristiques photoélectriques, l'intensité de la lumière est fixée à 12,05 $mW.cm^{-2}$ et la réponse temporelle de ce photo-détecteur à couches minces sous différentes tensions de polarisation a été étudiée. Lorsque cette tension de polarisation est de -20 V, le rapport "On/Off" du dispositif atteint 50, ce qui est comparable aux excellents résultats publiés précédemment. Le temps de réponse et le temps de récupération sont deux autres paramètres importants et on peut voir à partir des Figures 4c et 4d que ce temps est respectivement de 0,7 s et de 1,1 s. Il est également constaté que ce dispositif reste très stable même près plusieurs cycles "ON/OFF".

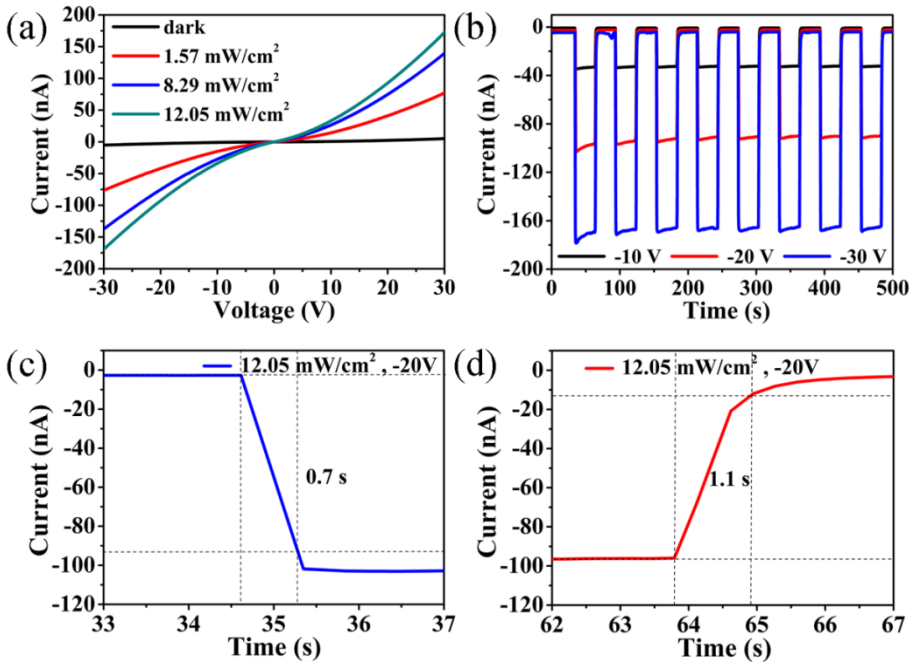

Figure 4. *Photoconductive performance of the photodetector based on the Sb_2Se_3 nanorod film. (a) Dark current and photocurrent at different incident power densities, (b) Time-resolved photoresponse with an incident light density of 12.05 mW cm^{-2}, Demonstration of (c) the response speed and (d) the recovery speed at a bias of -20 V and an incident light density of 12.05 mW cm^{-2}.*

2.3 Préparation et caractérisation de nano-tiges à hétérojonction $Sb_2Se_3/AgSbSe_2$

Dans ce travail, deux techniques sont proposées pour améliorer la faible conductivité des nano-tiges de Sb_2Se_3. La première consiste à l'associer à une deuxième phase de haute conductivité. Ici, un semi-conducteur ternaire $AgSbSe_2$ à haute conductivité avec un bandgap étroit, est sélectionné comme seconde phase, et des nano-tiges d'hétérojonction $Sb_2Se_3/AgSbSe_2$ sont préparées par injection à chaud. Différentes observations et analyses sous microscopes électroniques sont résumées sur la Figure 5. On peut constater que certaines petites nanoparticules sont incorporées dans la tige. Une analyse plus poussée des images HRTEM de différentes régions sélectionnées sur les nano-tiges a révélé que les tiges et les nanoparticules ont des structures cristallines différentes et que l'interface est claire et nette. L'image STEM intégrée dans la Figure 5c et la carte de distribution d'éléments, obtenue par EDS, indiquent que les nanoparticules de $AgSbSe_2$ sont développées à la surface des nano-tiges de Sb_2Se_3, formant ainsi une structure à hétérojonction.

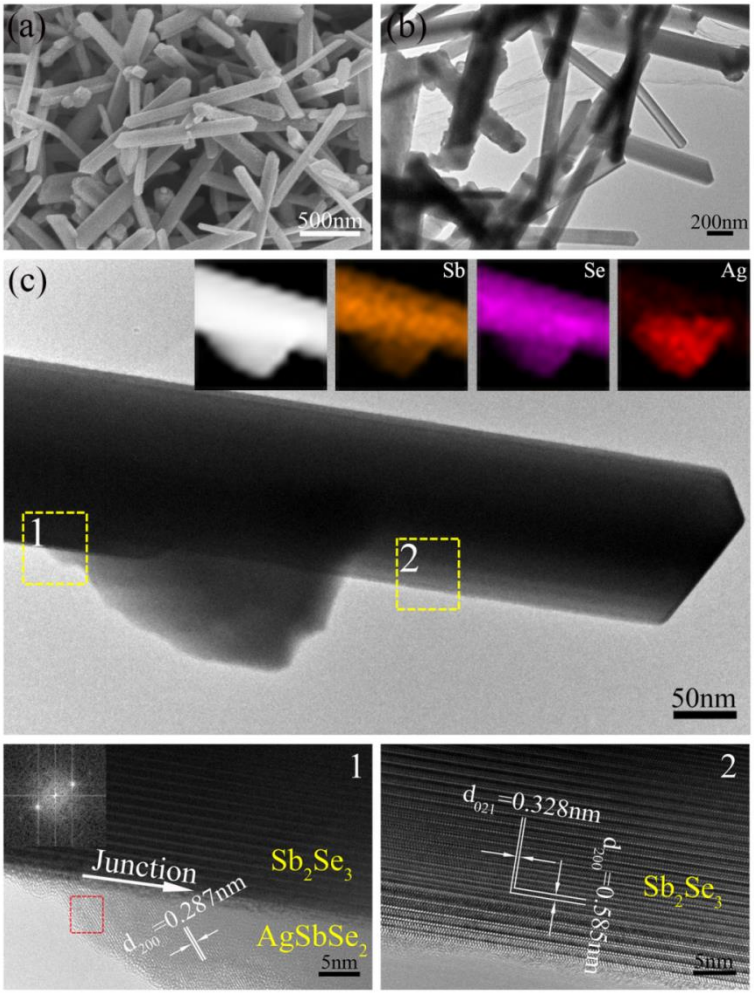

Figure 5. *Structural and morphological characterization of the hybrid nanorods with the $Sb_2Se_3/AgSbSe_2$ heterojunction structure. (a) SEM image, (b) TEM image, (c) TEM image and HRTEM images from the selected areas 1 and 2 of an individual hybrid nanorod (inset in the left HRTEM image is a FFT pattern from the red marked area), the inset of (c) shows a STEM image and the corresponding EDS mapping images of Sb, Se and Ag elements.*

2.4 Photo-détecteur en couches minces à base de nano-tiges à hétérojonction $Sb_2Se_3/AgSbSe_2$

La Figure 6 montre les propriétés photoélectriques d'un photo-détecteur en couche mince à hétérojonction $Sb_2Se_3/AgSbSe_2$. Comparé au dispositif identique à base de Sb_2Se_3, le courant d'obscurité de ce dispositif à hétérojonction est augmenté d'environ 20 fois (passant de -2 nA à -40 nA, à un bias de -20 V) et le photocourant est multiplié par 4,5 environ (passant de -100 nA à -450 nA, avec un bias de -20 V et une intensité d'illumination de 12,05 $mW.cm^{-2}$). Les calculs montrent que la sensibilité, R_{res}, de ce photo-détecteur à hétérojonction $Sb_2Se_3/AgSbSe_2$ est 4,2 fois supérieure à celle du photo-détecteur à base de Sb_2Se_3,

franchissant ainsi une étape importante pour promouvoir l'application de ce matériau. A partir de la courbe de réponse temporelle, on peut voir que le photo-détecteur à hétérojonction a un temps de réponse de 0,6 s et un temps de récupération de 2,7 s, avec en plus une grande stabilité. Ces résultats démontrent que des couches minces à hétérojonction sont un concept intéressant pour construire des photo-détecteurs performants.

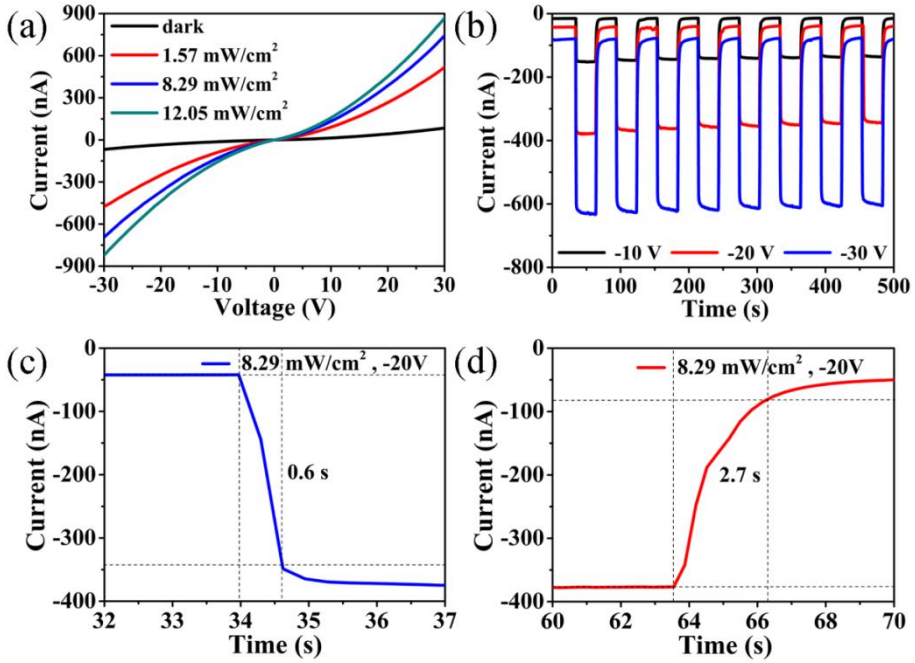

Figure 6. *Photoconductive performance of the photodetector based on the Sb_2Se_3/$AgSbSe_2$ hybrid nanorod film. (a) Dark current and photocurrents at different incident power densities; (b) Time-resolved photoresponse with an incident light density of 8.29 mW.cm^{-2}; (c) Response speed and (d) the recovery speed.*

2.5 Synthèse et caractérisation de nono-tiges de $(Sn_xSb_{1-x})_2Se_3$

La deuxième technique que nous avons utilisé pour augmenter la conductivité électrique de Sb_2Se_3 est le dopage. Sn est choisi comme dopant, qui est dans la même période que le Sb sur le tableau périodique, avec un rayon atomique très proche. L'influence du dopage sur les propriétés photoélectriques des nano-tiges de Sb_2Se_3 a été étudiée.

La Figure 7a est un diffractogramme XRD de nano-tiges $(Sn_xSb_{1-x})_2Se_3$ (x = 0,00, 0,01, 0,03, 0,05, 0,10) préparées par injection à chaud. Toutes les nano-tiges montrent des pics de diffraction intenses, attribuables tous au Sb_2Se_3 orthorhombique, montrant ainsi que la phase cristalline principale est toujours le Sb_2Se_3 avec une cristallinité élevée. Lorsque la concentration de dopage augmente, aucune seconde phase contenant Sn n'apparaît et aucun

autre pic d'impureté n'est détectable. Avec une augmentation de dopage en Sn, les pics de diffraction associés aux plans (221) et (301) se déplacent progressivement vers de plus grands angles de diffraction, indiquant que les paramètres de maille de $(Sn_xSb_{1-x})_2Se_3$ diminuent. Ceci peut être expliqué par le fait que les Sb^{3+} sont progressivement remplacés par des ions Sn^{4+} plus petits. Des mesures XPS confirment la présence des ions Sn^{4+} (Fig. 7c). La Fig. 7d montre des images SEM représentatives des nano-tiges de $(Sn_xSb_{1-x})_2Se_3$ avec une dimension uniforme, un diamètre compris entre 100 à 200 nm et une longueur de quelques microns. La surface est entièrement lisse dans la direction de croissance et aucune phase secondaire n'est observable, confirmant la réussite du dopage.

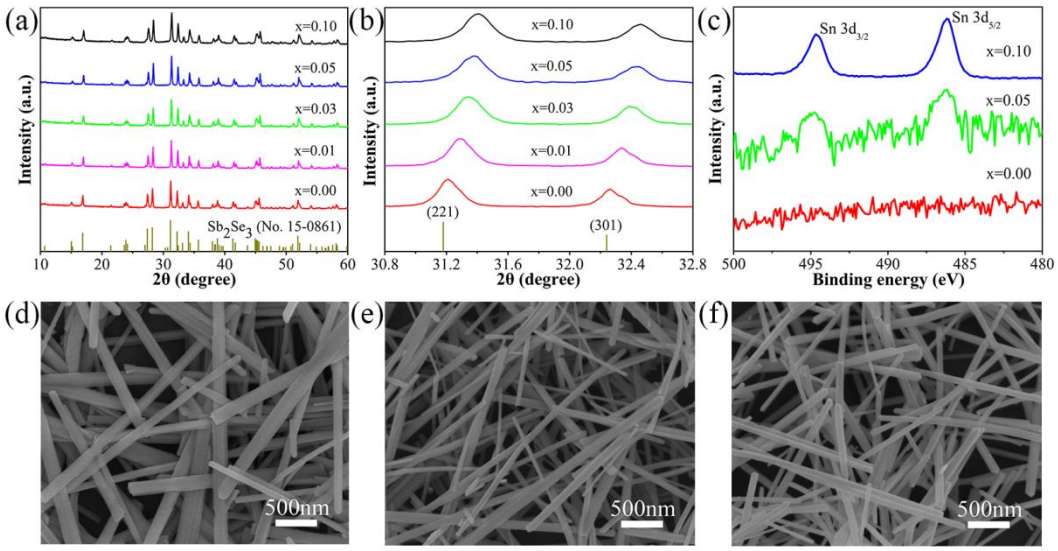

Figure 7. *(a) XRD patterns of $(Sn_xSb_{1-x})_2Se_3$ nanorods. (b) (221) and (301) XRD peaks of the same nanorods. (c) XPS spectrum of Sn-3d for the $(Sn_xSb_{1-x})_2Se_3$ nanorods. Representative SEM images of $(Sn_xSb_{1-x})_2Se_3$ nanorods: (d) x=0.00, (e) x=0.05, and (f) x=0.10*

2.6 Préparation et caractérisation de photo-détecteurs en couche mince à base de $(Sn_xSb_{1-x})_2Se_3$

Pour étudier l'effet du dopage de Sn sur la conductivité de Sb_2Se_3, L'effet Hall a été utilisé pour mesurer la résistivité, la concentration de porteurs de charge, la mobilité et le type de conduction de $(Sn_xSb_{1-x})_2Se_3$. La Figure 8a montre la relation entre ces propriétés et la concentration de dopage en Sn. Les nano-tiges de Sb_2Se_3 sans dopage ont une très faible conductivité et concentration de porteurs de charge. Lorsque les ions Sn^{4+} ont été dopés dans le Sb_2Se_3, la résistivité du matériau chute rapidement, passant de $1{,}229.10^7$ Ω·cm (x = 0,00) à $8{,}746.10^4$ Ω·cm (x = 0,10). A partir de cette Figure 8a, on peut également constater que la

concentration de porteurs de charge augmente aussi très rapidement avec la concentration de dopage, expliquant ainsi l'augmentation de la conductivité des $(Sn_xSb_{1-x})_2Se_3$.

Pour démontrer l'intérêt de l'amélioration de la conductivité, des photo-détecteurs à base de couches minces de $(Sn_xSb_{1-x})_2Se_3$ ont été fabriqués et caractérisés. Figure 8b représentant le courant à l'obscurité et le photocourant de ces détecteurs (tension appliquée de 10 V, illumination à 650 nm) en fonction de la concentration du dopants Sn^{4+}. Il est clair que ces deux courants augmentent très rapidement avec la teneur de Sn^{4+} dans le Sb_2Se_3.

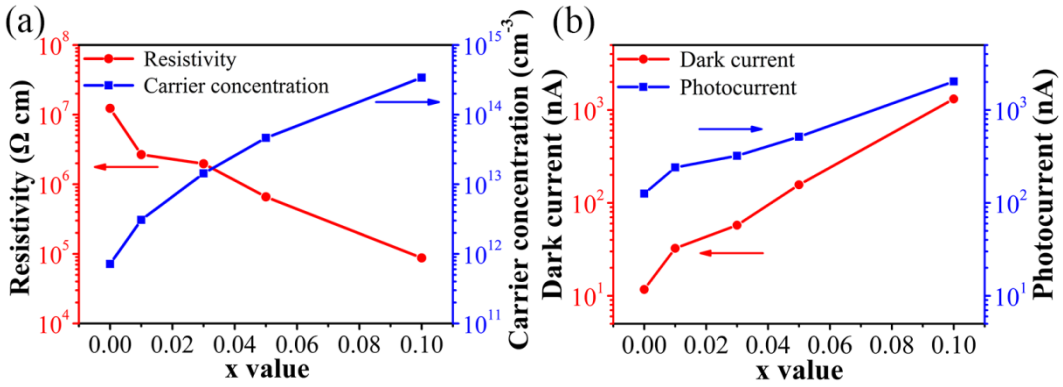

Figure 8. *(a) Dependence of resistivity and carrier concentration of the $(Sn_xSb_{1-x})_2Se_3$ nanorods on doping concentrations of Sn^{4+} ions (x value). (b) Dependence of dark current and photocurrent (under 650 nm light illumination at a bias voltage of 10 V) of the $(Sn_xSb_{1-x})_2Se_3$ nanorod film photodetectors on doping concentrations of Sn^{4+} ions (x value).*

Il est important pour un photo-détecteur d'être sensible sur une large bande spectrale. En lien avec le fort coefficient d'absorption et un bandgap étroit de $(Sn_xSb_{1-x})_2Se_3$, la réponse spectrale des détecteurs à base de ces semi-conducteurs a été mesurée de l'UV jusqu'à NIR. La Figure 9a montre la réponse, R_{Res}, de deux détecteurs à base respectivement des couches minces de Sb_2Se_3 et de $(Sn_{0.05}Sb_{0.95})$ en fonction de la longueur d'onde. Ces détecteurs sont sensibles entre 300 nm et 1100 nm avec la réponse la plus élevée à 850 nm. Il convient de noter que cette réponse spectrale large permet d'utiliser ces photo-détecteurs pour la détection multispectrale. Il est important de noter que le détecteur $(Sn_{0.05}Sb_{0.95})_2Se_3$ possède un R_{Res} 3-4 fois supérieure à celle de Sb_2Se_3 sur toute la bande spectrale, avec des performances comparables aux meilleurs résultats publiés. Le NEP, Noise Equivalent Power, est un indicateur de base concernant le bruit d'un dispositif. Figure 9b montre le NEP de ces deux détecteurs en fonction de la longueurs d'onde et la valeur minimale du NEP est de $3{,}14.10^{-13}$ $W/Hz^{1/2}$ pour le détecteur $(Sn_{0.05}Sb_{0.95})_2Se_3$. Cela signifie que même une lumière incidente très faible, de l'ordre de pico-watt, peut être détectée.

Les Figures 9c et 9d représentent le rendement quantique externe, EQE, et la détectivité, D*, de ces deux détecteurs en fonction de la longueur d'onde. Le EQE et la D * peuvent atteindre respectivement 906% et 5,03.10^{11} Jones), confirmant l'intérêt du composé $(Sn_{0.05}Sb_{0.95})Se_3$ comme excellent candidat pour la détection optique.

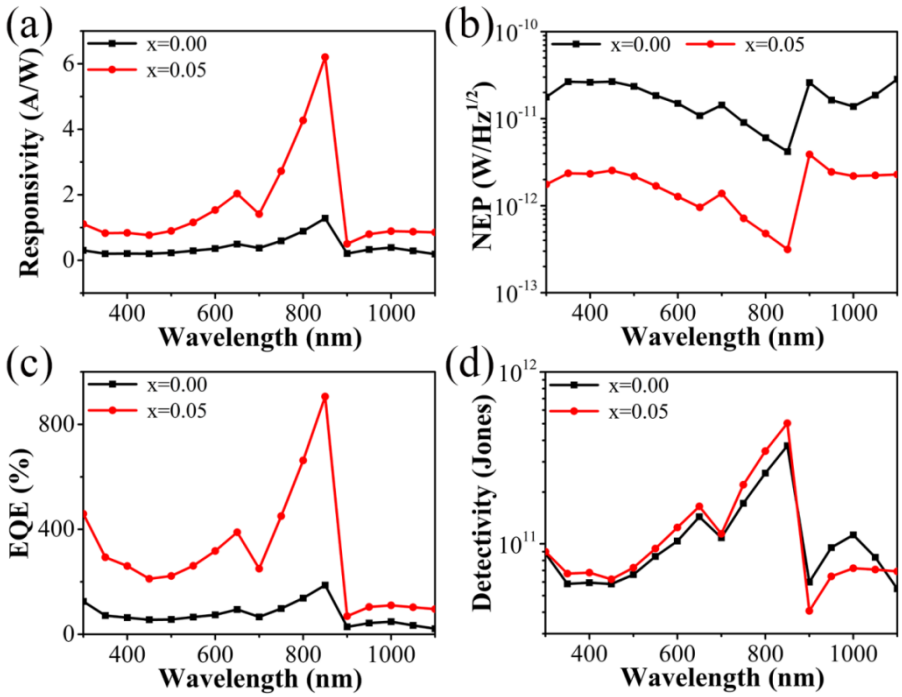

Figure 9. *Wavelength-dependent (a) responsivity; (b) noise equivalent power (NEP); (c) external quantum efficiency (EQE) and (d) detectivity (D*) of the Sb_2Se_3 nanorod film photodetector and the $(Sn_{0.05}Sb_{0.95})_2Se_3$ nanorod film photodetector.*

2.7 Conclusions

Des nano-tiges de Sb_2Se_3 de haute qualité ont été préparées avec la technique d'injection à chaud. La température et le temps de réaction ainsi que l'agent tensioactif influencent fortement la morphologie et la structure des nano-tiges. La résistivité intrinsèque de Sb_2Se_3 est très élevée, de l'ordre de 10^6 Ω·m, ce qui affecte grandement son application pratique. Nous avons réussi à l'améliorer considérablement en utilisant deux approches différentes. La première approche consiste à former un composite en utilisant une seconde phase conductrice, le $AgSbSe_2$ et une structure à hétérojonction $Sb_2Se_3/AgSbSe_2$ a été obtenue avec une conductivité nettement améliorée par rapport à Sb_2Se_3 pur. La deuxième approche est le dopage avec Sn pour introduire des ions Sn^{4+} dans la structure de Sb_2Se_3, qui a également permis d'augmenter la conductivité, par plusieurs ordres de grandeur.

Ces matériaux à base de Sb_2Se_3 ont été utilisés pour la fabrication de photo-détecteurs prototypes. Le photo-détecteur en couches minces à hétérojonction $Sb_2Se_3/AgSbSe_2$ présente une très bonne sensibilité, dans les domaines du visible et du proche-infrarouge, plus de quatre fois supérieure à celle du Sb_2Se_3 pur. Le photo-détecteur à base de Sb_2Se_3 dopé au Sn^{4+} montre également d'excellentes propriétés photoélectriques avec un NEP pouvant être aussi faible que $3{,}14.10^{-13}$ $W/Hz^{1/2}$, un EQE de 906% et une détectivité de $5{,}03.10^{11}$ Jones.

3. Conductivité et propriétés photoélectriques du Sb_2Se_3 dopé Sn

Le paragraphe précédent était axé sur les nano-tiges de Sb_2Se_3 avec des résultats intéressants pour les applications comme photo-détecteurs. Cependant, ces nano-tiges ne peuvent pas être utilisées directement pour la préparation de cellules solaires. Dans cette partie du travail, nous allons nous concentrer sur l'utilisation de la pulvérisation cathodique pour préparer des couches minces de Sb_2Se_3 pour applications en cellules solaires. Par conséquent, nous avons décidé d'étudier, plus en détail, les propriétés physiques et chimiques des matériaux à base de Sb_2Se_3 dopés aux Sn^{4+}, qui ont montré des propriétés photoélectriques très intéressantes. Une série de matériaux, $(Sn_xSb_{1-x})_2Se_3$ (x = 0,00, 0,03, 0,05, 0,07, 0,10), seront systématiquement étudiés et ils seront synthétisés par la méthode fusion-trempe, technique très utilisée pour la préparation de matériaux massifs à base de chalcogénures.

3.1 Synthèse et caractérisation de semi-conducteurs polycristallins $(Sn_xSb_{1-x})_2Se_3$

Les produits de départ de haute pureté, Sn (99,99%), Sb (99,999%) et Se (99,999%), sont scellés sous vide dans une ampoule de silice. Le mélange fondu et homogénéisé est refroidi rapidement en laissant le tube de silice trempé à l'air ou même dans l'eau. La série de matériaux étudiés est $(Sn_xSb_{1-x})_2Se_3$ (x = 0,00, 0,03, 0,05, 0,07, 0,10).

Fig. 10a montre les diffractogrammes de cette série de matériaux qui possèdent tous des pics de diffractions intenses et étroits, attribuables au Sb_2Se_3 orthorhombique et aucune phase secondaire contenant le Sn ou non n'est détectable. Ceci démontre une pureté cristallographique et une haute cristallinité de ces matériaux synthétisés. Les résultats XRD sont semblables avec un disque poli ou avec des poudres obtenues en broyant le disque, comme indiqué sur la Figure 10b, montrant ainsi que la cristallisation est uniforme dans le matériau massif.

Pour étudier l'effet de dopage Sn sur la structure cristalline de Sb_2Se_3, les paramètres de maille a, b, et c ont été calculés à partir des diffractogrammes XRD et sont présentés sur la Figure 10 c. Avec l'augmentation progressive de la concentration de dopage en Sn, une légère augmentation de ces paramètres de maille est observable, en accord avec la légère différence du rayon ionique de Sb^{3+} et de Sn^{4+}.

La Figure 10d montre les résultats XPS de Sn-3d. Par rapport au Sb_2Se_3 pur, $(Sn_{0.10}Sb_{0.90})_2Se_3$ présente deux pics supplémentaires à 494,7 eV et à 486,2 eV, caractéristiques de Sn-3d, confirmant que le Sn est entré dans le réseau de Sb_2Se_3 sous forme de Sn^{4+}.

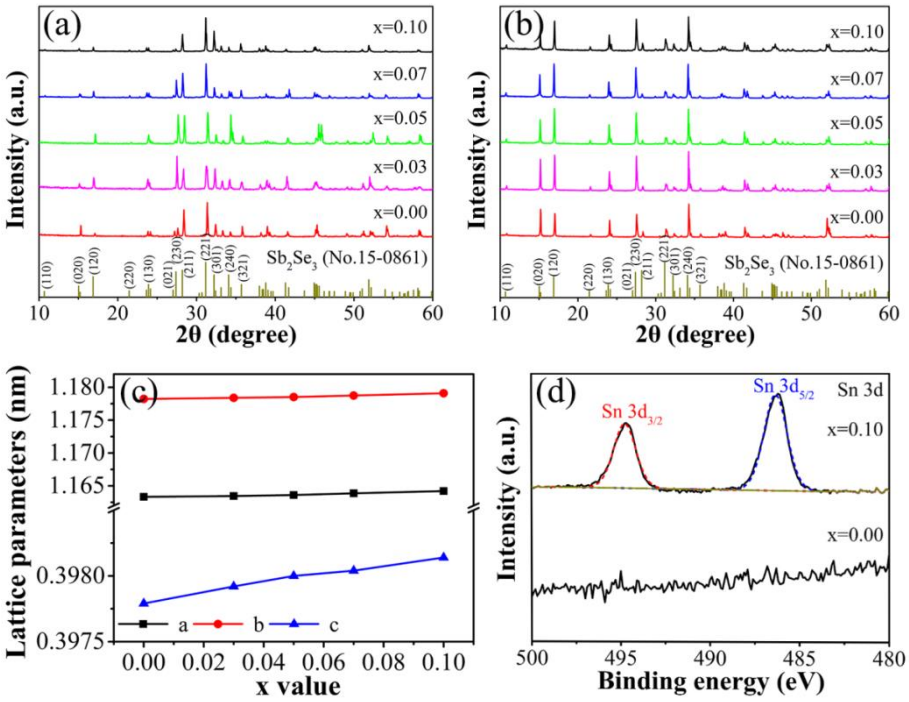

Figure 10. *(a) XRD patterns of the bulk $(Sn_xSb_{1-x})_2Se_3$ crystals (x=0.00, 0.03, 0.05, 0.07 and 0.10). (b) XRD patterns of the powdered $(Sn_xSb_{1-x})_2Se_3$ samples. (c) Lattice constants a, b and c, derived from powder XRD peaks, plotted as a funtion of Sn doping concentration (x value). (d) XPS spectrum of Sn-3d for the $(Sn_xSb_{1-x})_2Se_3$ crystals (x=0.00 and 0.10).*

Pour étudier plus en détail la morphologie et la taille de grain, la surface des échantillons $(Sn_xSb_{1-x})_2Se_3$ polis a été attaquée chimiquement avec une solution de NaOH à 1 mol/L pendant 20 minutes. La Figure 11a montre l'échantillon Sb_2Se_3 après l'attaque chimique et les joints de grains ne sont pas visibles. La Figure 11b est la micromorphologie d'un échantillon dopé représentatif, le $(Sn_{0.05}Sb_{0.95})_2Se_3$, après l'attaque chimique, qui montre clairement la distribution des grains et la taille moyenne des grains est d'environ 15 µm. La distribution des

éléments, obtenue par analyse EDS, montre clairement que le Sb et le Se sont uniformément distribués dans tout l'échantillon et que le dopant Sn est enrichi aux joints de grains.

Pour l'échantillon $(Sn_{0.10}Sb_{0,90})_2Se_3$ avec une concentration de dopage Sn plus élevée, l'enrichissement en Sn est encore plus évident aux joints de grains, comme le montre la Figure 11c. Ce phénomène peut s'expliquer par une séparation de phases en raison d'une solubilité limitée de Sn dans le Sb_2Se_3. L'analyse EDS montre que les zones enrichies en Sn présentent une composition similaire, proche de la composition stœchiométrique de $Sn_2Sb_4Se_8$.

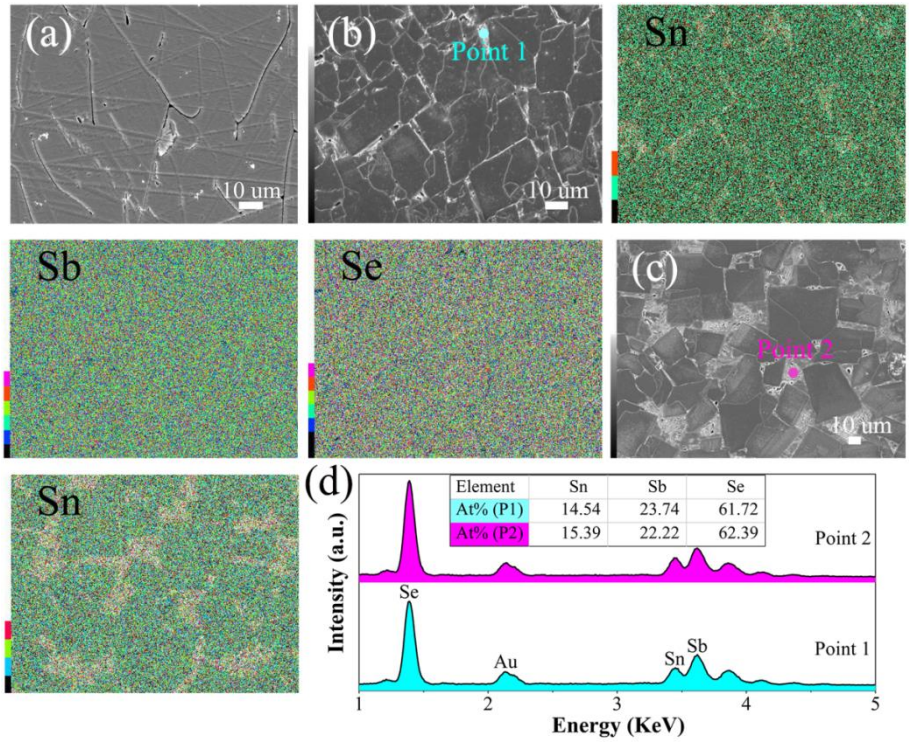

Figure 11. *(a-e) SEM images of (a) Sb_2Se_3 crystal, (b) $(Sn_{0.05}Sb_{0.95})_2Se_3$ crystal and (c) $(Sn_{0.10}Sb_{0.90})_2Se_3$ crystal surface with chemical etching by NaOH solution and the corresponding EDS elemental mappings of Sn, Sb and Se. (d) EDS spectra recorded from two different positions (Point 1 and Point 2).*

3.2 Propriétés photoélectriques des $(Sn_xSb_{1-x})_2Se_3$ polycristallins

L'effet Hall est utilisé pour étudier l'influence du dopage de Sn sur les propriétés électriques de Sb_2Se_3 et les résultats montrent que les matériaux dopés présentent une conductivité électrique, ainsi qu'une densité de porteurs de charge, plusieurs ordres de grandeur, plus élevées. Par exemple, cette densité de porteurs passe de $1,44.10^{11}$ cm^{-3} pour le Sb_2Se_3 non dopé, à $1,94.10^{16}$ cm^{-3} lorsque 10% de Sn est substitué par Sn.

La méthode classique de trois électrodes a été utilisée pour étudier les propriétés photo-électro-chimique (PEC) des semiconducteurs polycristallins $(Sn_xSb_{1-x})_2Se_3$. Une représentation schématique du montage est illustrée sur la Figure 12a. La Figure 12b représente la relation entre la densité de courant en fonction de la tension appliquée. Il ressort de cette Figure que la densité du courant d'obscurité et la densité de photocourant de Sb_2Se_3 non-dopé sont très faibles, en accord avec sa faible concentration de porteurs de charge. Pour les échantillons dopés en Sn, la densité de courant augmente de manière significative et cette augmentation est proportionnelle à la concentration de dopage en Sn. On peut également déduire de cette Figure que tous les échantillons, dopés ou non, sont des semi-conducteurs de type p, car leur densité de photocourant augmente lorsque la tension de polarisation est négative.

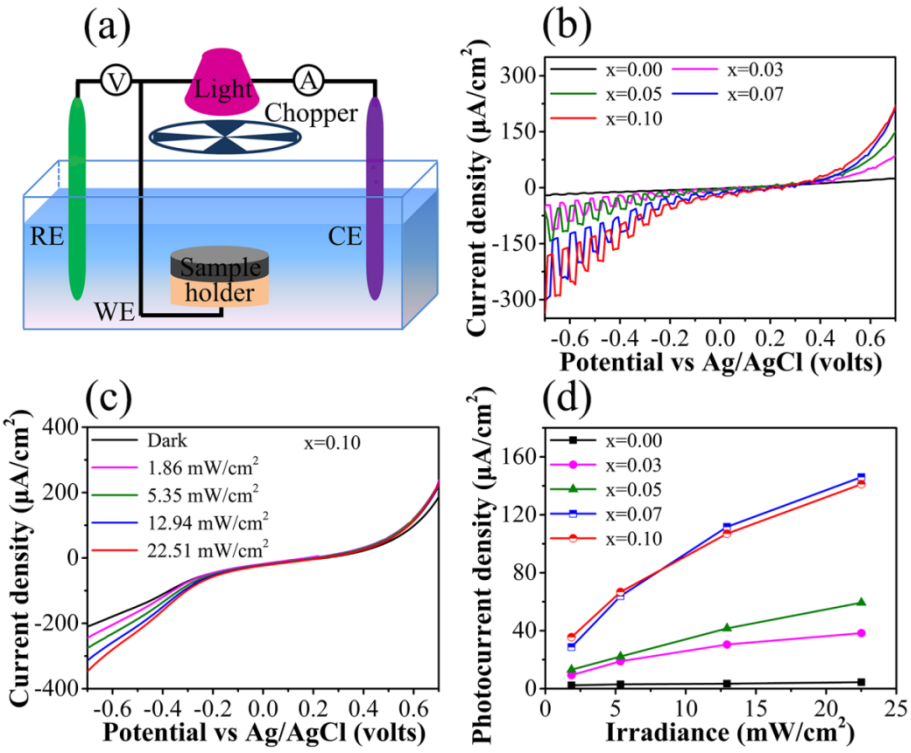

Figure 12. *(a) Schematic illustration of the 3-electrode photo-electro-chemical (PEC) measurement. (b) Current-voltage characteristics using $(Sn_xSb_{1-x})_2Se_3$ crystals as working electrodes. (c) Dark current density and photocurrent density with different illumination densities of a representative $(Sn_{0.10}Sb_{0.90})_2Se_3$ sample. (d) Photocurrent density as a function of incident light density at a bias voltage of −0.7 V.*

Nous avons également étudié la relation entre la densité de photocourant et l'intensité de l'illumination. Les résultats montrent que cette densité de photocourant augmente très

nettement par rapport à la densité de courant d'obscurité et elle augmente progressivement avec l'augmentation de l'intensité de l'illumination.

3.4 Conclusions

Le procédé de fusion-trempe a été utilisé avec succès pour la préparation des semiconducteurs polycristallins $(Sn_xSb_{1-x})_2Se_3$ (x = 0,00, 0,03, 0,05, 0,07, 0,10) avec une haute cristallinité. Il a été démontré que lorsque la concentration de Sn dépasse un certain seuil, une séparation de phases peut se produire avec une phase enrichis en Sn dans les joints de grains.

Lorsque la concentration en dopant Sn augmente, la conductivité des échantillons massifs $(Sn_xSb_{1-x})_2Se_3$ est améliorée de plusieurs ordres de grandeur. Tous les échantillons, dopés ou non, sont des semi-conducteurs de type p. L'échantillon $(Sn_{0.10}Sb_{0.90})_2Se_3$ présente, par rapport au Sb_2Se_3 pur, une densité de courant à l'obscurité 10 fois supérieure et une densité de photocourant environ 14 fois supérieur.

4. Couches minces et cellules solaires quasi-homojonction à base de Sb_2Se_3

Les cellules solaires en couches minces sont activement étudiées depuis de nombreuses années en raison de leurs nombreux avantages. Ce type de cellules solaires utilisant des matériaux inorganiques sont principalement à base de silicium (Si), de tellurure de cadmium (CdTe) et de Cu-In-Ga-Se(S) avec chacun ses avantages et inconvénients. Les applications réelles, en dehors du Si amorphe, sont encore limitées.

L'étude sur les cellules solaires de Sb_2Se_3 est relativement récente avec des progrès significatifs et un potentiel d'application intéressant. Le Sb_2Se_3 est un matériau semiconducteur inorganique avec des propriétés photoélectriques particulièrement intéressantes. Son bandgap d'environ 1,0 à 1,2 eV, permet d'espérer, d'après la théorie de Shockley-Queisser, une cellule solaire à jonction unique avec un rendement de conversion pouvant atteindre 30%. En plus, son coefficient d'absorption dans le domaine visible est supérieur à 10^5 cm^{-1}, de sorte qu'une couche de 500 nm d'épaisseur est suffisante pour absorber efficacement le spectre solaire. La constante diélectrique des couches minces de Sb_2Se_3 est relativement importante (environ 15), ce qui permet de réduire efficacement la perte par recombinaison provoquée par des défauts. La mobilité de porteurs de charge est également très élevée dans ce matériau et elle peut atteindre les 10 $cm^2V^{-1}s^{-1}$. Il est également intéressant de souligner que le Sb_2Se_3 est le composé unique dans ce système binaire Sb-Se. Il

est composé d'éléments non toxiques et abondants sur terre. Par conséquent, ce matériau possède donc des propriétés intrinsèques intéressantes pour fabriquer des cellules solaires à haut rendement.

Dans cette étude, nous avons utilisé le procédé de pulvérisation cathodique pour obtenir des couches minces à base de Sb_2Se_3. La composition, la structure cristalline et la morphologie de ces couches seront étudiées en relations avec leurs propriétés photoélectriques. Des cellules solaires en couches minces à base de ce matériau seront également fabriquées et caractérisées.

4.1 Préparation et caractérisation de cibles à base de Sb_2Se_3

Les cibles pour dépôt de couches par pulvérisation cathodique ont été préparées avec la technique de fusion-trempe décrite précédemment. Quatre compositions, Sb_2Se_3, $Sb_2Se_{3.3}$, $(Sn_{0.1}Sb_{0.9})_2Se_3$ et $Sb_2(Se_{0.9}I_{0.1})_3$ ont été préparées. La surface des cibles a été finement polie et ces cibles ont une épaisseur de 3 à 4 mm et un diamètre de 5 cm.

4.2 Préparation et caractérisation de couches minces à base de Sb_2Se_3

Le Sb_2Se_3 possède une faible conductivité électrique et par conséquent, la pulvérisation cathodique à radio fréquence est utilisée pour le dépôt de couches minces avec une distance substrat-cible fixée à 55 mm. L'équipement de pulvérisation est équipé d'un dispositif de contrôle optique in-situ et en temps réel pour contrôler l'épaisseur et la morphologie des couches en cours de dépôt.

Le substrat pendant le dépôt est à la température ambiante et les couches minces obtenues sont généralement amorphes et un recuit post-dépôt est nécessaire pour obtenir une couche mince cristallisée.

La Figure 13 montre les DRX des couches minces de Sb_2Se_3 (série T1), amorphe ou recuites à différentes températures, déposées sur un substrat en verre BK7 et d'une épaisseur de 400 nm. Tous les pics de diffractions sont attribuables au Sb_2Se_3 orthorhombique. Ces pics fins et intenses, sans aucun pic parasite, démontrent la bonne cristallinité et la pureté de ces couches minces.

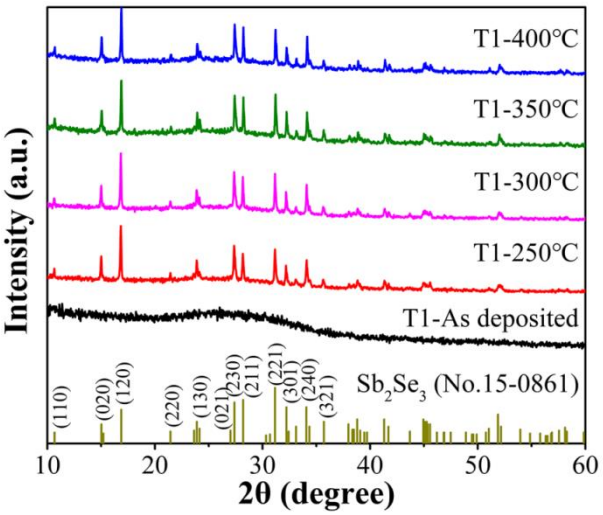

Figure 13. *XRD patterns of Sb_2Se_3 thin films annealed at different temperatures.*

La Figure 14 montre des images SEM des différentes couches minces après le traitement thermique à différentes températures. Pour la couche mince amorphe, la surface est lisse sans aucun grain cristallin. Après un traitement thermique à 250 ℃, comme indiqué sur la Figure 14b, la surface est devenue rugueuse, indiquant que la croissance cristalline est démarrée. Lorsque la température de traitement thermique est augmentée à 300 ℃, les grains cristallins deviennent plus visibles avec des joints de grains nets.

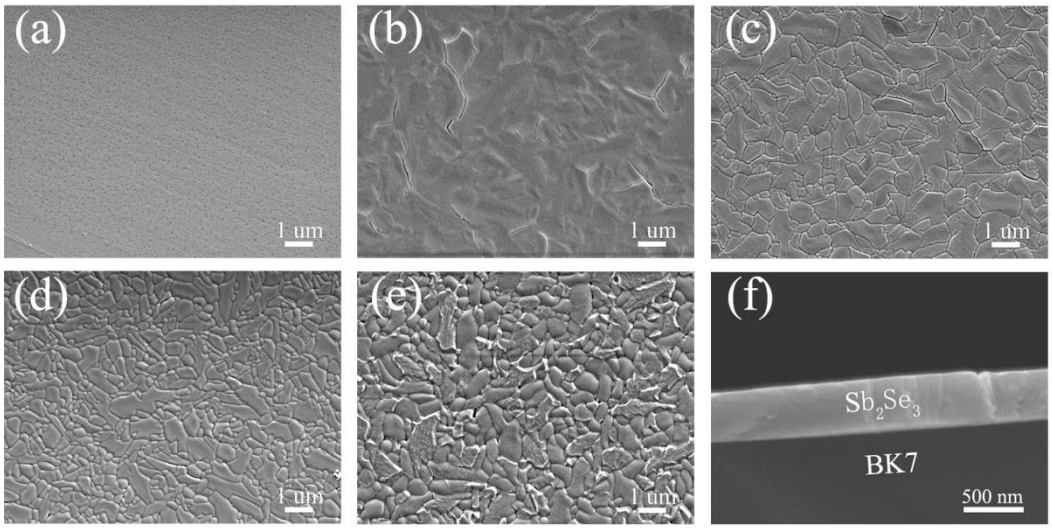

Figure 14. *SEM images of the Sb_2Se_3 thin films heat treated at different temperatures: (a) As-deposited; (b) 250 ℃; (c) 300 ℃; (d) 350 ℃; (e) 400 ℃; (f) Cross-sectional SEM image of the thin film heat treated at 350 ℃.*

Si la température de recuit continue d'augmenter, la morphologie ne sera pas modifiée significativement. Cependant, si la température de recuit est trop élevée, à 400 ℃ par

exemple, comme le montre la Figure 14e, la surface de la couche devient plus rugueuse avec un élargissement des joints de grains, dû à une évaporation préférentielle aux joints.

La Figure 14f montre la section de la couche recuite à 350 °C. L'interface avec le substrat de verre ne présente pas de défaut et l'épaisseur mesurée de la couche est d'environ 400 nm, en excellente conformité avec l'épaisseur mesurée par le système de contrôle optique en temps réel.

4.3 Propriétés optiques des couches minces à base de Sb_2Se_3

La largeur du bandgap est calculée en utilisant les spectres de réflexion et de transmission, mesurés dans un grand domaine spectral du l'UV jusqu'au proche infrarouge. Les Figures 15a-c montrent les spectres de transmission, les spectres de réflexion (face avant et face arrière) des couches amorphes et recuites à différentes températures. Ces spectres sont très différents.

La réflexion de la couche mince amorphe est inférieure à celle des couches cristallines dans la région de courtes longueurs d'onde où l'absorption est importante, dû à un indice de réfraction plus faible d'un réseau désordonné. Après un traitement thermique, l'ordre de la couche augmente, entrainant une augmentation de la réflectance. Si la température de recuit est trop élevée, la réflectance de la couche va diminuer, en raison d'une augmentation significative de sa rugosité. En résumé, la réflectivité des couches minces de Sb_2Se_3 est principalement affectée par la cristallinité et la rugosité de surface.

Le spectre de transmission de la couche mince amorphe montre une coupure de transmission, dans les courtes longueurs d'onde, vers 665 nm. Cette coupure est repoussée à environ 890 nm pour les couches minces cristallisées. Les calculs illustrés sur la Figure 15d indiquent que ce sont des semi-conducteurs à bandgap direct.

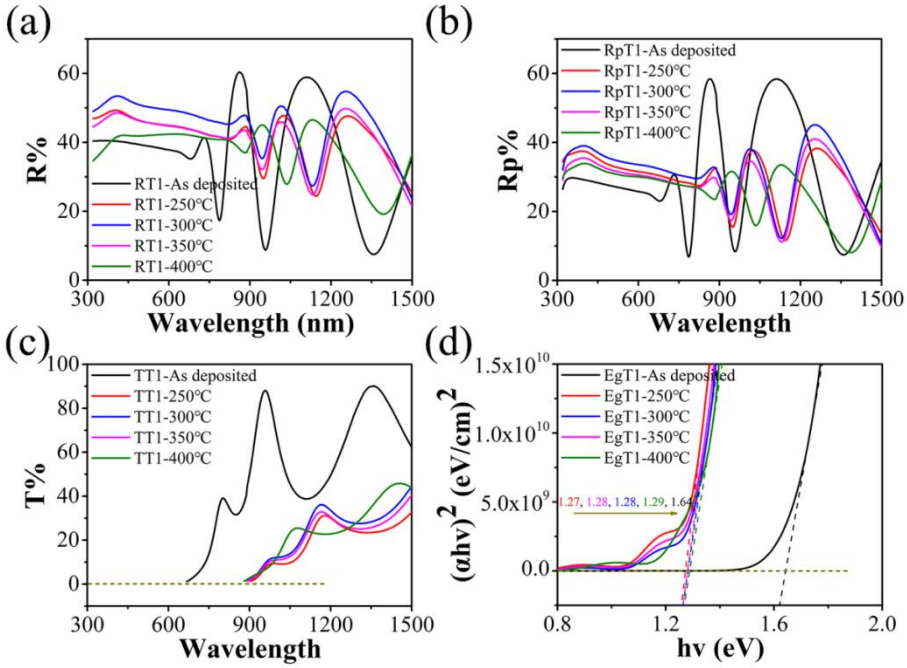

Figure 15. *Optical characterization of the Sb_2Se_3 thin films as a function of wavelength and with different temperatures of heat treatment. (a) Reflection spectra; (b) Back side reflection spectra, (c) Transmission spectra and (d) Plot of $(\alpha h\upsilon)^2$ vs. hv, from which direct band gap was obtained.*

4.4 Propriétés photoélectriques des couches minces à base de Sb_2Se_3

Ces propriétés ont été mesurées avec la méthode de trois électrodes, décrite précédemment. Les résultats sont présentés sur la Figure 16. La couche mince amorphe de Sb_2Se_3 présente un photocourant significatif avec un bias négatif, indiquant que c'est un semiconducteur du type p. Avec un recuit à 250 °C, la couche cristallisée est toujours du type P. Quand la température de recuit est élevée jusqu'à 350 °C, la densité du photocourant est nettement augmentée et la couche mince est devenue un semiconducteur du type n. Ce changement du type de conduction est probablement dû à une perte de sélénium lors du recuit à haute température.

La Figure 16-a4 montre la réponse temporelle d'une couche cristalline de Sb_2Se_3, recuite à 350 °C. La densité de courant augmente rapidement, de 28 uA.cm^{-2} à 202 uA.cm^{-2} sous une illumination de 25 mW.cm^{-2}. Ce processus est rapide, réversible et stable.

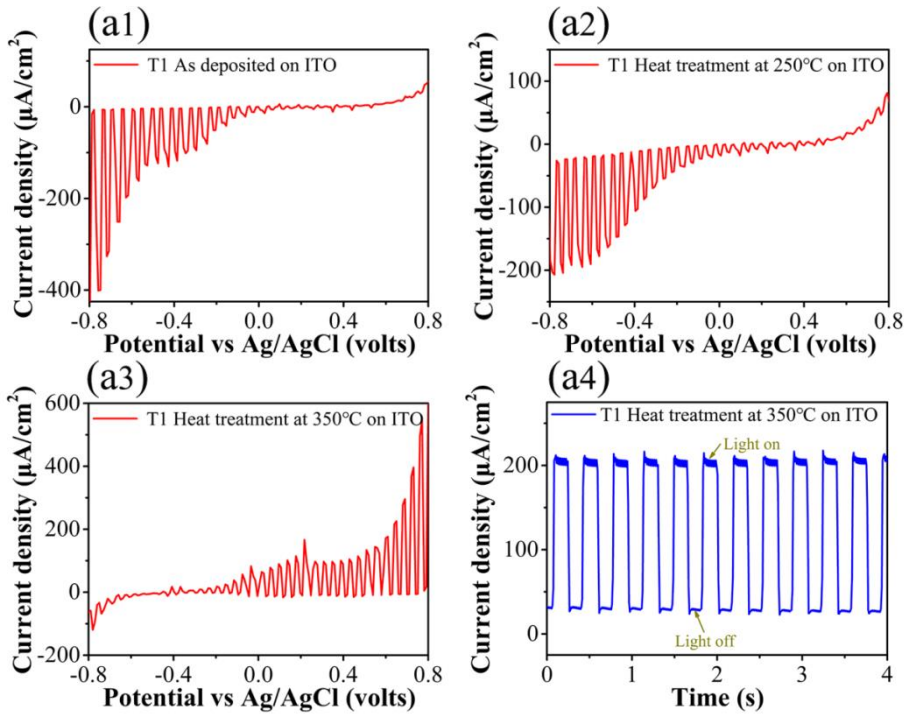

Figure 16. *Current density versus voltage curves obtained by using Sb_2Se_3 thin film as working electrode, where a1-a3 represent respectively amorphous Sb_2Se_3 thin film, Sb_2Se_3 crystalline thin films with heat treatment at 250 ℃ and 350 ℃. (a4) Time-resolved PEC photoresponse.*

4.5 Cellules solaires quasi-homojonction à base de Sb_2Se_3

Nous avons essayé de fabriquer une cellule solaire en couche mince avec une structure quasi-homojonction de Sb_2Se_3, qui peut être entièrement fabriquée sous vide. Cette structure est illustrée sur la Figure 17a. Figure 17b montre une courbe I-V avec une jonction $Sb_2(Se_{0.9}I_{0.1})_3/Sb_2Se_3$, où l'épaisseur de la première couche est de 70 nm et celle de la deuxième couche est de 400 nm. La température du traitement thermique des couches minces après dépôt est de 250 ℃. Un simulateur solaire AM 1,5G à 86 mW/cm^2 a été utilisé comme source d'éclairement. Ce dispositif présente une densité de courant de court-circuit (J_{SC}) de 7,62 mA/cm^2, une tension en circuit ouvert V (Voc) de 0,28 V et un taux de remplissage (FF) de 44,06%, conduisant ainsi à un rendement de conversion de 1,09%. En modifiant l'épaisseur de la couche absorbeur et la température du traitement thermique, la J_{SC} et le Voc du composant peuvent être améliorée. Cependant, en raison de la haute résistivité de la couche Sb_2Se_3, la résistance en série du composant lui-même est encore trop importante, ce qui limite l'amélioration du rendement de conversion.

Une nouvelle structure ITO/$Sb_2Se_{3.3}$/$Sb_2(Se_{0.9}I_{0.1})_3$/Au a été testée pour atténuer le problème lié à la haute résistivité du Sb_2Se_3. Cette fois-ci, la couche absorbeur est une couche relativement épaisse de $Sb_2(Se_{0.9}I_{0.1})_3$, de type n, avec une bonne conductivité. Elle forme une jonction p-n avec une couche de $Sb_2Se_{3.3}$. La courbe J-V, montrée sur la Figure 17c ne présente aucune hystérésis significative avec le balayage en voltage dans les deux directions. Ce dispositif donne un J_{SC} de 17,82 mA/cm^2, un V_{OC} de 0,32 V et un FF de 37,88%, ce qui donne un rendement de 2,65% pour cette cellule solaire photovoltaïque.

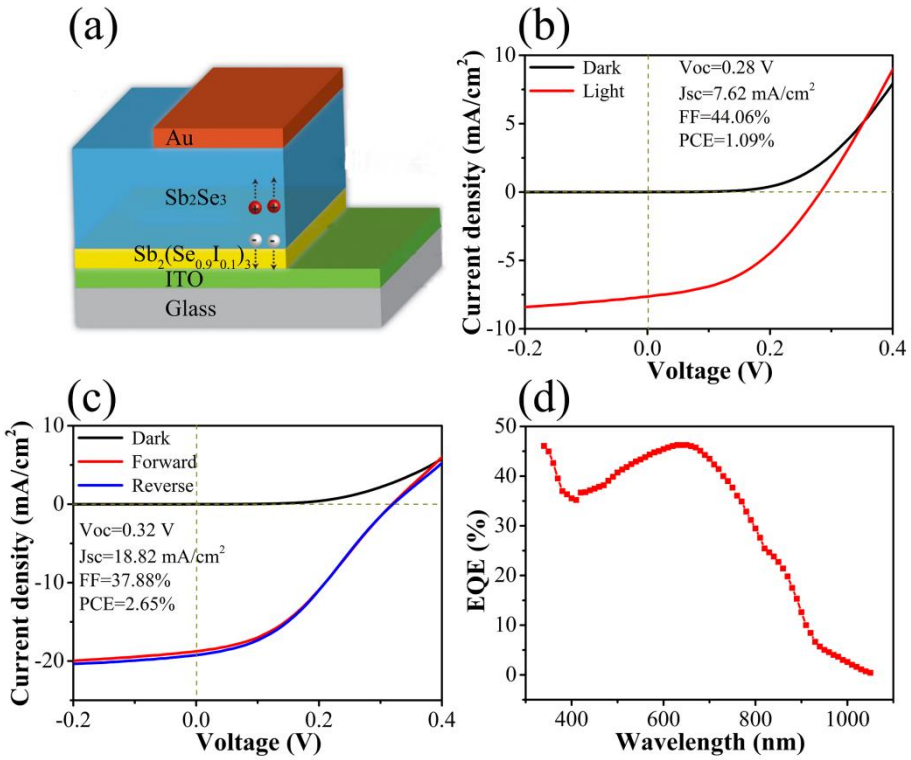

Figure 17. *(a) Schematic configuration of Sb_2Se_3 thin film solar cell with quasi-homojunction. (b) J-V curves of the $Sb_2(Se_{0.9}I_{0.1})_3$/Sb_2Se_3 thin film solar cell and (c) $Sb_2Se_{3.3}$/$Sb_2(Se_{0.9}I_{0.1})_3$ thin film solar cell under simulated AM1.5G illumination with intensity calibrated to 86 mW/cm^2, (d) EQE spectrum of the $Sb_2Se_{3.3}$/$Sb_2(Se_{0.9}I_{0.1})_3$ thin film solar cell.*

La Figure 17d montre le rendement quantique externe (EQE) de cette cellule solaire. Une valeur relativement faible de EQE est sans doute liée aux défauts présents à l'interface $Sb_2Se_{3.3}$/$Sb_2(Se_{0.9}I_{0.1})_3$, conduisant à des pertes importantes dues à une recombinaison des porteurs de charge photogénérés. L'amélioration de la qualité de cette interface et la passivation des surfaces sont certainement nécessaires pour améliorer le rendement de ces cellules photovoltaïques.

En comparaison avec les cellules solaires à base de Sb_2Se_3 publiées dans la littérature, notre cellule quasi-homojonction ne contient pas de couche tampon en ZnO ou en CdS et possède un EQE nettement plus élevé dans les courtes longueurs d'onde.

En résumé, C'est une 1ère étude sur les cellules solaires quasi-homojonction à base de Sb_2Se_3. Les premiers résultats sont déjà très intéressants et très encourageants.

4.6 conclusions

En utilisant la méthode de fusion sous vide, des cibles pour la pulvérisation cathodique de composition Sb_2Se_3, Sb_2Se_3., $(Sn_{0.1}Sb_{0.9})_2Se_3$ et $Sb_2(Se_{0.9}I_{0.1})_3$ ont été préparées. Toutes les couches minces déposées sur des substrats à température ambiante sont amorphes et leur cristallisation peut être contrôlée par un recuit thermique approprié. La température de recuit thermique peut changer le type de conduction des couches de Sb_2Se_3. La couche amorphe ou les couches minces recuites à basses températures sont de type p et un recuit à plus haut température donne une couche mince à conduction n en raison de perte partielle de sélénium pendant le recuit.

Le dopage permet d'obtenir des semiconducteurs de type p et n à base de Sb_2Se_3. Le dopage par Sn en remplacement de Sb donne un semiconducteur de type p and l'iode substituant le sélénium donne un semiconducteur de type n. Toutes ces couches donnent un photocourant relativement intense et stable.

Des cellules solaires quasi-homojonction à base de Sb_2Se_3 ont été conçues et fabriquées. La structure ITO/$Sb_2Se_{3.3}$/$Sb_2(Se_{0.9}I_{0.1})_3$/Au a été particulièrement étudiée. La couche $Sb_2(Se_{0.9}I_{0.1})_3$ a été utilisée comme couche absorbeur. Il a été démontré que la température de recuit des couches minces a une importance critique sur le rendement de la cellule solaire qui peut déjà atteindre 2,65%. Le rendement quantique est typiquement entre 40 et 48% avant la longueur d'onde de 700 nm et il chute rapidement dans les plus grandes longueurs d'onde. Ces premiers résultats sont très encourageants.

5. Préparation et caractérisation de photodiodes à hétérojonction γ-In_2Se_3/Si

Le séléniure d'indium (In_2Se_3) est un semi-conducteur important avec une structure en feuillet, un gap direct intéressant et un coefficient d'absorption élevé dans le domaine du visible. Ces propriétés en font un excellent candidat pour la conversion photoélectrique.

Il existe plusieurs composés stœchiométriques dans le système binaire In-Se avec plusieurs degrés d'oxydation de Sn. Plusieurs phases et structures peuvent même coexister. La clé pour développer des applications pour le Sn_2Se_3 est de synthétiser des matériaux chimiquement et cristallographiquement purs. A l'heure actuelle, la synthèse est généralement réalisée en phase liquide à pression atmosphérique ou avec les techniques hydrothermales/solvothermales.

La synthèse chimique colloïdale est une méthode de préparation plus sûre, plus simple et plus évolutive en raison de la réalisation à pression atmosphérique et en système ouvert. Il existe peu de publications sur la synthèse colloïdale des nanomatériaux de In_2Se_3. Dans ce travail, nous avons sélectionné la technique d'injection à chaud pour réaliser cette synthèse. Nous avons également développé et caractérisé des photodiodes à base de γ-In_2Se_3/Si afin de démontrer l'intérêt de ces matériaux.

5.1 Préparation et caractérisation de nanomatériaux à base de γ-In_2Se_3

Comme pour le Sb_2Se_3, la technique d'injection à chaud a également été utilisée pour synthétiser des nanoparticules de γ-In_2Se_3. Leurs structure et morphologie sont résumées sur la Figure 18. La Figure 18a montre le diffractogramme XRD de nanoparticules et tous les pics sont attribuables au γ-In_2Se_3 hexagonal sans aucun pic d'impureté, confirmant la pureté cristallographique de ce matériau.

L'image MEB montre un grand nombre de microsphères ressemblant à des boules de fleurs de l'ordre d'un µm de diamètre. Ces microsphères sont composées des feuillets bidimensionnels interconnectés d'une épaisseur d'environ 20 nm.

L'image HRTEM montre le réseau cristallin avec une distance inter-planaire de 0,354 nm, attribuable au plan (110) de la phase γ-In_2Se_3 (110) en accord avec les résultats DRX. La Fig. 18e montre quelques feuillets avec des réseaux de diffraction SAED, confirmant que la phase cristallisée est le γ-In_2Se_3 hexagonal. Enfin, l'analyse quantitative montre que la composition est proche de la composition stœchiométrique de In/Se=2/3.

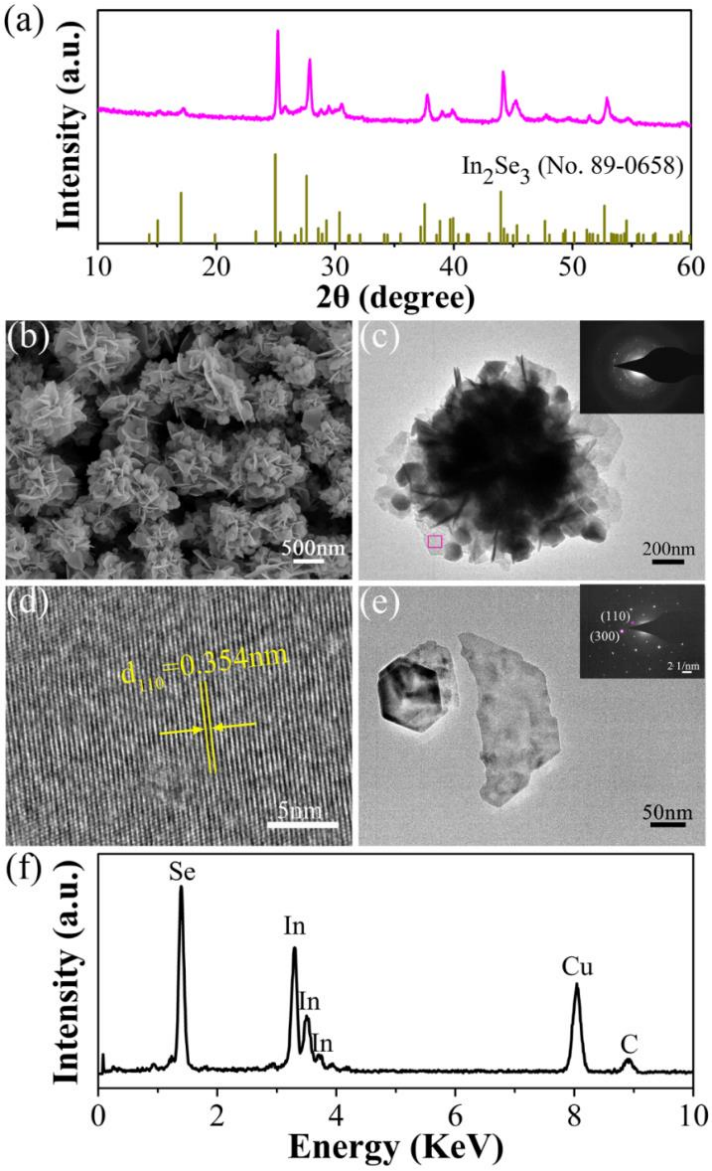

Figure 18. *Crystalline phase and morphological characterization of the γ-In_2Se_3 nanoflowers: (a) XRD pattern. (b) SEM image. (c) TEM image, the inset shows the corresponding SAED pattern. (d) HRTEM image from the pink marked area in (c). (e) TEM image of separated nanosheets from the nanoflower, the inset shows the SAED pattern of the right single nanosheet in (e). (f) EDX spectrum of a single nanoflower.*

5.2 Photodiode à hétérojonction γ-In_2Se_3/Si

Le spectre d'absorption, obtenu en mesurant la réflexion diffuse et illustré sur la Figure 19a, indiquent un bandgap direct d'environ 1,78 eV. Les mesures XPS montrent que le haut de la bande de vacance du γ-In_2Se_3 est situé à environ 0,46 eV.

Afin de démontrer le potentiel d'applications de ce semiconducteur, une photodiode à hétérojonction γ-In_2Se_3/Si, dont la structure est illustrée sur la Figure 19c, a été mise au point et caractérisée. Cette photodiode possède un champs électrique interne créé par cette hétérojonction dont le diagramme d'énergies est schématisé sur la Figure 19d qui illustre également le processus de transfert de charges photogénérées.

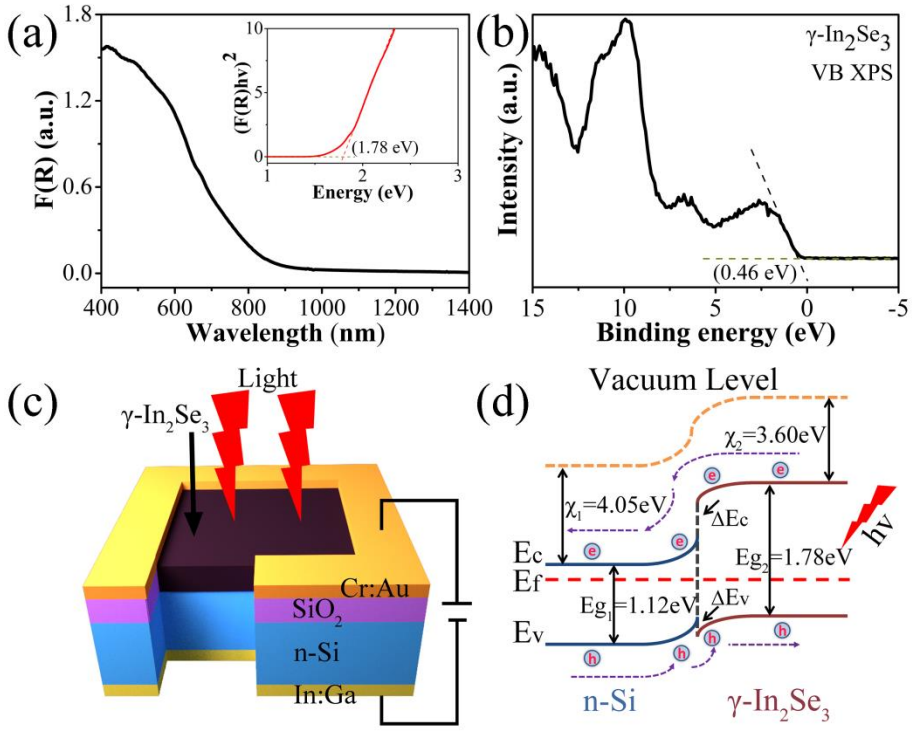

Figure 19. *(a) Optical absorption spectrum of γ-In_2Se_3 nanoflowers. Inset: A plot of $[F(R)hv]^2$ vs. photon energy, used to obtain direct band gap energy. (b) Valence-band XPS spectrum of γ-In_2Se_3 nanoflowers. (c) Schematic diagram of the γ-In_2Se_3/Si heterojunction photodiode. (d) Energy-band diagram of the heterojunction photodiode showing the photogenerated carriers transfer process under light illumination.*

La Figure 20a-c montre la relation entre le courant (I) et la tension appliquée (V) d'une photodiode à hétérojonction γ-In_2Se_3/Si dans le noir et sous illumination à différentes longueurs d'onde et avec différente intensités. Trois longueurs d'onde, 380 nm, 680 nm et 880 nm, d'une lampe au xénon ont été particulièrement étudiées. La courbe I-V dans le noir montre clairement les caractéristiques de rectification, indiquant l'existence d'une jonction p-n avec un courant d'obscurité très faible de -0,75 nA.

Sous illumination, le courant dans la région de polarisation négative augmente de manière significative et l'intensité du photocourant dépend directement de l'intensité d'illumination.

Comme montrée sur la Figure 20d, cette dépendance est quasiment linéaire. Les tests à différentes longueurs d'onde montrent que cette photodiode est sensible de l'UV jusqu'à proche IR.

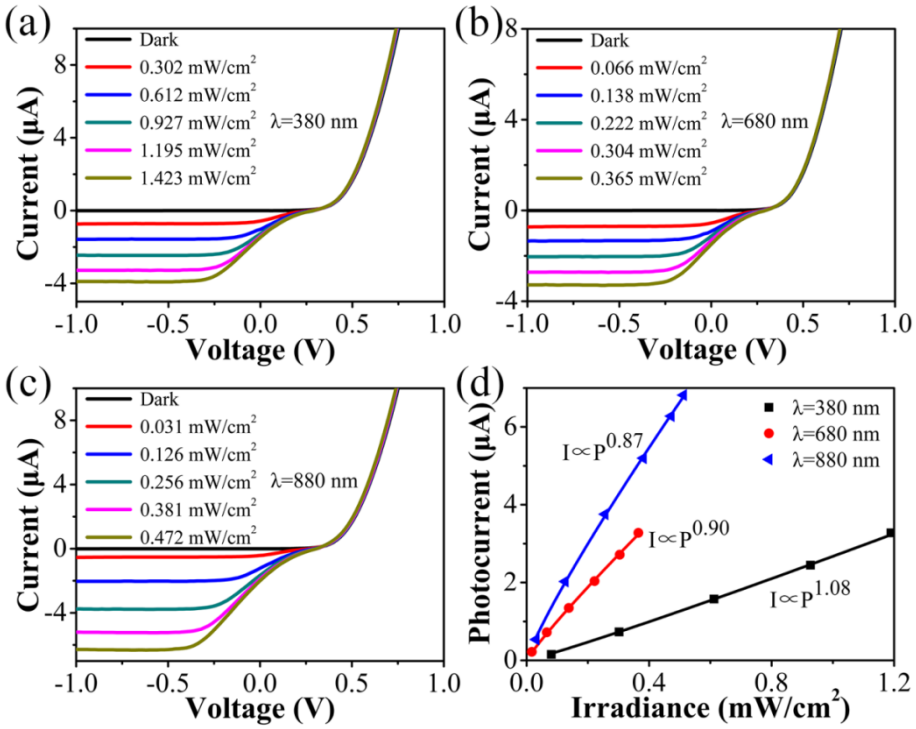

Fig. 20 *(a) Photoelectric properties of the γ-In_2Se_3/Si heterojunction photodiode under dark and illumination with different light intensities at various wavelengths. (a) 380 nm, (b) 680 nm and (c) 880 nm. (d) Relationships between the photocurrent and the light intensity at a bias of −1 V.*

Nous avons également étudié la réponse temporelle de la photodiode à hétérojonction γ - In_2Se_3/Si sous différentes tensions de polarisation. Les résultats montrent que cette photodiode peut s'autoalimenter et que le rapport «ON/OFF» atteint 1570, comparable aux meilleurs résultats publiés. Le temps de réponse et le temps de retour de la photodiode sont respectivement de 175 μs et 226 μs, également comparables aux meilleurs photo-détecteurs précédemment publiés.

Il a été également démontré que cette photodiode a une réponse spectrale très large, avec une sensibilité maximale de 5,67 A/W à 820 nm et une détectivité (D *) de 5,66 x 10^{13} Jones, confirmant l'excellente performance de cette photodiode à hétérojonction.

5.3 Conclusions

Des nanomatériaux à base de γ-In_2Se_3 ont été synthétisés avec la technique d'injection à chaud. Une photodiode, obtenue en déposant une couche de γ-In_2Se_3 de type p sur un substrat de Si de type n, a été conçue et réalisée. Cette photodiode peut s'autoalimenter avec une réponse rapide et une grande stabilité. Elle est sensible dans un large domaine spectral avec la plus haute sensibilité atteignant 5,67 A/W vers 820 nm. Les performances de cette photodiode sont comparables aux meilleurs détecteurs publiés dans la littérature, confirmant ainsi le potentiel d'application de cette photodiode à hétérojonction innovante.

6. Conclusions générales

Le développement de nouveaux matériaux semi-conducteurs est la base du développement de nombreuses applications. Dans ce travail, nous avons choisi d'étudier en particulier deux séléniures possédants d'excellente propriétés semiconductrices intrinsèques. Ce travail comprend la synthèse et la caractérisation de nanomatériaux et des composants photoélectriques utilisant ces matériaux.

Une photo-détecteur en couches minces à hétérojonction Sb_2Se_3/$AgSbSe_2$ a été préparée et caractérisée. Elle présente une très bonne sensibilité dans les domaines du visible et du proche-infrarouge, plus de quatre fois supérieure à celle du Sb_2Se_3 pur. Le photo-détecteur à base de Sb_2Se_3 dopé au Sn^{4+} démontre également d'excellentes propriétés photoélectriques avec notamment un NEP pouvant être aussi faible que $3{,}14 \times 10^{-13}$ W/$Hz^{1/2}$.

Le procédé de fusion-trempe a été utilisé avec succès pour la préparation des semiconducteurs polycristallins $(Sn_xSb_{1-x})_2Se_3$ et une série de semiconducteurs, de type p, a été obtenue avec une conductivité électrique contrôlable.

Le résultat le plus intéressant de ce travail concerne des cellules solaires photovoltaïques quasi-homojonction à base de Sb_2Se_3 avec en particulier la structure ITO/$Sb_2Se_{3.3}$/$Sb_2(Se_{0.9}I_{0.1})_3$/Au. La couche $Sb_2(Se_{0.9}I_{0.1})_3$ a été utilisée comme couche absorbeur. Il a été démontré que la température de recuit des couches minces a une importance critique sur le rendement de la cellule solaire qui peut déjà atteindre 2,65%. Le rendement quantique est typiquement entre 40% et 48% avant la longueur d'onde de 700 nm et il chute rapidement dans les plus grandes longueurs d'onde. Ces premiers résultats sont très encourageants.

Une partie de ce travail a été consacrée à l'étude de γ-In_2Se_3. Une photodiode à hétérojonction γ-In_2Se_3/Si a été préparée et caractérisée avec d'excellentes propriétés telles que un rapport «ON/OFF» pouvant atteindre 1570, une sensibilité maximale de 5,67 A/W à 820 nm et une détectivité (D*) de 5,66 x 10^{13} Jones.

Ces premiers travaux ont permis de démontrer le potentiel d'applications de ces deux semiconducteurs qui sont jusqu'au présent peu étudiés. Nous espérons que c'est une nouvelle étape dans la recherche et le développement de ces matériaux pour des applications notamment photoélectriques.

GENERAL INTRODUCTION

Since nearly half a century, semiconductor technology has made rapid development as the core of modern high technology. It has set off a new round of revolutionary movement of information technology, and has promoted the progressive climax of human civilization. Nowadays, new materials and functional devices based on semiconductor technology are emerging in an endless stream and play a vital role in all aspects of human life. Energy and environment are the two major global challenges today and in order to address these two issues, it is also urgent to develop appropriate semiconductor technology.

Semiconductor is a kind of functional materials with the conductive capacity between the conductors and the insulators. According to the chemical composition, semiconductors can be divided into three major categories, namely, elemental semiconductors, inorganic compound semiconductors and organic compound semiconductors. Among them, metal selenide semiconductors play a very important role and have drawn tremendous research attention. The band gap of selenide semiconductors is generally between 0.3 eV and 3 eV, covering a wide range of wavelengths from infrared to ultraviolet. Due to the excellent electrical and optical properties, they have been widely used for, such as solar cells, thermoelectric devices, light emitting and display devices, infrared detectors, lasers, nonlinear optical materials, hydrogen production via water splitting and photocatalytic waste degradation.

At present, selenide semiconductors mainly exist in three forms: bulk, nanomaterials and thin film materials in scientific research and practical applications. In general, they have a complex preparation processes and their excellent properties are mainly determined by the crystal structure, size, dimensions, surface structure and band structure. For example, bulk selenide semiconductors are typically prepared by a process combing the preparation of powdered raw materials and high-temperature sintering. They obey the solid theory, and the crystal structure determines the energy band structure and defect structure, which fundamentally affect the physical and chemical properties. When the size of a selenide semiconductor is reduced to nanometer scale, a series of new properties will appear, which are neither similar to the macroscopic bulk material nor belong to its single atomic molecule. The most studied effects include quantum size effect, small size effect, surface effect, macro quantum tunneling effect and dielectric confinement effect. Moreover, the emergence of these new properties for the selenide semiconductors will bring new optical, electrical, thermal and

magnetic properties, and then shows a broader perspective for practical applications. Selenide semiconductor nanomaterials are mainly synthesized with chemical reactions under specific conditions. Finally, the thin film form is still the focus of current research and applications for selenide semiconductors. Remarkable achievements have been achieved in the fields of thin film preparation process, properties optimization and functional devices applications.

With the continuous progress of our society, the requirements for semiconductor materials are also increasing, especially for materials used in the fields of home equipment, telecommunications, industrial production, aerospace and so on. Therefore, it is still of great significance to speed up the fundamental research and application development of selenide semiconductor materials. In this dissertation, two different selenide semiconductors (Sb_2Se_3 and In_2Se_3) with excellent properties are selected as our research targets, including controllable preparation of materials and exploration of applications as high performance photoelectric functional devices.

This thesis is structured into five chapters. In the first chapter, we will give a overview of the preparation technology for the selenide semiconductor materials, including bulk materials, nanomaterials and thin film materials. Then combined with our research project, the selenide semiconductor photodetectors and solar cells will be particularly discussed. In Chapter II, Sb_2Se_3 nanorods will be synthesized via hot-injection method, and the biggest challenge of low electrical conductivity of Sb_2Se_3 nanorods will be overcome successfully by forming heterojunction and/or doping. The high performance prototype photodetectors based on Sb_2Se_3 nanorods will be constructed and tested. The third Chapter is devoted to the investigation of the Sb_2Se_3 based bulk materials, prepared by using high-temperature melting process. In Chapter IV, the high-temperature melting method will also be used to obtain Sb_2Se_3-based targets, which can be further used for the preparation of thin films by Radio Frequency (RF) magnetron sputtering. The quasi-homojunction Sb_2Se_3 thin film solar cells will also be prepared based on those high-quality thin films, which show high application potential. In the last Chapter, uniform γ-In_2Se_3 nanoflowers will be synthesized via the hot-injection method. In combination with the mature Si-based semiconductor technology, a high performance γ-In_2Se_3/Si heterojunction photodiode will be fabricated for the first time.

CHAPTER I: SELENIDE SEMICONDUCTOR MATERIALS FOR PHOTOELECTRIC APPLICATIONS

1.1 Introduction

Since nearly half a century, semiconductor technology has made rapid development as the core of modern high technology. It has set off a new round of revolutionary movement of information technology, and has promoted the progressive climax of human civilization. Nowadays, new materials and functional devices based on semiconductor technology are emerging in an endless stream and play a vital role in all aspects of human life. A simple schematic illustration of the semiconductor industry is shown in Fig. 1.1 [1], where the semiconductor materials and devices are the pillar industry, playing a key role. As we all know, the basis for the development of semiconductor technology is the development of semiconductor materials.

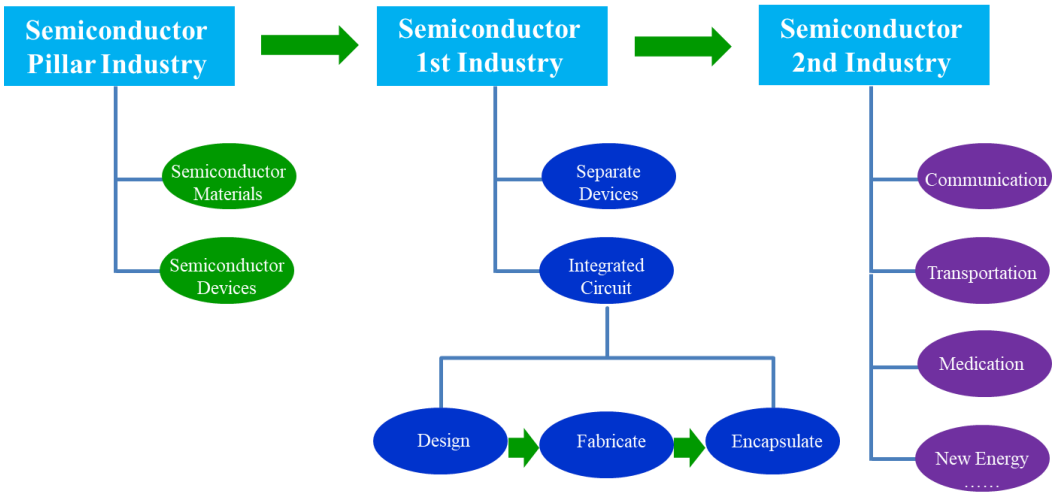

Fig. 1.1 A simple schematic illustration of the semiconductor industry

At first, we need to understand some basic knowledge of semiconductor materials. Semiconductor is a kind of functional materials with the conductive capacity between the conductors and the insulators. The conduction is mainly realized by electrons in the conduction band or holes in the valence band. When it is subjected to external light, heat or doping by trace impurities, its electrical conductivity may change significantly. There are many kinds of classification of semiconductor materials. According to the chemical composition, they can be divided into three major categories, namely, elemental semiconductors, inorganic compound semiconductors and organic compound semiconductors. Among them, the elemental semiconductors include 11 elements with semiconductor characteristics. Due to the stability of the element itself and the limitation of the preparation process, only three elemental semiconductors, Ge, Si and Se show practical application values

at present. Inorganic compound semiconductors can be further divided into binary systems, ternary systems, and higher-order systems. Common binary compound semiconductors including groups of I-VI (eg, Ag_2Se, Cu_2S, etc.), II-VI (eg, CdSe, ZnS etc.), III-V (eg, GaAs, InAs etc.), IV-IV (eg, SiC, GeSi etc.), IV-VI (eg, SnSe, PbS etc.) and V-VI (Sb_2Se_3, Bi_2S_3 etc.). The ternary and higher-order compound semiconductors mainly include groups of I-III-VI (e.g., $CuInSe_2$, $AgInS_2$ etc.), I-II-IV-VI (e.g., $Cu_2ZnSnSe_4$, Cu_2CdSnS_4 etc.) and some solid solutions (e.g., $CdS_{1-x}Se_x$, $CuIn_xGa_{1-x}S_2$ etc.). The organic compound semiconductors are well-known such as naphthalene, anthracene, polyacrylonitrile, phthalocyanine, and some aromatic compounds.

As can be seen from the above classification of semiconductor materials, metal selenide semiconductors play a very important role in the entire semiconductor materials family. The band gap of selenide semiconductors is generally between 0.3 eV and 3 eV, covering a wide range of wavelengths from infrared to ultraviolet. They have drawn tremendous research attention and have been widely used for, such as solar cells, thermoelectric devices, light emitting and display devices, infrared detectors, lasers, nonlinear optical materials, hydrogen production via water splitting and photocatalytic waste degradation.

At present, selenide semiconductors mainly exist in three forms: bulk, nanomaterials and thin film materials in scientific research and practical applications. In general, their excellent properties are determined by the crystal structure, size, dimensions, surface structure and band structure. For example, bulk selenide semiconductors obey the solid theory, and the crystal structure determines the energy band structure and defect structure, which fundamentally affect the physical and chemical properties. When the size of a selenide semiconductor is reduced to nanometer scale, a series of new properties will exhibit, which are neither similar to the macroscopic bulk material nor belong to its single atomic molecule, such as quantum size effect, small size effect, surface effect, and macro quantum tunneling effect and dielectric confinement effect. Moreover, the emergence of these new properties for the selenide semiconductors will bring new optical, electrical, thermal and magnetic properties, and then shows a broader perspective in practical applications. Finally, the thin film form is still the focus of current research and applications for selenide semiconductors. Remarkable achievements have been achieved in the fields of thin film preparation process, properties optimization and functional devices applications.

With the continuous progress of our society, the requirements for semiconductor materials are

also increasing, especially for the materials used in the fields of home equipment, telecommunications, industrial production, aerospace and so on. Therefore, it is of great significance to speed up the fundamental research and application development of selenide semiconductor materials.

1.2 Preparation technology of selenide semiconductors

1.2.1 Preparation of bulk selenide semiconductors

Bulk selenide semiconductors refer to solid materials that have a three-dimensional structure and are relatively large in size. They have the inherent optical and electrical properties with large-scale, thus show a certain application value in the fields of optoelectronics, thermoelectrics, and magnetic semiconductors [2-4]. Bulk selenide semiconductors can be prepared in a variety of ways including Melting, Powder Metallurgy, Hot Pressing Sintering, Spark Plasma Sintering.

(1) Melting is a traditional production process in which the solid raw materials are melted into liquids, accompanied by a certain physical and chemical reaction at high temperature, and finally the desired solid product is obtained after cooling. It needs to go through a liquid-to-solid phase conversion, and the reaction process can be affected by the melting point, chemical activity, and saturated vapor pressure. Therefore, for selenide semiconductors, vacuum melting and zone melting are more widely used in practical applications [5,6]. In vacuum melting, the raw materials are vacuum-sealed into a quartz tube and put into a resistance furnace for high-temperature melting. Compared with ordinary melting processes, the advantages of vacuum melting are as follows: i. Raw materials are isolated from the external environment during the melting process, which can minimize the presence of impurities; ii. The evaporation of the components is impossible during vacuum melting process in closed system, which is very important for Se with high vapor pressure when melted; iii. The vacuum melting process is simple in operation, short in production cycle, and has great application value in practical industrial production. Another technique named zone melting was first presented by Keek and Golay in 1953 [7]. For this method, only a part of the raw materials is melted at any time during the entire growth process, and the melting zone is supported by the surface tension. Therefore, it is also called “float-zone method”. The raw materials are generally sintered rods, and then are fixed with two chucks and placed horizontally or vertically in the tubular furnace. Using a high-frequency coil or focused

infrared heating the localized portion of the sintered rod, the melting zone is gradually moved from one side to the other to complete the crystallization process. The crystals grown by this method are of high quality and are commonly used for the physical purification of materials and also for the growth of crystals, especially single crystals. In recent years, with the rising research attention on selenide optoelectronic and thermoelectric materials, reports on the preparation of high-quality bulk selenide semiconductors using the above-mentioned melting techniques are also emerging rapidly [8,9].

(2) Powder metallurgy is a method for preparing metallic materials, semiconductor materials, composite materials and ceramic materials by using forming and sintering processes. The general process of powder metallurgy is milling-pressing-sintering-post treatment. In the preparation of transition metal selenide semiconductors, powder metallurgy is a common and effective method [10].

(3) Traditional polycrystalline bulk semiconductor materials are mostly formed by cold pressing coupled with sintering. The obtained samples show low bulk density, making the mechanical properties difficult to meet the processing requirements. In addition, the higher internal void ratio significantly reduces carrier mobility, resulting in a lower electrical conductivity compared to its single crystal. Afterwards, efforts have been put on the development of new forming and sintering processes [11-16]. At present, great progress has been made in the hot-press-sintering process.

Hot-press sintering refers to a process for sample preparation by filling the dry powders into a mold with limited space and then heat it while pressing from a uniaxial or isostatic direction. Fig. 1.2 shows a typical schematic of vacuum hot-press sintering and the corresponding heat treatment program [11].

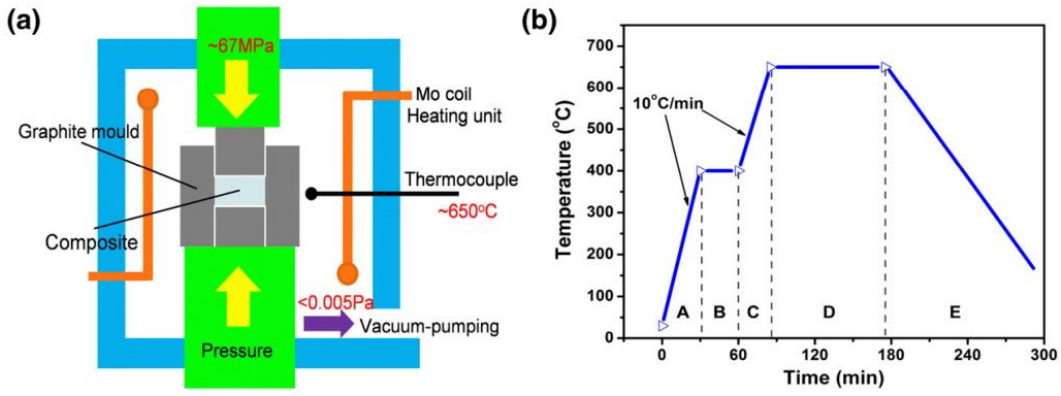

Fig. 1.2 (a) Illustration of the vacuum hot pressing; (b) the typical sintering procedure

Hot-press sintering has the following advantages: i. During the hot-pressing, because the powder is in thermoplastic state, the deformation resistance is small, plastic flow and densification will be easier, leading to a lower forming pressure; ii. Synchronizing the pressure and the heating is helpful for the contact, diffusion and flow of grains, thus greatly reducing the sintering temperature and shortening the sintering time, which is also the biggest feature of hot-press sintering; iii. Hot-press sintering allows obtaining easily sintered samples close to the theoretical density, with preferred crystal orientation and also with fine grains. In general, it is easy to obtain a bulk material with excellent mechanical and electrical properties by hot-press sintering.

Hot-press sintering technique has been widely used in the preparation of bulk selenide semiconductors [12-14]. Herein, using In_4Se_3 bulk thermoelectric material as an example, it was prepared using melting-pulverizing process combined with hot-press sintering in the early stage. Shi et al. firstly melted and crushed the raw material powders, and then sintered the as-prepared powders to bulk In_4Se_3 at 450 ℃. The maximum relative density reached 95.9%, and the sample had a ZT value of 0.6 at 700 K [15]. Then, in order to overcome the segregation of impurities caused by the melting process, the powder was mechanically alloyed, and the In_4Se_3 bulk thermoelectric material was prepared by hot-press sintering. This sintering method can effectively prevent the volatilization of In and Se elements in the molten state, therefore improving also the utilization rate of raw materials. Moreover, the obtained bulk material had uniform composition and fine grain structure, which can significantly improve the thermoelectric properties. For example, Yang et al. reported using high-purity In and Se as raw materials for mechanical alloying for 1 hour, then the powder was hot-press sintered into bulk In_4Se_3 and the maximum ZT value could reach 0.93 [14].

(4) Spark Plasma Sintering (SPS) is a new technology for sintering bulk materials by using discharge plasma. Compared with the traditional sintering techniques, it has some advantages such as heating uniformly, heating rapidly, sintering at a lower temperature and shorter sintering time. It is suitable for obtaining samples with features of fine crystal structure and high density. Fig. 1.3 is a schematic illustration of a typical SPS instrument, mainly composed of a pulsed DC generator, a vacuum system, a pressure system, a cooling system, and a control system.

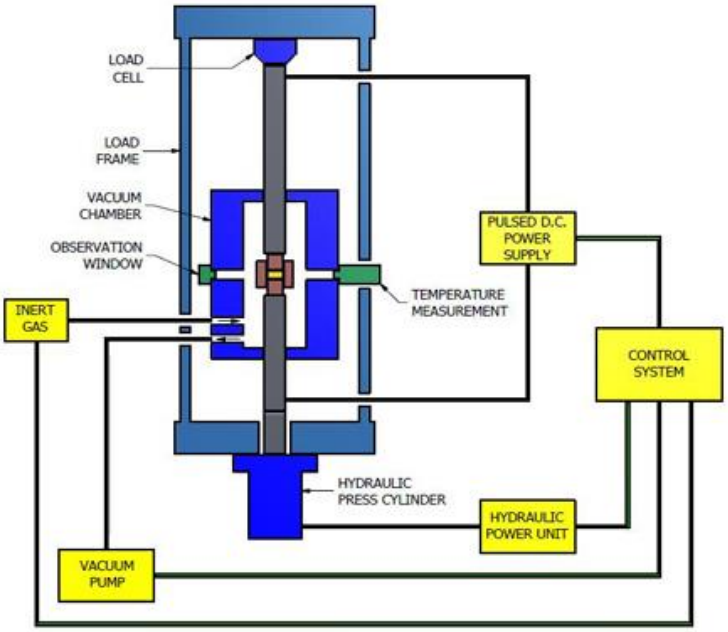

Fig. 1.3 Illustration of Spark Plasma Sintering

In recent years, researches on the preparation of new materials using SPS have mainly focused on ceramics, metal alloys, intermetallic compounds, composite materials, and other functional materials [16]. Among them, the most studied are functional materials, including thermoelectric materials [17], magnetic materials [18], functionally graded materials [19], composite functional materials [20], and nano-functional materials [21]. The application of SPS is also more and more widely used for selenide semiconductors [9, 22-25]. In the preparation of thermoelectric materials, Fu et al. used zone melting in combination with SPS to prepare SnSe polycrystalline semiconductor thermoelectric materials with a ZT value higher than 1.0 [9]; Samanta et al. successfully prepared n-type BiSe bulk semiconductors with low thermal conductivity and high thermoelectric property by using vacuum melting combined with SPS [22]. Preparation of thermoelectric semiconductors using SPS is not only superior in thermoelectric performance but also in process advantages, such as direct process into wafers, eliminating the need of cutting processes, which can effectively save materials and increase production efficiency. For the preparation of other selenide functional materials, SPS has gradually played an important role. Wei et al. presented a combined process of ball milling and SPS to prepare high density ZnSe bulk semiconductor, which provided a meaningful basis for subsequent optical applications [23]. Tyagi et al. reported the preparation of Cu_2Se photovoltaic materials using SPS [24], Maier et al. reported that a novel quaternary $Ba_2FePnSe_5$ (Pn=Sb, Bi) phase transition polycrystalline bulk could be prepared by ball milling combined with SPS process [25].

1.2.2 Preparation of selenide semiconductor nanomaterials

Nanomaterials are defined as materials in which at least one dimension is at nanometer size (0.1-100 nm) or consist of them as a basic unit. The preparation methods of the selenide semiconductor nanomaterials mainly include physical methods and chemical methods. Among them, the former usually involves optical, electrical etching or physical construction techniques. Such preparation processes are often in harsh conditions and need expensive equipment. Therefore, it is often not the best choice for preparing nanomaterials. Chemical methods can be divided into three categories: solid-phase method, liquid-phase method and gas-phase method. All these three methods are based on the chemical reactions under certain conditions. The solid-phase method means preparing a nanomaterial by using the corresponding solid phase reaction directly. This process is simple and scalable. However, this technique leads generally to low purity materials with difficultly controllable morphology. Similarly, the gas-phase method uses gaseous reactants to chemically obtain the expected nanomaterials. Unlike the solid-phase method, the as-prepared nanomaterials in this way show higher purity and morphology controllability. The most common method belongs to the gas-phase methods is Chemical Vapor Deposition (CVD), which mainly refers to the formation of nanomaterials by reacting chemical elements generated by one or more gaseous elements or compounds on a heated substrate. This process is particularly applicable to the preparation of layered transition metal selenide semiconductors. For example, Chang et al. used CVD to prepare monolayer $MoSe_2$ with fast photodetection properties (Fig. 1.4) [26]. Liu et al. used WO_3 and Se powders as raw materials, and a single layer of WSe_2 was successfully prepared in a CVD reactor [27]. Cho et al. reported a one-step CVD method for preparing a gas sensor based on the two-dimensional $NbSe_2/WSe_2$ alloy junction [28]. In addition, it is worth mentioning that Vapor-Liquid-Solid (VLS) synthesis process has unique advantages in the preparation of one-dimensional selenide nano-semiconductors, and has been widely used. Akhtar et al. used a single precursor source combined with VLS process to control the synthesis of highly crystalline, defect-free and monodisperse one-dimensional PbSe nanowires with nanowire diameters ranging from 8 to 25 nm and lengths up to micrometers [29]. Yang et al. used $Sb(NMe_2)_3$ and Et_2Se_2 as raw materials to synthesize Sb_2Se_3 nanowire arrays on Si substrates under the assistance of Au catalysts (Fig. 1.5) [30].

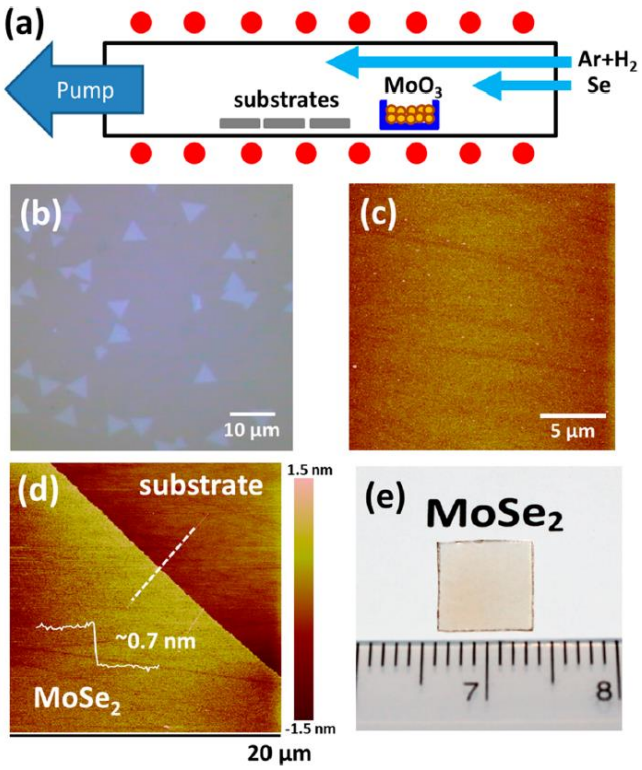

Fig. 1.4 (a) Schematic illustration for the growth of $MoSe_2$ layers on sapphire substrates by the selenization of MoO_3 powders in a CVD furnace. (b) Optical microscopic (OM) image and (c) AFM image of the monolayer $MoSe_2$ flakes and monolayer film grown at 800 °C. (d) AFM image and (e) photo of a monolayer $MoSe_2$ film grown at 800 °C on a sapphire substrate

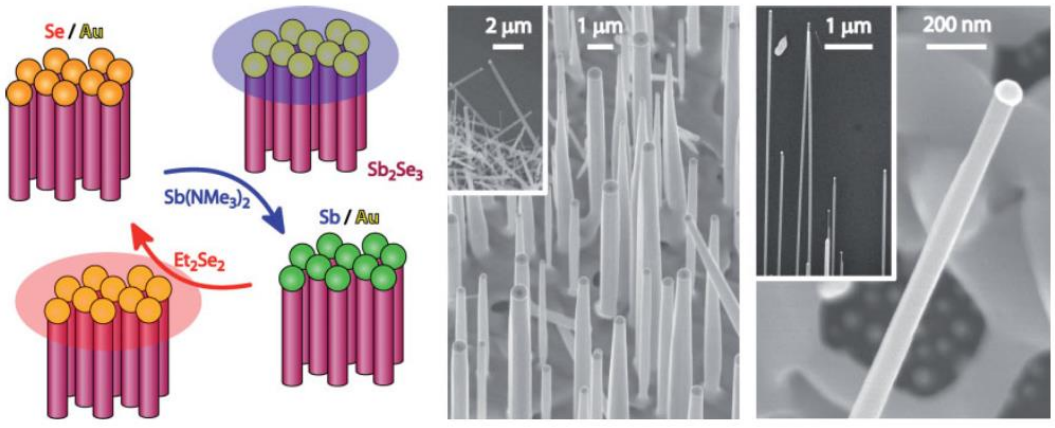

Fig. 1.5 Aspects of antimony sulfide and selenide wires. Left, illustration displaying the principle of the pulsed growth (shown for Sb_2Se_3): upon exposure to the Sb precursor (blue cloud), the Se present in the Au catalyst reacts to form Sb_2Se_3 wire grows. Then excess Sb dissolves to saturation; similarly, subsequent reaction of Sb in Au with the Se precursor (red cloud) grows Sb_2Se_3 further and leaves Se-saturated Au ready for the next cycle. Center, SEM image of Sb_2S_3 wires. Right, SEM image of Sb_2Se_3 wires

Finally, the liquid-phase method is a process for preparing nanomaterials via chemical reaction in solution. In comparison, the reaction condition is relatively facile, and it is convenient to control and to adjust the reaction process. For example, the nucleation growth rate of the nanocrystals can be controlled by changing the reaction temperature, the size of the nanocrystals can be regulated by changing the concentration of the precursor, and the various morphologies can be achieved by adding different surfactants. In general, the liquid-phase method is also the most common method for preparing selenide semiconductor nanomaterials. The following paragraph will focus on several liquid-phase synthesis processes that are widely used.

1.2.2.1 Thermal decomposition

The thermal decomposition method refers here to prepare nanomaterials using organometallic precursors via thermal decomposition reaction at a certain temperature. This method was originally mainly used for the preparation of II-VI and IV-VI semiconductor nanocrystals. Bawendi et al. presented this method for the first time in 1993 to prepare CdSe nanoparticles [31]. During the process, $Cd(CH_3)_2$ was used as a cadmium source and $(SiMe_3)_2Se$ was used as selenium source, TOP/TOPO (trioctylphosphine/trioctylphosphine oxide) were used as solvents, the obtained CdSe nanocrystals showed high-quality and are monodispersed. Tremendous research attention started to focus on the semiconductor nanocrystals since this report. Moreover, researchers began to explore more green synthetic processes. Firstly, because the organic metal source $Cd(CH_3)_2$ is highly toxic and explosive, Peng et al. used the safe inorganic sources, CdO [32], $Cd(AC)_2$ [33], and $CdCO_3$ [34] as the substitutes to prepare high-quality CdSe nanomaterials. Then, in order to eliminate the use of highly polluting coordinating solvents (TOP/TOPO), some low toxicity non-coordinating solvents gradually attracted great attention. In 2005, Boatman et al. used CdO as a cadmium source, octadecene as solvent and oleic acid as surfactant. CdSe quantum dots (QDs) with different sizes were successfully synthesized by dissolving Se into a non-coordinating solvent octadecene (ODE). Under ambient light, the color of colloidal suspensions of CdSe QDs changes from yellow-green to orange-red as the size increases. It gradually changes from blue to yellow under ultraviolet light (Fig. 1.6) [35].

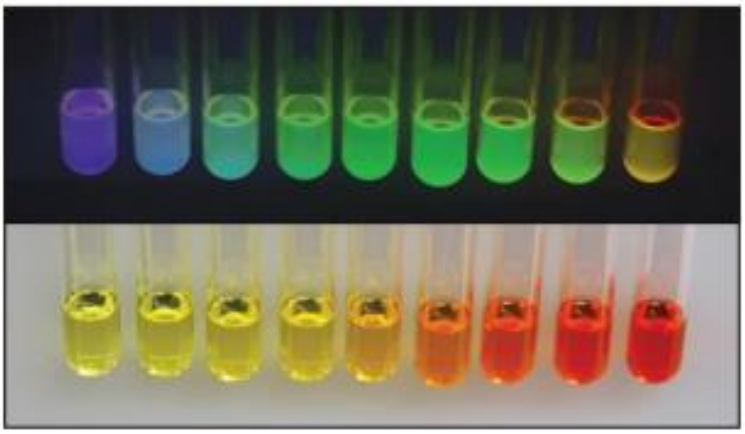

Fig. 1.6 Colloidal suspensions of CdSe quantum dots of increasing size from left to right. Bottom: Samples under ambient light. Top: The same samples under under long-wave ultraviolet illumination

With the thermal decomposition method becoming more and more sophisticated, other selenide semiconductor nanomaterials can also be prepared. For example, Deng et al. reported a simple low-cost thermal decomposition process involving hot-injection method to synthesize $Sb_2Se_{3-x}S_x$ ($0 \leq x \leq 3$) nanotubes. The schematic illustration of the proposed nanotube formation mechanism is shown in Fig. 1.7 [36]. Castro et al. prepared ternary $CuInSe_2$ nanocrystals by thermal decomposition of $(PPh_3)_2CuIn(SePh)_4$ [37]. Ng et al. synthesized $AgInSe_2$ nanorods with orthorhombic phase structure by thermally decomposing a single precursor with mixed solvents of oleylamine and dodecanethiol [38].

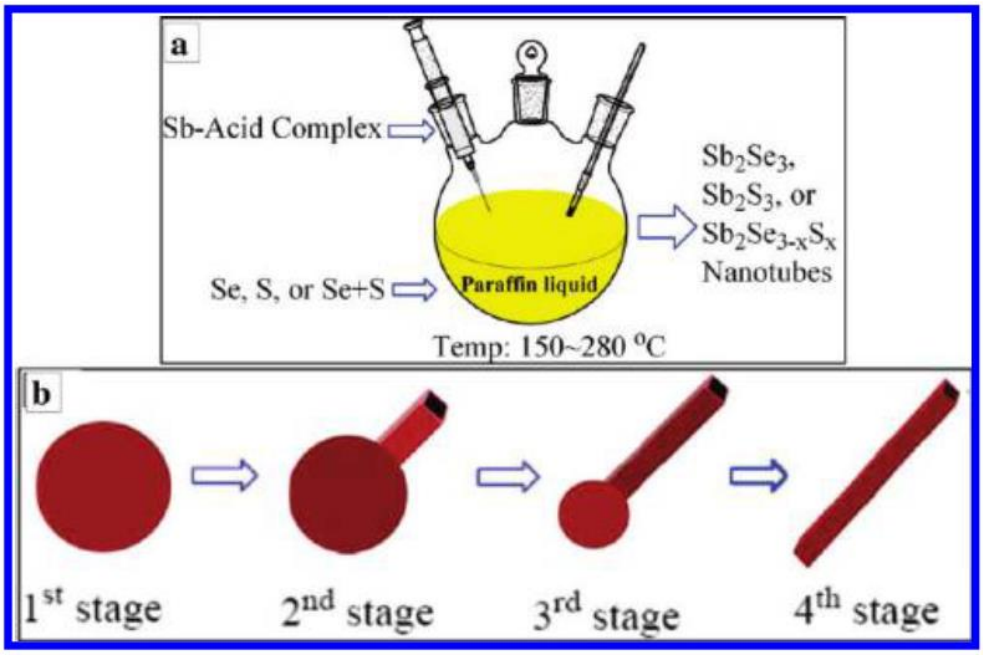

Fig. 1.7 (a) Overall Synthetic Scheme of Sb_2S_3, $Sb_2Se_{3-x}S_x$ ($0<x<3$), and Sb_2Se_3 Nanotubes; (b) Schematic Illustration of the Proposed Nanotube Formation Mechanism

In general, the thermal decomposition method has some unique advantages in the preparation of selenide semiconductor nanomaterials: i. The reaction occurred in organic solvents can effectively inhibit the oxidation, which is very important for the synthesis of high-purity nanomaterials; ii. In organic solvents, the reactivity of the reactants is generally higher. Therefore, it is easy to achieve soft chemical synthesis, thereby obtaining metastable phases with special optical, electrical and magnetic properties; iii. Some non-reactive substances can be decomposed or chemically reacted in a high-temperature organic solvents system.

1.2.2.2 Hydrothermal/Solvothermal Methods

Hydrothermal and Solvothermal refer to the use of aqueous solution, organic solvent, or a mixture of water and organic solvent as reaction medium in a closed reaction vessel (such as an autoclave). It is an effective method for materials preparation by heating to a specific temperature and creating a high-pressure local environment in the reaction system. Among them, solvothermal method is generally favored for those reactions with insolubles at ambient pressure or containing water-insensitive constitutes. Compared to other liquid-phase synthesis processes, the hydrothermal/solvothermal process has several significant advantages. Firstly, the reaction occurs in a closed vessel, under relatively high pressure conditions, thus the nanomaterials can be synthesized at a lower temperature. Secondly, the activity of the reactants are actually changed and improved, therefore, some special compound nanomaterials can be prepared. Thirdly, it is easy to control the morphology, size and also surface modification of the products by changing the reaction conditions such as reaction temperature, time, precursor concentration, solvents and so on. The as-synthesized nanomaterials usually show high crystallinity, high purity and good dispersibility.

In the preparation of selenide semiconductor nanomaterials, hydrothermal/solvothermal methods have also been widely used. Ma et al. reported the hydrothermal synthesis of one-dimensional Sb_2Se_3 nanowires (Fig. 1.8) [39]. The size and morphology of the samples can be effectively controlled by the concentration of the reactants and the reaction temperature, and the sample morphology directly influences its electrochemical hydrogen storage capacity. Gu et al. used CuCl and Se powders as raw materials to prepare hexagonal CuSe nanosheets by hydrothermal method. Experimental studies showed that the solvent NaOH solution and surfactant polyvinylpyrrolidone (PVP) play an important role in the formation of the nanosheets [40]. Yang et al. reported the solvothermal preparation of γ-In_2Se_3 nanoflowers, which were easily synthesized via the reaction of indium chloride and selenium powders with

the assistance of ascorbic acid at 220 ℃ for 20 h in an ethanol-solvothermal system [41]. Dong et al. reported a facile solvothermal method for the synthesis of Ag_2Se QDs with strong luminescent properties [42]. The solvothermal method using a mixed organic/water solvents system is also an effective route. For example, Gao et al. reported that the Fe_7Se_8 nanocrystals containing two (001) planes and twelve (012) planes can be synthesized in a mixed solvent of diethylenetriamine and deionized water at 140 ℃ for 12 h [43].

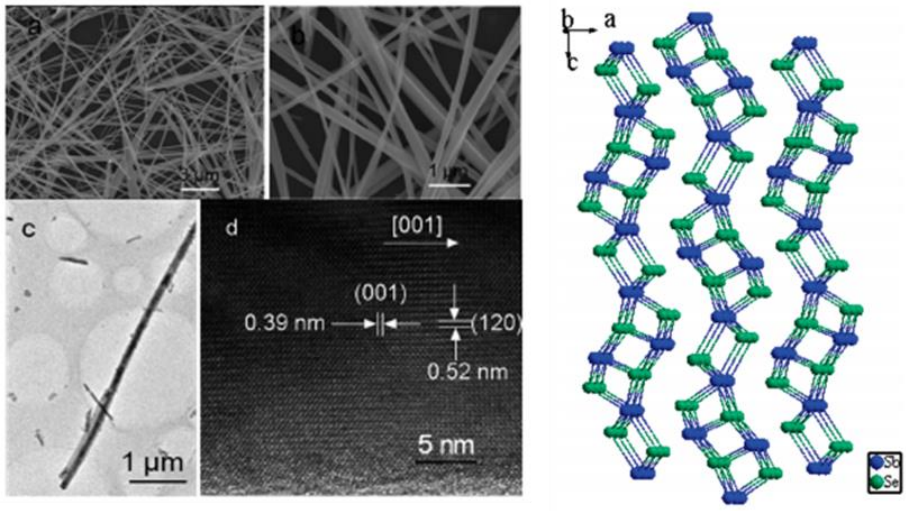

Fig. 1.8 One-dimensional Sb_2Se_3 nanowires synthesized via hydrothermal method. Left: (a, b) Typical SEM images of as-prepared nanowires; (c) a part of an individual nanowire; and (d) corresponding HRTEM image of the individual nanowire. Right: Crystal structure of Sb_2Se_3

1.2.2.3 Microemulsion method

The microemulsion method refers to two kinds of incompatible solvents forming an emulsion under the action of surfactant. Nanomaterials will be obtained through nucleation, agglomeration and heat treatment in microbubbles. It is characterized by monodisperse and good interfacial properties of the obtained nanoparticles. II-VI semiconductor nanoparticles are commonly prepared with this method [44-46]. Microemulsions are thermodynamically stable, transparent or translucent, dispersed solution systems with a particle size distribution of 1-100 nm. The commonly used microemulsion systems include oil-in-water (O/W type) normal micelles and water-in-oil (W/O type) reverse micelle structures (Fig. 1.9) [47]. Among them, the selenide semiconductor nanomaterials generally adopted the W/O type reversed-phase micelle systems, and mainly consist of surfactants, cosurfactants, water and organic solvents.

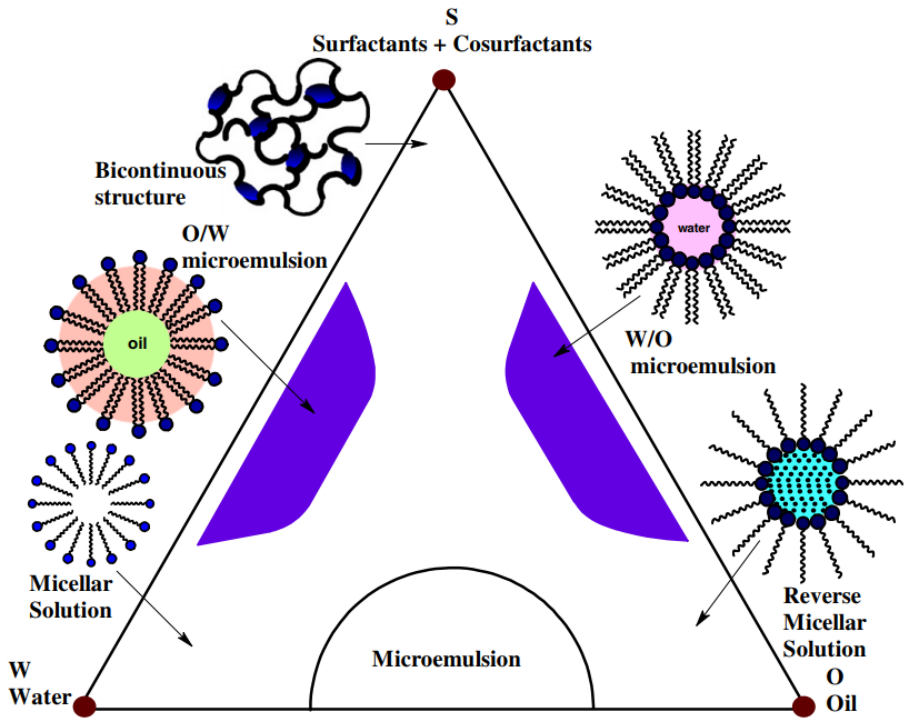

Fig. 1.9 Hypothetical phase regions of microemulsion systems

Water-in-oil (W/O) microemulsions are formed by the dispersion of nanometer-sized water droplets in a continuous oil phase, similar to that in which colloids are dissolved, while surfactant molecules are located at the water-oil interface to stabilize these water droplets. The size and morphology of the nanoparticles formed in the microemulsion system are not only related to the crystal structure, but also controlled by the water/oil ratio and by the content of the surfactant molecules. The specific working mechanism is to change the strength of the film at the interface, thereby changing the size, curvature and shape of the formed water droplets, and ultimately regulate the collision, aggregation and crystallization processes of the reaction materials. Since the first report on the preparation of CdS nanoparticles by the microemulsion method in 1984 [48], there have been numerous reports on the preparation of selenide semiconductor nanomaterials via this method. Xi et al. used hydrated hydrazine and AOT as surfactants to successfully synthesize CdSe nanorods at 100 ℃ using a water-in-oil microemulsion method. Experiments showed that the hydrazine hydrate acted as both a reducing agent and a templating agent that favors the formation of a rod-like structure [49]. Karanikolos et al. reported the preparation of ZnSe nanoparticles with controllable size and luminescence properties by microemulsion method [50]. Moreover, it can also be used to prepare nanocomposites, such as CdS/CdSe, CdSe/ZnS, CdSe/ZnSe. [47].

In addition to the above methods, there are also other important liquid-phase synthesis

processes in the preparation of selenide semiconductor nanomaterials, such as coprecipitation [51], sol-gel [52], template [53,54], ultrasonic [55] and microwave-assisted methods [56, 57]. In general, with the continuous development of nanomaterials synthesis methods, it is possible to obtain the nanomaterials with specific shapes and properties. Current synthetic technology is still perfectible for developing specific materials according to various application requirements. The development of a simple, controllable, versatile, and environmentally friendly method for the synthesis of nanomaterials is still a hot research topic.

1.2.3 Preparation of selenide semiconductor thin films

The preparation of bulk selenide semiconductors and nanomaterials has been summarized above. However, it is worth noting that most applications of selenide semiconductors are still in film form. Extensive researchers have been focused on the preparation of selenide semiconductor thin films. The corresponding preparation methods can be divided into physical and chemical categories according to the working mechanisms. The former generally utilizes physical reactions based on high temperature or high energy, and the latter method realizes film deposition through chemical reactions. According to the film growth environments, the corresponding preparation methods can be divided into gas-phase methods and liquid-phase methods, summarized in Table 1.1.

Table 1.1 Typical thin film preparation methods [58]

Preparation methods	Chemical methods	Physical methods
Gas-phase methods	Low pressure CVD, Spray pyrolysis, Plasma enhanced CVD, Metal organic CVD, Atomic layer deposition	Vacuum evaporation deposition, Plasma deposition, Sputtering deposition, Molecular beam epitaxy
Liquid-phase methods	Chemical bath deposition, Sol-gel method, Continuous ion layer adsorption, Electrodeposition	Liquid-phase epitaxy, LB method

As can be seen from Table 1.1, in the preparation of selenide semiconductor thin films, gas-phase methods are mostly based on vacuum technology, with relatively high requirements of equipment. Differently, chemical liquid methods are simple, low-cost, but probably more difficulty for controlling the film quality. The following paragraph will describe some common methods in detail, compare their advantages and disadvantages, and provide

references for further research.

1.2.3.1 Evaporation deposition

Evaporation deposition refers to the use of resistance heating or electron beam and laser bombardment to heat the evaporation source materials to a certain temperature under vacuum, so that the thermal vibration energy of molecules or atoms in the material exceeds the surface binding energy. A large number of atoms will then evaporate or sublimate, and finally condensate on the substrate to form thin films. The vaporization process, with or without gas injection can lead to thin films with different chemical composition.

Evaporation deposition has been widely used in the preparation of selenide semiconductor thin films. For most binary metal selenides, high-purity selenide powders are generally used as raw materials to be directly vaporize and to form the corresponding thin films on substrates. Typical examples are ZnSe [59], CdSe [60], Sb_2Se_3 [61], PbSe [62]. Then for multi-metal selenide semiconductors, multi-source co-evaporation or multi-step evaporation can be used, followed by diffusion, reaction, and other processes to form the expected multi-metal selenide semiconductor thin films. For example, Amara et al. used Cu, In-Ga, and Se as evaporation sources to obtain polycrystalline $Cu(In,Ga)Se_2$ thin film by co-evaporation [63]; Park et al. reported the sequential thermal evaporation of In_2Se_3 and Cu_2Se on glass substrates, and $CuInSe_2$ films were formed by annealing them in a Se atmosphere at 550 ℃ [64]. Sharma et al. presented thermally and sequentially evaporated the Cu/In/Se stacked layers on a Mo-coated glass substrate to prepare $CuInSe_2$ thin film (Fig. 1.10) [65]. For another common multi-selenide semiconductor, $Cu_2ZnSnSe_4$, the corresponding thin films can also be obtained by co-evaporation or multi-step evaporation [66,67]. It has also been reported that the reactive evaporation (such as SnSe [68], Ag_2Se [69], etc.) and post selenization are efficient techniques for thin film deposition of selenide compounds [70].

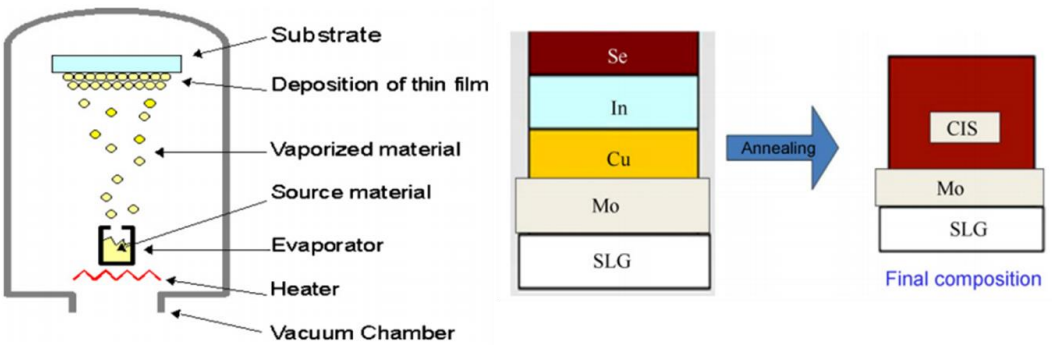

Fig. 1.10 Schematic diagram of vacuum thermal evaporation of $CuInSe_2$ thin film

The evaporation method has the advantages of easy operation, high-speed film formation and high production efficiency. It is one of the most widely used techniques in films preparation. The main drawback of this technology is the low use rate of raw materials. This can be an issue especially when precious materials are used.

1.2.3.2 Chemical Vapor Deposition (CVD)

CVD method involving chemical reactions usually occurs in a high temperature space. The main process consist of supplying gaseous constitutes to the substrate. Then a chemical reaction (including thermal decomposition, redox, combination reaction etc.) occurs on the surface of the substrate to form the expected thin films. According to the difference in raw materials, the CVD methods can be divided into metal organic vapor deposition (MOCVD) and atomic vapor deposition (ALCVD).

CVD method is also widely used in the preparation of selenide semiconductor thin films, including binary selenide films such as WSe_2 [71], Cu_2Se [72], $SnSe/SnSe_2$ [73], In_2Se_3 [74], ternary $CuInSe_2$ films [75] and quaternary $Cu_2ZnSnSe_4$ films [76]. The advantages of CVD method include: i. The film formation speed is fast, generally several micrometers per minute; ii. The obtained films usually show good adhesion, high-purity and high-crystallinity.

1.2.3.3 Sputtering deposition

In recent years, the sputtering deposition method has been developed rapidly and has a wide range of applications in many fields such as metallization of thin film semiconductor materials, coating of architectural glass surfaces, reflective coatings on polymers, wear-resistant coatings on mechanical surfaces, and even decorative coatings [77]. The basic principle of sputtering deposition is to bombard the surface of a solid target with high-energy particles (usually positive ions accelerated by an electric field), so that surface target atoms or molecules exchange kinetic energy with incident high-energy particles and are then ejected from the surface and are re-deposited into thin film on the substrate. This technique can generally give an excellent composition transfer from the target to the thin film. Reactive sputtering deposition can also be realized with the assistance of reactive gas. Moreover, if a magnetic field is established on the surface of the cathode target, it is then possible to control the movements of secondary electrons, which are trapped in the plasma area near the target surface. The ionization rate of the gas will be greatly increased, leading to significantly higher deposition rate. This method is called magnetron sputtering.

Sputtering methods also have specific applications in the preparation of selenide semiconductor thin films. The common preparation routes include the following three types: i. Deposited by radio frequency sputtering using the metal selenide as a target, which is widely reported for the preparation of $Cu_{2-x}Se$ [78], In_2Se_3 [79], Sb_2Se_3 [80], $Cu(InGa)Se_2$ [81] and other thin films. ii. Sputtering metal (or alloy) layers, which are then post-selenized. This process is easily scalable and a typical application is the preparation of $Cu(In,Ga)Se_2$ thin films. For example, Kushiya et al. reported that a Cu-Ga/In alloy was used as raw material to sputter a prefabricated layer on Mo-coated glass substrate and then selenized to obtain a solar cell absorber layer with a size of 30 cm×30 cm [82]. iii. Reactive sputtering, this process can achieve high-quality in-situ deposition of metal selenide semiconductor thin films. However, it uses the highly toxic reaction gas of H_2Se and its practical application is limited [83].

1.2.3.4 Electrochemical Deposition

Electrochemical deposition is a process in which a loop is formed by cathode and anode in a certain electrolyte solution under the action of electric field, when the oxidation-reduction reaction occurs, ions in the solution will be deposited on the electrode surface to obtain the desired thin film. Fig. 1.11 is a schematic diagram of the typical electrochemical deposition process. An external power supply is used to control the potential or current of the electrode during operation. Therefore, in terms of control mechanism, the most common methods are potentiostatic electrodeposition, galvanostatic electrodeposition and pulsed electrodeposition. Among them, potentiostatic electrodeposition is characterized by the constant deposition voltage and it is often used for the preparation of uniform alloy or compound films. At present, most of the metal selenide semiconductor thin films are prepared by potentiostatic electrodeposition method. For example, group IB Ag_2Se film [84], group IIB ZnSe [85], CdSe [86] films, group VIB $MoSe_2$ [87] film, Group IIIA In_2Se_3 [88] film, group IVA SnSe [89] , PbSe [90] films, group VA Bi_2Se_3 [90], Sb_2Se_3 [91] films and so on. Galvanostatic electrodeposition can be achieved by controlling the intensity of the current flowing through the electrodes during deposition. It is relatively simple, and has strong applicability to the electrodeposition of metal materials. Some selenide semiconductor thin films, such as ZnSe [92], CdSe [92], Bi_2Se_3 [93] and $CuInSe_2$ [94] have been prepared through galvanostatic electrodeposition. The main advantage of the final pulsed electrodeposition is the reduction of the concentration polarization, which can significantly improve the physical properties of the deposited films. In the preparation of metal selenide semiconductor films, this technique has also been widely used for the preparation of ZnSe [95], In_2Se_3 [96], $CuInSe_2$ [97], Cu (In,Ga)

Se_2 [98], $Cu_2ZnSnSe_4$ [98] thin films etc.

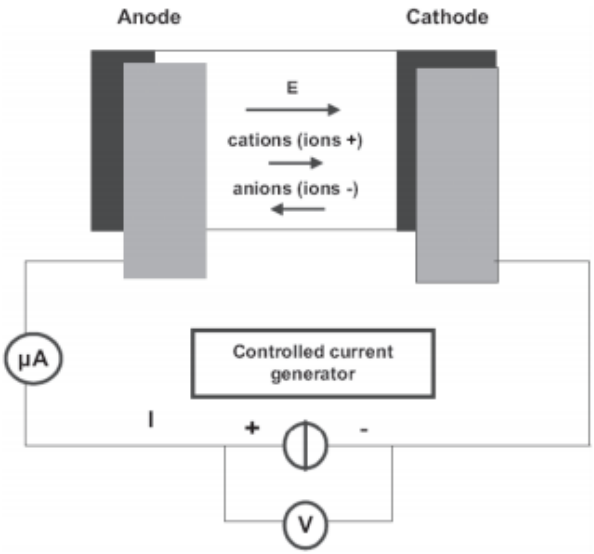

Fig. 1.11 General schematic diagram of the electrodeposition process

In summary, electrochemical deposition of selenide semiconductor thin films has some obvious advantages, like low deposition temperature, low-cost process and easy controllability of thin films. However, it has also some deficiencies. For example, it is difficult to electrochemically deposit selenide semiconductor thin films with complex composition. In addition, the growth of the crystal nucleus on the substrate surface is difficult to control, thus generally resulting in polycrystalline or amorphous nature of the as-deposited thin films.

1.3 Introduction of selenide semiconductor photodetectors

This section will focus on the applications of selenide semiconductors in functional devices. Combined with the research project of this thesis, theirs applications as photodetectors and thin film solar cells will be particularly discussed. Firstly, a semiconductor photodetector is a device based on the intrinsic light absorption and the associated effects such as photoconductivity, photovoltaic effect. Photodetector is an important photon-electron conversion device.

In recent years, semiconductor photodetectors have played an important role in a wide range of applications such as visible light detection, industrial automation control, thermal imaging, infrared remote sensing and missile guidance [99]. In the commercial markets, they can be applied for circuit isolators, intrusion alarms and fiber optic communications. For efficient

operation, semiconductor photodetectors must show high sensitivity, high response speed, relatively low noise and high reliability. Nowadays, a large number of application requirements and scientific research have promoted the continuous development and maturation of semiconductor photodetectors technology.

1.3.1 Working mechanism of semiconductor photodetectors

1.3.1.1 Optical absorption of semiconductor materials

The principle of light generated current in a photodetector is based on the photoelectric effect of the semiconductor materials. Therefore, it is necessary to understand the light absorption of semiconductor materials, which can be roughly classified into intrinsic absorption, exciton absorption, impurity absorption, and free carrier absorption.

(1) Intrinsic absorption

In pure semiconductors, free carriers and impurities are generally low in concentration. If photons with sufficient energy are applied to the semiconductor, the electrons in valence band may be excited to the conduction band by generating electron-hole pairs. In the frequency range of intrinsic absorption, the absorption spectrum contains information of the band structure. Moreover, for direct band gap and indirect band gap semiconductors, the nature of the absorption transition is different, because in the electronic transition process, energy and momentum conservation need to be satisfied at the same time. Fig. 1.12 represents the photon absorption in a direct bandgap semiconductor and an indirect bandgap semiconductor, respectively [100].

In the transition of photon, the momentum conservation is given by:

$$\hbar k' - \hbar k = \hbar k_l \quad (1.1)$$

Where k and k' are the wave vectors of the initial and final states of electrons, k_l is the wave vector of photons, and $k_l = 2\pi/\lambda$, but the momentum of the photons involved in the transition is much smaller than the electron momentum. So it can be approximately described as:

$$\hbar k' = \hbar k \quad (1.2)$$

That is, in the transition process, the wave vectors of the electrons remain unchanged. From the energy band diagram, it is equivalent to the vertical transition of electrons from the valence band to the conduction band, which is called direct transition. In direct bandgap semiconductors, electrons transitions generally exist in this form.

The indirect bandgap semiconductors show the transition of the electrons from the top of the valence band toward the bottom of the conduction band with different k values, which are called indirect transitions. Momentum conservation can be described by the following equation:

$$\hbar k' - \hbar k = \pm \hbar q \quad (1.3)$$

Where q is the wave vector of the phonon, "+" and "–" correspond to the process of absorption and emission, respectively. The corresponding energy conservation can be expressed as:

$$E_{k'} - E_k = \hbar w \pm \hbar w_q \quad (1.4)$$

Where $\hbar w$ and $\hbar w_q$ are photon energy and phonon energy, respectively. This indirect transition involving photons and phonons is generally less probable.

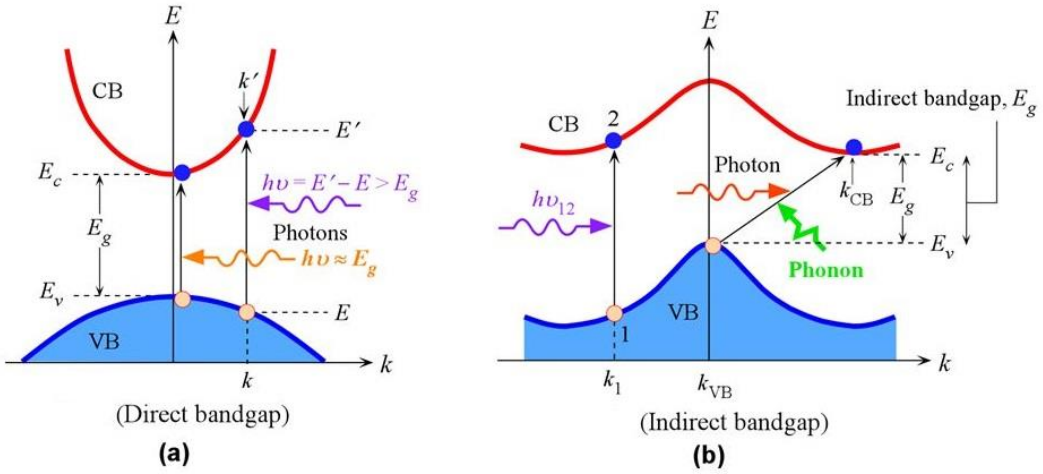

Fig. 1.12 Illustration of (a) direct transition of electrons in direct bandgap semiconductor and (b) indirect transition of electrons in indirect bandgap semiconductor

(2) Exciton Absorption

In the band theory of single electron, the Coulomb interaction between a single electron and hole is not included. This Coulomb interaction can lead to the formation of bound states between electrons and holes, which are called excitons. In the exciton state, electrons and holes as a whole can move freely in the crystal. However, this process does not generate current flow due to its electrically neutral nature as a whole. Photoexcitation can generate excitons, and the required photon energy to form excitons is lower than that of free electrons and holes. The absorption spectrum in the vicinity of the intrinsic absorption threshold is referred to as an absorption edge, and the additional absorption due to the formation of excitons in the vicinity of the absorption edge is referred to as exciton absorption.

(3) Impurity absorption

Under the action of photons with appropriate energy, electrons and holes bound by impurity levels can also induce optical transitions. It mainly includes shallow ionized impurities, neutral impurities, and electronic transitions between energy bands. The absorption of transitions between the impurity levels and the adjacent main energy band can be used to form the photoconductive effect. This principle has been applied in infrared photodetectors.

(4) Free carrier absorption

Free carriers are carriers that can move freely within the band. In the semiconductor, they refer to the electrons of the conduction band and the holes of the valence band. Even if the energy of the incident photon is not enough to cause electron transitions or excitons from the valence band to the conduction band, free carriers can be allowed to have transition between different energy levels of the conduction band or valence band. The light absorption of free electrons in the conduction band is caused by the transitions between the conduction states of the different electronic states of the wave vector k in the energy valley and is an indirect transition process. The light absorption of the valence band free holes is a direct transition between the different branches of the valence band, similar to the direct transition absorption between the valence band and the conduction band. It is worth noting that free carriers generally induce light absorption in the broad infrared spectral region.

1.3.1.2 Response of semiconductor junctions to light illumination

The interaction of photons with electrons in semiconductor materials is called the photoelectric effect. According to the location and the nature of the effect, it is usually divided into external photoelectric effect and internal photoelectric effect. The external photoelectric effect refers to the photoelectric conversion phenomenon that occurs on the surface of the material. If the incident photon energy is large enough, it interacts with the electrons in the material and causes the electrons to escape from the surface, which is also called photo-emissive effect. The internal photoelectric effect refers to the phenomenon of photoelectric conversion that occurs within a substance, that is, a phenomenon in which an electron-hole pair is generated after absorbing a photon and the carrier concentration in the semiconductor is therefore changed. Semiconductor photodetectors use this internal photoelectric effect to detect optical signals.

The detection of optical signals can generally be divided into three steps: i. Light absorption and electron-hole pairs generation; ii. The transmission of generated electron-hole pairs with or without gain; iii. Collection and conduction of carriers to external circuit.

Photodetectors mainly use the intrinsic absorption of semiconductor materials. When the incident photon energy is higher than the band gap energy, the electrons in the valence band are excited to the conduction band, leaving one hole in the valence band. The induced electron-hole pairs generate a photocurrent under the effect of an electric field. Therefore, the detection is closely related to the wavelength of the incident light. The relationship between the energy and the wavelength of the photon is:

$$E=hv=hc/\lambda \tag{1.5}$$

In this equation, h is Planck's constant, c is the speed of light in vacuum and λ is the wavelength of the incident light. Furthermore, the detection cut-off wavelength corresponding to the intrinsic absorption limit of the semiconductor material can also be obtained.

If the light with power P_0 is incident on the semiconductor material with surface area of A and surface reflectance of R, then the light intensity P(x) from the light incident surface x can be expressed as [101]:

$$P(x)= P_0(1-R)\exp(-\alpha x) \tag{1.6}$$

Where α is the absorption coefficient of the semiconductor material. Therefore, the light generation rate G(x) is defined as:

$$G(x)=\frac{P(x)-P(x+\Delta x)}{\Delta x A h v}=\frac{\alpha P(x)}{A h v} \tag{1.7}$$

According to the above analysis, it can be seen that the light generation rate is closely related to the absorption coefficient of the semiconductor material, and the detection wavelength of the photodetector is also closely related to the band gap. For selenide semiconductors, the absorption coefficient is generally large with also narrow band gap. Therefore, they show high potential for applications as broadband high-performance photodetectors.

Then, the internal photoelectric effects can be divided into photoconductive effect and photovoltaic effect, in which the former is the change of the conductivity caused by light illumination. For intrinsic semiconductors, without light illumination, only minority carriers have transition from the valence band to the conduction band due to thermal excitation. The corresponding conductivity is generally very low, which is called the dark conductivity. Under illumination, the incident photons excite electrons from the valence band to the conduction

band, which increases the number of electrons and holes, causing a significant change in electrical conductivity. The photodetector based on this effect is generally a photoconductive type device, such as photo-resistor.

Another effect is called the photovoltaic effect, which usually occurs in non-uniform semiconductor materials or semiconductor junctions. Due to the presence of the barrier layer, a potential difference is generated at different locations. A simplest p-n junction is here taken as an example to introduce its working principle. In Fig. 1.13, a built-in electric field from the n region to the p region exists in the p-n junction region.

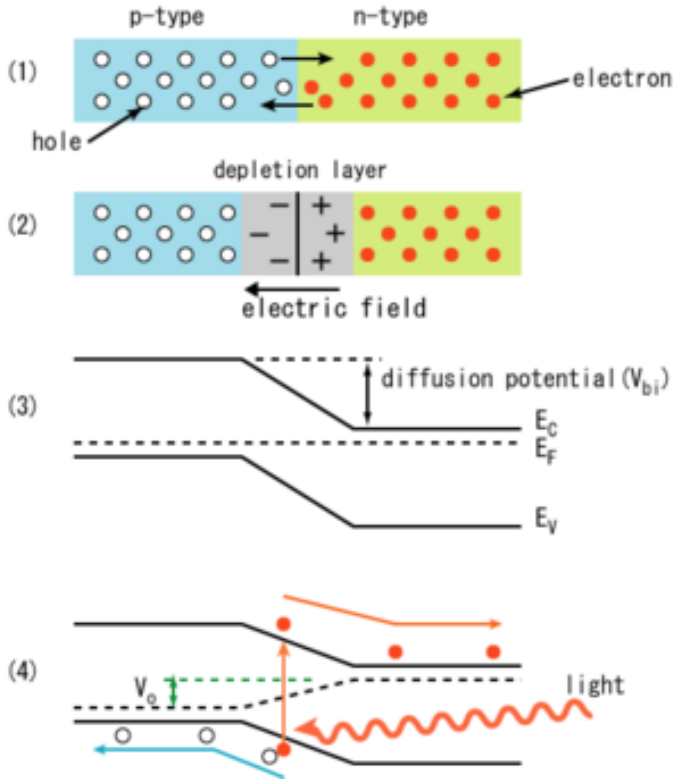

Fig. 1.13 Schematic diagram of p-n junction photovoltaic effect

When light is irradiated to the p-n junction, the majority carriers in the p region and the n region are blocked by the barrier and cannot pass through the junction. Only minority carriers can cause photovoltaic effects: the photo-generated electrons in the p region and the photo-generated holes in the n region diffuse into the vicinity of the junction electric field, drift through the junction under the action of the built-in electric field. Then the photo-generated electron-hole pairs in the depletion region are separated, electrons and holes move to the n and p regions, respectively, thereby forming charge accumulations on both sides of the barrier layer, by generating a photo-generated electric field opposite to that of the built-in electric field, which reduces the built-in electric field barrier. The photo-generated current is in the

same direction as that of p-n junction. The current is independent of the bias voltage and is proportional to the intensity of light and the rate of charge generation. The devices with this effect include photodiodes, phototransistors etc.

1.3.2 Classification of semiconductor photodetectors

According to the working mechanism of semiconductor photodetectors, they are classified into photoconductive type and photovoltaic type. The photoconductive type includes various kinds of photoconductive components and photosensitive resistors. Photovoltaic types include photovoltaic cells, photodiodes, avalanche photodiodes, Schottky barrier photodiodes, and phototransistors.

1.3.2.1 Photoconductive detectors

The working mechanism of photoconductive photodetectors is mainly based on the intrinsic or impurity photoconductive effects in semiconductor materials. When the light is irradiated to the semiconductor materials, the photon energy larger than the band gap will be absorbed, exciting the electrons from valence band or impurity energy levels to the conduction band and producing free electron-hole pairs. This will increase the carrier concentration, resulting in an increase in the conductivity of the semiconductor materials. The semiconductor materials used generally exhibit homogeneous phase and with no polarity. The change in electrical conductivity is closely related to the light intensity. Therefore, they are also called light guides or light-sensitive resistors.

Selenide semiconductors have been widely studied in the application of photoconductive photodetectors. Herein, we mainly introduce photodetectors based on selenide nanomaterials. Firstly, for zero-dimensional quantum dots, due to the quantum confinement effect, the energy band structure can be regulated by the size and shape of the nanoparticles. With high specific surface area and light absorption efficiency, they can be used for fabricating high performance photodetectors. Currently, CdSe [102], PbSe [103] etc. have been reported. Secondly, one-dimensional selenide semiconductor nanomaterials, including nanowires, nanorods, nanoribbons and nanotubes, have high specific area and Debye length due to the one-dimensional nanostructures, leading to excellent optical and electrical properties. A variety of photodetectors based on single one-dimensional nanomaterial or film and array assembled from many one-dimensional nanomaterials have achieved remarkable results. Examples include CdSe [104], ZnSe [105], In_2Se_3 [106], InSe [107], Sb_2Se_3 [108, 109] and alloys

$Zn_{0.31}Cd_{0.69}Se$ [110], Sb-Bi-Se [111]. Fig. 1.14 [108] and Fig. 1.15 [109] represent Sb_2Se_3 single nanowire photodetector and nanowire film photodetector, respectively.

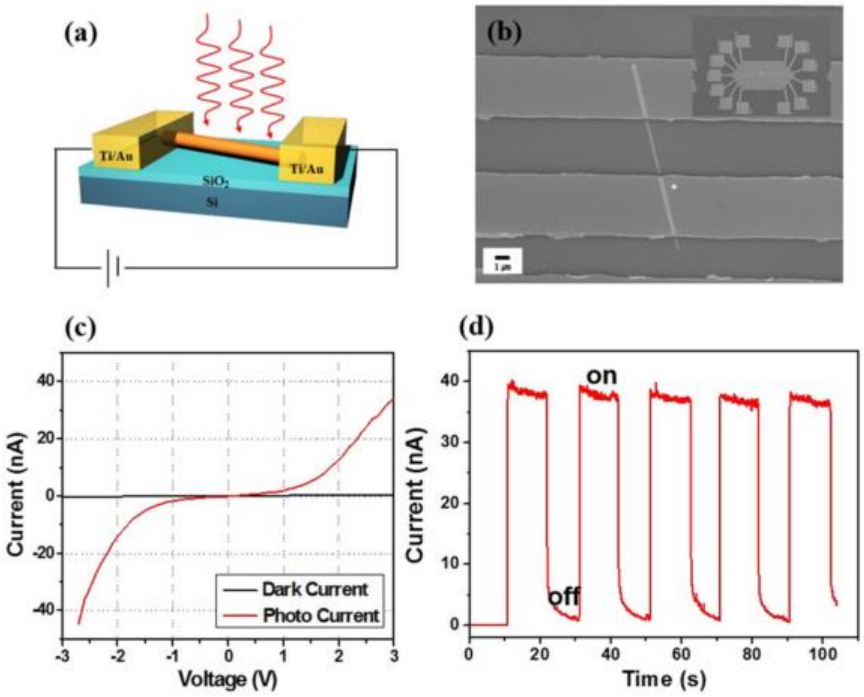

Fig. 1.14 Photoconductive properties of Sb_2Se_3 nanowires. (a) Schematic illustration and (b) SEM image of nanowire device. (c) I-V curves of Sb_2Se_3 single nanowire in the dark condition and under 655 nm light illumination. (d) Time dependent photocurrent response

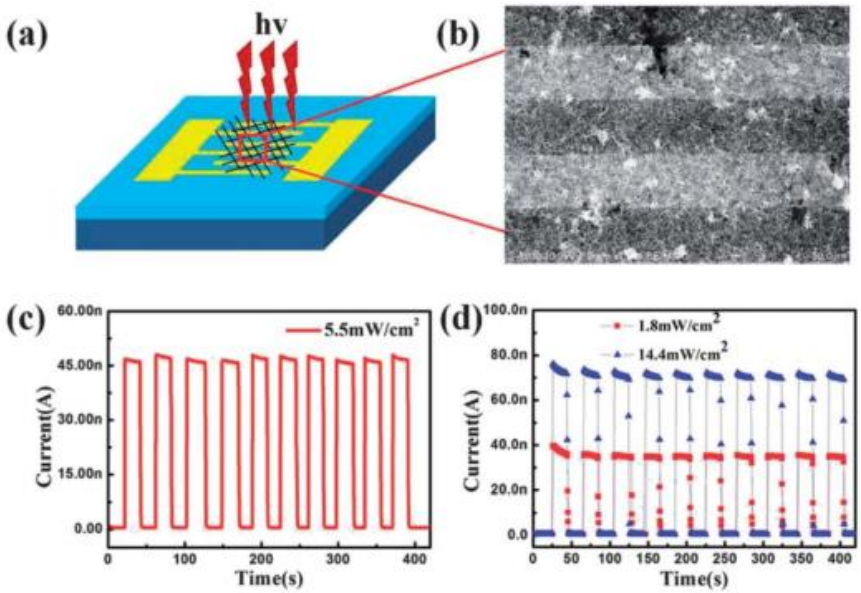

Fig. 1.15 (a) Schematic illustration and (b) representative SEM image of the device based on the Sb_2Se_3 nanowire film. (c) Time-resolved photoresponse at a bias of 10 V and an incident light density of 5.5 mW/cm^2. (d) Time-resolved photoresponse at a bias of 10 V and an incident light density of 1.8 and 14.4 mW/cm^2

Finally, some photodetectors based on two-dimensional layered selenide semiconductor nanomaterials also exhibit excellent performance, such as WSe_2 [112], GaSe [113], InSe [114] and In_2Se_3 [115].

1.3.2.2 Photovoltaic detectors

Selenide semiconductors can also be used for photovoltaic photodetectors [116-118]. The working principle is the following: when incident light is irradiated onto a photovoltaic detector, electron-hole pairs are generated in the depletion region of the semiconductor. These carriers will drift to their respective electrodes under the effect of the electric field in the depletion region, then form photocurrent in the external circuit and the detection of the incident light is then realized. Due to the existence of semiconductor junctions, the dark current of the photovoltaic photodetectors is small, the signal-to-noise ratio is low and the response time is also short. According to the difference of forming barrier of the built-in electric field, the photovoltaic photodetectors can contain p-n junction, p-i-n junction, Schottky barrier or metal-semiconductor-metal structure.

(1) p-n junction photodetector

For a p-n junction photodetector, when incident light is applied on the junction region, photo-generated carriers form photocurrent under the action of the built-in electric field. From the basic theory of p-n junctions, when it is positively biased, the dark current is much higher than the photocurrent, but when the bias is reversed, the dark current is small, so the detector usually works in the reverse bias state. In this situation, the photocurrent in the p-n junction is along the reverse bias direction. And due to the effect of the electric field, the response speed is generally very fast, which is also referred to as instantaneous photocurrent. Fig. 1.16 is the schematic diagram of a typical p-n photodiode and its current-voltage (I-V) curve [119].

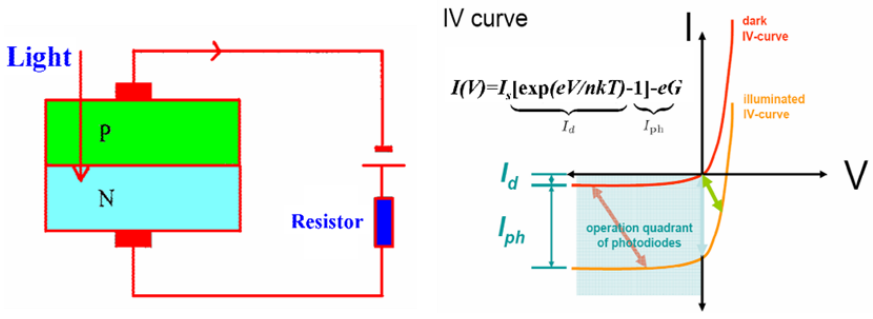

Fig. 1.16 The schematic structure and I-V characteristic of a typical p-n photodiode

(2) p-i-n photodetector

The response speed is an important performance indicator of the photodetector. In order to achieve faster response, the device structure must be modified. The p-i-n junction is an effective choice, which is to sandwich a thicker intrinsic semiconductor layer (i layer) inside the p-n structure. The presence of this layer will enlarge the distance between the junctions, the width of the depletion layer increases, and the junction capacitance decreases, thus improving the response speed. Fig. 1.17 is a schematic diagram of the p-i-n photodetector.

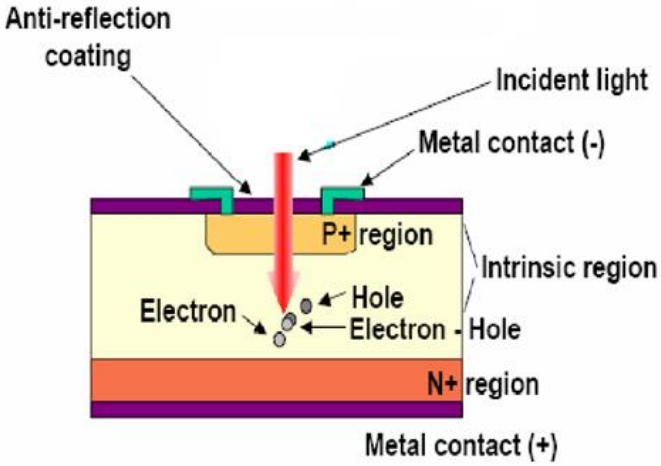

Fig. 1.17 The schematic structure of a typical p-i-n photodetector

(3) Schottky photodetector

Fig. 1.18 represents the schematic diagram of a Schottky photodetector and its working principle [119]. This device is composed of metal (Au, Pt, Ni, etc.) and semiconductor, and the Schottky barrier exists at the junction. In order to increase the light absorption of the semiconductor materials in the device, it is necessary to reduce the absorption and reflection of light by the metal layer on the surface, which requires the thickness of the metal layer to be thin. These devices have the advantages of high responsivity, short response time, high barrier height, and self-powered.

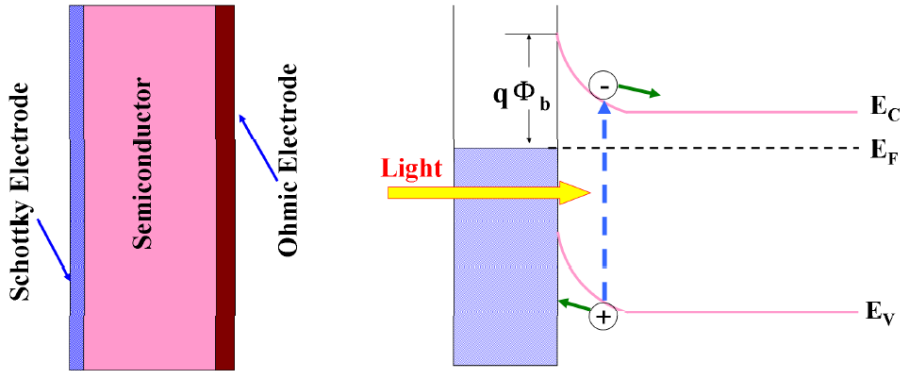

Fig. 1.18 The schematic structure (a) and operation (b) of the Schottky photodetector

(4) Metal-Semiconductor-Metal (MSM) Photodetectors

The structure of the MSM photodetector is shown in Fig. 1.19 [119]. It is composed of two back-to-back Schottky diodes by using an interdigitated electrode configuration on top of an active light collection region. The MSM detector has the advantages of easy preparation, simple structure, low dark current, small capacitance and fast response. Due to the existence of symmetric dual Schottky junctions, this device needs to operate with an applied bias.

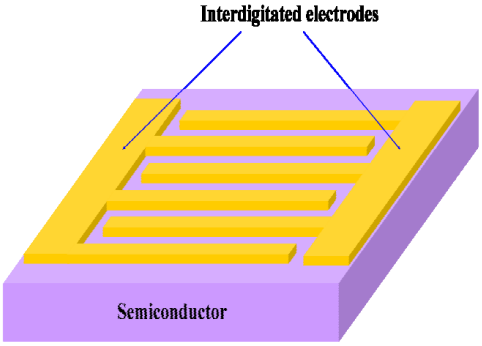

Fig. 1.19 The schematic structure of the Metal-Semiconductor-Metal (MSM) photodetector

1.3.3 The main performance parameters of the photodetector

The main performance parameters of semiconductor photodetectors include responsivity, quantum efficiency, response speed, detectivity and noise equivalent power.

(1) Responsivity (R_{res})

The responsivity represents the ability of photodetector to convert incident light into electrical signal, characterizing the photoelectric conversion efficiency of a photodetector, and can be calculated using the following equation [115]:

$$R_{res}=\frac{I_{ph}}{I_{irr}\times A}=\frac{I_{light}-I_{dark}}{I_{irr}\times A} \quad (1.8)$$

Where I_{ph} is the current after deducting background, ie, the difference between photocurrent and dark current ($I_{light}-I_{dark}$); I_{irr} is the power density of incident light; A is the effective device area. It can be seen that the larger R_{res} value, the higher photoelectric conversion capability, the better detection performance and the higher sensitivity of a photodetector.

(2) Quantum efficiency (η)

Quantum efficiency refers to the number of electron-hole pairs generated by each incident photon in the photodetector, which is related to the energy of the incident light, and is defined as Equation 1.9 [115]:

$$\eta=\frac{I_{ph}/e}{I/hv}=\frac{hv}{e}R_{res}=\frac{hc}{\lambda e}R_{res} \quad (1.9)$$

Where I/hv is the average number of incident photons per unit time; I_{ph}/e is the average number of photoelectrons generated per unit time; λ is the wavelength of the incident light; h is the Planck's constant; c is the speed of light in vacuum. It is noted that the quantum efficiency and the responsivity are closely related.

(3) Response speed

The response speed including the time required for the current to rise after receiving the optical signal and the time required for the current to drop after the optical signal is turned off. Under normal circumstances, when the incident light source suddenly turns on or off, the photocurrent will not immediately rise to the maximum value or fall to zero, there will be rising and falling edges before carrier concentration reaches a stable value. The concepts are called response time and recovery time, respectively.

(4) Noise Equivalent Power (NEP)

The noise equivalent power is mainly used to describe the detector's ability to detect weak light signals. It is defined as the radiation power incident on the detector when the RMS voltage of the photodetector's output signal is equal to the noise RMS.

(5) Detectivity (D*)

Detectivity is an important performance corresponds to the limit detection capability of weak signals. It is of great significance for the application in weak light detection, which can be described as [117]:

$$D^*=R_{res}/(2eJ_d)^{1/2} \quad (1.10)$$

Where R_{res} is the responsivity; e is the unit charge; J_d is the dark current density.

1.4 Semiconductor solar cells

Solar cells are another important application of photoelectric functional devices for selenide semiconductors. Solar cell, also named photovoltaic cell, is a device that converts light energy directly into electrical energy. The development of photovoltaic cells can be traced back to 170 years ago. The French physicist E. Becquerel first discovered the photovoltaic effect of liquids and opened the gate for the research and application of solar cells [120]. In the early stage, solar cells were mainly used in aviation and military fields due to the high cost. With the deepening of theoretical research on photovoltaic effects and advances in preparation technology, solar cells have begun to play an important role in the civilian sectors. The “oil crisis” in the 1970s and the concept of sustainable development in the early 1990s greatly promoted demands for clean and renewable energy and accelerated the pace of solar cells research. From the perspective of new ideas, new materials and new technologies, researchers have pushed the development and application of solar cells to a new climax.

1.4.1 The working principle of semiconductor based solar cells

The basis of the working principle of solar cells is the photovoltaic effect of semiconductor p-n junctions. The p-n junction is a space charge region formed by an interface between p-type and n-type semiconductor. When we bring these two semiconductors together, diffusion occurs on the surface between them. Electrons start to diffuse from n-type to p-type. Similarly, holes diffuse from p-type region to n-type region. This diffusion creates an electron-hole free region in a very short distance at the interface region. This thin layer is called space region or charge depletion region. Then an electric field from the n-side to the p-side of the depletion region will be created. Since the electrons are negative charges, this electric field applies a force to electrons entering the depletion region. Any electron generated by sun light in the vicinity of the depletion region may pass to the n-side of the junction very easily. If an extern circuit is formed by connecting the ends of n-type and p-type regions, electrons will flow to the p-type through the external circuit. External energy is needed to create this current by pushing the electrons in the p-type region to enter the depletion region. Solar radiation is an excellent energy source to do this job. Fig. 1.20a is a schematic diagram of this working principle, and Fig. 1.20b represents a typical solar cell structure [121].

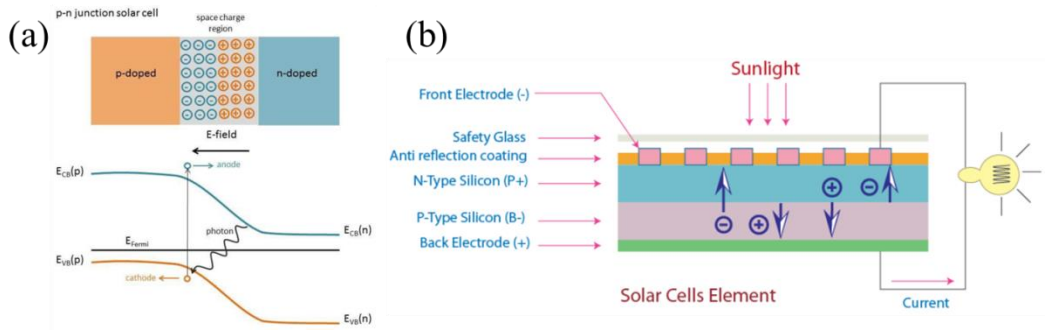

Fig. 1.20 (a) Schematic diagram of the photovoltaic solar cell and (b) Representative device structure

1.4.2 State-of-the-art of solar cells

A wide variety of solar cells have been reported so far, and the National Energy Department's Renewable Energy Laboratory (NREL) in the USA has presented statistical charts of the latest conversion efficiencies of different solar cells, as shown in Fig. 1.21. In the whole development process of solar cells, they can be divided into three generations [122].

(1) The first generation is crystalline silicon-based solar cells that have been industrialized with large scale, including single crystal and polycrystalline silicon cells with comparable market share. Single crystal silicon solar cells have the advantages of high efficiency and good weather resistance. However, they are also accompanied by high production cost. Polycrystalline silicon solar cells are less efficient with also lower production cost.

(2) The second generation can be considered as thin film solar cells in particular silicon thin films, copper indium gallium selenide (CIGS), cadmium telluride (CdTe). Silicon thin films include amorphous silicon and microcrystalline silicon. These thin film solar cells generally show features of high efficiency and high stability. Copper indium gallium selenide (CIGS) is developed on the basis of copper indium selenide (CIS). By replacing partially gallium with indium, the semiconductor band gap is continuously adjustable from 1.02 eV to 1.68 eV, to better match the solar spectrum in order to improve the conversion efficiency. Up to now, the highest conversion efficiency of the CIGS single-junction solar cell can reach 22.6% [123]. Although the reported efficiency has steadily increased, the relatively high cost of In, Ga raw materials and the industrial reproducibility have limited their market shares. CdTe is a binary p-type semiconductor with electron mobility up to 1100 cm^2/V s. The band gap is 1.45 eV and the absorption coefficient in the visible light region is high, which is very suitable for the preparation of thin film solar cells. The theoretical photoelectric conversion efficiency can reach 32%. The efficiency of CdTe solar cells in the early stage ranged from 10% to 16%

[124]. With the development of back surface copper expansion technology [125] and high-temperature $CdCl_2$ atmosphere treatment, the highest efficiency reported in the laboratory can reach 22.1% [126], approaching the efficiency of single crystal silicon solar cells.

(3) The third generation refers to new concept solar cells, such as organic-dye-sensitized solar cells, quantum dot cells, perovskite solar cells and new compound thin film solar cells, including copper zinc tin sulfide (CZTS), cuprous oxide, stannous sulfide, ferrous sulfide, antimony sulfide and antimony selenide. Dye-sensitized solar cells are using low-cost titanium dioxide and photosensitive dyes as the main raw materials, mimicking the principle of photosynthesis, converting solar energy into electrical energy. The record efficiency of dye-sensitized solar cells is 11.9% [127]. Dye-sensitized solar cells have the advantages of abundant raw materials, low-cost, simple fabrication technology and large area production features. At present, the design and development of low-cost, high-stability sensitizer dyes with a wider absorption spectrum has become the research focus. Quantum dot solar cells are using quantum dots to absorb light. Representative quantum dots are PbS [128] and PbSe [129]. The corresponding solar cells have some unique advantages, such as multiple exciton effects, quantum confinement effects and simple full solution process. Currently, quantum dot solar cells have not been commercialized in large areas. How to further improve the conversion efficiency, device stability and processability is still under critical research. Perovskite solar cells have drawn tremendous research attention due to its excellent light absorption and charge transfer efficiency. Since first report by Japan's Miyasaka et al. in 2009 [130], cell efficiency records have been continuously refreshed during the last 10 years. Now, the highest reported efficiency is 22.7% [131]. The perovskite solar cells also have some drawbacks, including containing toxic element Pb in light absorbing layer. The environmental sensitivity and low thermodynamic stability also hindered their practical applications. Among the various new compounds thin film solar cells, CZTS-based solar cells are the most studied and the reported efficiency exceeds 10% [127]. However, the complex elemental composition induces increasing defects, which restricts the further improvement of the cell efficiency. Other compounds, such as Cu_2O [132], SnS [133] and Sb_2Se_3 [134], are currently reported to be inefficient, even they have the advantages of low toxicity, low-cost, earth-abundant. In recent years, they have received intense attention with some significant progress.

In relation with the objective of this thesis, the state-of-the-art of Sb_2Se_3 thin film solar cells will be discussed in detail

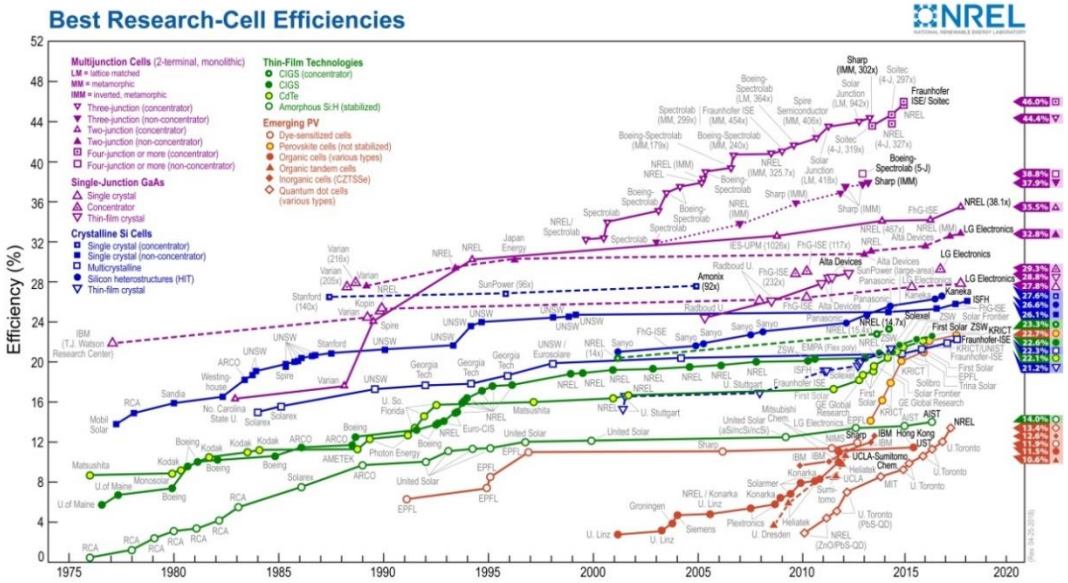

Fig. 1.21 Record efficiencies for different types of solar cells in the laboratory

1.4.3 Antimony selenide thin film solar cells

1.4.3.1 Sb_2Se_3 materials and the optoelectronic properties

Sb_2Se_3 is an inorganic compound semiconductor with density of 5.84 g/cm^3, which can exist naturally in the form of stibnite. Sb_2Se_3 has an orthorhombic crystal structure and a space group of Pnma 62, with lattice constants a = 11.633 Å, b = 11.780 Å, c = 3.985 Å, and a primitive cell volume of 0.524 nm^3. As a material composed of 1D ribbons, the $[Sb_4Se_6]_n$ ribbons are accumulated through van der Waals forces along a and b axes, whereas inside the 1D nanoribbon strong covalent bonds exist. The crystal structure of Sb_2Se_3 is shown in Fig. 1.22 [61,135]. It is worth noting that the unique one-dimensional structure of Sb_2Se_3 makes it different from traditional inorganic solar cell materials, such as Si, GaAs, ZnO, because in the orthogonal direction, the parallel-stacked ribbons would substantially provide no dangling bonds even at grain boundaries (GBs), which probably help to minimize recombination losses.

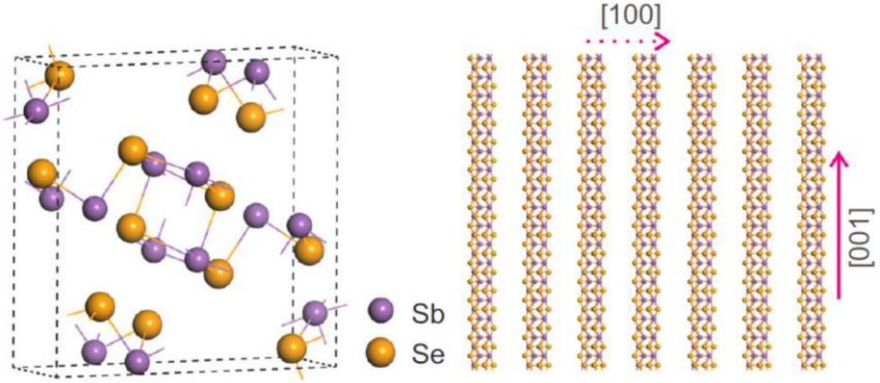

Fig. 1.22 Crystal structure of Sb_2Se_3

As a simple binary compound, Sb_2Se_3 has only an orthorhombic phase at normal temperature and pressure, thus avoiding the complexity of composition and phase control. The melting point of Sb_2Se_3 is 885 K, far lower than that of CdTe (1366 K). Reported experimental data reveal that Sb_2Se_3 crystals can be obtained at micron size when sintered at 300 ℃–400 ℃, implying the possibility of building flexible solar cells on polyimide (PI) substrate. The raw material of Sb_2Se_3 is low-toxic, earth-abundant and relatively inexpensive.

Sb_2Se_3 has a series of particularly excellent material properties (as shown in Table 1.2) [135], making it suitable for fabricating solar cells. In terms of optical properties, Sb_2Se_3 is a narrow bandgap semiconductor with a band gap of approximately 1.0-1.2 eV. Calculated by the Shockly–Queisser theory [19], the theoretical solar conversion efficiency of a single-junction solar cell can reach up to 30%. The absorption coefficient of Sb_2Se_3 is larger than 10^5 cm^{-1} in ultraviolet and visible spectrum, allowing sufficient absorption of the solar spectrum within a 500 nm thin film. In terms of electrical properties, Sb_2Se_3 thin film normally exhibits p-type conductivity. Its electron mobility is determined to be 15 $cm^2V^{-1}s^{-1}$, and the hole mobility is 42 $cm^2V^{-1}s^{-1}$, comparable with that of CdTe (p=60 $cm^2V^{-1}s^{-1}$). Moreover, its dielectric constant is larger than that of CIGS (13.6) and CdTe (7.1) leading to a lower exciton binding energy that implies easier separation of electrons and holes upon photo-generation. Similarly, the depth of defects should also be lower as it is inversely proportional to the square of the relative dielectric constant. Therefore, the recombination loss caused by the defects should drop considerably, possibly leading to higher power conversion efficiency (PCE).

Table 1.2 Material properties of Sb_2Se_3

Property		Value
Crystal lattice	a(Å)	11.6330
	b(Å)	11.7800
	c(Å)	3.9850
Density(g cm^{-3})		5.84
Space group		Pnma 62
Melting point(K)		885
Bandgap(eV)	direct	1.17 (300K)
	indirect	1.03 (300K)
Absorption coefficient(cm^{-1})		$>10^5$
Relative dielectric constant		15
Mobility	μ_e($cm^2V^{-1}s^{-1}$)	15
	μ_p($cm^2V^{-1}s^{-1}$)	42

In summary, Sb_2Se_3 has excellent material properties and is particularly suitable for the application of low-cost, non-toxic, high efficiency thin film solar cells.

1.4.3.2 State-of-the-art of Sb_2Se_3 thin film solar cells

Up to now, the researches of Sb_2Se_3-based solar cells are focused on two major device structures: sensitized structure and thin film structure. The former mainly uses Sb_2Se_3 as an ultra-thin absorbing layer to sensitize micron-thickness mesoporous TiO_2 to construct a solar cell. The highest efficiency is 6.6% reported by Choi et al. and the device structure is FTO/bl-TiO_2/mp-TiO_2/$Sb_2(S,Se)_3$/HTM/HTL/Au [136]. The other structure is thin film solar cell using Sb_2Se_3 as light absorbing layer to construct planar heterojunction structures. The research progress of Sb_2Se_3 thin film solar cells will be discussed more in detail here. The preparation of Sb_2Se_3 thin film solar cells mainly includes chemical methods and physical methods.

(1) Chemical methods

In 2009, Messina et al. reported on the preparation of $Sb_2Se_{3-x}S_x$:Sb_2O_3 absorbing layer using chemical bath deposition and then TCO/CdS/$Sb_2Se_{3-x}S_x$:Sb_2O_3/PbS thin film solar cell with device efficiency of 0.66% was fabricated [137]. In 2014, Zhou et al. reported a hydrazine (N_2H_4) solution method to deposit Sb_2Se_3 thin film on classical TiO_2 buffer layer to build a heterojunction TiO_2/Sb_2Se_3 solar cell and the device achieved an efficiency of 2.26% (V_{oc}= 0.52 V, J_{sc}=10.3 mA/cm^2, FF=42.3%) [138]. In 2015, Xia et al. reported the dissolution of bulk metal chalcogenides of V_2VI_3 (V = Sb, As; VI = S, Se, Te) in $(NH_4)_2S$ aqueous solution, followed by spraying pyrolysis the $Sb_2(S_{1-x},Se_x)_3$ alloy absorbing layer. The FTO/TiO_2/$Sb_2(S_{0.44},Se_{0.56})_3$/Au planar heterojunction thin film solar cell with conversion efficiency of 1.43% was obtained (V_{oc}=0.49 V, J_{sc}=6.6 mA/cm^2, F =44.2%) [139].

(2) Physical methods

The preparation of Sb_2Se_3 absorbing films by thermal evaporation is the most common method for Sb_2Se_3 thin film solar cells. Sb_2Se_3 has a melting point of 885 K and a very high vapor pressure, making it ideal for thermal evaporation. Prof. Tang's group from Huazhong University of Science and Technology in China has done the most in-depth research in this area. In 2014, Luo et al. firstly built a thermally evaporated Sb_2Se_3 solar cell using CBD-deposited CdS as n-buffer layer and followed by a superstrate structure of

FTO/CdS/Sb_2Se_3/Au with an efficiency of 1.9% [140]. Meanwhile, systematic physic analysis of the device was performed, revealing that bulk defects and unfavorable band diagram are the main limiting factors for device performance. In addition to superstrate configuration, Liu et al. designed a substrate Sb_2Se_3 solar cell analogous to CIGS structure (FTO/Sb_2Se_3/CdS/i-ZnO/AZO/Au) and yielded a PCE of 2.1% [141]. Based on the deep analysis of temperature-dependent vapor pressure of Sb_2Se_3, Sb and Se, one problem associated with the evaporation process is that large amount of selenium vacancies (V_{Se}) are generated due to the higher vapor pressure of Se, compared to Sb. Selenium vacancies are n-type donors that not only reduce the effective p-type doping density of Sb_2Se_3 film, but also act as recombination centers trapping and annihilating photo-generated carriers. To diminish V_{Se}-related recombination loss, Li et al. reported the co-evaporation of Se and Sb_2Se_3 to prepare a Sb_2Se_3-based solar cell with an interesting efficiency of 3.47 % [142]. Leng et al. utilized a post-selenization process after thermal evaporation. The selenization process provided excess Se to compensate for the V_{Se} and hence increased the doping density and attenuated the recombination loss. Meanwhile, selenization also helped in improving CdS/Sb_2Se_3 heterojunction quality, thus increasing device V_{oc} and FF. The solar cell performance was enhanced with a PCE of 3.7% [143].

In addition to the traditional thermal evaporation process, Prof. Tang's group recently introduced the rapid thermal evaporation (RTE) method to produce high-quality Sb_2Se_3 thin film using a tube furnace. Sb_2Se_3 powder was directly applied via evaporation under low vacuum pressure. Once heated up, Sb_2Se_3 powder evaporated and condensed on the substrate because of temperature gradient, forming the Sb_2Se_3 thin film. In 2015, Zhou et al. reported the RTE process to prepare Sb_2Se_3 thin film and based on the structure of FTO/CdS/Sb_2Se_3/Au, the device efficiency reached as high as 5.6% [61]. However, it is known that the strong absorption by the CdS layer in this Sb_2Se_3 solar cell and the recombination losses of carriers at the back are likely to contribute to the EQE decline at the short-wavelength and long-wavelength region. Recently, Wang et al. reported Sb_2Se_3 photovoltaics by substituting the CdS buffer layer with ZnO and the highest efficiency is close to 6% [134], as shown in Fig. 1.23 including the structure and the corresponding J-V curves of this device.

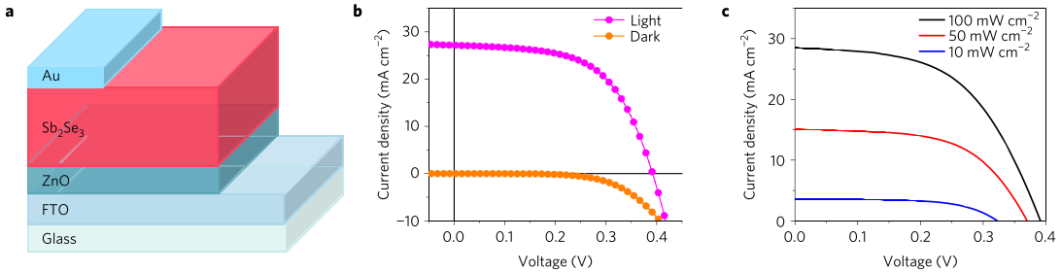

Fig. 1.23 (a) Schematic of the ZnO/Sb_2Se_3 device architecture. (b) Dark and light current density–voltage (J–V) curves of the champion device. (c) J–V curves of a representative r-ZnO/Sb_2Se_3 device under different intensities of simulated AM1.5G illumination

Another physical method for preparing the Sb_2Se_3 absorbing layer is magnetron sputtering. Liang et al. reported that the Sb_2Se_3 thin films with different crystallinity and surface morphology could be obtained by changing the substrate temperature via RF magnetron sputtering. Then planar junction Mo/Sb_2Se_3/CdS/ZnO/AZO/Ag thin film solar cell was constructed and a power conversion efficiency of 3.35% was achieved [80]. At present, there is only a few reports on magnetron sputtered Sb_2Se_3 thin film solar cells and the conversion efficiency is lower than that obtained by the thermal evaporation process. The adjustment of the preparation process, the performance analysis of the films and the optimization of the device structure still need further research.

In general, Sb_2Se_3-based thin film solar cells have a viable prospect because of their suitable band gap, high absorption coefficient, excellent electronic properties, non-toxicity, low-cost, earth-abundant constituents and intrinsically benign grain boundaries. At present, Sb_2Se_3 thin film solar cells prepared by chemical and physical methods have been reported, and the highest power conversion efficiency is 6%. Although the efficiency has been improved rapidly compared with the initial reported value, it is still far away from the theoretical efficiency (above 30%). Therefore, a systematic optimization of the film quality, device structure and interfacial engineering is compulsory to approach higher power conversion efficiency.

1.5 Summary

During the last half century, semiconductor technology has achieved rapid development as the core of modern high technology. Various new materials and functional devices based on semiconductor technology affect all aspects of our life. It is known that the fundamental research and application of semiconductor materials are the basis for developing

semiconductor technology, which is also an important source of motivation for numerous scientific researchers.

In this dissertation, two different selenide semiconductors with excellent properties are selected as our research targets, including controllable preparation of materials and exploration of applications as high performance photoelectric functional devices. Firstly, Sb_2Se_3 nanorods were synthesized via hot-injection method, and the biggest challenge of low conductivity of Sb_2Se_3 nanorods were overcomed successfully by forming heterojunction and/or doping. The high performance prototype photodetectors based on Sb_2Se_3 nanorods were constructed and tested. Then the Sn-doped Sb_2Se_3 crystals with controllable electrical conductivity and photoconductivity were prepared by high-temperature melting process. Afterwards, the same technique was used to obtain Sb_2Se_3-based targets, which can be further used for the preparation of thin films by Radio Frequency (RF) magnetron sputtering. The quasi-homojunction Sb_2Se_3 thin film solar cells were also explored based on those high-quality thin films, which show high application potential. Moreover, the uniform γ-In_2Se_3 nanoflowers were also synthesized via the hot-injection method. In combination with the mature Si-based semiconductor technology, a high performance γ-In_2Se_3/Si heterojunction photodiode was fabricated for the first time.

1.6 References

[1] http://www.sohu.com/a/163276953_119960.

[2] Eggleton, B. J.; Luther-Davies, B.; Richardson, K., Chalcogenide photonics. Nature Photonics 2011, 5 (3), 141-148.

[3] Rhyee, J. S.; Ahn, K.; Lee, K. H.; Ji, H. S.; Shim, J. H., Enhancement of the thermoelectric figure-of-merit in a wide temperature range in $In_4Se_{3-x}Cl_{0.03}$ bulk crystals. Advanced Materials 2011, 23 (19), 2191-2194.

[4] Kioseoglou, G.; Hanbicki, A. T.; Sullivan, J. M.; van 't Erve, O. M.; Li, C. H.; Erwin, S. C.; Mallory, R.; Yasar, M.; Petrou, A.; Jonker, B. T., Electrical spin injection from an n-type ferromagnetic semiconductor into a III-V device heterostructure. Nature Materials 2004, 3 (11), 799-803.

[5] Tyagi, K.; Gahtori, B.; Bathula, S.; Singh, N. K.; Bishnoi, S.; Auluck, S.; Srivastava, A. K.; Dhar, A., Electrical transport and mechanical properties of thermoelectric tin selenide. RSC Advances 2016, 6 (14), 11562-11569.

[6] Lin, W. C.; Tamargo, M. C.; Steiner, J.; Wei, H. Y.; Sarney, W.; Salamanca-Riba, L.;

Fitzpatrick, B. J., Growth and characterization of hexagonal (Zn,Mg)(S,Se) bulk substrates. Journal of Crystal Growth 2000, 212 (1), 83-91.

[7] Pfann, W. G., Zone Melting. Science 1962, 135 (3509), 1101-1109.

[8] Ni, Y.; Wu, H.; Huang, C.; Mao, M.; Wang, Z.; Cheng, X., Growth and quality of gallium selenide (GaSe) crystals. Journal of Crystal Growth 2013, 381, 10-14.

[9] Fu, Y.; Xu, J.; Liu, G. Q.; Yang, J.; Tan, X.; Liu, Z.; Qin, H.; Shao, H.; Jiang, H.; Liang, B.; Jiang, J., Enhanced thermoelectric performance in p-type polycrystalline SnSe benefiting from texture modulation. Journal of Materials Chemistry C 2016, 4 (6), 1201-1207.

[10] Chen, B.; Yang, J.; Zhang, Q.; Huang, H.; Li, H.; Tang, H.; Li, C., Tribological properties of copper-based composites with copper coated $NbSe_2$ and CNT. Materials & Design 2015, 75, 24-31.

[11] Tan, Z.; Li, Z.; Fan, G.; Kai, X.; Ji, G.; Zhang, L.; Zhang, D., Diamond/aluminum composites processed by vacuum hot pressing: Microstructure characteristics and thermal properties. Diamond and Related Materials 2013, 31, 1-5.

[12] Yu, B.; Liu, W.; Chen, S.; Wang, H.; Wang, H.; Chen, G.; Ren, Z., Thermoelectric properties of copper selenide with ordered selenium layer and disordered copper layer. Nano Energy 2012, 1 (3), 472-478.

[13] Pei, Y.; Shi, X.; LaLonde, A.; Wang, H.; Chen, L.; Snyder, G. J., Convergence of electronic bands for high performance bulk thermoelectrics. Nature 2011, 473 (7345), 66-69.

[14] Yang, J. Y.; Wu, J.; Li, G.; Zhang, J. S.; Peng, J., Preparation and Thermoelectric Properties of Polycrystalline In_4Sn_{3-x} by Mechanical Alloying and Hot Pressing. Journal of Electronic Materials 2012, 41 (6), 1077-1080.

[15] Shi, X.; Cho, J. Y.; Salvador, J. R.; Yang, J.; Wang, H., Thermoelectric properties of polycrystalline In_4Se_3 and In_4Te_3. Applied Physics Letters 2010, 96 (16), 162108.

[16] Munir, Z. A.; Anselmi-Tamburini, U.; Ohyanagi, M., The effect of electric field and pressure on the synthesis and consolidation of materials: A review of the spark plasma sintering method. Journal of Materials Science 2006, 41 (3), 763-777.

[17] Soni, A.; Shen, Y.; Yin, M.; Zhao, Y.; Yu, L.; Hu, X.; Dong, Z.; Khor, K. A.; Dresselhaus, M. S.; Xiong, Q., Interface driven energy filtering of thermoelectric power in spark plasma sintered $Bi_2Te_{2.7}Se_{0.3}$ nanoplatelet composites. Nano Letters 2012, 12 (8), 4305-4310.

[18] Lefèvre, R.; Berthebaud, D.; Perez, O.; Pelloquin, D.; Hébert, S.; Gascoin, F., Polar Transition-Metal Chalcogenide: Structure and Properties of the New Pseudo-Hollandite $Ba_{0.5}Cr_5Se_8$. Chemistry of Materials 2015, 27 (20), 7110-7118.

[19] Feng, H.; Meng, Q.; Zhou, Y.; Jia, D., Spark plasma sintering of functionally graded

material in the Ti–TiB_2–B system. Materials Science and Engineering: A 2005, 397 (1-2), 92-97.

[20] Zhan, G. D.; Kuntz, J. D.; Wan, J.; Mukherjee, A. K., Single-wall carbon nanotubes as attractive toughening agents in alumina-based nanocomposites. Nature Materials 2003, 2 (1), 38-42.

[21] Dong, G. H.; Zhu, Y. J.; Chen, L. D., Microwave-assisted rapid synthesis of Sb_2Te_3 nanosheets and thermoelectric properties of bulk samples prepared by spark plasma sintering. Journal of Materials Chemistry 2010, 20 (10), 1976.

[22] Samanta, M.; Pal, K.; Pal, P.; Waghmare, U. V.; Biswas, K., Localized Vibrations of Bi Bilayer Leading to Ultralow Lattice Thermal Conductivity and High Thermoelectric Performance in Weak Topological Insulator n-Type BiSe. Journal of the American Chemical Society 2018, 140 (17), 5866-5872.

[23] Wei, S.; Zhang, L.; Yang, H.; Zhou, T.; Wong, C.; Zhang, Q.; Chen, H., Preliminary study of 3D ball-milled powder processing and SPS-accelerated densification of ZnSe ceramics. Optical Materials Express 2017, 7 (4), 1131.

[24] Tyagi, K.; Gahtori, B.; Bathula, S.; Jayasimhadri, M.; Sharma, S.; Singh, N. K.; Haranath, D.; Srivastava, A. K.; Dhar, A., Crystal structure and mechanical properties of spark plasma sintered Cu_2Se: An efficient photovoltaic and thermoelectric material. Solid State Communications 2015, 207, 21-25.

[25] Maier, S.; Hebert, S.; Kabbour, H.; Pelloquin, D.; Perez, O.; Berthebaud, D.; Gascoin, F., Synthesis, electronic structure and physical properties of polycrystalline $Ba_2FePnSe_5$ (Pn = Sb, Bi). Materials Chemistry and Physics 2018, 203, 202-211.

[26] Chang, Y. H.; Zhang, W.; Zhu, Y.; Han, Y.; Pu, J.; Chang, J. K.; Hsu, W. T.; Huang, J. K.; Hsu, C. L.; Chiu, M. H.; Takenobu, T.; Li, H.; Wu, C. I.; Chang, W. H.; Wee, A. T. S.; Li, L. J., Monolayer $MoSe_2$ Grown by Chemical Vapor Deposition for Fast Photodetection. Acs Nano 2014, 8 (8), 8582-8590.

[27] Liu, B. L.; Fathi, M.; Chen, L.; Abbas, A.; Ma, Y. Q.; Zhou, C. W., Chemical Vapor Deposition Growth of Monolayer WSe_2 with Tunable Device Characteristics and Growth Mechanism Study. Acs Nano 2015, 9 (6), 6119-6127.

[28] Cho, B.; Kim, A. R.; Kim, D. J.; Chung, H. S.; Choi, S. Y.; Kwon, J. D.; Park, S. W.; Kim, Y.; Lee, B. H.; Lee, K. H.; Kim, D. H.; Nam, J.; Hahm, M. G., Two-Dimensional Atomic-Layered Alloy Junctions for High-Performance Wearable Chemical Sensor. ACS Applied Materials & Interfaces 2016, 8 (30), 19635-19642.

[29] Akhtar, J.; Akhtar, M.; Malik, M. A.; O'Brien, P.; Raftery, J., A single-source precursor

route to unusual PbSe nanostructures by a solution-liquid-solid method. Journal of the American Chemical Society 2012, 134 (5), 2485-2487.

[30] Yang, R. B.; Bachmann, J.; Pippel, E.; Berger, A.; Woltersdorf, J.; Gösele, U.; Nielsch, K., Pulsed Vapor-Liquid-Solid Growth of Antimony Selenide and Antimony Sulfide Nanowires. Advanced Materials 2009, 21 (31), 3170-3174.

[31] Murray, C. B.; Norris, D. J.; Bawendi, M. G., Synthesis and Characterization of Nearly Monodisperse CdE (E=S, Se, Te) Semiconductor Nanocrystallites. Journal of the American Chemical Society 1993, 115 (19), 8706-8715.

[32] Peng, Z. A.; Peng, X. G., Formation of high-quality CdTe, CdSe, and CdS nanocrystals using CdO as precursor. Journal of the American Chemical Society 2001, 123 (1), 183-184.

[33] Qu, L. H.; Peng, Z. A.; Peng, X. G., Alternative routes toward high quality CdSe nanocrystals. Nano Lettersers 2001, 1 (6), 333-337.

[34] Peng, X. G., Green chemical approaches toward high-quality semiconductor nanocrystals. Chemistry-a European Journal 2002, 8 (2), 335-339.

[35] Boatman, E. M.; Lisensky, G. C.; Nordell, K. J., A safer, easier, faster synthesis for CdSe quantum dot nanocrystals. Journal of Chemical Education 2005, 82 (11), 1697-1699.

[36] Deng, Z. T.; Mansuripur, M.; Muscat, A. J., Simple Colloidal Synthesis of Single-Crystal Sb-Se-S Nanotubes with Composition Dependent Band-Gap Energy in the Near-Infrared. Nano Lettersers 2009, 9 (5), 2015-2020.

[37] Castro, S. L.; Bailey, S. G.; Raffaelle, R. P.; Banger, K. K.; Hepp, A. F., Nanocrystalline chalcopyrite materials ($CuInS_2$ and $CuInSe_2$) via low-temperature pyrolysis of molecular single-source precursors. Chemistry of Materials 2003, 15 (16), 3142-3147.

[38] Ng, M. T.; Boothroyd, C. B.; Vittal, J. J., One-pot synthesis of new-phase $AgInSe_2$ nanorods. Journal of the American Chemical Society 2006, 128 (22), 7118-7119.

[39] Ma, J. M.; Wang, Y. P.; Wang, Y. J.; Chen, Q.; Lian, J. B.; Zheng, W. J., Controlled Synthesis of One-Dimensional Sb_2Se_3 Nanostructures and Their Electrochemical Properties. Journal of Physical Chemistry C 2009, 113 (31), 13588-13592.

[40] Gu, Y.; Su, Y.; Chen, D.; Geng, H.; Li, Z.; Zhang, L.; Zhang, Y., Hydrothermal synthesis of hexagonal CuSe nanoflakes with excellent sunlight-driven photocatalytic activity. CrystEngComm 2014, 16 (39), 9185-9190.

[41] Tan, X.; Zhou, J.; Yang, Q., Ascorbic acid-assisted solvothermal growth of γ-In_2Se_3 hierarchical flowerlike architectures. CrystEngComm 2011, 13 (7), 2792.

[42] Dong, B.; Li, C.; Chen, G.; Zhang, Y.; Zhang, Y.; Deng, M.; Wang, Q., Facile Synthesis of Highly Photoluminescent Ag_2Se Quantum Dots as a New Fluorescent Probe in the Second

Near-Infrared Window for in Vivo Imaging. Chemistry of Materials 2013, 25 (12), 2503-2509.
[43] Gao, M. R.; Lin, Z. Y.; Jiang, J.; Yao, H. B.; Lu, Y. M.; Gao, Q.; Yao, W. T.; Yu, S. H., Selective synthesis of Fe_7Se_8 polyhedra with exposed high-index facets and Fe_7Se_8 nanorods by a solvothermal process in a binary solution and their collective intrinsic properties. Chemistry 2011, 17 (18), 5068-5075.
[44] Selvan, S. T.; Tan, T. T.; Ying, J. Y., Robust, non-cytotoxic, silica-coated CdSe quantum dots with efficient photoluminescence. Advanced Materials 2005, 17 (13), 1620-1625.
[45] Yang, L.; Xie, R.; Liu, L.; Xiao, D.; Zhu, J., Synthesis and Characterization of ZnSe Nanocrystals by W/O Reverse Microemulsion Method: The Effect of Cosurfactant. The Journal of Physical Chemistry C 2011, 115 (40), 19507-19512.
[46] Ganguli, A. K.; Ganguly, A.; Vaidya, S., Microemulsion-based synthesis of nanocrystalline materials. Chemical Society Reviews 2010, 39 (2), 474-485.
[47] Malik, M. A.; Wani, M. Y.; Hashim, M. A., Microemulsion method: A novel route to synthesize organic and inorganic nanomaterials. Arabian Journal of Chemistry 2012, 5 (4), 397-417.
[48] Robinson, B. H.; Towey, T. F.; Zourab, S.; Visser, A.; Vanhoek, A., Characterization of cadmium-sulfide colloids in reverse micelles. Colloids and Surfaces 1991, 61, 175-188.
[49] Xi, L. F.; Lam, Y. M., Synthesis and characterization of CdSe nanorods using a novel microemulsion method at moderate temperature. Journal of Colloid and Interface Science 2007, 316 (2), 771-778.
[50] Karanikolos, G. N.; Alexandridis, P.; Itskos, G.; Petrou, A.; Mountziaris, T. J., Synthesis and size control of luminescent ZnSe nanocrystals by a microemulsion-gas contacting technique. Langmuir 2004, 20 (3), 550-553.
[51] Jiang, X. C.; Mayers, B.; Herricks, T.; Xia, Y. N., Direct synthesis of Se@CdSe nanocables and CdSe nanotubes by reacting cadmium salts with Se nanowires. Advanced Materials 2003, 15 (20), 1740-1743.
[52] Esakkiraj, E.; Mohanraj, K.; Sivakumar, G.; Henry, J., On the optical properties of lead chalcogenide nanoparticles. Optik - International Journal for Light and Electron Optics 2015, 126 (19), 2133-2137.
[53] Zhang, S. Y.; Fang, C. X.; Tian, Y. P.; Zhu, K. R.; Jin, B. K.; Shen, Y. H.; Yang, J. X., Synthesis and characterization of hexagonal CuSe nanotubes by templating against trigonal Se nanotubes. Crystal Growth & Design 2006, 6 (12), 2809-2813.
[54] Wu, X. J.; Huang, X.; Liu, J.; Li, H.; Yang, J.; Li, B.; Huang, W.; Zhang, H., Two-dimensional CuSe nanosheets with microscale lateral size: synthesis and template-assisted

phase transformation. Angewandte Chemie, International Edition in English 2014, 53 (20), 5083-5087.

[55] Esmaeili-Zare, M.; Salavati-Niasari, M.; Sobhani, A., Sonochemical synthesis of HgSe nanoparticles: Effect of metal salt, reaction time and reductant agent. Journal of Industrial and Engineering Chemistry 2014, 20 (5), 3518-3523.

[56] Liu, Y. Q.; Wang, F. X.; Xiao, Y.; Peng, H. D.; Zhong, H. J.; Liu, Z. H.; Pan, G. B., Facile microwave-assisted synthesis of Klockmannite CuSe nanosheets and their exceptional electrical properties. Scientific Reports 2014, 4, 5998.

[57] Mehta, R. J.; Karthik, C.; Jiang, W.; Singh, B.; Shi, Y. F.; Siegel, R. W.; Borca-Tasciuc, T.; Ramanath, G., High Electrical Conductivity Antimony Selenide Nanocrystals and Assemblies. Nano Letters 2010, 10 (11), 4417-4422.

[58] Liu F. Y. Electrodeposition of metal selenide thin films and the basic theoretical research, Chinese thesis, 2011.

[59] Prakash, D.; Shaaban, E. R.; Shapaan, M.; Mohamed, S. H.; Othman, A. A.; Verma, K. D., Thickness-dependent dispersion parameters, energy gap and nonlinear refractive index of ZnSe thin films. Materials Research Bulletin 2016, 80, 120-126.

[60] Mahmoud, S. A.; Ashour, A.; Badawi, E. A., Processing parameters and transport properties of vacuum evaporated CdSe thin films. Applied Surface Science 2006, 253 (5), 2969-2972.

[61] Zhou, Y.; Wang, L.; Chen, S. Y.; Qin, S. K.; Liu, X. S.; Chen, J.; Xue, D. J.; Luo, M.; Cao, Y. Z.; Cheng, Y. B.; Sargent, E. H.; Tang, J., Thin-film Sb_2Se_3 photovoltaics with oriented one-dimensional ribbons and benign grain boundaries. Nature Photonics 2015, 9 (6), 409-416.

[62] Feng, W.; Zhou, H.; Chen, F., Impact of thickness on crystal structure and optical properties for thermally evaporated PbSe thin films. Vacuum 2015, 114, 82-85.

[63] Amara, A.; Ferdi, A.; Drici, A.; Bernède, J. C.; Morsli, M.; Guerioune, M., Electrical and optical study of Cu(In,Ga)Se_2 co-evaporated thin films. Catalysis Today 2006, 113 (3-4), 251-256.

[64] Park, S. C.; Lee, D. Y.; Ahn, B. T.; Yoon, K. H.; Song, J., Fabrication of $CuInSe_2$ films and solar cells by the sequential evaporation of In_2Se_3 and Cu_2Se binary compounds. Solar Energy Materials and Solar Cells 2001, 69 (2), 99-105.

[65] Sharma, M. C.; Tripathi, B.; Kumar, S.; Srivastava, S.; Vijay, Y. K., Low cost CuInSe2 thin films production by stacked elemental layers process for large area fabrication of solar cell application. Materials Chemistry and Physics 2012, 131 (3), 600-604.

[66] Lee, Y. S.; Gershon, T.; Gunawan, O.; Todorov, T. K.; Gokmen, T.; Virgus, Y.; Guha, S.,

$Cu_2ZnSnSe_4$ Thin-Film Solar Cells by Thermal Co-evaporation with 11.6% Efficiency and Improved Minority Carrier Diffusion Length. Advanced Energy Materials 2015, 5 (7), 1401372.

[67] Kaune, G.; Hartnauer, S.; Syrowatka, F.; Scheer, R., Phase formation in $Cu_2ZnSnSe_4$ thin films deposited with multi-stage co-evaporation processes. Solar Energy Materials and Solar Cells 2014, 120, 596-602.

[68] Bindu, K.; Nair, P. K., Semiconducting tin selenide thin films prepared by heating Se–Sn layers. Semiconductor Science and Technology 2004, 19 (12), 1348-1353.

[69] Bedi, R. K.; Pathak, D.; Deepak; Kaur, D., Structural and optical properties of $AgInSe_2$ films. Zeitschrift Fur Kristallographie 2008, 177-183.

[70] Guillen, C.; Herrero, J., Structure, morphology and photoelectrochemical activity of $CuInSe_2$ thin films as determined by the characteristics of evaporated metallic precursors. Solar Energy Materials and Solar Cells 2002, 73 (2), 141-149.

[71] Boscher, N. D.; Carmalt, C. J.; Parkin, I. P., Atmospheric pressure chemical vapor deposition of WSe_2 thin films on glass-highly hydrophobic sticky surfaces. Journal of Materials Chemistry 2006, 16 (1), 122-127.

[72] Hu, Y.; Afzaal, M.; Malik, M. A.; O'Brien, P., Deposition of copper selenide thin films and nanoparticles. Journal of Crystal Growth 2006, 297 (1), 61-65.

[73] Boscher, N. D.; Carmalt, C. J.; Palgrave, R. G.; Parkin, I. P., Atmospheric pressure chemical vapour deposition of SnSe and $SnSe_2$ thin films on glass. Thin Solid Films 2008, 516 (15), 4750-4757.

[74] Park, J. H.; Afzaal, M.; Helliwell, M.; Malik, M. A.; O'Brien, P.; Raftery, J., Chemical vapor deposition of indium selenide and gallium selenide thin films from mixed alkyl/dialkylselenophosphorylamides. Chemistry of Materials 2003, 15 (22), 4205-4210.

[75] Yoon, S. H.; Seo, K. W.; Lee, S. S.; Shim, I.-W., Preparation of $CuInSe_2$ thin films through metal organic chemical vapor deposition method by using di-μ-methylselenobis(dimethylindium) and bis(ethylisobutyrylacetato) copper(II) precursors. Thin Solid Films 2006, 515 (4), 1544-1547.

[76] Kevin, P.; Malik, S. N.; Malik, M. A.; O′Brien, P., Growth of $Cu_2ZnSnSe_4$ and $Cu_2FeSnSe_4$ thin films by AACVD from molecular precursors. Materials Letters 2015, 152, 60-64.

[77] Bräuer, G.; Szyszka, B.; Vergöhl, M.; Bandorf, R., Magnetron sputtering-Milestones of 30 years. Vacuum 2010, 84 (12), 1354-1359.

[78] Li, Y. Z.; Gao, X. D.; Yang, C.; Huang, F. Q., The effects of sputtering power on optical

and electrical properties of copper selenide thin films deposited by magnetron sputtering. Journal of Alloys and Compounds 2010, 505 (2), 623-627.

[79] Li, S.; Yan, Y.; Zhang, Y.; Ou, Y.; Ji, Y.; Liu, L.; Yan, C.; Zhao, Y.; Yu, Z., Monophase γ-In_2Se_3 thin film deposited by magnetron radio-frequency sputtering. Vacuum 2014, 99, 228-232.

[80] Liang, G. X.; Zheng, Z. H.; Fan, P.; Luo, J. T.; Hu, J. G.; Zhang, X. H.; Ma, H. L.; Fan, B.; Luo, Z. K.; Zhang, D. P., Thermally induced structural evolution and performance of Sb_2Se_3 films and nanorods prepared by an easy sputtering method. Solar Energy Materials and Solar Cells 2018, 174, 263-270.

[81] Shi, J. H.; Li, Z. Q.; Zhang, D. W.; Liu, Q. Q.; Sun, Z.; Huang, S. M., Fabrication of Cu(In,Ga)Se_2 thin films by sputtering from a single quaternary chalcogenide target. Progress in Photovoltaics: Research and Applications 2011, 19 (2), 160-164.

[82] Kushiya, K.; Ohshita, M.; Hara, I.; Tanaka, Y.; Sang, B.; Nagoya, Y.; Tachiyuki, M.; Yamase, O., Yield issues on the fabrication of 30 cm × 30 cm-sized Cu(In,Ga)Se_2-based thin-film modules. Solar Energy Materials and Solar Cells 2003, 75 (1-2), 171-178.

[83] Wang, K. C.; Hsu, H. R.; Chen, H. S., Study of surface sulfurization of $Cu_2ZnSn(S, Se)_4$ thin film solar cell by sequential H_2Se-selenization/H_2S-sulfurization. Solar Energy Materials and Solar Cells 2017, 163, 31-37.

[84] Chen, R.; Xu, D.; Guo, G.; Tang, Y., Electrodeposition of silver selenide thin films from aqueous solutions. Journal of Materials Chemistry 2002, 12 (5), 1437-1441.

[85] Gromboni, M. F.; Mascaro, L. H., Optical and structural study of electrodeposited zinc selenide thin films. Journal of Electroanalytical Chemistry 2016, 780, 360-366.

[86] Shaikh, A. V.; Mane, R. S.; Joo, O. S.; Han, S. H.; Pathan, H. M., Electrochemical deposition of cadmium selenide films and their properties: a review. Journal of Solid State Electrochemistry 2017, 21 (9), 2517-2530.

[87] Dukstiene, N.; Kazancev, K.; Prosicevas, I.; Guobiene, A., Electrodeposition of Mo-Se thin films from a sulfamatic electrolyte. Journal of Solid State Electrochemistry 2004, 8 (5), 330-336.

[88] Yadav, A. A.; Salunke, S. D., Photoelectrochemical properties of In_2Se_3 thin films: Effect of substrate temperature. Journal of Alloys and Compounds 2015, 640, 534-539.

[89] Biçer, M.; Şişman, İ., Electrodeposition and growth mechanism of SnSe thin films. Applied Surface Science 2011, 257 (7), 2944-2949.

[90] Xiao, F.; Hangarter, C.; Yoo, B.; Rheem, Y.; Lee, K.-H.; Myung, N. V., Recent progress in electrodeposition of thermoelectric thin films and nanostructures. Electrochimica Acta 2008,

53 (28), 8103-8117.

[91] Kwon, Y. H.; Kim, Y. B.; Jeong, M.; Do, H. W.; Cho, H. K.; Lee, J. Y., Crystal growth direction-controlled antimony selenide thin film absorbers produced using an electrochemical approach and intermediate thermal treatment. Solar Energy Materials and Solar Cells 2017, 172, 11-17.

[92] Singh, K.; Mishra, S. S. D., Photoelectrochemical studies on galvanostatically formed multiple band gap materials based on CdSe and ZnSe. Solar Energy Materials and Solar Cells 2002, 71 (1), 115-129.

[93] Jana, A.; Datta, J., Enhancement of photo-characteristics of Bi_2Se_3 thin films by post heat treatment at optimal temperature range. Journal of Electroanalytical Chemistry 2013, 689, 31-41.

[94] Sa ïdi, H.; Boujmil, M. F.; Durand, B.; Lazzari, J. L.; Boua ïcha, M., Elaboration and characterization of $CuInSe_2$ thin films using one-step electrodeposition method on silicon substrate for photovoltaic application. Materials Research Express 2018, 5 (1), 016414.

[95] Xue, M.-Z.; Fu, Z.-W., Fabrication and electrochemical characterization of zinc selenide thin film by pulsed laser deposition. Electrochimica Acta 2006, 52 (3), 988-995.

[96] Czerniawski, J. M.; Stickney, J. L., Electrodeposition of In_2Se_3 Using Potential Pulse Atomic Layer Deposition. The Journal of Physical Chemistry C 2016, 120 (29), 16162-16167.

[97] Koutsikou, R.; Bouroushian, M., Pulse potential electrodeposition of (112)-textured chalcopyrite $CuInSe_2$ films from acidic aqueous solutions. Electrochimica Acta 2015, 178, 856-870.

[98] Bi, J.; Yao, L.; Ao, J.; Gao, S.; Sun, G.; He, Q.; Zhou, Z.; Sun, Y.; Zhang, Y., Pulse electro-deposition of copper on molybdenum for $Cu(In,Ga)Se_2$ and $Cu_2ZnSnSe_4$ solar cell applications. Journal of Power Sources 2016, 326, 211-219.

[99] Koppens, F. H.; Mueller, T.; Avouris, P.; Ferrari, A. C.; Vitiello, M. S.; Polini, M., Photodetectors based on graphene, other two-dimensional materials and hybrid systems. Nature Nanotechnology 2014, 9 (10), 780-793.

[100] https://en.wikipedia.org/wiki/Direct_and_indirect_band_gaps.

[101] Tivanov, M.; Patryn, A.; Drozdov, N.; Fedotov, A.; Mazanik, A., Determination of solar cell parameters from its current–voltage and spectral characteristics. Solar Energy Materials and Solar Cells 2005, 87 (1-4), 457-465.

[102] Konstantatos, G.; Sargent, E. H., Nanostructured materials for photon detection. Nature Nanotechnology 2010, 5 (6), 391-400.

[103] Sukhovatkin, V.; Hinds, S.; Brzozowski, L.; Sargent, E. H., Colloidal Quantum-Dot

Photodetectors Exploiting Multiexciton Generation. Science 2009, 324 (5934), 1542-1544.
[104] Shalev, E.; Oksenberg, E.; Rechav, K.; Popovitz-Biro, R.; Joselevich, E., Guided CdSe Nanowires Parallelly Integrated into Fast Visible-Range Photodetectors. Acs Nano 2017, 11 (1), 213-220.
[105] Fang, X. S.; Xiong, S. L.; Zhai, T. Y.; Bando, Y.; Liao, M. Y.; Gautam, U. K.; Koide, Y.; Zhang, X.; Qian, Y. T.; Golberg, D., High-Performance Blue/Ultraviolet-Light-Sensitive ZnSe-Nanobelt Photodetectors. Advanced Materials 2009, 21 (48), 5016-5021.
[106] Zhai, T. Y.; Fang, X. S.; Liao, M. Y.; Xu, X. J.; Li, L.; Liu, B. D.; Koide, Y.; Ma, Y.; Yao, J. N.; Bando, Y.; Golberg, D., Fabrication of High-Quality In_2Se_3 Nanowire Arrays toward High-Performance Visible-Light Photodetectors. Acs Nano 2010, 4 (3), 1596-1602.
[107] Wang, J. J.; Cao, F. F.; Jiang, L.; Guo, Y. G.; Hu, W. P.; Wan, L. J., High Performance Photodetectors of Individual InSe Single Crystalline Nanowire. J Am Chem Soc 2009, 131 (43), 15602-15603.
[108] Choi, D.; Jang, Y.; Lee, J.; Jeong, G. H.; Whang, D.; Hwang, S. W.; Cho, K. S.; Kim, S. W., Diameter-Controlled and Surface-Modified Sb_2Se_3 Nanowires and Their Photodetector Performance. Scientific Reports 2014, 4, 6714.
[109] Liu, Y. Q.; Zhang, M.; Wang, F. X.; Pan, G. B., Facile microwave-assisted synthesis of uniform Sb_2Se_3 nanowires for high performance photodetectors. Journal of Materials Chemistry C 2014, 2 (2), 240-244.
[110] Yoon, Y. J.; Park, K. S.; Heo, J. H.; Park, J. G.; Nahm, S.; Choi, K. J., Synthesis of $Zn_xCd_{1-x}Se$ ($0 \leq x \leq 1$) alloyed nanowires for variable-wavelength photodetectors. Journal of Materials Chemistry 2010, 20 (12), 2386.
[111] Huang, R.; Zhang, J.; Wei, F.; Shi, L.; Kong, T.; Cheng, G., Ultrahigh Responsivity of Ternary Sb-Bi-Se Nanowire Photodetectors. Advanced Functional Materials 2014, 24 (23), 3581-3586.
[112] Mak, K. F.; Shan, J., Photonics and optoelectronics of 2D semiconductor transition metal dichalcogenides. Nature Photonics 2016, 10 (4), 216-226.
[113] Hu, P. A.; Wen, Z. Z.; Wang, L. F.; Tan, P. H.; Xiao, K., Synthesis of Few-Layer GaSe Nanosheets for High Performance Photodetectors. Acs Nano 2012, 6 (7), 5988-5994.
[114] Tamalampudi, S. R.; Lu, Y. Y.; Kumar, U. R.; Sankar, R.; Liao, C. D.; Moorthy, B. K.; Cheng, C. H.; Chou, F. C.; Chen, Y. T., High performance and bendable few-layered InSe photodetectors with broad spectral response. Nano Letters 2014, 14 (5), 2800-2806.
[115] Jacobs-Gedrim, R. B.; Shanmugam, M.; Jain, N.; Durcan, C. A.; Murphy, M. T.; Murray, T. M.; Matyi, R. J.; Moore, R. L.; Yu, B., Extraordinary Photoresponse in Two-Dimensional

In_2Se_3 Nanosheets. Acs Nano 2014, 8 (1), 514-521.

[116] Monroy, E.; Omnes, F.; Calle, F., Wide-bandgap semiconductor ultraviolet photodetectors. Semiconductor Science and Technology 2003, 18 (4), R33-R51.

[117] Tuğluoğlu, N.; Karadeniz, S.; Şahin, M.; Şafak, H., Temperature dependence of current–voltage characteristics of Ag/p-SnSe Schottky diodes. Applied Surface Science 2004, 233 (1-4), 320-327.

[118] Zhang, H.; Zhang, X.; Liu, C.; Lee, S. T.; Jie, J., High-Responsivity, High-Detectivity, Ultrafast Topological Insulator Bi_2Se_3/Silicon Heterostructure Broadband Photodetectors. Acs Nano 2016, 10 (5), 5113-5122.

[119] Liu, K.; Sakurai, M.; Aono, M., ZnO-based ultraviolet photodetectors. Sensors (Basel) 2010, 10 (9), 8604-8634.

[120] A. Becquerel. On electric effects under the influence of solar radiation. CR Acad Sci, 1839, 9, 711-714.

[121] http://cdmd.cnki.com.cn/Article/CDMD-10335-1017040361.htm

[122] http://cdmd.cnki.com.cn/Article/CDMD-10487-1016088556.htm

[123] Jackson, P.; Wuerz, R.; Hariskos, D.; Lotter, E.; Witte, W.; Powalla, M., Effects of heavy alkali elements in $Cu(In,Ga)Se_2$ solar cells with efficiencies up to 22.6%. physica status solidi (RRL)-Rapid Research Letters 2016, 10 (8), 583-586.

[124] Wu, X., High-efficiency polycrystalline CdTe thin-film solar cells. Solar Energy 2004, 77 (6), 803-814.

[125] Dobson, K. D.; Visoly-Fisher, I.; Hodes, G.; Cahen, D., Stabilizing CdTe/CdS solar cells with Cu-containing contacts to p-CdTe. Advanced Materials 2001, 13 (19), 1495-1499.

[126] Emziane, M.; Durose, K.; Romeo, N.; Bosio, A.; Halliday, D. P., Effect of $CdCl_2$ activation on the impurity distribution in CdTe/CdS solar cell structures. Thin Solid Films 2005, 480-481, 377-381.

[127] Green, M. A.; Hishikawa, Y.; Warta, W.; Dunlop, E. D.; Levi, D. H.; Hohl-Ebinger, J.; Ho-Baillie, A. W. H., Solar cell efficiency tables (version 50). Progress in Photovoltaics: Research and Applications 2017, 25 (7), 668-676.

[128] Xu, J.; Voznyy, O.; Liu, M.; Kirmani, A. R.; Walters, G.; Munir, R.; Abdelsamie, M.; Proppe, A. H.; Sarkar, A.; Garcia de Arquer, F. P.; Wei, M.; Sun, B.; Liu, M.; Ouellette, O.; Quintero-Bermudez, R.; Li, J.; Fan, J.; Quan, L.; Todorovic, P.; Tan, H.; Hoogland, S.; Kelley, S. O.; Stefik, M.; Amassian, A.; Sargent, E. H., 2D matrix engineering for homogeneous quantum dot coupling in photovoltaic solids. Nature Nanotechnology 2018, 13 (6), 456-462.

[129] Semonin, O. E.; Luther, J. M.; Choi, S.; Chen, H. Y.; Gao, J. B.; Nozik, A. J.; Beard, M.

C., Peak External Photocurrent Quantum Efficiency Exceeding 100% via MEG in a Quantum Dot Solar Cell. Science 2011, 334 (6062), 1530-1533.

[130] Kojima, A.; Teshima, K.; Shirai, Y.; Miyasaka, T., Organometal Halide Perovskites as Visible-Light Sensitizers for Photovoltaic Cells. Journal of the American Chemical Society 2009, 131 (17), 6050-6051.

[131] Saliba, M.; Correa-Baena, J. P.; Gratzel, M.; Hagfeldt, A.; Abate, A., Perovskite Solar Cells: From the Atomic Level to Film Quality and Device Performance. Angewandte Chemie, International Edition in English 2018, 57 (10), 2554-2569.

[132] Ievskaya, Y.; Hoye, R. L. Z.; Sadhanala, A.; Musselman, K. P.; MacManus-Driscoll, J. L., Fabrication of ZnO/Cu_2O heterojunctions in atmospheric conditions: Improved interface quality and solar cell performance. Solar Energy Materials and Solar Cells 2015, 135, 43-48.

[133] Lim, D.; Suh, H.; Suryawanshi, M.; Song, G. Y.; Cho, J. Y.; Kim, J. H.; Jang, J. H.; Jeon, C. W.; Cho, A.; Ahn, S.; Heo, J., Kinetically Controlled Growth of Phase-Pure SnS Absorbers for Thin Film Solar Cells: Achieving Efficiency Near 3% with Long-Term Stability Using an SnS/CdS Heterojunction. Advanced Energy Materials 2018, 8 (10), 1702605.

[134] Wang, L.; Li, D.-B.; Li, K.; Chen, C.; Deng, H. X.; Gao, L.; Zhao, Y.; Jiang, F.; Li, L.; Huang, F.; He, Y.; Song, H.; Niu, G.; Tang, J., Stable 6%-efficient Sb_2Se_3 solar cells with a ZnO buffer layer. Nature Energy 2017, 2, 17046.

[135] Zeng, K.; Xue, D. J.; Tang, J., Antimony selenide thin-film solar cells. Semiconductor Science and Technology 2016, 31 (6).

[136] Choi, Y. C.; Lee, Y. H.; Im, S. H.; Noh, J. H.; Mandal, T. N.; Yang, W. S.; Seok, S. I., Efficient Inorganic-Organic Heterojunction Solar Cells Employing $Sb_2(S_x/Se_{1-x})_3$ Graded-Composition Sensitizers. Advanced Energy Materials 2014, 4 (7), 1301680.

[137] Messina, S.; Nair, M. T. S.; Nair, P. K., Antimony Selenide Absorber Thin Films in All-Chemically Deposited Solar Cells. Journal of the Electrochemical Society 2009, 156 (5), H327.

[138] Zhou, Y.; Leng, M. Y.; Xia, Z.; Zhong, J.; Song, H. B.; Liu, X. S.; Yang, B.; Zhang, J. P.; Chen, J.; Zhou, K. H.; Han, J. B.; Cheng, Y. B.; Tang, J., Solution-Processed Antimony Selenide Heterojunction Solar Cells. Advanced Energy Materials 2014, 4 (8).

[139] Xia, Z.; Zhong, J.; Leng, M.; Hu, L.; Xue, D.-J.; Yang, B.; Zhou, Y.; Liu, X.; Qin, S.; Cheng, Y.-B.; Tang, J., Generalized Water-Processed Metal Chalcogenide Complexes: Synthesis and Applications. Chemistry of Materials 2015, 27 (23), 8048-8057.

[140] Luo, M.; Leng, M. Y.; Liu, X. S.; Chen, J.; Chen, C.; Qin, S. K.; Tang, J., Thermal evaporation and characterization of superstrate CdS/Sb_2Se_3 solar cells. Applied Physics

Letters 2014, 104 (17).

[141] Liu, X. S.; Chen, J.; Luo, M.; Leng, M. Y.; Xia, Z.; Zhou, Y.; Qin, S. K.; Xue, D. J.; Lv, L.; Huang, H.; Niu, D. M.; Tang, J., Thermal Evaporation and Characterization of Sb_2Se_3 Thin Film for Substrate Sb_2Se_3/CdS Solar Cells. ACS Applied Materials & Interfaces 2014, 6 (13), 10687-10695.

[142] Li, Z. Q.; Zhu, H. B.; Guo, Y. T.; Niu, X. N.; Chen, X.; Zhang, C.; Zhang, W.; Liang, X. Y.; Zhou, D.; Chen, J. W.; Mai, Y. H., Efficiency enhancement of Sb_2Se_3 thin-film solar cells by the co-evaporation of Se and Sb_2Se_3. Applied Physics Express 2016, 9 (5).

[143] Leng, M. Y.; Luo, M.; Chen, C.; Qin, S. K.; Chen, J.; Zhong, J.; Tang, J., Selenization of Sb_2Se_3 absorber layer: An efficient step to improve device performance of CdS/Sb_2Se_3 solar cells. Applied Physics Letters 2014, 105 (8).

CHAPTER II: PREPARATION OF SB2SE3 NANORODS FOR HIGH PERFORMANCE PHOTODETECTORS

2.1 Introduction

Since its birth in 1980s, nanoscience and technology have been developed rapidly, attracting more and more attention. As the foundation, the preparation and applications of new nanomaterials have become one of the most important and dynamic branches of nanotechnology. Among them, semiconductor nanomaterials are one of researching hotspots due to their unique physical and chemical properties. Moreover, the corresponding functional devices also play an indispensable role in actual industrial production and social development.

Among various kinds of semiconductor nanomaterials, metal chalcogenide semiconductors are among the most rapidly developed and promising materials in recent years. Early research was focused on the IV-VI groups represented by PbS, PbSe and the II-VI groups by ZnS, CdS. For the V-VI semiconductors, which are less studied, the main objective is to realize a controllable preparation of nanomaterials suitable for applications particularly in the fields of photoelectric and thermoelectric applications. Among these semiconductors, antimony selenide (Sb_2Se_3) is an important narrow band gap binary semiconductor, with highly anisotropic structure crystallizing in layers parallel to the growth direction. Its useful properties (e.g., photovoltaic, photoconduction, photo-catalysis, Peltier effect) make it promising candidate for many important applications in diverse areas such as solar energy conversion, thermoelectric cooling, thermoelectric power generation, photodetection and opto-electronic devices in the near-infrared region [1-6]. The initial research of Sb_2Se_3 was mainly focused on the preparation of thin films. Some other mature preparation processes include spray pyrolysis, solution growth, direct fusion of selenium and antimony, electrochemical deposition, thermal evaporation etc. [7-13]. During the past decades, considerable efforts have been devoted to the synthesis of Sb_2Se_3 nanomaterials, such as hydrothermal or solvothermal routes, surfactant or polymer-assisted hydrothermal technique, microwave irradiation method and colloidal process [1,6,14-16]. Due to its unique crystal structure, composed of one-dimensional (1D) covalently linked $(Sb_4Se_6)_n$ ribbons stacked together via van der Waals forces, Sb_2Se_3 nanomaterials can be synthesized with 1D morphology, including nanowires, nanorods, nanoribbons and nanotubes. These novel 1D semiconductor nanostructures have unique properties that will play an important role for future applications. Therefore, it is of great significance to carry out research on Sb_2Se_3 nanomaterials.

Although the current research on Sb_2Se_3 has achieved considerable results, the practical

application is still limited. One of the main reasons is the intrinsic low electrical conductivity ($10^{-6}\ \Omega^{-1}m^{-1}$ in bulk state), resulting in low thermoelectric power factor, low spectral response and low external quantum efficiency [1]. To overcome this challenge, few works to improve electrical conductivity of the Sb_2Se_3 nanomaterials have been reported. For example, Choi et al. developed Sb_2Se_3 nanowires decorated with Ag_2Se nanoparticles, which increased the electrical conductivity [1]. Zhang et al. explained an interpenetrating iodine-doped-Sb_2Se_3/Cu_2GeSe_3 heterojunction network fabricated by controlling the crystallization of a chalcogenide glass which can improve the photoelectric performance [17]. However, the synthesis of the Sb_2Se_3 nanomaterials with tunable electrical conductivity has been rarely reported and still needs further exploration.

In this chapter, we first used the hot-injection method to controllably synthesize Sb_2Se_3 nanorods. The synthesis process is safe, facile and environmentally friendly. The nucleation and growth mechanism of Sb_2Se_3 nanorods and the effect of various organic solvents in the reaction system were studied systematically. Then, we used two effective approaches to improve the electrical conductivity of Sb_2Se_3 nanorods. One was the formation of composites with a high conductivity second phase and the hybrid nanorods with $Sb_2Se_3/AgSbSe_2$ heterojunction structure were prepared accordingly. Those interconnected heterojunction structures could significantly improve the electrical conductivity of the Sb_2Se_3 nanorods. The other approach was doping, which is an efficient approach to tune the electrical and photoelectrical performances of semiconductors and has been widely adopted throughout the semiconductor industry. For example, the In-doped Ga_2O_3 nanobelt-based photodetector showed a higher sensitivity, responsivity and quantum efficiency compared with the undoped Ga_2O_3 nanobelt photodetector [18]. The S-doped In_2Se_3 nanowires presented much higher conductivity and spectra responsivity to visible light than the undoped In_2Se_3 nanowires [19]. Herein, for the first time, we reported an effective hot-injection method for the synthesis of the Sn-doped Sb_2Se_3 ($(Sn_xSb_{1-x})_2Se_3$) nanorods. The electrical conductivity of the Sb_2Se_3 nanorods was significantly increased by incorporating Sn^{4+} ions into the Sb_2Se_3 host.

Finally, in order to demonstrate the application potential of the Sb_2Se_3 nanorods, the performance of undoped Sb_2Se_3 nanorods, hybrid nanorods with the $Sb_2Se_3/AgSbSe_2$ heterojunction structure and $(Sn_xSb_{1-x})_2Se_3$ nanorods, as photodetectors has been compared.

2.2 Experimental section

2.2.1 Materials

Antimony acetate (Aladdin, 99.99%), Silver acetate (Aladdin, 99.5%), Tin chloride (Aladdin, 99.99%), Selenium dioxide (Aladdin, 99%), 1-Hexadecylamine (Aladdin, 90%), 1-Octadecene (Aladdin, 90%) and Oleic acid (Aladdin, AR). Chloroform and Isopropyl alcohol were purchased from Sinopharm Chemical Reagent Co., Ltd. All reagents were used for the synthesis without further purification.

2.2.2 Principle of nanomaterials preparation by hot-injection

The hot-injection method is an efficient new way to prepare nanomaterials. Compared with other methods, it has many advantages, such as short reaction cycle, low-cost for equipment, high purity of obtained samples and easy control of the sample morphology. Hot-injection method refers to the rapid injection of one cold precursor solution into another high-temperature solvent during the reaction, thereby causing an instantaneous large amount of nucleation. In this way, the precursor concentration in the reaction system is lowered below the critical nucleation concentration, and the temperature of the mixture drops. Then the nucleus grows at a lower temperature to avoid secondary nucleation, thus ensuring a uniform particle size distribution. Therefore, the most important feature of this preparation process is to separate the nucleation and growth processes. The time-dependent growth process of nanomaterials can be described by the LaMer curve, as shown in Fig. 2.1 [20].

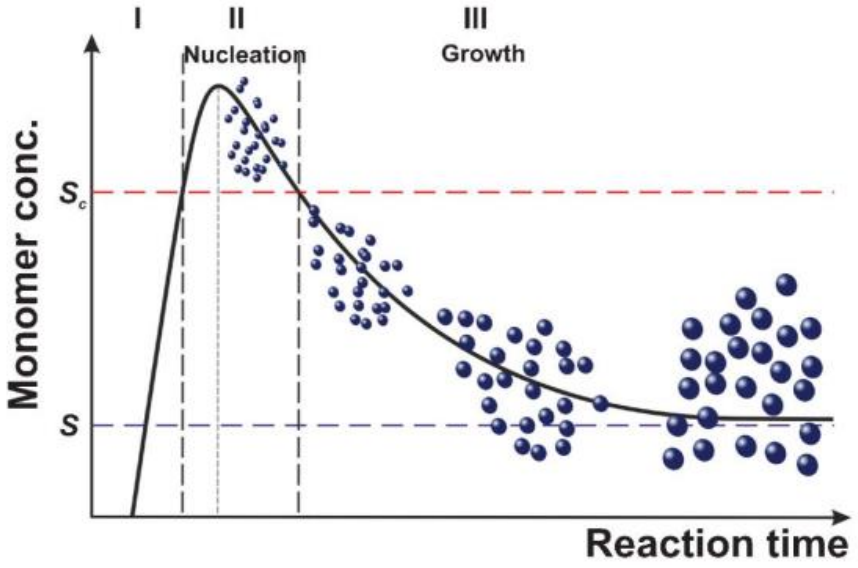

Fig. 2.1 LaMer plot illustrating the separation of nucleation and growth during the synthesis of monodisperse NPs. S and S_c are supersaturation and critical supersaturation, respectively

Specifically, when the organic-chalcogen precursor is rapidly injected into a high-temperature and vigorously stirred reaction vessel containing metal precursor and coordinating organic solvents, the solution concentration exceeds the critical nucleation concentration and nucleation starts. The rapid nucleation instantaneously causes the monomer concentration in the solution to rapidly decrease below the supersaturation concentration and the nucleation is then stopped. As long as the monomer consumption rate of the nanocrystal growth is faster than the decomposition rate of the precursor, no new crystal nucleus will be generated because the monomer concentration is lower than the supersaturation concentration. In this way, each crystal has the same growth process, and the uniformity can be ensured. The growth rate can be controlled by the diffusion rate and the reaction rate, which can be further controlled by the precursor concentration, the surfactant concentration, the reaction temperature, and the ratio of the cation/anion in the solution. Finally, the growth and dissolution of the nanocrystals can be balanced.

Since many nanomaterials are easily oxidized and the organic solvents used are also susceptible to explosion due to oxidation at high temperatures, the preparation usually needs to be carried out under anhydrous and anaerobic conditions. One mature solution is to adopt the Schlenk line technical route, as shown in Fig. 2.2 for the hot-injection method. The entire equipment provides heating, stirring and atmosphere protection for the reaction, ensuring the preparation of high quality semiconductor nanomaterials.

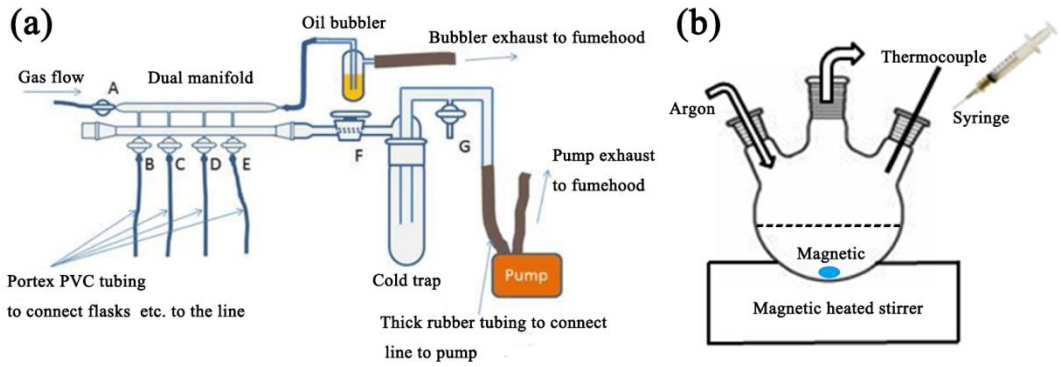

Fig. 2.2 (a) Schematic diagram of the Schlenk line technology and (b) hot-injection method

2.2.3 Synthesis of Sb_2Se_3 nanorods

A simple colloidal process involving hot-injection was used to synthesize 1D Sb_2Se_3 nanorods. At first, 24 mmol selenium dioxide and 30 ml 1-octadecene were added into a 100 mL three-neck flask and heated to 200 ℃ for several hours with stirring under argon atmosphere until

selenium dioxide was completely dissolved, which formed a 0.8 M selenium precursor solution. To prepare antimony precursor solution, 1 mmol antimony acetate, 8 mmol 1-hexadecylamine, 15 ml 1-octadecene and 6 ml oleic acid in another flask were degassed at room temperature and then heated to 220 ℃ for 1 h, which formed a transparent yellow solution. Subsequently, 8 ml 0.8 M selenium precursor solution was swiftly injected into the yellow antimony precursor solution which was heated to 240 ℃ beforehand. The mixture was stirred for 10 min and then cooled to room temperature. The obtained solid Sb_2Se_3 nanorods were collected by centrifugation, washed with chloroform and isopropyl alcohol for several times, and finally dried at 60 ℃ under vacuum. In order to study the effects of different reaction conditions on the synthesis of Sb_2Se_3 nanorods, the reaction temperature, reaction time and modification of organic solvents were changed accordingly.

2.2.4 Synthesis of hybrid nanorods with $Sb_2Se_3/AgSbSe_2$ heterojunction structure

Herein, a two-step selenization process was used to synthesize hybrid nanorods with $Sb_2Se_3/AgSbSe_2$ heterojunction structure. 2 ml 0.8 M selenium precursor solution was swiftly injected into 240 ℃ antimony precursor solution in the flask. Then 0.2 mmol silver acetate was added into the flask. After the mixture was stirred for several minutes, another 6 ml 0.8 M selenium precursor was swiftly injected into the flask. The mixture was stirred for 10 minutes and then cooled to room temperature. The obtained hybrid nanorods with $Sb_2Se_3/AgSbSe_2$ heterojunction structure were collected by centrifugation, washed with chloroform and isopropyl alcohol for several times, and finally dried at 60 ℃ under vacuum.

2.2.5 Synthesis of $AgSbSe_2$ nanoparticles

$AgSbSe_2$ nanoparticles were also synthesized via hot-injection. The preparation of the 0.8 M Se-ODE precursor solution was described earlier in 2.2.3. 1 mmol antimony acetate, 1 mmol silver acetate, 8 mmol 1-hexadecylamine, 20 ml 1-octadecene and 8 ml oleic acid were mixed at 220 ℃ for 1 h in another flask, which formed a transparent yellow antimony-silver precursor solution. The temperature of the antimony-silver precursor solution was heated up to 240 ℃, and then 8 ml 0.8 M selenium precursor solution which had been cooled to room temperature was swiftly injected. The mixture was stirred for 10 min and then cooled to room temperature. The obtained $AgSbSe_2$ nanoparticles were collected by centrifugation, washed with chloroform and isopropyl alcohol for several times, and finally dried at 60 ℃ under vacuum.

2.2.6 Synthesis of $(Sn_xSb_{1-x})_2Se_3$ nanorods

Similar to the preparation process of Sb_2Se_3 nanorods, the $(Sn_xSb_{1-x})_2Se_3$ (x=0.00, 0.01, 0.03, 0.05, 0.10) nanorods were also synthesized via hot-injection. The biggest difference was that the antimony (tin) precursor solution was injected into the selenium precursor solution. The detailed preparation procedure was as follows: At first, a uniform mixture of (1-x) mmol antimony acetate and x mmol tin chloride was added into a 25 mL three-neck flask with 8 ml oleic acid as solvent. The mixture was degassed and then heated to 220 ℃ for 1 h under argon atmosphere to form a transparent yellow solution (antimony and tin precursor solution). To prepare selenium precursor solution, 6 mmol selenium dioxide and 15 ml 1-octadecene in another flask were heated up to 200 ℃ for several hours with stirring until the solid was completely dissolved, forming a 0.4 M selenium precursor solution. Subsequently, the antimony and tin precursor solution was rapidly injected into the selenium precursor solution which was heated up to 240 ℃ beforehand. The mixture was stirred for about 10 min and then cooled down to room temperature. Finally, the washing, purification and drying steps of the nanorods were also applied.

2.2.7 Fabrication of the nanorod film photodetector

To explore the photoconductive properties of Sb_2Se_3 nanorods, hybrid nanordos with $Sb_2Se_3/AgSbSe_2$ heterojunction structure and $(Sn_xSb_{1-x})_2Se_3$ (x=0.00, 0.01, 0.03, 0.05, 0.10) nanorods, a film-based prototype photodetector was constructed. Fig. 2.3 is a schematic illustration of the photodetector with nanorod film across the interdigital Au electrodes with fingers (dimensions: width 20 μm, length 200 μm, interfinger spacing 20 μm) fabricated on SiO_2/Si substrates using lithography. It was noted that the interdigital Au electrodes with a total area of 6×10^{-4} cm^2 were fully covered by the nanorod film.

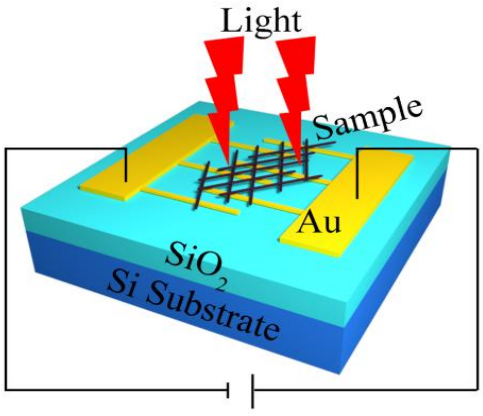

Fig. 2.3 Schematic illustration of the photodetector based on the Sb_2Se_3 nanorod film

To better perform the measurements, the as-prepared nanorods were repeatedly purified by washing and then ultrasonically dispersed in chloroform, drop-cast on pre-patterned electrodes, and dried by vacuum-annealing at 40 ℃ for 30 min before the photocurrent measurements.

2.2.8 Characterization

(i) X-ray diffraction (XRD) analysis. XRD analysis was carried out on PAN alytical B.V. Empyrean 200895 x-ray diffractometer with Cu Kα radiation (λ = 1.54 Å), and the scan speed was 2.00 deg/min.

(ii) Scanning electron microscope (SEM) analysis. A Hitachi S-4800 field emission scanning electron microscope was used to observe the morphologies.

(iii) Transmission electron microscope (TEM) analysis. TEM, HRTEM (High Resolution TEM), SAED (Selected Area Electron Diffraction), STEM (Scanning TEM) images and the corresponding EDS (Energy Dispersive Spectrometer) mapping images were obtained from a FEI Tecnai G2F20 field emission transmission electron microscope operating at an acceleration voltage of 200 kV. Samples were prepared by placing a drop of a dilute chloroform dispersion of the nanorods on the surface of a copper grid.

(iv) EDS analysis. EDS analysis has been performed with an EDAX instrument.

(v) X-ray photoelectron spectroscopy (XPS) analysis. The elemental composition and the valence state were analyzed by XPS with the corresponding equipment of ESCALAB. In addition, the $Sb_2Se_3/AgSbSe_2$ semiconductor heterojunction type can be further determined by combining the XPS valence band spectrum.

(vi) Diffuse reflectance spectroscopy analysis. Analysis of optical absorption spectra is one of the most effective tools for understanding and/or engineering the band structure and energy gaps of semiconductor materials, and it also provides a theoretical basis for the subsequent construction of high-performance photoelectric devices. However, due to the scattering of the solid powder samples, it is not possible to obtain the absorption spectrum directly. Thus, the diffuse reflection spectrum was measured firstly, and then the corresponding absorption spectrum can be obtained by using Kubelka-Munk conversion formula:

$$F(R)= \alpha/\Lambda=(1-R)^2/(2R) \quad (2.1)$$

where F(R) is the calculated absorption value, R is the reflectance, α and Λ are the absorption coefficient and the scattering coefficient, respectively [21]. Furthermore, the energy band gap (E_g) of the semiconductor can be calculated by the Tauc formula:

$$F(R)hv=C(hv-E_g)^n \quad (2.2)$$

where C is a constant, h is the Planck's constant, v is the photon frequency, n is an index, and n = 0.5 when the sample is a direct bandgap semiconductor, n = 2 when the sample is an indirect bandgap semiconductor. Then E_g can be determined by extrapolating the linear part of the spectrum to zero. Herein, the diffuse reflectance spectra of the as-synthesized nanomaterials were taken from a SHIMADZU UV-3150 spectrophotometer.

(vii) Hall-effect measurements. The electric and electronic properties, including resistivity, carrier concentration, mobility and the conduction type were investigated by Hall-effect measurements using the Van der Pauw configuration (BID-RAD HL5500PC) at room temperature.

(viii) The photoconductive performance of the photodetectors were recorded using a Keithley 2450 SCS and SUSS PM8 probe station in a clean and shielded box. A xenon lamp or laser with controllable light intensities was used as the light source. Moreover, the xenon lamp equipped with a monochromator was used to measure the spectral response with a wavelength interval of 50 nm.

2.3 Results and discussion

2.3.1 Preparation and characterization of Sb_2Se_3 nanorods

1. Effect of reaction temperature on Sb_2Se_3 nanorods

Fig. 2.4 shows the XRD patterns of Sb_2Se_3 nanorods synthesized at different temperatures (160 ℃, 200 ℃, 240 ℃ and 280 ℃). All the four spectra show sharp diffraction peaks, indicating a high crystallinity and large grain size of the as-synthesized Sb_2Se_3 nanorods. Furthermore, the sample obtained at 160 ℃ show a trace amount of Sb_2O_3 impurity. It was because the reaction temperature was low, the Sb precursor was not completely used for forming Sb_2Se_3 nucleus, and the slow growth rate at low temperature also caused an incomplete reaction within 10 minutes. For the samples obtained from the other three reaction temperatures, the XRD patterns exhibit prominent peaks in agreement with the JCPDS standard card (15-0861) of the orthorhombic phase of Sb_2Se_3 without a second phase, indicating the absence of any detectable impurities such as Se or Sb_2O_3. In addition, the calculated unit cell parameters of the samples are consistent with the lattice constants corresponding to the standard card (a=1.1633 nm, b=1.1780 nm, c=0.3985 nm), which further indicating the high purity and high crystallinity nature.

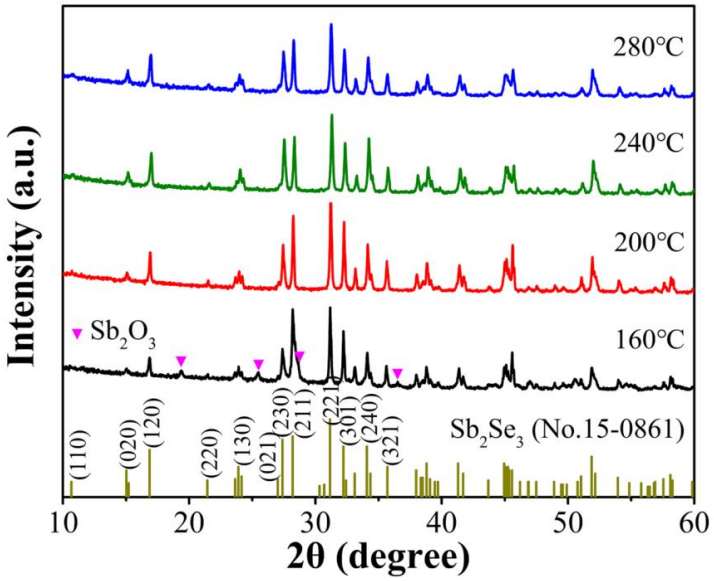

Fig. 2.4 XRD patterns of the Sb_2Se_3 nanorods synthesized at different temperatures (160 ℃, 200 ℃, 240 ℃ and 280 ℃)

Fig. 2.5a-d are the SEM images of the samples obtained at different reaction temperatures (160 ℃, 200 ℃, 240 ℃ and 280 ℃). When the reaction temperature was low (160 ℃), some particles remained on the surface of the nanorod, which was consistent with the presence of trace impurities in the XRD pattern. When the reaction temperature was raised to 200 ℃, the particles disappear and all the nanorods have smooth surface throughout the entire length with a diameter of ~ 100-300 nm, and a typical length of several micrometers. When the temperature is raised to 240 ℃, the diameter is mostly around 200 nm and the uniformity is obviously improved. Finally, at the relatively high reaction temperature of 280 ℃, some nanorods grew too fast, resulting in poor uniformity. Meanwhile, high reaction temperature creates issues associated with the high pressure of solvents and safety issues. The optimal reaction temperature for preparing Sb_2Se_3 nanorods via hot-injection method is determined to be 240 ℃.

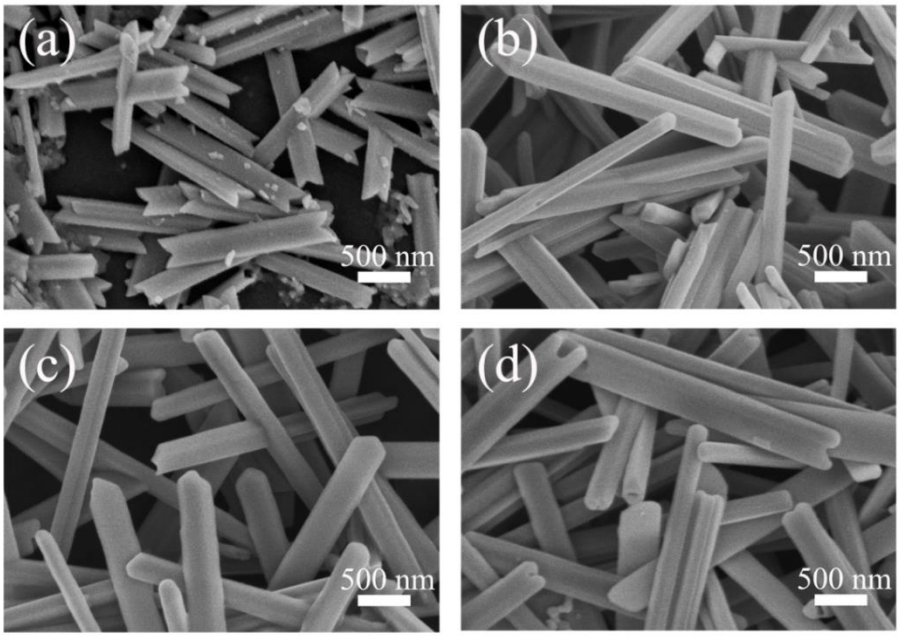

Fig. 2.5 SEM images of Sb_2Se_3 nanorods synthesized at different temperatures: (a) 160 ℃; (b) 200 ℃; (c) 240 ℃; (d) 280 ℃

The micro-morphology and structure of the nanorods were further characterized. Fig. 2.6a and Fig. 2.6b are the SEM image and TEM image of the Sb_2Se_3 nanorods synthesized at 240 ℃ for 10 min, respectively. The images reveal the formation of highly uniform Sb_2Se_3 nanorods, with smooth surfaces throughout the entire length, a diameter of ~ 150-200 nm and a typical length of several micrometers. HRTEM image and corresponding selected-area Fast Fourier Transform (FFT) pattern of a randomly selected nanorod (Fig. 2.6c) confirmed its highly crystalline nature with orthorhombic phase lattice fringes associated with the (001) planes (*d*-spacing of 0.392 nm) along the nanorod, indicating that the nanorod grew along this direction (c-axis). Moreover, the XRD patterns of the orthorhombic phase Sb_2Se_3 exhibit strong intensity of those (hk0) peaks, confirming that Sb_2Se_3 are preferentially grown along the (001) direction. According to the recent theoretical and experimental studies, the preferential growth is indeed determined intrinsically by the anisotropic Sb-Se atom chain and layer structure of orthorhombic Sb_2Se_3 [2]. The EDS spectrum (Fig. 2.6d) of an individual nanorod exhibits strong Sb and Se peaks, and the atomic ratio of Sb and Se corresponds to the 2:3 stoichiometry within the precision of the measurements.

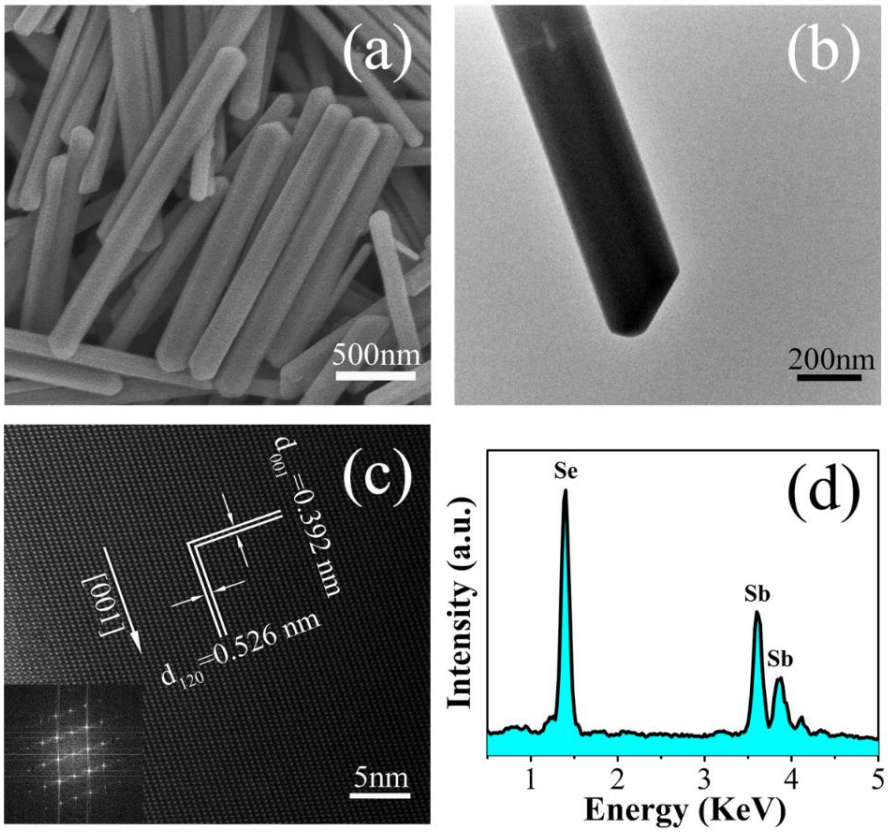

Fig. 2.6 Morphological and structural characterization of the Sb_2Se_3 nanorods: (a) SEM image; (b) TEM image; (c) HRTEM image, the bottom inset is a selected-area FFT pattern; (d) EDS spectrum

2. Effect of reaction time on Sb_2Se_3 nanorods

Fig. 2.7a shows the XRD patterns of the samples obtained by reacting at 240 ℃ for 10 s, 30 s, and 60 s, which all exhibit prominent peaks in agreement with the JCPDS standard card of the orthorhombic phase of Sb_2Se_3. It is worth noting that the nanorods with a very short reaction time still have high crystallinity and high purity. Fig. 2.7b-d is the corresponding SEM images. As the reaction time prolongs, the diameter and the length of the nanorods show small variation, and the homogeneity is maintained, indicating that the nucleation and growth rate of the nanorods is very fast. This fact is closely related to the mechanism of the hot-injection method. Specifically, the cold Se-ODE precursor solution was quickly injected into the Sb precursor solution at 240 ℃. The temperature of the mixture dropped, but was still higher than the nucleation temperature. Therefore, a large amount of nuclei was generated instantaneously. The concentration of the precursor in the reaction system was then reduced below the critical nucleation concentration, and the secondary nucleation could not be initiated, ensuring the uniformity of the obtained nanorods.

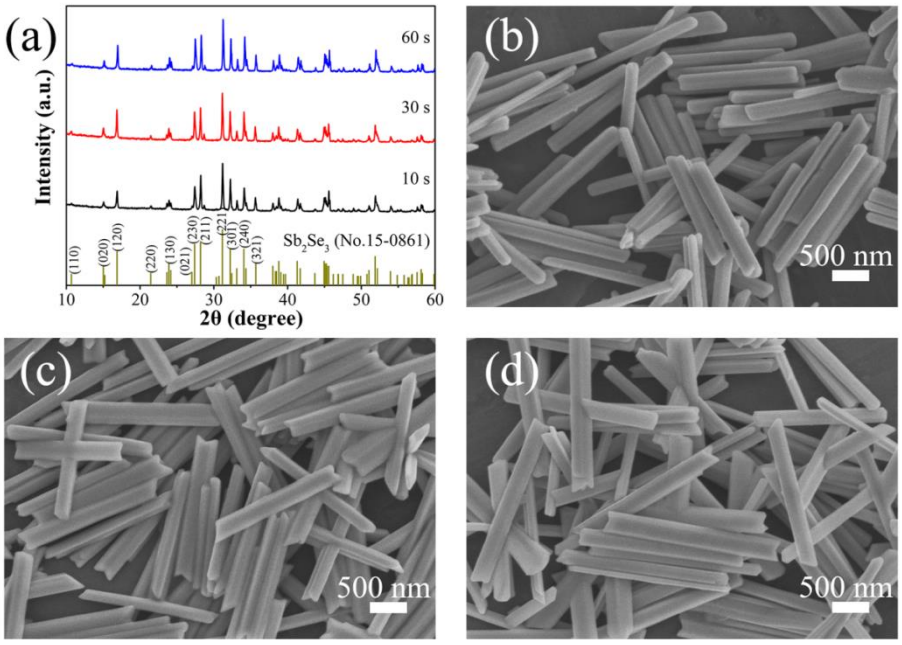

Fig. 2.7 Synthesis of Sb_2Se_3 nanorods with different reaction time at 240 ℃: (a) XRD patterns; (b)-(d) SEM images of the obtained samples with the reaction time of 10 s, 30 s and 60 s, respectively

In order to further study the kinetic growth process of 1D Sb_2Se_3 nanorod structure, a lower reaction temperature (160 ℃) was selected to reduce the nucleation and growth rate. An equal amount of the reaction mixture was taken out from the reaction flask every 30 s, then washed and purified in a mixed solvent of chloroform and isopropyl alcohol before SEM characterization. Fig. 2.8a-f are the corresponding SEM images with reaction time of 60 s, 90 s, 120 s, 150 s, 180 s, and 210 s respectively. When the Se-ODE precursor solution was rapidly injected into the Sb precursor solution at 160 ℃, the temperature of the mixture decreased, and the color of the solution remained transparent yellow within 60 s, indicating the absence of Sb_2Se_3. After that, the temperature of the mixture gradually increased and the color gradually changed from yellow to grayish black, indicating that the target products began to nucleate and to grow as expected. Fig. 2.8b presents nanospheres with a diameter of ~ 100-200 nm. When the reaction time was extended to 120 s, short nanorods began to appear on the surface of the nanospheres. By continually extending the reaction time, relatively long nanorods can be observed and the nanospheres gradually decrease. Up to 210 s of reaction, sample with uniform nanorods can be obtained (Fig. 2.8f). In summary, unlike the rapid nucleation and growth process at high temperature, the growth mechanism of Sb_2Se_3 at lower temperature is gradually changed from nanosphere to 1D nanorod structure.

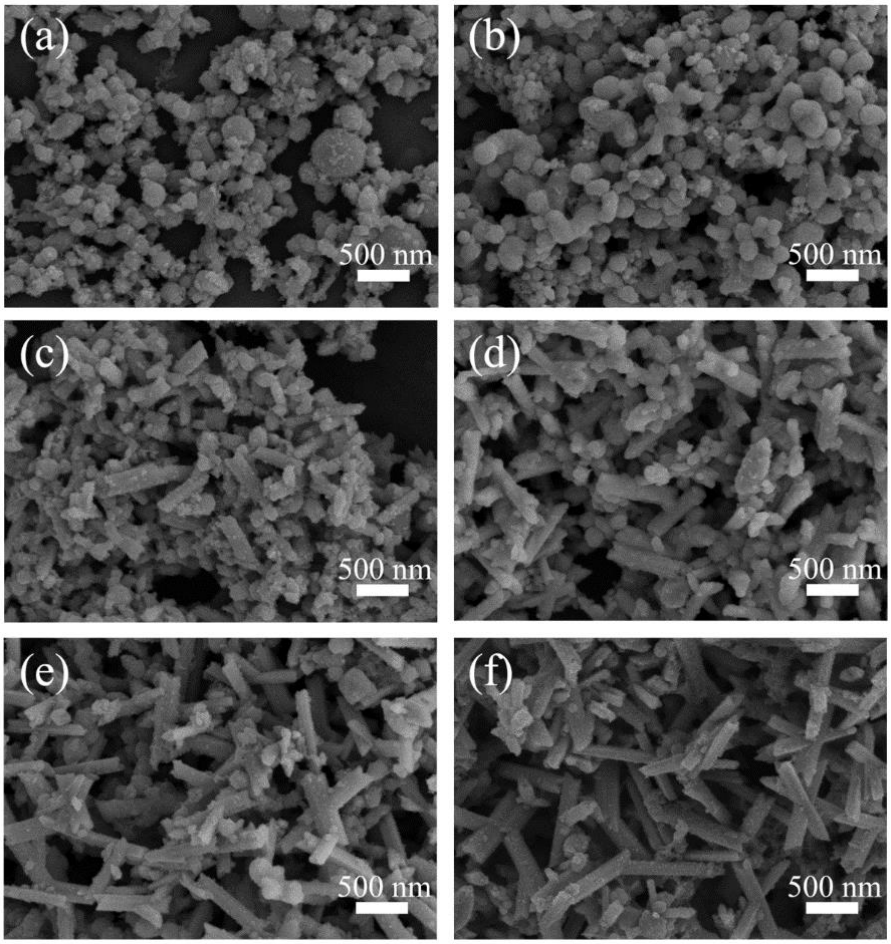

Fig. 2.8 SEM images of Sb_2Se_3 nanorods with different reaction time at 160 ℃: (a) 60 s; (b) 90 s; (c) 120 s; (d) 150 s; (e) 180 s; (f) 210 s

3. Effect of reaction solvents on Sb_2Se_3 nanorods

In addition to the reaction temperature and reaction time, the reaction solvents also play a very important role in the synthesis of nanomaterials. The organic solvents used in this experiment include octadecene (ODE), hexadecylamine (HDA), and oleic acid (OA). Firstly, ODE is a non-coordinating solvent. According to the literature, the initial successful synthesis of chalcogenide semiconductor nanocrystals via colloidal chemical processes was carried out in the organic coordination solvent trioctylphosphine oxide (TOPO) [22]. From 2005, ODE as a non-coordinating solvent, which is in addition inexpensive and more environmentally friendly, began to replace TOPO [23]. In this work, SeO_2 was directly dissolved in ODE, which can be considered as phosphine-free green preparation process. In the antimony precursor system, another two surfactants, named HDA and OA, were also added. In order to study the effects of these two active agents, each of them was separately added, and the other conditions were kept constant. Fig. 2.9a and 2.9b represent the SEM images of the nanorods

synthesized at 240 ℃ for 10 min using respectively HDA and OA as surfactants. Compared with the HDA/OA dual solvents system (Fig. 2.5c), the size of the nanorods obtained with HDA was significantly reduced, while it was the opposite for the role of OA. Moreover, it was found that without adding OA, the antimony precursor solution was a white suspension, indicating a ligand role of OA, and the coordination of OA and antimony ions greatly improved the reactivity of the precursor, thus the samples could be obtained in a short time. However, the excessive concentration of OA inhibited the reactivity, the number of nanocrystalline cores formed during the nucleation stage was reduced, and the precursors for the reaction stage were increased, resulting in an increase in the diameter of the nanorods. The role of HDA was to accelerate the nucleation process and reduce the growth rate, so the size of the nanorods was smaller. Therefore, when two surfactants were added, the nucleation and growth of Sb_2Se_3 could reach a relative balance, and their adsorption on the surface of the nanorods prevented irreversible agglomeration occur between the nanorods during the growth process. Finally, the nanorods with excellent dispersion and uniformity have been synthesized.

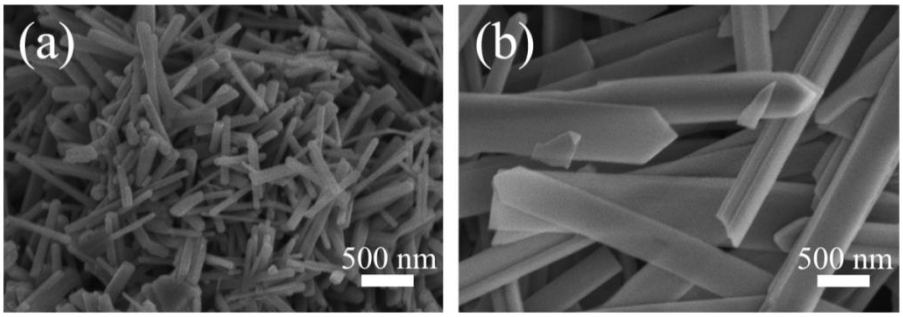

Fig. 2.9 SEM images of Sb_2Se_3 nanorods with different surfactants at 240 ℃: (a) HDA as surfactant and (b) OA as the surfactant

2.3.2 Photoconductive performance of the Sb_2Se_3 nanorod film photodetector

Photoconductivity is a well-known property of semiconductors which describes the electrical conductivity changes with the incident light. The photoconductive characteristics of the Sb_2Se_3 nanorods are investigated here by using the Sb_2Se_3 nanorod film-based photodetector. Fig. 2.10a shows the I-V curves of the Sb_2Se_3 nanorod film photodetector. The electrical conductivity of the Sb_2Se_3 nanorods in dark condition is very low and similar to the bulk Sb_2Se_3 ($\sigma \sim 10^{-6}\ \Omega^{-1}m^{-1}$) [1]. The thin film device shows much higher photosensitivity at different incident light densities, compared to bulk Sb_2Se_3. The photocurrent was significantly increased with increasing light intensity. To further investigate the photoresponse characteristics, a plot of time-resolved photoresponse at the bias of −10 V, −20 V and −30 V

(incident light density of 12.05 $mWcm^{-2}$) is shown in Fig. 2.10b. When the applied voltage was −20 V, with the light irradiation on and off, the current across the nanorod film dramatically increases from −2 nA (OFF state, dark condition) to −100 nA (ON state, light illumination). The switching "ON/OFF" ratio is as high as 50, which is comparable to the very good results previously reported [2,24].

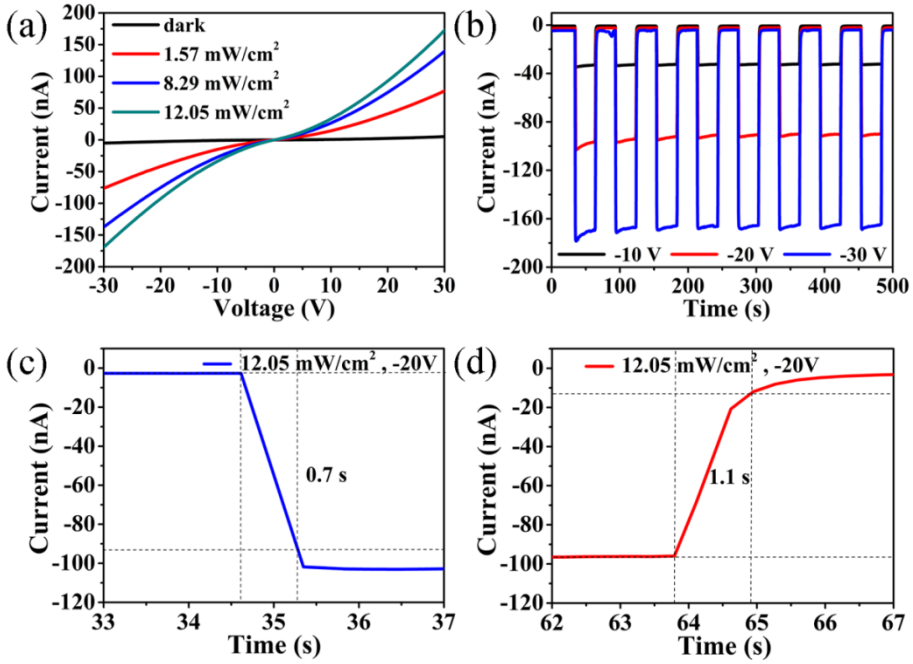

Fig.2.10 Photoconductive performance of the photodetector based on the Sb_2Se_3 nanorod film. (a) Dark current and photocurrents at different incident power densities, (b) Time-resolved photoresponse at the bias of -10 V, -20 V and -30 V with an incident light density of 12.05 mW cm^{-2}, Demonstration of (c) the response speed and (d) the recovery speed at a bias of -20 V and an incident light density of 12.05 mW cm^{-2}

In addition, the response and the recovery times are other important parameters allowing to evaluate the speed of the ON/OFF switching processes. These two times are respectively defined as the time necessary for reaching 90% of the ΔI (ΔI is the difference between the maximum current and the minimum current) when the light is on and the time for returning from the maximum current to 10% of the ΔI. As shown in Fig. 2.10c and 2.10d, 0.7 s response time and 1.1 s recovery times can be obtained, and this performance is remained even over 8 cycles, demonstrating the stability of the device.

The Sb_2Se_3 nanorods used in this device were synthesized using a hot-injection method and were expected to be more resistant to oxidation and contained fewer surface defects. It is known that with a superior crystal quality, the density of traps induced by defects is

dramatically reduced and the photocurrent rapidly reaches a steady state both on rise and decay stages [25]. It is also noticed that the high photo-detectivity of the nanorods is due to the high density of the surface sates inducing the depletion space charge layer. In Sb_2Se_3 nanorods, a depletion space charge layer is formed due to the surface state and Fermi-level pinning, which allows for physical separation of electrons and holes. It has reported that when the critical diameter is reached, the depletion layer remains fully depleted and the recombination barrier increases. The photocurrent may further increase as the nanorods diameter increases [1]. Therefore, the high photodetectivity of the Sb_2Se_3 nanorods could also be attributed to the larger diameter of Sb_2Se_3 nanorods (~150-200 nm).

2.3.3 Preparation and characterization of the hybrid nanorods with $Sb_2Se_3/AgSbSe_2$ heterojunction structure

In the introduction of this chapter, two approaches are proposed to overcome the critical challenge of low electrical conductivity of Sb_2Se_3. One was the formation of composites with a high conductivity second phase. Herein, the ternary semiconductor $AgSbSe_2$ was chosen as the second phase. It is worth noting that $AgSbSe_2$ shows an excellent electrical conductivity of 154 $S.cm^{-1}$. In addition to this prominent intrinsic property, $AgSbSe_2$ is a narrow band gap semiconductor (~1 eV) with valence band structure composed of multiple flat valleys, favourable for electrical conductivity improvement through doping or by forming functional junctions [27,28]. Therefore, we have tried to prepare $Sb_2Se_3/AgSbSe_2$ heterojunction nanorods via hot-injection method.

Fig. 2.11 shows the XRD patterns of the as-synthesized Sb_2Se_3 nanorods, $AgSbSe_2$ nanoparticles and the hybrid nanorods with $Sb_2Se_3/AgSbSe_2$ heterojunction structure. For pure Sb_2Se_3, all the diffraction peaks are in agreement with the JCPDS standard card (No. 15-0861) of the orthorhombic phase of Sb_2Se_3. The XRD pattern of the $AgSbSe_2$ nanoparticles completely coincides with the cubic crystal phase of $AgSbSe_2$ with the JCPDS standard card (No. 65-6604) and no second phase or other impurities are detected. Finally, the XRD pattern of the hybrid nanorods with $Sb_2Se_3/AgSbSe_2$ heterojunction structure shows that all diffraction peaks can match very well with the standard card of Sb_2Se_3 (JCPDS 15-0861) or $AgSbSe_2$ (JCPDS 65-6604) without any visible peak of impurities, indicating the high crystallinity and high purity of the hybrid nanorods.

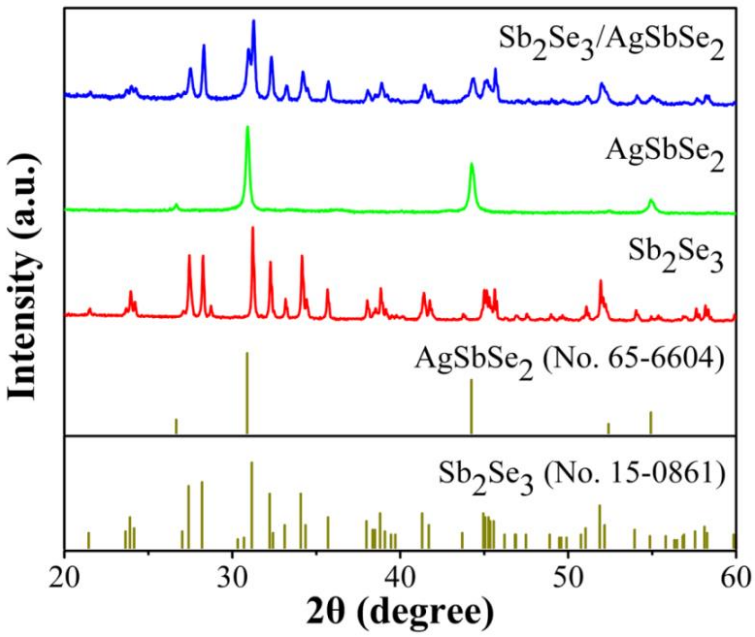

Fig. 2.11 XRD patterns of Sb_2Se_3 nanorods, $AgSbSe_2$ nanoparticles and the hybrid nanorods with the $Sb_2Se_3/AgSbSe_2$ heterojunction structure

Fig. 2.12 shows the SEM, TEM, HRTEM, STEM images and the corresponding EDS mapping images of the hybrid nanorods. Some small nanoparticles incorporated onto the nanorods can be observed. The representative HRTEM images obtained from the selected areas 1 and 2 of Fig. 2.12c show that the nanoparticle and the nanorod have different lattice structures and a visible interface. The interplanar d-spacing of 0.287 nm correspond to the (200) plane of $AgSbSe_2$, the selected-area Fast Fourier Transform (FFT) pattern (inset in the left HRTEM image) from the red marked area further confirms the presence of $AgSbSe_2$ crystalline phase. The interplanar d-spacings of 0.585 nm and 0.328 nm agree well with the distance of the (200) and (021) lattice planes of Sb_2Se_3, respectively.

Finally, the EDS mapping images show that Sb and Se atoms are homogenously distributed in both the nanorod and the nanoparticles. However, Ag distribution was restricted to the specific areas corresponding to the position of the nanoparticles and to a small part of the nanorod near to the nanoparticles, which indicated the formation of $AgSbSe_2$ nanoparticles on the surface of the Sb_2Se_3 nanorod. It is obvious that the nanoparticles belong to $AgSbSe_2$ phase and the nanorods to Sb_2Se_3 phase

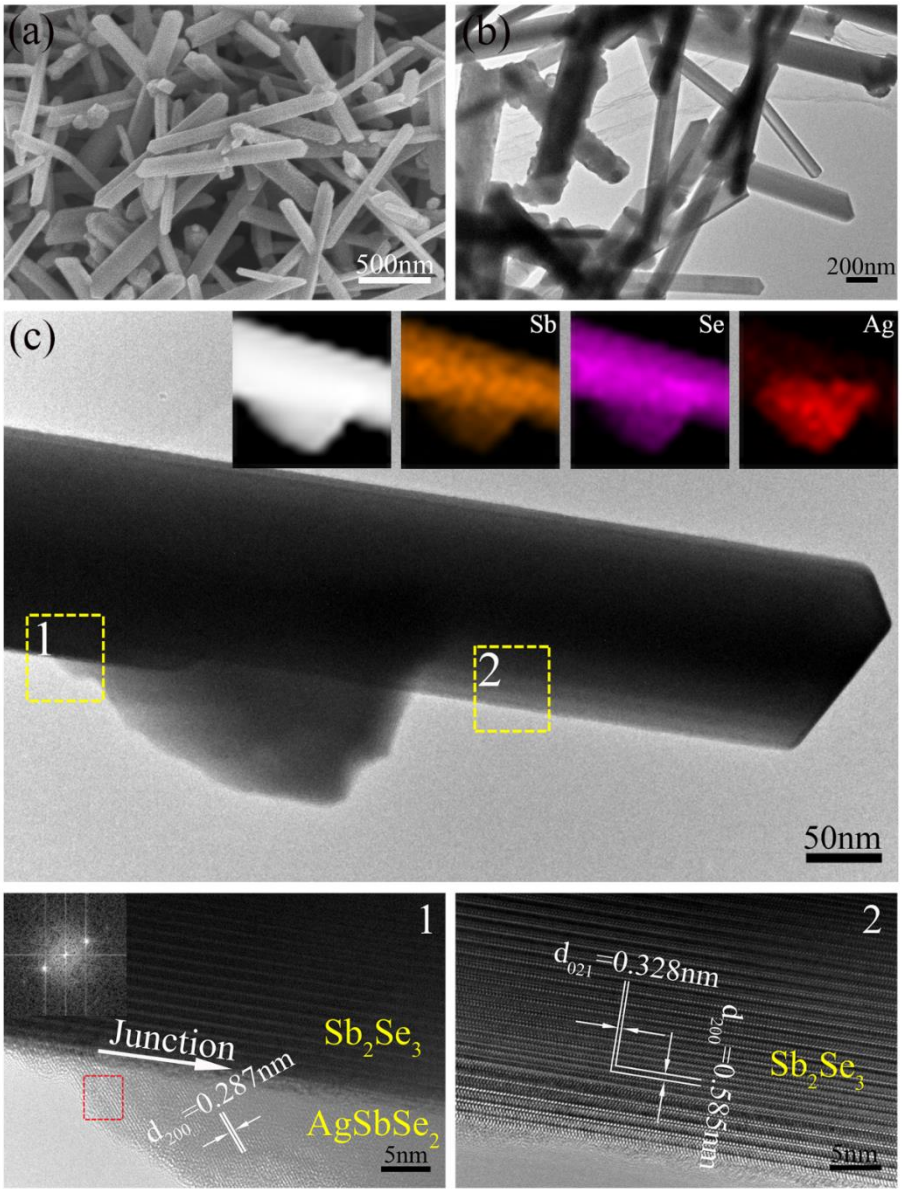

Fig. 2.12 Structural and morphological characterization of the hybrid nanorods with the $Sb_2Se_3/AgSbSe_2$ heterojunction structure. (a) SEM image, (b) TEM image, (c) TEM image and HRTEM images from the selected areas 1 and 2 of an individual hybrid nanorod (inset in the left HRTEM image is a FFT pattern from the red marked area), the inset of (c) shows a STEM image and the EDS mapping images of Sb, Se and Ag elements, respectively

It can be concluded from Fig. 2.11 and Fig. 2.12 that the $Sb_2Se_3/AgSbSe_2$ heterojunction nanorods are composed of rod-shaped Sb_2Se_3 and granular $AgSbSe_2$. In order to understand the formation mechanism of the heterojunction structure. The two phases have been synthesized separately. The $AgSbSe_2$ nanoparticles were synthesized using hot-injection method. As shown in Fig. 2.13, according to the typical TEM image, the diameter of the nanoparticles is typically between 10-20 nm, which is not completely monodisperse. The EDS spectrum (Fig. 2.13b) confirms the presence of only Ag, Sb and Se elements with the atomic

ratio of Ag : Sb : Se close to the standard stoichiometry of 1 : 1 : 2.

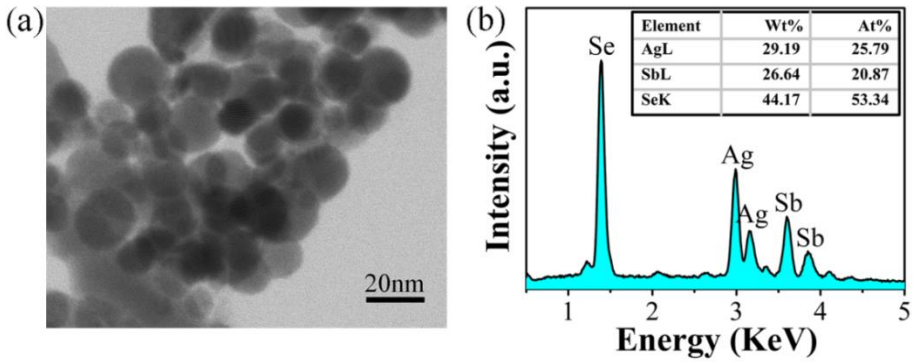

Fig. 2.13 (a) TEM image of the as-synthesized $AgSbSe_2$ nanoparticles; (b) EDS spectrum

Fig. 2.14 illustrates the formation mechanism of Sb_2Se_3 nanorods and the hybrid nanorods with $Sb_2Se_3/AgSbSe_2$ heterojunction structure, including the corresponding SEM images. For the pure Sb_2Se_3, an excessive amount of selenium precursor solution was rapidly injected into the antimony precursor, and the reaction was quickly completed to obtain the uniform Sb_2Se_3 nanorods. Then the hybrid nanorods with $Sb_2Se_3/AgSbSe_2$ heterojunction structure were synthesized by a two-step selenization method. For the first selenization step, uniform Sb_2Se_3 nanorods were obtained and then silver precursor was added. In this case, some Sb_2Se_3 rods were covered with nanoparticles or some silver-rich clusters due to the deficiency of selenium precursor. Then at the second selenization step, Sb_2Se_3 nanorods act as a substrate for $AgSbSe_2$ nanoparticles growth, leading to the formation of semiconductor heterojunction. Additionally, some pure Sb_2Se_3 nanorods can be formed with the excessive antimony precursor in the reaction mixture, as shown in the SEM images.

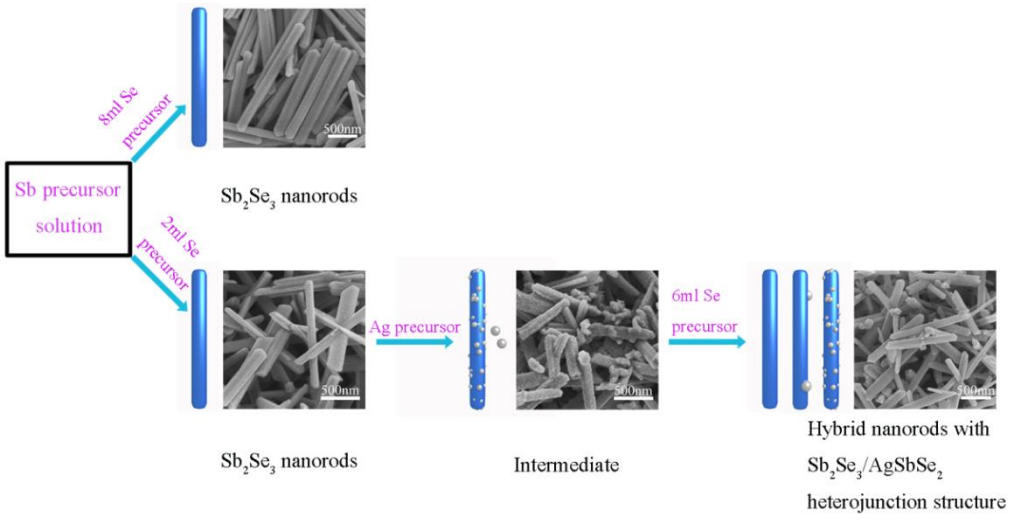

Fig. 2.14 Schematic illustration of the formation mechanism and the corresponding SEM images of the Sb_2Se_3 nanorods and the hybrid nanorods with the $Sb_2Se_3/AgSbSe_2$ heterojunction structure

In order to further study the element valence state of the samples, XPS analysis was performed on Sb_2Se_3 nanorods, $AgSbSe_2$ nanoparticles and hybrid nanorods with $Sb_2Se_3/AgSbSe_2$ heterojunction structure. Fig. 2.15 shows the corresponding Sb-3d, Se-3d and Ag-3d XPS spectra.

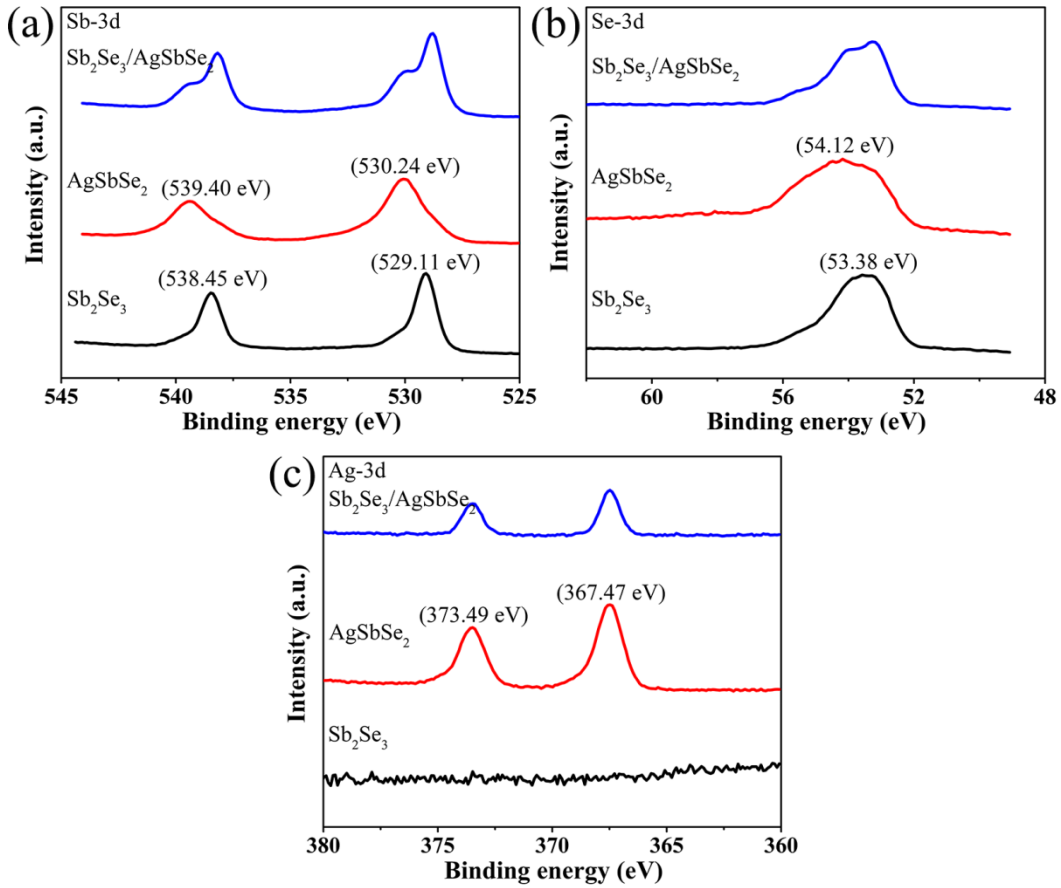

Fig. 2.15 XPS spectra of the Sb_2Se_3 nanorods, $AgSbSe_2$ nanoparticles and the hybrid nanorods with the $Sb_2Se_3/AgSbSe_2$ heterojunction structure: (a) Sb-3d; (b) Se-3d; (c) Ag-3d

As shown in Fig. 2.15a, the Sb-3d of Sb_2Se_3 splits into two peaks due to spin coupling, namely $3d_{5/2}$ (529.11 eV) and $3d_{3/2}$ (538.45 eV) with a spacing of 9.34 eV. A similar phenomenon is also observed for $AgSbSe_2$, and the peak splits into $3d_{5/2}$ (530.24 eV) and $3d_{3/2}$ (539.40 eV) peaks with a spacing of 9.16 eV. After analysis, the valence state of Sb can be defined as Sb^{3+} [29] and the small shift of the Sb-3d peaks between these two semiconductors is due to the different chemical potential caused by the Sb-bond neighbor atoms. Taking the $Sb_2Se_3/AgSbSe_2$ hybrid nanorods into consideration, Sb-3d splits into $3d_{5/2}$, $3d_{3/2}$ doublet and each peak of this doublet splits again into another two small peaks. The binding energy and peaks spacing are consistent with pure Sb_2Se_3 and $AgSbSe_2$, respectively, which further demonstrates the heterojunction structure of the hybrid nanorods. Similarly, the element Se in

the hybrid nanorod exists as Se^{2-} and the XPS spectrum is well matched with Sb_2Se_3 and $AgSbSe_2$ (Fig. 2.15b). Finally, no Ag-3d characteristic peaks can be detected in the Sb_2Se_3 nanorods. The Ag-3d peak of the $Sb_2Se_3/AgSbSe_2$ hybrid nanorods is completely consistent with that of the $AgSbSe_2$ nanoparticles. Moreover, $Ag3d_{5/2}$ (367.47 eV) and $Ag3d_{3/2}$ (373.49 eV) are clearly assigned to Ag+.

It is known that a proper band gap of semiconductor is important to fabricate high performance photodetectors. In this work, optical absorption spectra have been used to investigate the optical properties of the as-synthesized Sb_2Se_3 nanorods, $AgSbSe_2$ nanoparticles and the hybrid nanorods with $Sb_2Se_3/AgSbSe_2$ heterojunction. Herein, the absorption data were calculated from diffuse reflectance data using Kubelka−Munk equations: $F(R)=\alpha/\Lambda=(1-R)^2/(2R)$, where R is the reflectance, α and Λ are the absorption and scattering coefficients, respectively [21]. As shown in Fig. 2.16a, the onset of absorption for Sb_2Se_3 nanorods starts near 1100 nm. A plot of $[F(R)hv]^2$ versus energy (hv) yielded a direct band gap of 1.19 eV (inset in Fig. 2.16a). Similarly, Fig. 2.16b shows that the onset of absorption for $AgSbSe_2$ nanoparticles starts near 1600 nm and the corresponding direct band gap is 0.83 eV. The absorption spectrum of the hybrid nanorods with $Sb_2Se_3/AgSbSe_2$ heterojunction (Fig. 2.16c) exhibits two optical absorption peaks, and the onsets match very well with $AgSbSe_2$ and Sb_2Se_3, respectively.

To further investigate the band offset of the $Sb_2Se_3/AgSbSe_2$ heterojunction, XPS valence band analysis has been extensively employed, which lies on a core-level photoemission-based method, using a linear extrapolation method to determine the valence band maximum [31]. The valence-band offset (ΔE_V) is obtained by the following expression:

$$\Delta E_V=(E_{Sb\text{-}3d}-E_V)_{Sb_2Se_3}-(E_{Sb\text{-}3d}-E_V)_{AgSbSe_2}-(E_{Sb\text{-}3d}-E_{Sb\text{-}3d})_{Sb_2Se_3/AgSbSe_2} \quad (2.3)$$

According to the Sb-3d XPS spectra (Fig. 2.15) and the valence-band edge (VBE) spectra (Fig. 2.16d), the ΔE_V is calculated to be 0.44 eV, and the conduction-band offset is deduced to be 0.08 eV. It was found that $Sb_2Se_3/AgSbSe_2$ heterojunction has a type-II band alignment (inset in Fig. 2.16d). Accordingly, as a direct band gap semiconductor, the experimental band gaps for the as-synthesized semiconductors are close to the optimum value for photovoltaic conversion, implying their promising applications in photoelectric devices, including high performance photodetectors.

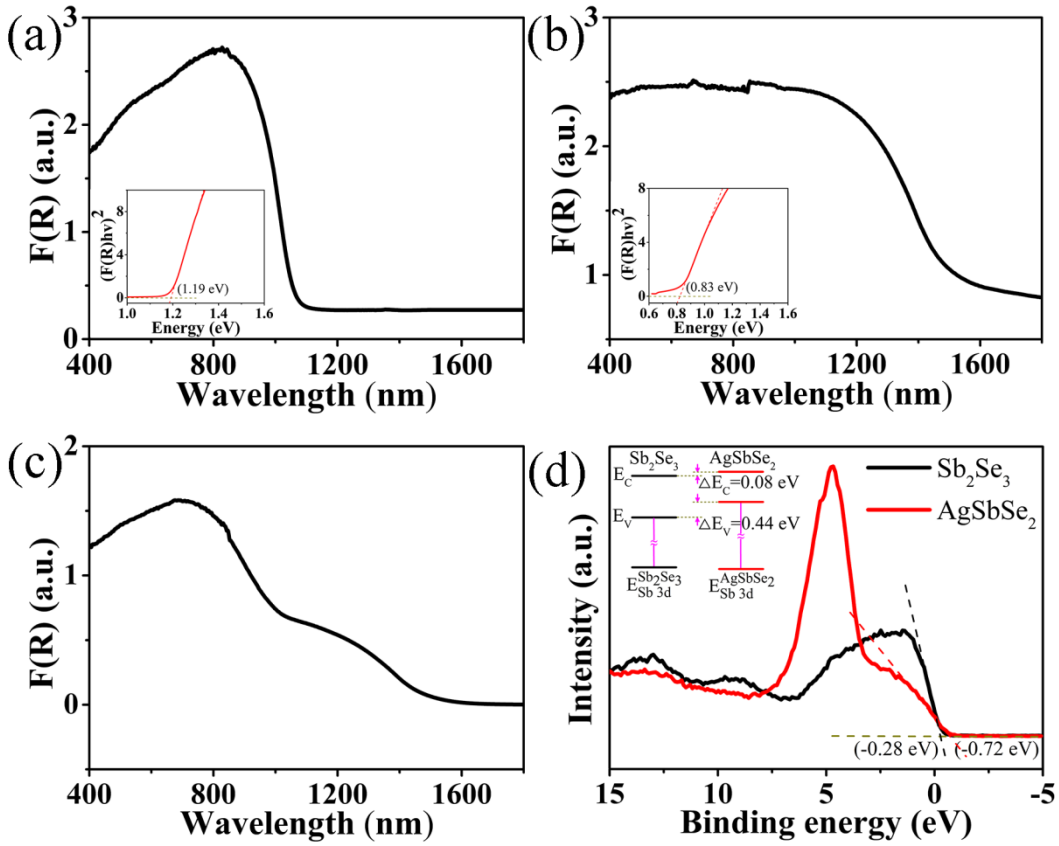

Fig. 2.16 (a) Optical absorption spectra (calculated from diffuse reflectance data) for Sb_2Se_3 nanorods. Inset: A plot of $[F(R)hv]^2$ vs. energy for the Sb_2Se_3 nanorods, from which direct band gap energy was obtained; (b) Absorption spectra for $AgSbSe_2$ nanoparticles. Inset: A plot of $[F(R)hv]^2$ vs. energy; (c) Absorption spectra for the hybrid nanorods with $Sb_2Se_3/AgSbSe_2$ heterojunction, (d) VBE spectra for Sb_2Se_3 nanorods and $AgSbSe_2$ nanoparticles. Inset: Schematic diagram of type-II band alignment of the heterojunction

2.3.4 Photoconductive performance of the $Sb_2Se_3/AgSbSe_2$ hybrid nanorod film Photodetector

Fig. 2.17 shows the photoconductive performance of the $Sb_2Se_3/AgSbSe_2$ hybrid nanorod film photodetector. Compared with the photodetector based on the Sb_2Se_3 nanorod film, the current under dark conditions is increased approximately by 20 times (from -2 nA to -40 nA at -20 V) and the photocurrent is increased approximately by 4.5 times (from -100 nA to -450 nA at -20 V, 12.05 $mWcm^{-2}$). A useful figure of merit for the photodetector is the responsivity (R_{res}), which can be calculated from:

$$R_{res} = I_{ph}/I_{irr}A \quad (2.4)$$

where I_{ph} is the background substituted photocurrent ($I_{illumination}$-I_{dark}), I_{irr} is the irradiance of the incident light and A is the effective device area [32]. The R_{res} of the $Sb_2Se_3/AgSbSe_2$

hybrid nanorod film photodetector is about 4.2 times as much as that of the Sb_2Se_3 nanorod film photodetector. As shown earlier in Fig. 2.12, $AgSbSe_2$ nanoparticles grow on the surface of Sb_2Se_3 nanorods, leading to the formation of a $Sb_2Se_3/AgSbSe_2$ heterojunction. The $AgSbSe_2$ nanoparticles with higher electrical conductivity might connect to each other along the rod orientation, thereby improving the electrical conductivity of the $Sb_2Se_3/AgSbSe_2$ hybrid nanorods and eventually increasing the electrical conductivity under dark.

To further confirm the results, hall-effect measurement was carried out to examine the electrical properties of the as-synthesized Sb_2Se_3 nanorods, $AgSbSe_2$ nanoparticles and $Sb_2Se_3/AgSbSe_2$ hybrid nanorods. The typical values are shown in Table 2.1. It can be seen that Sb_2Se_3 exhibits a weak p-type conductivity with the lowest carrier concentration. Compared with Sb_2Se_3 nanorods, the electrical conductivity for the $Sb_2Se_3/AgSbSe_2$ hybrid nanorods have a significant improvement with several orders of magnitude. Previous studies have already revealed that the formation of $ZnO/\alpha\text{-}Fe_2O_3$ semiconductor nano-heterostructures significantly enhances the electrical conductivity [33]. In this work, when the $Sb_2Se_3/AgSbSe_2$ heterojunction was formed, the free electrons from $AgSbSe_2$ nanoparticles can easily migrate to the Sb_2Se_3 nanorods due to the potential difference at the heterojunction interface. Moreover, the formation of the heterojunction results in more effective interfacial charge separation and higher carrier concentration, which can significantly enhance the electrical conductivity of the hybrid nanorods with $Sb_2Se_3/AgSbSe_2$ heterojunction. Thus the photo-generated carriers can be transported efficiently through the conductive channels in the nanorod film. In addition, the light absorption efficiency can be increased in the hybrid nanorods by particle induced light scattering. It is obvious that the improved light absorption efficiency and the higher electrical conductivity will significantly increase the photocurrent of the $Sb_2Se_3/AgSbSe_2$ hybrid nanorods.

Fig. 2.17c and 2.17d give the response/recovery times of 0.6/2.7 s for light intensity of 8.29 $mW.cm^{-2}$ at a bias of -20 V. These performances are stable even after 8 cycles, demonstrating the excellent photoresponse stability of the $Sb_2Se_3/AgSbSe_2$ hybrid nanorod film photodetector. It is obvious that this photodetector has appropriately balanced the conductivity and the photo responsivity. The demonstrated performances make it a promising candidate for applications as high performance photodetectors.

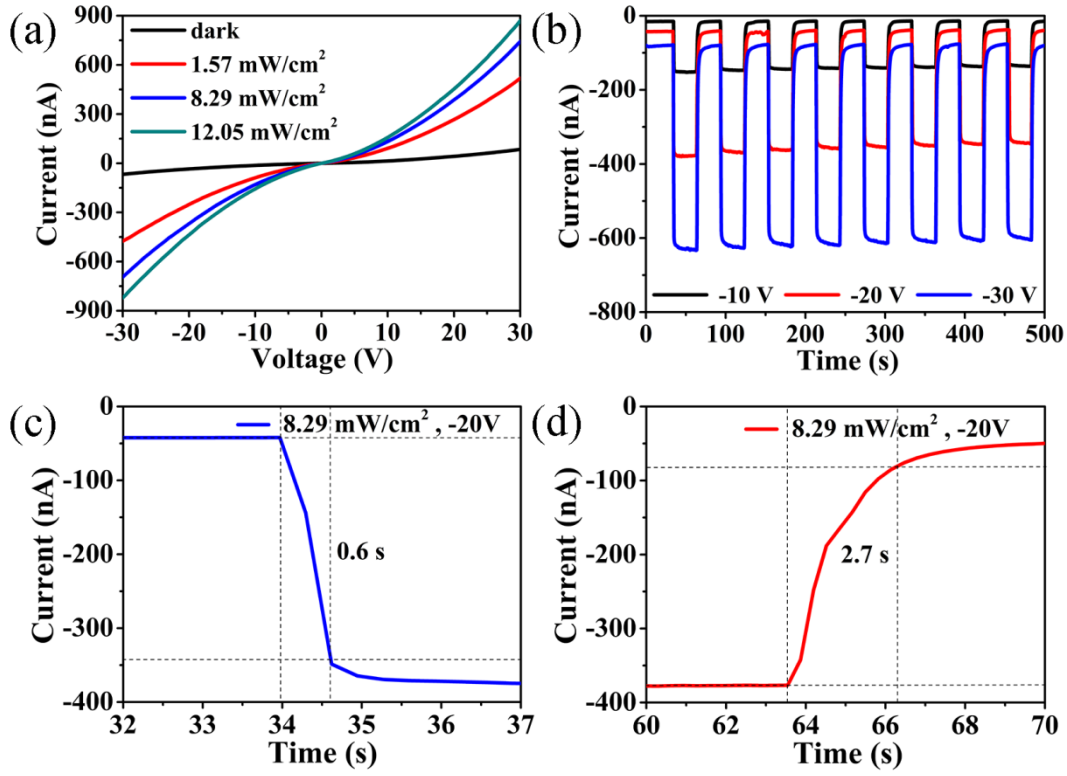

Fig. 2.17 Photoconductive performance of the photodetector based on the Sb_2Se_3/$AgSbSe_2$ hybrid nanorod film. (a) Dark current and photocurrents at different incident power densities; (b) Time-resolved photoresponse at the bias of -10 V, -20 V and -30 V with an incident light density of 8.29 mW cm^{-2}; (c) Response speed and (d) the recovery speed at a bias of -20 V

Table 2.1 Electrical properties of the Sb_2Se_3 nanorods, $AgSbSe_2$ nanoparticles and the hybrid nanorods with the Sb_2Se_3/$AgSbSe_2$ heterojunction structure

Sample	Resistivity (Ω cm)	Hall mobility (cm^2 V^{-1} s^{-1})	Carrier concentration (cm^{-3})	Conduction type
Sb_2Se_3	9.57×10^6	6.89	9.46×10^{10}	p
$AgSbSe_2$	17.71	4.91	7.19×10^{16}	p
Sb_2Se_3/$AgSbSe_2$	1.05×10^3	4.04	1.47×10^{15}	p

In order to simultaneously analyze the photoconductive properties of the as-synthesized $AgSbSe_2$ nanoparticles, which is the second phase of the heterojunction, the $AgSbSe_2$ nanoparticle film photodetector was also fabricated and the device performance was investigated. The I-V curve is shown in Fig. 2.18. It can be seen that both the dark current and photocurrent of the device are very large, which is consistent with the high electrical

conductivity of $AgSbSe_2$ nanoparticles, however, the "ON/OFF" ratio is very small (~1.1, −30 V), which limits its practical application.

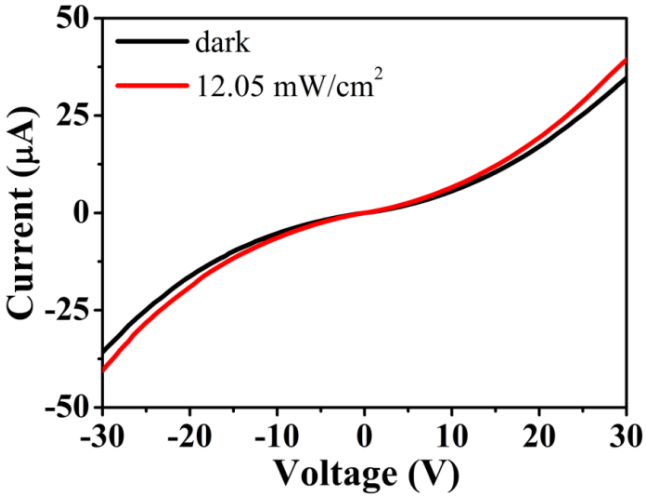

Fig. 2.18 I-V curves of the photodetector based on the $AgSbSe_2$ nanoparticle film

To clearly show the selective spectral response of the photodetectors, photodetection at monochromatic wavelength from UV to IR has been studied. Fig. 2.19a shows the wavelength-dependent responsivity (R_{res}) of the Sb_2Se_3 nanorod film and Sb_2Se_3/$AgSbSe_2$ hybrid nanorod film photodetectors. These two photodetectors show a similar selective response with a broad spectral response from 450 nm to 950 nm with the highest responsivity at 850 nm. The R_{res} value of the Sb_2Se_3/$AgSbSe_2$ hybrid nanorod film photodetector is about 3-4 times that of the Sb_2Se_3 nanorod film photodetector, and the value is comparable to some reported inorganic photodetectors [34]. To further characterize the performance of these photodetectors, it is important to determine the noise characteristics. The noise equivalent power (NEP), which is the incident power at which the signal is equal to the RMS dark noise density (S_I), measured within a specified bandwidth (commonly 1 Hz), that is, $NEP=S_I/R_{res}$ [35]. To obtain S_I, a large sequence of current fluctuations (I_{noise}) was measured with 0.5 s integration time (which corresponds to a bandwidth of 1 Hz), while keeping the photodetectors in darkness. The RMS noise density was then calculated as $S_I=(\langle I^2_{noise}\rangle/1\ Hz)^{1/2}$. The obtained NEP across the working spectrum is shown in Fig. 2.19b. It was found that the NEP can be as low as 4×10^{-10} $W/Hz^{1/2}$ for the Sb_2Se_3 nanorod film photodetector and 5×10^{-11} $W/Hz^{1/2}$ for the Sb_2Se_3/$AgSbSe_2$ hybrid nanorod film photodetector at 850 nm. It is worthwhile to note that these outstanding NEP values are comparable to that of state-of-the-art devices [36].

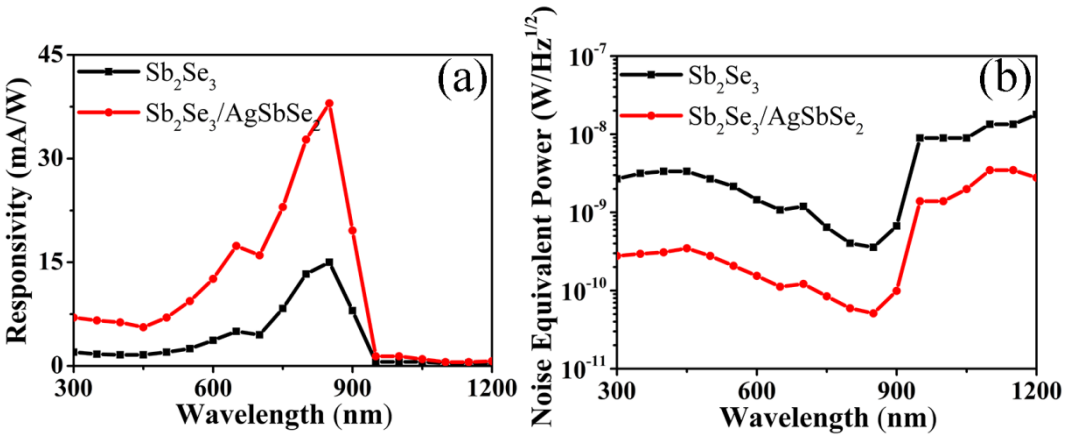

Fig. 2.19 Wavelength-dependent (a) responsivity and (b) noise equivalent power (NEP) of the photodetectors at a bias of -20 V

2.3.5 Preparation and characterization of $(Sn_xSb_{1-x})_2Se_3$ nanorods

In addition to the above-mentioned formation of semiconductor heterojunction to improve the electrical conductivity of Sb_2Se_3 nanorods, another method of semiconductor doping was also adopted, where Sn was chosen as the dopant due to its small difference of atomic radius with Sb. The electrical properties and photoconductive properties of the Sn-doped Sb_2Se_3 nanorods have been investigated.

Fig. 2.20a shows the XRD patterns of the as-synthesized $(Sn_xSb_{1-x})_2Se_3$ (x=0.00, 0.01, 0.03, 0.05 and 0.10) nanorods, which all exhibit prominent peaks in agreement with the JCPDS standard card (No. 15-0861) of the orthorhombic phase of Sb_2Se_3. No diffraction peak corresponding to the detrimental Se or Sb_2O_3 can be detected. From Fig. 2.20b it can be found that the (221) and (301) diffraction peaks shifted gradually toward larger angles with increasing dopant concentration of Sn^{4+}, implying the decreasing lattice constants of the $(Sn_xSb_{1-x})_2Se_3$ nanorods due to gradual substitution of larger Sb^{3+} ions by the smaller Sn^{4+} ions in $(Sn_xSb_{1-x})_2Se_3$ lattice [37]. The experimentally determined lattice parameters a, b and c of the $(Sn_xSb_{1-x})_2Se_3$ nanorods as a function of dopant concentration of Sn^{4+} (x value) further confirm that the dopant ions (Sn^{4+}) are successfully doped into the host lattice (Fig. 2.21). Successful doping can be attributed to the smaller difference (about 9.2%) in the ion radius between Sb^{3+} (0.076 nm) and Sn^{4+} (0.069 nm). This mismatch fulfills the Hume-Rothery criteria (≤15%) for substitution solubility of metals [37].

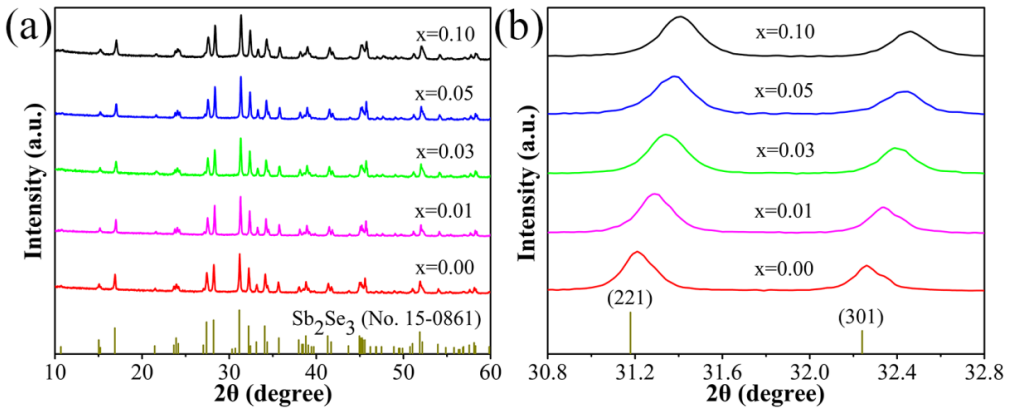

Fig. 2.20 (a) XRD patterns of $(Sn_xSb_{1-x})_2Se_3$ nanorods. (b) (221) and (301) XRD peaks of the same nanorods in panel (a)

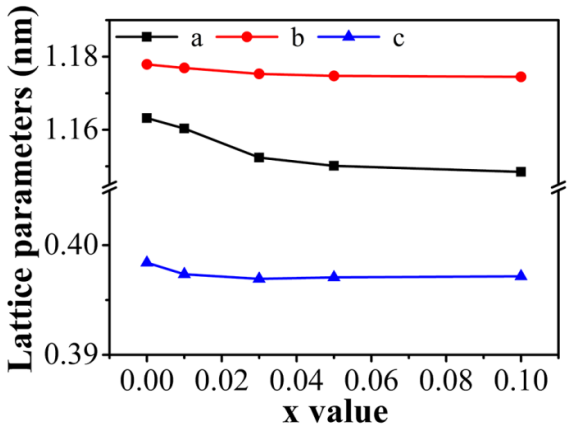

Fig. 2.21 Lattice constants a, b and c, derived from XRD diffraction peaks, plotted as a funtion of Sn doping concentration (x value) for $(Sn_xSb_{1-x})_2Se_3$ nanorods

Fig. 2.22 shows the XPS spectra of Sn-3d for the $(Sn_xSb_{1-x})_2Se_3$ nanorods (x=0.00, 0.05 and 0.10). Two observable peaks located at 494.6 and 486.2 eV indicated the existence of only Sn^{4+} (without Sn^{2+}) ions, which was in accordance with the XRD results.

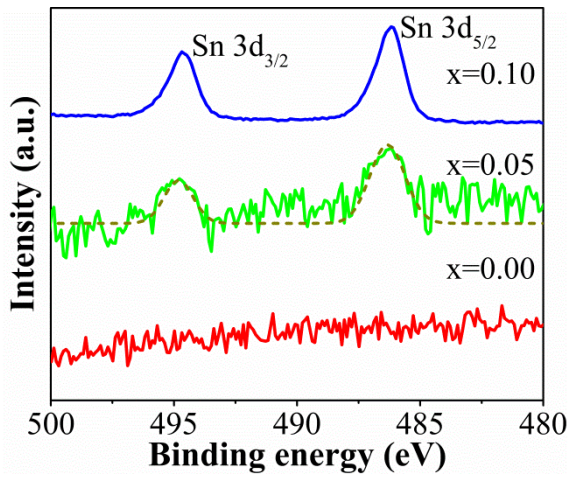

Fig. 2.22 XPS spectrum of Sn-3d for the $(Sn_xSb_{1-x})_2Se_3$ nanorods

The SEM images of the $(Sn_xSb_{1-x})_2Se_3$ nanorods (Fig. 2.23) reveal the formation of high quality nanorods with a diameter of ~100-200 nm and a typical length of several micrometers. By comparing the modification of the nanorods before and after doping, it can be seen that the diameter of the doped nanorods is slightly smaller, which is caused by the change of the Sb precursor concentration required for the nucleation of the nanorods after doping. The absence of a second phase confirms the successful doping.

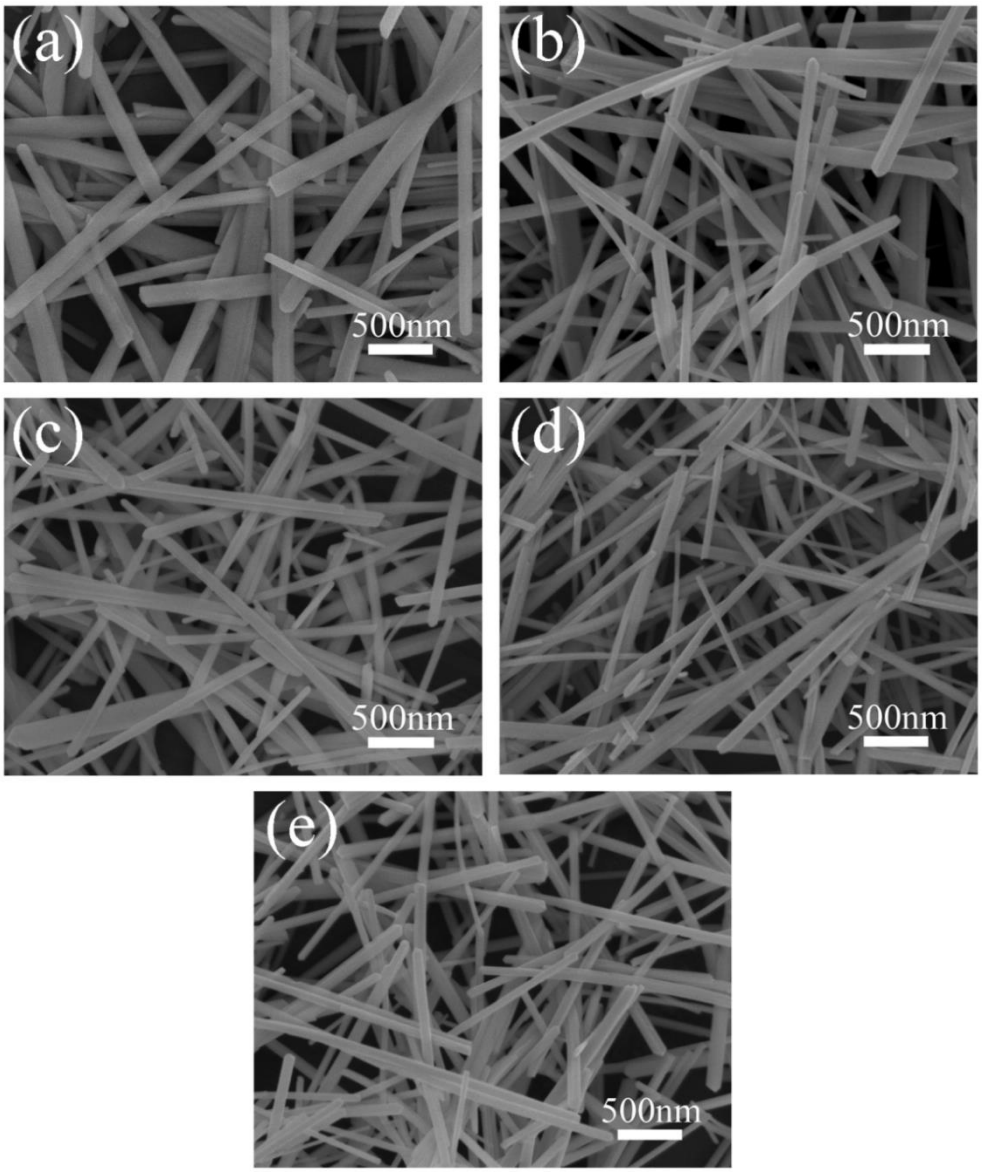

Fig. 2.23 SEM images of $(Sn_xSb_{1-x})_2Se_3$ nanorods: (a) x=0.00; (b) x=0.01; (c) x=0.03; (d) x=0.05 and (e) x=0.10

Fig. 2.24a presents the TEM, STEM and the corresponding EDS mapping images of an individual $(Sn_{0.05}Sb_{0.95})_2Se_3$ nanorod, with well-defined rod geometry and a uniform diameter. HRTEM image and the corresponding Fast Fourier Transform (FFT) pattern (Fig. 2.24b)

confirm the high crystalline nature with orthorhombic phase lattice fringes associated with (001) planes (*d*-spacing of 0.392 nm) along the nanorod, indicating the preferential growth direction of the $(Sn_{0.05}Sb_{0.95})_2Se_3$ nanorod. The preferential c-axis grow of the Sb_2Se_3 is determined intrinsically by the anisotropic Sb-Se atom chain and layer structure [2]. It is obvious that the intrinsic crystal quality of the Sb_2Se_3 nanorods has not been considerably affected when the Sb^{3+} ions were substituted by the Sn^{4+} ions. EDS spectrum (Fig. 2.24c) of an individual $(Sn_{0.05}Sb_{0.95})_2Se_3$ nanorod exhibits strong Sb and Se peaks with lower X-ray energy. An observable Sn-Kα peak located at 25.2 eV indicates the successful doping of Sn^{4+} in the nanorod. The EDS mapping results (inset in Fig. 2.24a) showed that all the elements (Se, Sb, and Sn) have uniform distribution throughout the nanorod.

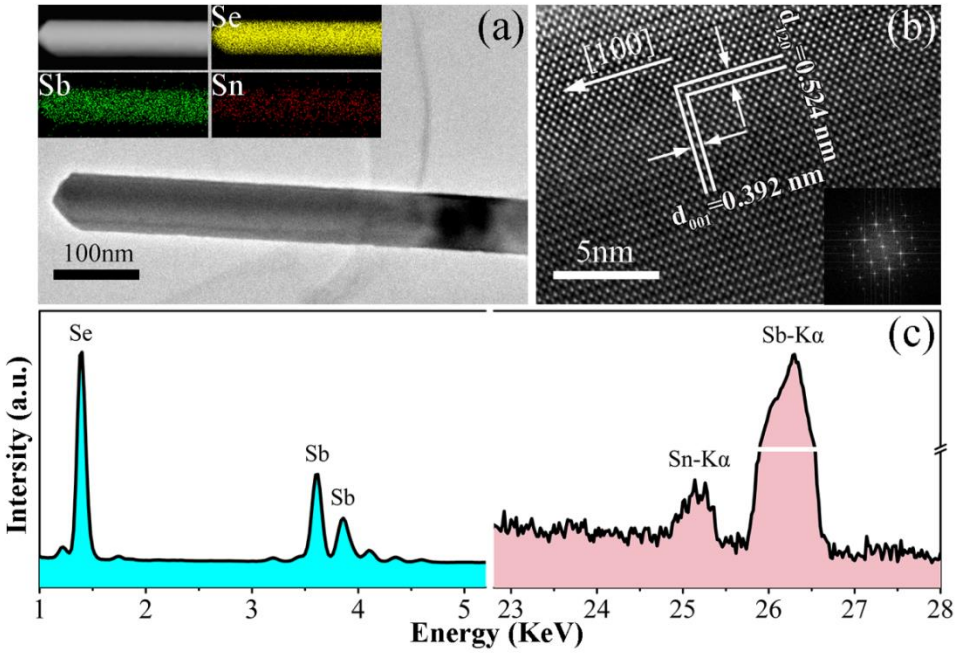

Fig. 2.24 Structural and morphological characterization of the representative $(Sn_{0.05}Sb_{0.95})_2Se_3$ nanorod. (a) TEM image, the inset of (a) shows a STEM image and the corresponding EDS mapping images of Se, Sb and Sn elements, respectively. (b) HRTEM image and a corresponding selected-area FFT pattern (inset). (c) EDS spectrum

The optical properties of the as-synthesized $(Sn_xSb_{1-x})_2Se_3$ nanorods have been investigated through analysing the absorption spectra. The absorption data have been calculated from diffuse reflectance data using the Kubelka-Munk equation described earlier. As shown in Fig. 2.25a, the onset of the absorption of the Sb_2Se_3 nanorods is near 1100 nm, and then shows a gradual shift toward longer wavelength with increasing dopant concentration of Sn^{4+}. Fig. 2.25b shows a plot of $[F(R)hv]^2$ versus energy (hv). The direct band gap of the $(Sn_xSb_{1-x})_2Se_3$

nanorods decreases from 1.24 eV (x=0.00) to 1.20 eV (x=0.10), which can be attributed to the cooperation of the Burstein-Moss shift and the renormalization effect. This mechanism exists in narrow band gap semiconductors with specific doping level, an illustration of this mechanism is shown in Fig. 2.26 [38]. It is worth noting that the tunable band gap of the $(Sn_xSb_{1-x})_2Se_3$ nanorods overlaps well with the solar spectrum, making them attractive candidates for efficient photoelectric devices, including high performance broadband photodetectors.

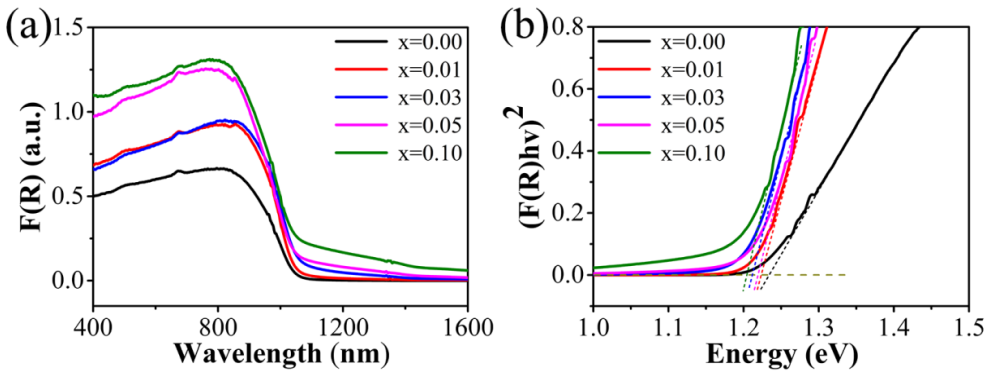

Fig. 2.25 (a) Optical absorption spectra (calculated from diffuse reflectance data) of the $(Sn_xSb_{1-x})_2Se_3$ nanorods. (b) A plot of $[F(R)hv]^2$ vs. energy, from which direct band gap was obtained

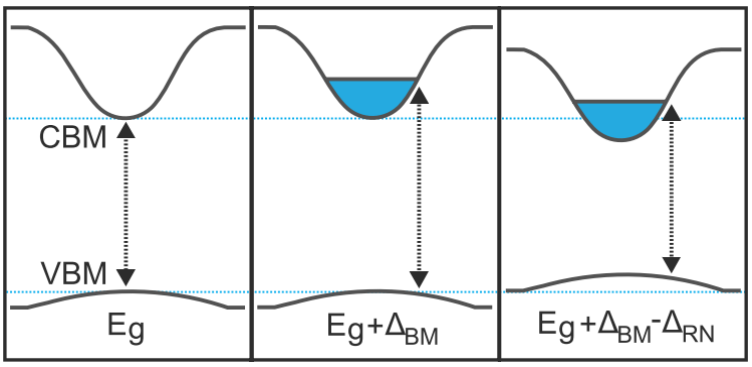

Fig. 2.26 Illustrated effect of charge carriers transition from valence to conduction bands of a doped semiconductor where Δ_{BM} is the Burstein-Moss shift and Δ_{RN} represents band gap renormalization. Note that a positive Δ_{RN} term refers to a band gap reduction

2.3.6 Photoconductive performance of the $(Sn_xSb_{1-x})_2Se_3$ nanorod film Photodetector

Due to a small band gap (approximately 1.2 eV) and a high absorption coefficient ($\sim 10^5$ cm^{-1}), the Sb_2Se_3 has been used to fabricate visible and near-infrared photodetectors. However, low spectral response (R_λ) and low external quantum efficiency (EQE) of the Sb_2Se_3-based photodetector limited its application for high-sensitivity photodetection. In this work, the

photodetection performances of the Sb_2Se_3-based photodetectors have been significantly improved by increasing the electrical conductivity of the Sb_2Se_3 nanorod via Sn^{4+} doping in the Sb_2Se_3 nanorod.

To investigate the influence of the Sn^{4+} ions on the electrical conductivity of the $(Sn_xSb_{1-x})_2Se_3$ nanorods, a method based on Hall-effect measurements was used. Fig. 2.27a shows the resistivity and the carrier concentration of the $(Sn_xSb_{1-x})_2Se_3$ nanorods as a function of doping concentrations of the Sn^{4+} ions (x value). The Sb_2Se_3 nanorods exhibit a weak conductivity with a low carrier concentration. When the Sn^{4+} ions are introduced into the Sb_2Se_3 nanorods, a significant decrease of the resistivity can be observed. The resistivity of the $(Sn_xSb_{1-x})_2Se_3$ nanorods demonstrates a nearly logarithmic relationship with x value, which rapidly decreases from 1.229×10^7 Ω·cm (x=0.00) to 8.746×10^4 Ω·cm (x=0.10). Fig. 27a also shows a significant increase of the carrier concentration from 7.16×10^{11} cm^{-3} (x=0.00) to 3.40×10^{14} cm^{-3} (x=0.10). The relationship between the conductivity and the carrier concentration can be described by the following expression:

$$\sigma = ne\mu \quad (2.5)$$

where σ is the electrical conductivity, n is the charge carrier concentration, e is the electron charge and μ is the mobility [39]. The measured μ values of the $(Sn_xSb_{1-x})_2Se_3$ nanorods are 0.709 (x=0.00), 0.760 (x=0.01), 0.221 (x=0.03), 0.204 (x=0.05), and 0.210 (x=0.10) respectively. Considering the μ values are at the same order of magnitude for the $(Sn_xSb_{1-x})_2Se_3$ nanorods, the main factor accounting for the improvement of electrical conductivity is the increase of carrier concentration when the Sn^{4+} ions are introduced into the Sb_2Se_3 nanorods. A similar mechanism with increasing carrier density has also been described in thermally evaporated Sb_2Se_3:Sn amorphous films [40]. In addition, the conductive type of the as-synthesized $(Sn_xSb_{1-x})_2Se_3$ nanorods is determined by the Hall-effect measurements, and all the samples are p-type. According to the previous studies, Sb_2Se_3 show intrinsic p-type conductivity with major carrier of hole because of its acceptor defect Se_{Sb} (antisite, Se replacing Sb) [41] Herein, it is noted that the valance shell configurations of Sb^{3+} and Sn^{4+} are [Kr] $4d^{10}5s^25p^0$ and [Kr] $4d^{10}5s^05p^0$, respectively. Obviously, Sn^{4+} ion has two less valance electrons compared to Sb^{3+} ion. Therefore, Sn^{4+} ion acts like a hole donor at the doped site and thus enhances the electrical conductivity of the initial p-type Sb_2Se_3 system.

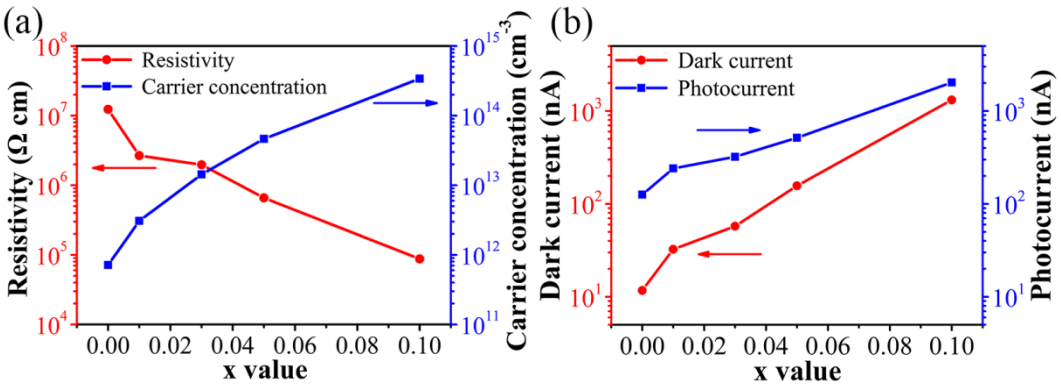

Fig. 2.27 (a) Dependence of resistivity and carrier concentration of the $(Sn_xSb_{1-x})_2Se_3$ nanorods on doping concentrations of Sn^{4+} ions (x value). (b) Dependence of dark currents and photocurrents (under 650 nm light illumination at a bias voltage of 10 V) of the $(Sn_xSb_{1-x})_2Se_3$ nanorod film photodetectors on doping concentrations of Sn^{4+} ions (x value)

To demonstrate the potential application of the $(Sn_xSb_{1-x})_2Se_3$ nanorods with enhanced electrical conductivity, we also fabricated a typical two-electrode photodetector based on $(Sn_xSb_{1-x})_2Se_3$ nanorod film, as shown earlier in Fig. 2.3. Fig. 2.28a-e shows the I-V curves of the $(Sn_xSb_{1-x})_2Se_3$ nanorod film photodetector under dark and illumination at different light intensities using a 650 nm laser as illumination source. When x=0.00, the dark current is very low (about −11 nA at −10 V), implying that the electrical conductivity of the Sb_2Se_3 nanorods in dark condition is very low and similar to the bulk Sb_2Se_3 ($\sigma\sim10^{-6}$-10^{-2} $\Omega^{-1}m^{-1}$). Upon illumination, the photocurrent is significantly increased with increase of the light intensity. The doped nanorods show similar results and x=0.05 sample is taken as an example. Fig. 2.28d presents the I-V curves of the $(Sn_{0.05}Sb_{0.95})_2Se_3$ nanorod film photodetector under the same measuring conditions. Compared with the Sb_2Se_3 nanorod film photodetector, the dark current is increased approximately by 12.7 times (from −11 nA to −140 nA at −10 V) and the photocurrent is increased by approximately 4.8 times (from −137 nA to −655 nA at −10 V, 6.35 mW/cm^2). The R_{res} of the $(Sn_{0.05}Sb_{0.95})_2Se_3$ nanorod film photodetector is calculated to be about 4.1 times higher than that of the undoped Sb_2Se_3 nanorod. This significant improvement could be considered as an important step to promote the Sb_2Se_3-based nanorod film for application as high performance photodetectors. Fig. 2.28f shows the photocurrent of the photodetector based on the $(Sn_xSb_{1-x})_2Se_3$ (x=0.00, 0.01, 0.03 and 0.05) nanorod film as a function of light intensity. The photocurrent is nearly linear to the light power density and the dependence could be described by the power law：

$$I_{ph}=CP^{\theta} \quad (2.6)$$

where I_{ph} represents the photocurrent, P is the power density of the incident light, C is a

constant at a specific wavelength, and θ is an exponent [42]. The fitting curves show that θ =0.52 (x=0.00), 0.50 (x=0.01), 0.49 (x=0.03), and 0.51 (x=0.05) respectively. All these θ values are non-unity, indicating that some surface defects and carrier trapping at the localized states could result in a complex electron-hole non radiative recombination process [2].

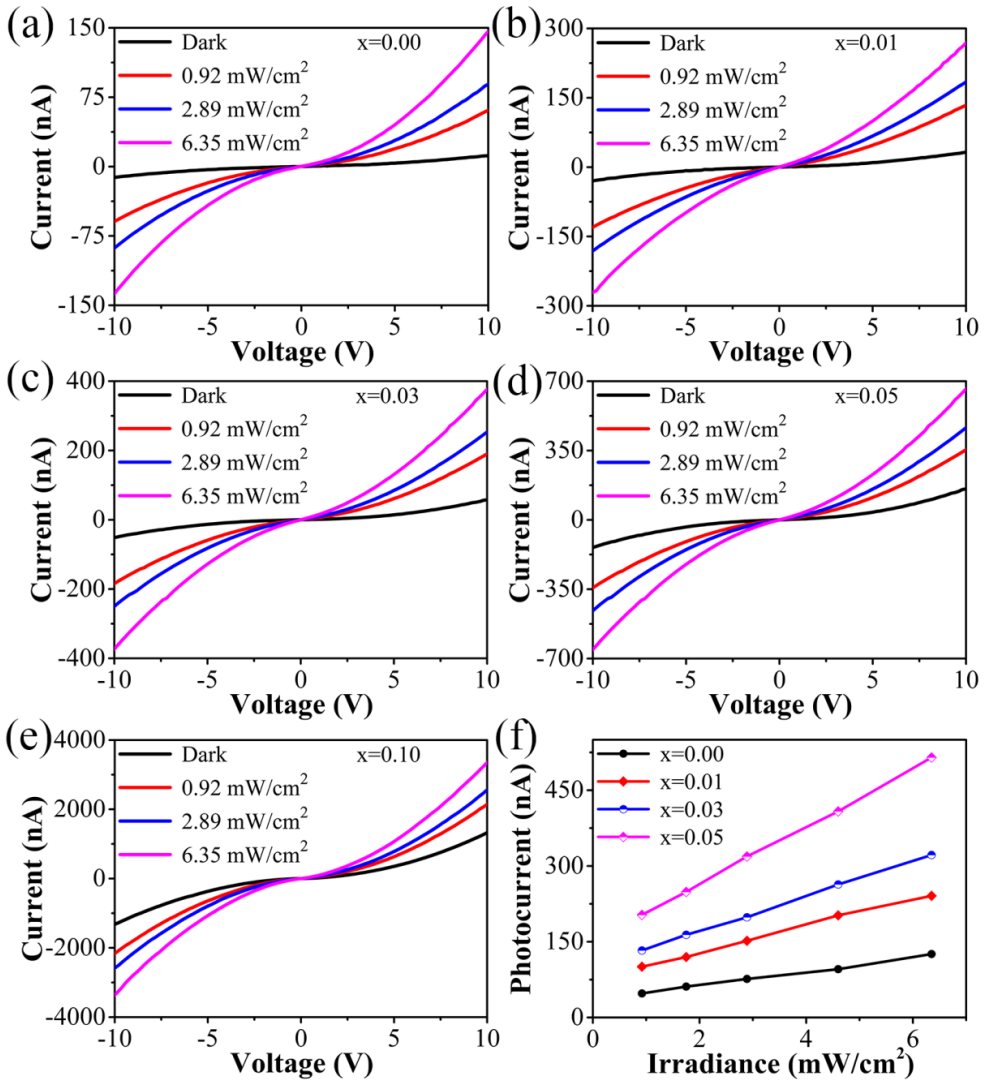

Fig. 2.28 (a-e) Dark currents and photocurrents at different power densities of $(Sn_xSb_{1-x})_2Se_3$ nanorod film photodetector: (a) x=0.00; (b) x=0.01; (c) x=0.03; (d) x=0.05 and (e) x=0.10. (f) Photocurrents measured as a function of incident light density at a bias voltage of 10 V

Fig. 2.27b shows the dark currents and photocurrents (under 650 nm light illumination at a bias voltage of 10 V) of the $(Sn_xSb_{1-x})_2Se_3$ nanorod film photodetectors as a function of doping concentrations of the Sn^{4+} ions (x value). Both dark currents and the photocurrents of the $(Sn_xSb_{1-x})_2Se_3$ nanorod film photodetectors demonstrate a nearly logarithmic relationship with x value, which implies significant influence of the doped Sn^{4+} ions on the electrical conductivity and photoresponsivity. When the Sn^{4+} ions are introduced into Sb_2Se_3 nanorod,

the Sb^{3+} ions were substituted by the Sn^{4+} ions, which might result in elevated dark current and photocurrent due to the lattice intrinsic defects.

The time response is also a key factor for photodetector performance, which demonstrates the capability of a device to follow a fast-varying optical signal. Fig. 2.29a and 2.29b show the time-resolved photoresponse of the photodetectors based on the Sb_2Se_3 nonorod film and the $(Sn_{0.05}Sb_{0.95})_2Se_3$ nanorod film, respectively. These two photodetectors are under illumination of 650 nm laser with controllable incident light density of 0.92, 2.89 and 6.35 mW/cm^2. When the applied voltage is 10 V and the light is turned ON, as shown in Fig. 2.29a, the current of the Sb_2Se_3 nanorod film photodetector dramatically increases from 10 nA (dark condition) to 136 nA (with 6.35 mW/cm^2 light illumination), and then sharply is returned to its initial value as the light is turned OFF. This light response remains the same after multiple cycles, demonstrating the excellent stability and reproducibility of the photodetector. For the $(Sn_{0.05}Sb_{0.95})_2Se_3$ nanorod film photodetector, the same phenomena can be observed with a larger photocurrent (Fig. 2.29b). Fig. 2.29c and 2.29d show the magnified plot of one response cycle. In the time domain, the response time (τ_{res}) and the recovery time (τ_{rec}) are described earlier, for the Sb_2Se_3 nonorod film photodetector are 0.34 s and 0.36 s respectively. For $(Sn_{0.05}Sb_{0.95})_2Se_3$ nanorod film photodetector, the τ_{res} decreased to 0.04 s and the τ_{rec} increased to 0.85 s respectively. This could be explained by the doping creating interfacial states, deep states and dangling bonds in the nanostructures [43]. These states can trap one particular type of charge carrier and thus decreases the overall electron-hole recombination. As a result, large photocarrier lifetime and external quantum efficiency (EQE) can be expected in doped nanostructures. Specifically, the major trapping mechanism for Sb_2Se_3 nanorods is based on the existence of chemisorbed oxygen molecules. Then for the $(Sn_{0.05}Sb_{0.95})_2Se_3$ nanorods, since Sn^{4+} exist in the lattice, which might act as additional trapping sites for the photo-generated electrons through charge transfer reaction $Sn^{4+} \rightarrow Sn^{2+}$ [40], leaving the unpaired holes to increase the conductivity. This could be the reason for the observed larger photocurrent and lower response time (τ_{res}) in $(Sn_{0.05}Sb_{0.95})_2Se_3$ in comparison with Sb_2Se_3. However, defect sites introduced in the doping process can also increase the recovery time (τ_{rec}) as trapped charge carriers are not immediately available for the recombination when the light is switched OFF. Such response has been observed previously in similar systems [44]. Furthermore, it was worth noting that the fast response time obtained here is comparable to the very good results previously reported [45].

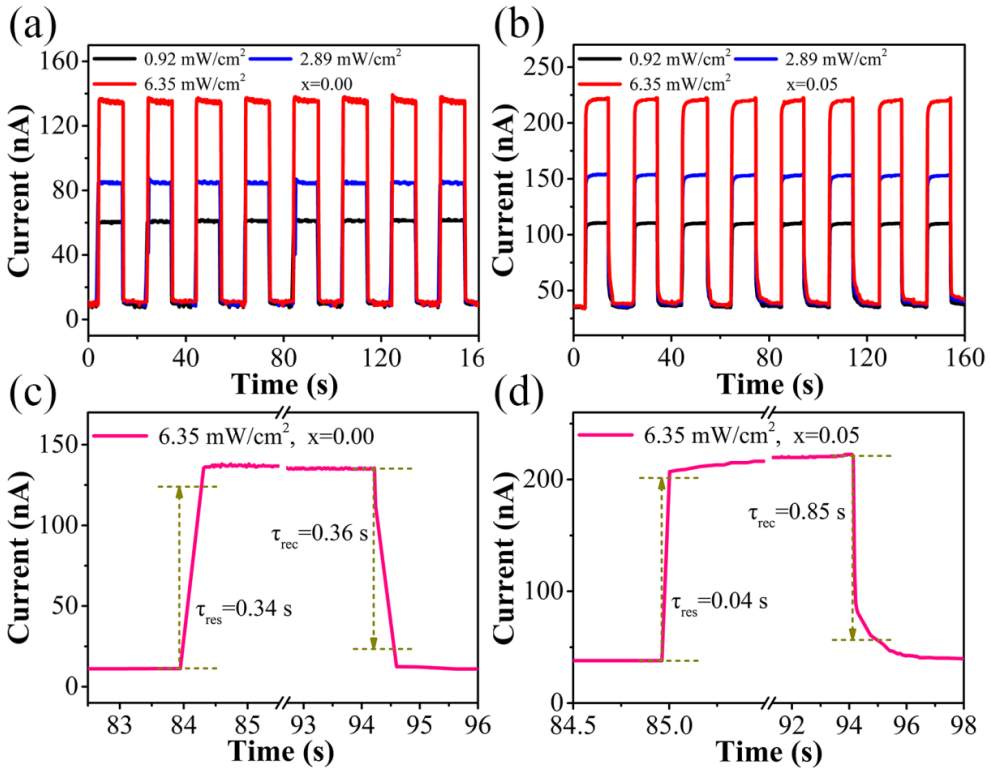

Fig. 2.29 (a) Time-resolved photoresponse of the Sb_2Se_3 nanorod film photodetector at a bias of 10 V and an incident light density of 0.92, 2.89 and 6.35 mW/cm^2. (b) Time-resolved photoresponse of the $(Sn_{0.05}Sb_{0.95})_2Se_3$ nanorod film photodetector at a bias of 5 V and an incident light density of 0.92, 2.89 and 6.35 mW/cm^2. (c) Magnified plot of one response cycle in (a), and (d) one response cycle in (b), used to obtain the response and the recovery time

Broad spectral detection is beneficial for extending the application of photodetectors. According to the optical absorption spectra and the band gap of the $(Sn_xSb_{1-x})_2Se_3$ nanorods, the photodetection at monochromatic wavelength crossing over the UV-visible-NIR range has been studied for the nanorod film photodetector.

Fig. 2.30a shows the wavelength-dependent responsivity (R_{res}) of the photodetectors based on the Sb_2Se_3 nanorod film and the $(Sn_{0.05}Sb_{0.95})_2Se_3$ nanorod film. Both two photodetectors present a similar selective spectral response from 300 nm to 1100 nm with the highest responsivity at 850 nm. It was worth noting that the broad spectral response made the photodetectors useful for multispectral applications. More importantly, the R_{res} of the $(Sn_{0.05}Sb_{0.95})_2Se_3$ nanorod film photodetector can be 3-4 times of the Sb_2Se_3 nanorod film photodetector and this detectivity is comparable to some excellent results reported for inorganic photodetectors [46]. Fig. 2.30b shows the noise equivalent power NEP across the working spectrum in this study. It was found that the NEP is 4.18×10^{-12} W/Hz$^{1/2}$ for the Sb_2Se_3 nanorod film photodetector and 3.14×10^{-13} W/Hz$^{1/2}$ for the $(Sn_{0.05}Sb_{0.95})_2Se_3$ nanorod

film photodetector at 850 nm. The low value for $(Sn_{0.05}Sb_{0.95})_2Se_3$ nanorod film indicates that very weak incidence light (~picowatt) above the noise level can be detected. These NEP values are comparable to state-of-the-art devices [47]. Fig. 2.30c and 2.30d present the external quantum efficiency (EQE) and the spectral detectivity (D*) of the Sb_2Se_3 nanorod film photodetector and the $(Sn_{0.05}Sb_{0.95})_2Se_3$ nanorod film photodetector, which could be calculated using equations: $EQE=hcR_{res}/e\lambda$ and $D^*=R_{res}/(2eJ_d)^{1/2}$, where h is Planck's constant, c is the velocity of light, R_{res} is the responsivity, e is the electron charge, λ is the wavelength, and J_d is the dark current [32,42]. The corresponding highest values of EQE (906%) and D* (5.03×10^{11} Jones) confirm the excellent detection performance of the $(Sn_{0.05}Sb_{0.95})_2Se_3$ nanorod film photodetector.

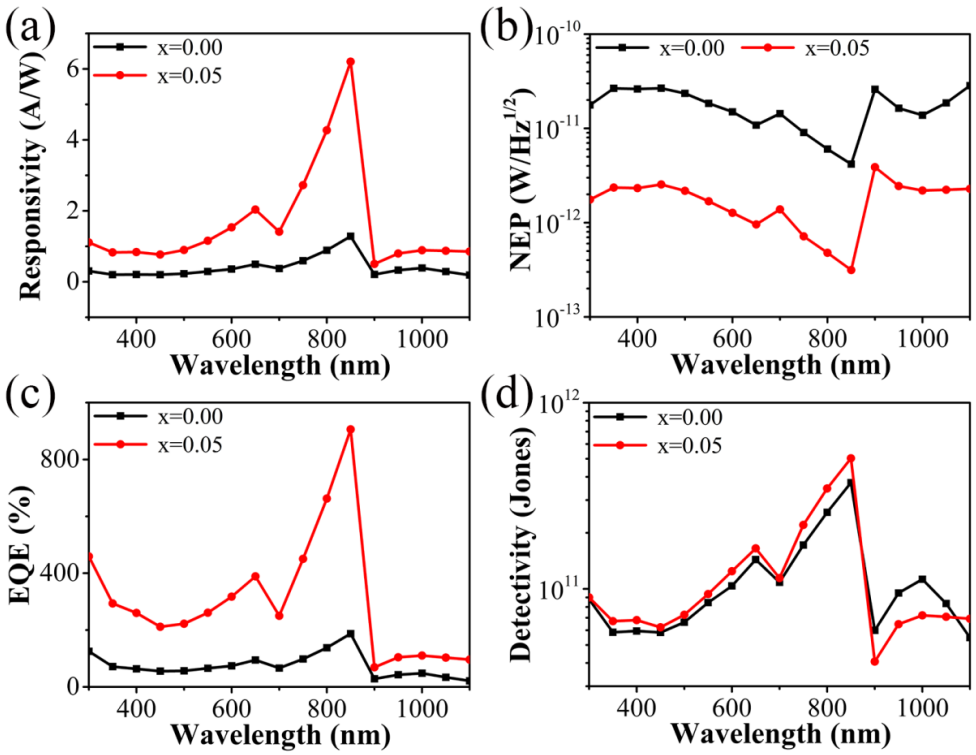

Fig. 2.30 Wavelength-dependent (a) responsivity; (b) noise equivalent power (NEP); (c) external quantum efficiency (EQE) and (d) detectivity (D*) of the Sb_2Se_3 nanorod film photodetector and the $(Sn_{0.05}Sb_{0.95})_2Se_3$ nanorod film photodetector (at a bias of 20 V)

2.4 Conclusions

In this chapter, uniform single-crystalline Sb_2Se_3 nanorods have been successfully synthesized by a hot-injection method. The reaction temperature, reaction time and the used surfactants show important impact on the morphology and structure of the nanorods.

The intrinsic resistivity of Sb_2Se_3 is as high as 10^6 Ω·m, which greatly limits its applications. To overcome this challenge, two effective approaches have been developed. One is the formation of composites with a conductive second phase and the hybrid nanorods with $Sb_2Se_3/AgSbSe_2$ heterojunction structure have been prepared successfully. Those interconnected heterojunction structures can significantly improve the electrical conductivity of the Sb_2Se_3 nanorods. The other approach is doping, where Sn was chosen as a dopant. With increasing Sn^{4+} doping concentration, $(Sn_xSb_{1-x})_2Se_3$ nanorods exhibit a great improvement of electrical conductivity with several orders of magnitude due to a much higher carrier concentration.

Finally, the as-synthesized Sb_2Se_3 nanorods, hybrid nanorods with the $Sb_2Se_3/AgSbSe_2$ heterojunction structure and $(Sn_xSb_{1-x})_2Se_3$ nanorods have been directly used for fabricating prototype photodetectors. The results show that the $Sb_2Se_3/AgSbSe_2$ heterojunction nanorod film photodetector has a remarkable response to visible light, about 4.2 times higher than that of undoped Sb_2Se_3 nanorod film photodetector. The $(Sn_xSb_{1-x})_2Se_3$ nanorod film photodetector also exhibits high responsivity and detectivity over a wide spectral range from ultraviolet to near-infrared. The highest responsivity is 6.21 A/W and the external quantum efficiency can reach 906% with appropriate Sn doping, which is much higher than that of the undoped Sb_2Se_3 nonorod film photodetector. In summary, the Sb_2Se_3 based nanorods with enhanced electrical conductivity show great application potential as highly efficient photodetectors.

2.5 References

[1] Choi, D.; Jang, Y.; Lee, J.; Jeong, G. H.; Whang, D.; Hwang, S. W.; Cho, K. S.; Kim, S. W., Diameter-Controlled and Surface-Modified Sb_2Se_3 Nanowires and Their Photodetector Performance. Scientific Reports 2014, 4, 6714.

[2] Liu, Y. Q.; Zhang, M.; Wang, F. X.; Pan, G. B., Facile microwave-assisted synthesis of uniform Sb_2Se_3 nanowires for high performance photodetectors. Journal of Materials Chemistry C 2014, 2 (2), 240-244.

[3] Zeng, K.; Xue, D. J.; Tang, J., Antimony selenide thin-film solar cells. Semiconductor Science and Technology 2016, 31 (6).

[4] Wu, H.-j.; Lee, P.-c.; Chiu, F.-y.; Chen, S.-w.; Chen, Y.-y., Self-assisted nucleation and growth of [010]-oriented Sb_2Se_3 whiskers: the crystal structure and thermoelectric properties. Journal of Materials Chemistry C 2015, 3 (40), 10488-10493.

[5] Zhang, L.; Li, Y.; Li, C.; Chen, Q.; Zhen, Z.; Jiang, X.; Zhong, M.; Zhang, F.; Zhu, H.,

Scalable Low-Band-Gap Sb_2Se_3 Thin-Film Photocathodes for Efficient Visible-Near-Infrared Solar Hydrogen Evolution. Acs Nano 2017.

[6] Jin, R.; Chen, G.; Wang, Q.; Sun, J.; Wang, Y., A facile solvothermal synthesis of hierarchical Sb_2Se_3 nanostructures with high electrochemical hydrogen storage ability. Journal of Materials Chemistry 2011, 21 (18), 6628.

[7] Zhou, Y.; Wang, L.; Chen, S.; Qin, S.; Liu, X.; Chen, J.; Xue, D.-J.; Luo, M.; Cao, Y.; Cheng, Y.; Sargent, E. H.; Tang, J., Thin-film Sb_2Se_3 photovoltaics with oriented one-dimensional ribbons and benign grain boundaries. Nature Photonics 2015, 9 (6), 409-415.

[8] Kwon, Y. H.; Kim, Y. B.; Jeong, M.; Do, H. W.; Cho, H. K.; Lee, J. Y., Crystal growth direction-controlled antimony selenide thin film absorbers produced using an electrochemical approach and intermediate thermal treatment. Solar Energy Materials and Solar Cells 2017, 172, 11-17.

[9] Zhou, Y.; Leng, M. Y.; Xia, Z.; Zhong, J.; Song, H. B.; Liu, X. S.; Yang, B.; Zhang, J. P.; Chen, J.; Zhou, K. H.; Han, J. B.; Cheng, Y. B.; Tang, J., Solution-Processed Antimony Selenide Heterojunction Solar Cells. Advanced Energy Materials 2014, 4 (8).

[10] Xia, Z.; Zhong, J.; Leng, M.; Hu, L.; Xue, D.-J.; Yang, B.; Zhou, Y.; Liu, X.; Qin, S.; Cheng, Y.-B.; Tang, J., Generalized Water-Processed Metal Chalcogenide Complexes: Synthesis and Applications. Chemistry of Materials 2015, 27 (23), 8048-8057.

[11] Luo, M.; Leng, M. Y.; Liu, X. S.; Chen, J.; Chen, C.; Qin, S. K.; Tang, J., Thermal evaporation and characterization of superstrate CdS/Sb_2Se_3 solar cells. Applied Physics Letters 2014, 104 (17).

[12] Li, Z. Q.; Zhu, H. B.; Guo, Y. T.; Niu, X. N.; Chen, X.; Zhang, C.; Zhang, W.; Liang, X. Y.; Zhou, D.; Chen, J. W.; Mai, Y. H., Efficiency enhancement of Sb_2Se_3 thin-film solar cells by the co-evaporation of Se and Sb2Se3. Applied Physics Express 2016, 9 (5).

[13] Leng, M. Y.; Luo, M.; Chen, C.; Qin, S. K.; Chen, J.; Zhong, J.; Tang, J., Selenization of Sb_2Se_3 absorber layer: An efficient step to improve device performance of CdS/Sb_2Se_3 solar cells. Applied Physics Letters 2014, 105 (8).

[14] Yang, R. B.; Bachmann, J.; Pippel, E.; Berger, A.; Woltersdorf, J.; Gösele, U.; Nielsch, K., Pulsed Vapor-Liquid-Solid Growth of Antimony Selenide and Antimony Sulfide Nanowires. Advanced Materials 2009, 21 (31), 3170-3174.

[15] Ma, J. M.; Wang, Y. P.; Wang, Y. J.; Chen, Q.; Lian, J. B.; Zheng, W. J., Controlled Synthesis of One-Dimensional Sb_2Se_3 Nanostructures and Their Electrochemical Properties. Journal of Physical Chemistry C 2009, 113 (31), 13588-13592.

[16] Mehta, R. J.; Karthik, C.; Jiang, W.; Singh, B.; Shi, Y.; Siegel, R. W.; Borca-Tasciuc, T.;

Ramanath, G., High electrical conductivity antimony selenide nanocrystals and assemblies. Nano Letters 2010, 10 (11), 4417-4422.

[17] Zhang, X. H.; Xu, Y.; Shen, Q. H.; Fan, B.; Qiao, X. S.; Fan, X. P.; Yang, H.; Luo, Q.; Calvez, L.; Ma, H. L.; Cathelinaud, M.; Simond, J. J., Enhancement of charge photo-generation and transport via an internal network of Sb_2Se_3/Cu_2GeSe_3 heterojunctions. Journal of Materials Chemistry A 2014, 2 (40), 17099-17106.

[18] Tian, W.; Zhi, C. Y.; Zhai, T. Y.; Chen, S. M.; Wang, X.; Liao, M. Y.; Golberg, D.; Bando, Y., In-doped Ga_2O_3 nanobelt based photodetector with high sensitivity and wide-range photoresponse. Journal of Materials Chemistry 2012, 22 (34), 17984-17991.

[19] Zhai, T.; Ma, Y.; Li, L.; Fang, X.; Liao, M.; Koide, Y.; Yao, J.; Bando, Y.; Golberg, D., Morphology-tunable In_2Se_3 nanostructures with enhanced electrical and photoelectrical performances via sulfur doping. Journal of Materials Chemistry 2010, 20 (32), 6630.

[20] Schladt, T. D.; Schneider, K.; Schild, H.; Tremel, W., Synthesis and bio-functionalization of magnetic nanoparticles for medical diagnosis and treatment. Dalton Trans 2011, 40 (24), 6315-6343.

[21] Vaughn, D. D.; Patel, R. J.; Hickner, M. A.; Schaak, R. E., Single-Crystal Colloidal Nanosheets of GeS and GeSe. Journal of the American Chemical Society 2010, 132 (43), 15170-15172.

[22] Murray, C. B.; Norris, D. J.; Bawendi, M. G., SYNTHESIS AND CHARACTERIZATION OF NEARLY MONODISPERSE CDE (E = S, SE, TE) SEMICONDUCTOR NANOCRYSTALLITES. Journal of the American Chemical Society 1993, 115 (19), 8706-8715.

[23] Boatman, E. M.; Lisensky, G. C.; Nordell, K. J., A safer, easier, faster synthesis for CdSe quantum dot nanocrystals. Journal of Chemical Education 2005, 82 (11), 1697-1699.

[24] O'Brien, G. A.; Quinn, A. J.; Tanner, D. A.; Redmond, G., A Single Polymer Nanowire Photodetector. Advanced Materials 2006, 18 (18), 2379-2383.

[25] Zhai, T. Y.; Fang, X. S.; Liao, M. Y.; Xu, X. J.; Li, L.; Liu, B. D.; Koide, Y.; Ma, Y.; Yao, J. N.; Bando, Y.; Golberg, D., Fabrication of High-Quality In_2Se_3 Nanowire Arrays toward High-Performance Visible-Light Photodetectors. Acs Nano 2010, 4 (3), 1596-1602.

[26] Calarco, R.; Marso, M.; Richter, T.; Aykanat, A. I.; Meijers, R.; Hart, A. V.; Stoica, T.; Luth, H., Size-dependent photoconductivity in MBE-grown GaN-nanowires. Nano Lett 2005, 5 (5), 981-984.

[27] Wojciechowski, K.; Tobola, J.; Schmidt, M.; Zybala, R., Crystal structure, electronic and transport properties of $AgSbSe_2$ and $AgSbTe_2$. Journal of Physics and Chemistry of Solids

2008, 69 (11), 2748-2755.

[28] Guin, S. N.; Negi, D. S.; Datta, R.; Biswas, K., Nanostructuring, carrier engineering and bond anharmonicity synergistically boost the thermoelectric performance of p-type $AgSbSe_2$–ZnSe. Journal of Materials Chemistry A 2014, 2 (12), 4324.

[29] Liang, G. X.; Zheng, Z. H.; Fan, P.; Luo, J. T.; Hu, J. G.; Zhang, X. H.; Ma, H. L.; Fan, B.; Luo, Z. K.; Zhang, D. P., Thermally induced structural evolution and performance of Sb_2Se_3 films and nanorods prepared by an easy sputtering method. Solar Energy Materials and Solar Cells 2018, 174, 263-270.

[30] Deng, Z. T.; Mansuripur, M.; Muscat, A. J., Simple Colloidal Synthesis of Single-Crystal Sb-Se-S Nanotubes with Composition Dependent Band-Gap Energy in the Near-Infrared. Nano Letters 2009, 9 (5), 2015-2020.

[31] Deng, R.; Yao, B.; Li, Y. F.; Zhao, Y. M.; Li, B. H.; Shan, C. X.; Zhang, Z. Z.; Zhao, D. X.; Zhang, J. Y.; Shen, D. Z.; Fan, X. W., X-ray photoelectron spectroscopy measurement of n-ZnO/p-NiO heterostructure valence-band offset. Applied Physics Letters 2009, 94 (2), 022108.

[32] Jacobs-Gedrim, R. B.; Shanmugam, M.; Jain, N.; Durcan, C. A.; Murphy, M. T.; Murray, T. M.; Matyi, R. J.; Moore, R. L.; Yu, B., Extraordinary Photoresponse in Two-Dimensional In_2Se_3 Nanosheets. Acs Nano 2014, 8 (1), 514-521.

[33] Sarkar, D.; Khan, G. G.; Singh, A. K.; Mandal, K., Enhanced Electrical, Optical, and Magnetic Properties in Multifunctional ZnO/α-Fe_2O_3 Semiconductor Nanoheterostructures by Heterojunction Engineering. The Journal of Physical Chemistry C 2012, 116 (44), 23540-23546.

[34] Xie, Y.; Gong, M. G.; Shastry, T. A.; Lohrman, J.; Hersam, M. C.; Ren, S. Q., Broad-Spectral-Response Nanocarbon Bulk-Heterojunction Excitonic Photodetectors. Advanced Materials 2013, 25 (25), 3433-3437.

[35] An, X.; Liu, F.; Jung, Y. J.; Kar, S., Tunable graphene-silicon heterojunctions for ultrasensitive photodetection. Nano Letters 2013, 13 (3), 909-916.

[36] Wei, H.; Fang, Y.; Yuan, Y.; Shen, L.; Huang, J., Trap Engineering of CdTe Nanoparticle for High Gain, Fast Response, and Low Noise P_3HT:CdTe Nanocomposite Photodetectors. Advanced Materials 2015, 27 (34), 4975-4981.

[37] Hu, C. H.; Chiang, M. H.; Hsieh, M. S.; Lin, W. T.; Fu, Y. S.; Guo, T. F., Phase formation, morphology evolution and tunable bandgap of $Sn_{1-x}Sb_xSe$ nanocrystals. CrystEngComm 2014, 16 (9), 1786.

[38] Walsh, A.; Da Silva, J. L. F.; Wei, S.-H., Origins of band-gap renormalization in

degenerately doped semiconductors. Physical Review B 2008, 78 (7).

[39] Ahn, K.; Cho, E.; Rhyee, J. S.; Kim, S. I.; Hwang, S.; Kim, H. S.; Lee, S. M.; Lee, K. H., Improvement in the thermoelectric performance of the crystals of halogen-substituted $In_4Se_{3-x}H_{0.03}$ (H = F, Cl, Br, I): Effect of halogen-substitution on the thermoelectric properties in In_4Se_{3-x}. Journal of Materials Chemistry 2012, 22 (12), 5730.

[40] Kumar, P.; Thangaraj, R., Effect of Sn addition on the photoconductivity of narrow-gap Sb_2Se_3 films. Philosophical Magazine Letters 2009, 89 (4), 241-249.

[41] Liu, X.; Xiao, X.; Yang, Y.; Xue, D. J.; Li, D. B.; Chen, C.; Lu, S.; Gao, L.; He, Y.; Beard, M. C.; Wang, G.; Chen, S.; Tang, J., Enhanced Sb_2Se_3 solar cell performance through theory-guided defect control. Progress in Photovoltaics: Research and Applications 2017.

[42] Zhang, H.; Zhang, X.; Liu, C.; Lee, S. T.; Jie, J., High-Responsivity, High-Detectivity, Ultrafast Topological Insulator Bi_2Se_3/Silicon Heterostructure Broadband Photodetectors. Acs Nano 2016, 10 (5), 5113-5122.

[43] Zhou, W. C.; Peng, Y. H.; Yin, Y. L.; Zhou, Y.; Zhang, Y.; Tang, D. S., Broad spectral response photodetector based on individual tin-doped CdS nanowire. Aip Advances 2014, 4 (12).

[44] Wu, C.; Jie, J.; Wang, L.; Yu, Y.; Peng, Q.; Zhang, X.; Cai, J.; Guo, H.; Wu, D.; Jiang, Y., Chlorine-doped n-type CdS nanowires with enhanced photoconductivity. Nanotechnology 2010, 21 (50), 505203.

[45] Tamalampudi, S. R.; Lu, Y. Y.; Kumar, U. R.; Sankar, R.; Liao, C. D.; Moorthy, B. K.; Cheng, C. H.; Chou, F. C.; Chen, Y. T., High performance and bendable few-layered InSe photodetectors with broad spectral response. Nano Letters 2014, 14 (5), 2800-2806.

[46] Chen, G. H.; Yu, Y. Q.; Zheng, K.; Ding, T.; Wang, W. L.; Jiang, Y.; Yang, Q., Fabrication of Ultrathin Bi_2S_3 Nanosheets for High-Performance, Flexible, Visible-NIR Photodetectors. Small 2015, 11 (24), 2848-2855.

[47] Du, S.; Lu, W.; Ali, A.; Zhao, P.; Shehzad, K.; Guo, H.; Ma, L.; Liu, X.; Pi, X.; Wang, P.; Fang, H.; Xu, Z.; Gao, C.; Dan, Y.; Tan, P.; Wang, H.; Lin, C.; Yang, J.; Dong, S.; Cheng, Z.; Li, E.; Yin, W.; Luo, J.; Yu, B.; Hasan, T.; Xu, Y.; Hu, W.; Duan, X., A Broadband Fluorographene Photodetector. Adv. Mater. 2017, 29, 1700463.

CHAPTER III: SYNTHESIS AND PROPERTIES OF SN-DOPED BULK SB2SE3 CRYSTALS

3.1 Introduction

In the previous Chapter II, it has been demonstrated that Sb_2Se_3 based materials have excellent photoelectric properties and are among good candidate materials for fabricating solar cells. Previous research on Sb_2Se_3 in this thesis was mainly focused on the preparation of 1D Sb_2Se_3 nanorods by liquid phase method. Heterojunction nanorods and doped nanorods with enhanced conductivity have been obtained with promising application potential as photodetectors. However, these 1D nanorods cannot be directly applied to the preparation of solar cells, where dense thin films are necessary. Therefore, the research on Sb_2Se_3 bulk crystals is of great significance for understanding the inherent physical and chemical properties of the bulk materials and also for providing raw materials for photoelectric device fabrication.

In the last chapter, Sn-doped Sb_2Se_3 nanorods, ie $(Sn_xSb_{1-x})_2Se_3$ (x=0.00, 0.01, 0.03, 0.05 and 0.10) were synthesized by using hot-injection method. The results showed that Sn doping can significantly increase the electrical conductivity of Sb_2Se_3 nanorods, and the corresponding nanorod film photodetector showed higher device performance. Therefore, based on this concept, in this chapter, we will use a conventional high-temperature melting method to controllably synthesize high-quality and doped $(Sn_xSb_{1-x})_2Se_3$ semiconducting crystals with Sn ratio x ranging from 0.00 to 0.10.

3.2 Experimental section

3.2.1 Synthesis of $(Sn_xSb_{1-x})_2Se_3$ crystals

A conventional high-temperature melting method using high purity tin (99.99%), antimony (99.999%) and selenium (99.999%) as raw materials was used to synthesize $(Sn_xSb_{1-x})_2Se_3$ crystals. A schematic illustration of the preparation process is shown in Fig. 3.1. At first, a mixture of 12 g raw materials according to the chemical composition $(Sn_xSb_{1-x})_2Se_3$ (where x=0.00, 0.03, 0.05, 0.07 and 0.10 respectively) was loaded into a fully cleaned silica tube of 1 cm internal diameter. A vacuum trap that placed in liquid nitrogen was used to condense any volatile products and also to improve the vacuum. The silica tube was sealed under a typical vacuum of around 10^{-5} mbar and then was put into a rocking furnace. The mixture was heated to 700 ℃ at a rate of 1.5 ℃/min and held for about 8 hours to ensure complete melting and homogenization. Then it was cooled down to 650 ℃ during 2 hours and quenched in water at

room temperature. Finally, in order to reduce the stress generated from the thermal shock in the quenching process, the as-synthesized crystals were annealed at 350 ℃ for 3 hours.

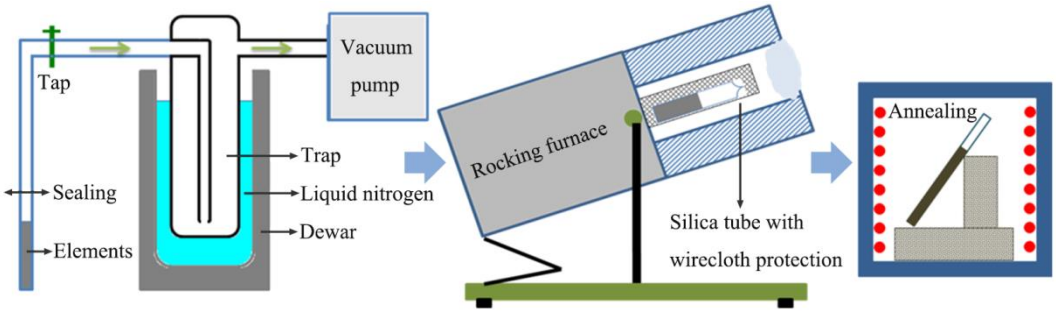

Fig. 3.1 Schematic illustration of the $(Sn_xSb_{1-x})_2Se_3$ crystals preparation process

3.2.2 Characterization

X-ray diffraction (XRD) analysis was carried out on a PANalytical's X-ray diffractometer with a step width of 0.02 ° and a counting duration of 0.13 s/step. Scanning electron microscope (SEM) images and the corresponding Energy Dispersive Spectrometer (EDS) elemental mappings were obtained from a JEOL JSM-7100F thermal field emission electron microscope equipped with an EDAX instrument. TEM, HRTEM and SAED images were obtained from a JEOL JEM-2100 field emission transmission electron microscope. Bulk sample was milled and then dissolved in chloroform before being placed on the surface of a copper grid for further TEM measurement. The quality and composition of the crystals were also analyzed by x-ray photoelectron spectroscopy (XPS, ESCALAB). Before electrical conductivity and photoconductivity measurements, the as-synthesized $(Sn_xSb_{1-x})_2Se_3$ crystals were sliced into small discs with a thickness of about 2 mm, which were then polished. Electrical resistivity and bulk carrier density were measured using a van der Pauw Ecopia HMS-3000 Hall Measurement System (Ecopia Corporation, Anyang, South Korea). The temperature-dependent resistivity was measured by the conventional four-probe method in the temperature range of 300-400 K. To characterize the photoelectric performance, the photo-electro-chemical (PEC) measurement has been carried out by using the classical 3-electrode method, where Ag/AgCl in saturated KCl was used as the reference electrode, Pt-wire as the counter electrode and our sample as the working electrode. Additionally, to prepare the working electrode, the as-synthesized bulk $(Sn_xSb_{1-x})_2Se_3$ crystals were sliced into small discs with diameter of 10 mm and thickness of about 2 mm, then the surface was finely polished and cleaned. After that, silver paint was homogeneously applied on one face of the disc-like sample, acting as the back contact, which was connected with a copper wire and then covered

with a layer of epoxy resin to be isolated from the electrolyte during the PEC test. Then these electrodes were immersed into the electrolyte (0.5 mol/L $LiClO_4$ solution), a white light tungsten halogen lamp with controllable light intensities was used as light source. A mechanical chopper was used to obtain the chopped light and an Autolab Metrohm potentiostat was used to record the current-voltage characteristics. Overall, a schematic illustration of this PEC measurement is presented in Fig. 3.2a, Fig. 3.2b is a representative photograph of the working electrode.

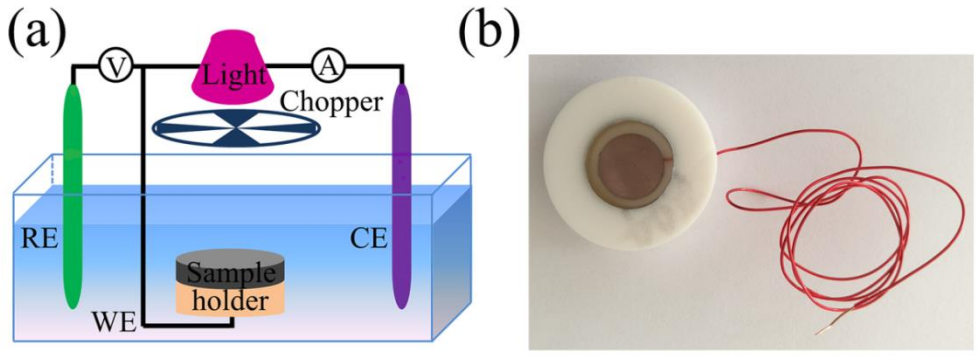

Fig. 3.2 (a) Schematic diagram of the 3-electrode photo-electro-chemical (PEC) measurement; (b) photograph of the working electrode

3.3 Results and discussion

3.3.1 Characterization of $(Sn_xSb_{1-x})_2Se_3$ crystals

Fig. 3.3a shows the XRD patterns of the as-synthesized $(Sn_xSb_{1-x})_2Se_3$ polycrystalline semiconductors (x=0.00, 0.03, 0.05, 0.07 and 0.10) acquired on sliced and polished disc-like samples, which all exhibit prominent peaks in agreement with the JCPDS standard card (15-0861) of the orthorhombic phase of Sb_2Se_3 without a second phase, indicating the absence of any detectable impurity. These results indicate that the $(Sn_xSb_{1-x})_2Se_3$ crystals do not contain a second crystalline phase after Sn doping. Then the XRD patterns of the corresponding powdered samples obtained by grinding the bulk crystals into fine powders can also be indexed to the same crystalline phase, as shown in Fig. 3.3b, suggesting that the crystallization process takes place uniformly inside the bulk sample and is not restricted to the surface. The relative peak intensity is different between the powder and the bulk because the preferential orientation in the bulk is destroyed during the grinding of the powders.

The lattice parameters: a, b and c were determined by refining the diffraction patterns through

Rietveld method implemented in the FULLPROF program [1], which show a slight increase when increasing Sn doping concentration (Fig. 3.3c). This can be attributed to the small difference of atomic radius between Sb (0.160 nm) and Sn (0.158 nm). And this light difference satisfies the criterion for substitution solubility proposed by Hume-Rothery who pointed out that an extensive solid solubility of one metal in another only occurs if the diameter of the atoms differs by less than 15% [2]. Furthermore, the calculated unit cell volume of the $(Sn_xSb_{1-x})_2Se_3$ crystals gradually increase from 545.23 $Å^3$ (x=0.00) to 546.53 $Å^3$ (x=0.10). Fig. 3.3d shows the XPS spectrum of Sn-3d, compared to the pure Sb_2Se_3. Two obvious peaks located at 494.7 and 486.2 eV from $(Sn_{0.10}Sb_{0.90})_2Se_3$ crystals indicate the existence of Sn, further confirming the successful doping.

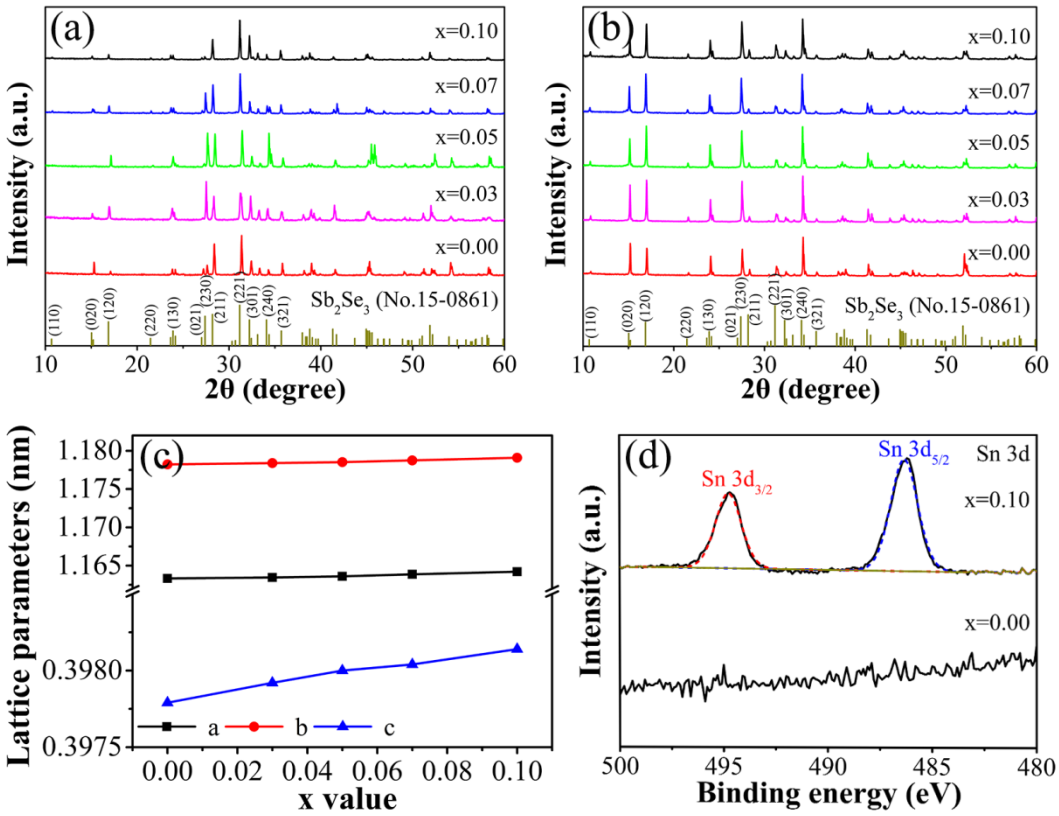

Fig. 3.3 (a) XRD patterns of the bulk $(Sn_xSb_{1-x})_2Se_3$ crystals (x=0.00, 0.03, 0.05, 0.07 and 0.10). (b) XRD patterns of the powdered $(Sn_xSb_{1-x})_2Se_3$ samples. (c) Lattice constants a, b and c, derived from powder XRD peaks, plotted as a funtion of Sn doping concentration (x value). (d) XPS spectrum of Sn-3d for the $(Sn_xSb_{1-x})_2Se_3$ crystals (x=0.00 and 0.10)

The analysis of the XRD pattern in Fig. 3.3 shows that there is only one crystal phase, and the presence of any second phase is not detected even if the Sn doping concentration is increased to 10% (x = 0.10). It is worth mentioning here that we have also studied the effect of higher doping concentration. If the Sn doping concentration is further increased (x=0.12, x=0.15),

the appearance of new diffraction peaks can be observed, as shown in Fig. 3.4. After analysis, the newly added diffraction peaks are matched well with the JCPDS standard card (36-1206) of the orthorhombic phase of $Sn_2Sb_4Se_8$, indicating the exsitence of a second phase. This is the reason why the maximum doping of Sn is limited to 10% in this work.

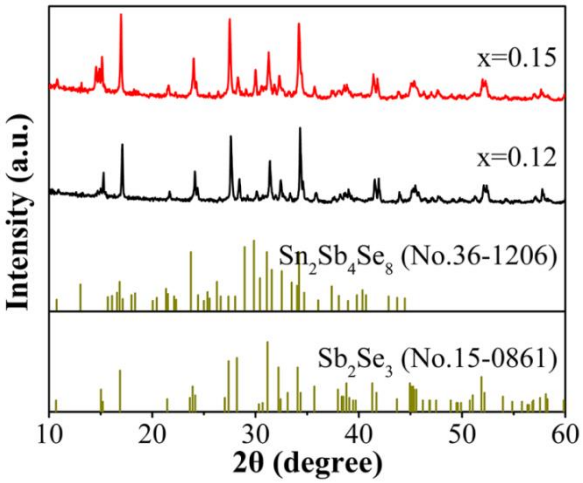

Fig. 3.4 XRD patterns of the powdered $(Sn_xSb_{1-x})_2Se_3$ samples (x=0.12 and 0.15)

The $(Sn_xSb_{1-x})_2Se_3$ crystals' (x=0.00, 0.03, 0.05, 0.07 and 0.10) morphology of freshly fractured surface observed by SEM is shown in Fig. 3.5. All the samples are consisted of large crystals with layered-like structure and clear strips, indicating a preferential orientation. According to the theoretical and experimental studies, bulk Sb_2Se_3 has an orthorhombic crystal structure and is composed of 1D ribbon-like $(Sb_4Se_6)_n$ units stacking together via Van der Waals interactions. Its preferential growth is indeed determined intrinsically by the anisotropic Sb–Se atom chain or layer structure [3].

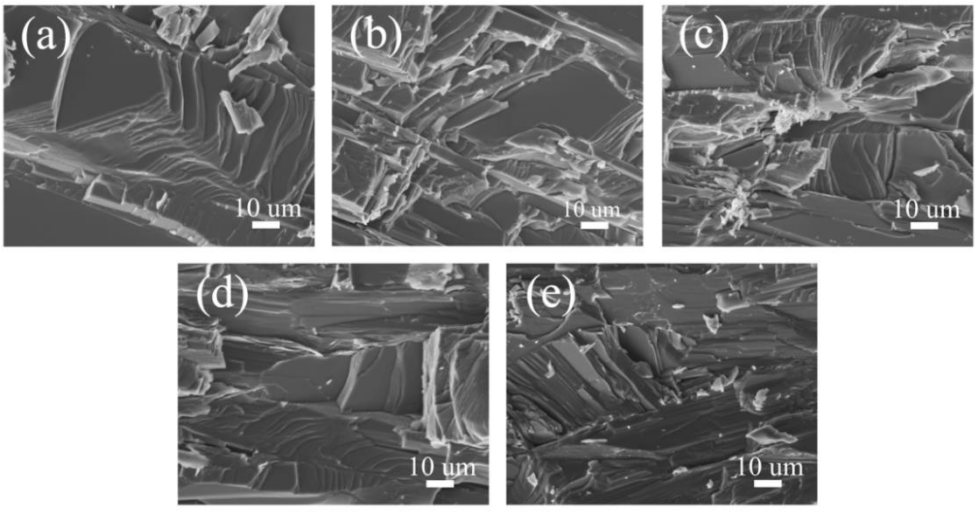

Fig. 3.5 (a-e) SEM images of the fractured surface of $(Sn_xSb_{1-x})_2Se_3$ crystals with Sn concentration x of 0.00, 0.03, 0.05, 0.07 and 0.10, respectively

To further investigate the doping nature and also the grain size of the $(Sn_xSb_{1-x})_2Se_3$ crystals, finely polished disk-like samples were etched chemically by 1 mol/L NaOH solution for 20 min at the room temperature. The principle of this chemical etching is that the physical and chemical states of the atoms show big difference between the grain boundary and inside the grain. For example, the solute atoms and the impurity atoms are easily segregated at the grain boundary, where new phase is easily formed. Herein, the choice of NaOH solution is based on the comprehensive consideration of the chemical etching principle and a more sensitive characteristic for the chalcogenide semiconductors in alkaline solution [4].

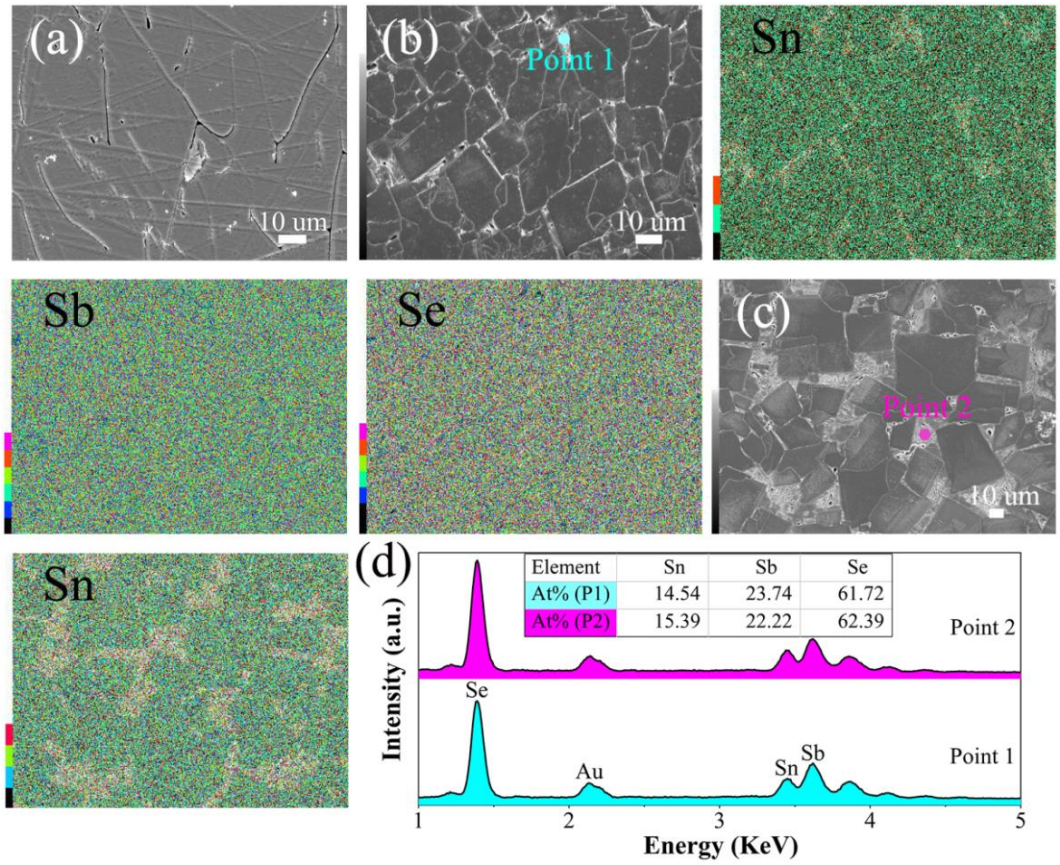

Fig. 3.6 (a-e) SEM images of (a) Sb_2Se_3 crystal, (b) $(Sn_{0.05}Sb_{0.95})_2Se_3$ crystal and (c) $(Sn_{0.10}Sb_{0.90})_2Se_3$ crystal surface after chemical etching by NaOH solution and following the corresponding EDS elemental mappings of Sn, Sb and Se. (d) EDS spectra recorded from two different positions (Point 1 in Fig. 3.5b and Point 2 in Fig. 3.5c)

As shown in Fig. 3.6a, the Sb_2Se_3 crystal consists of some big micron-sized grains. Fig. 3.6b shows a representative etched microstructure of the $(Sn_{0.05}Sb_{0.95})_2Se_3$ crystal. The grains are clearly revealed with an average size of approximately 15 um. In addition, compositional spatial distribution was determined by EDS elemental mappings for Sn, Sb and Se elements, which reveals a uniform distribution of Sb and Se within the crystal. And a few Sn-rich zones

between the grain boundaries can also be observed after chemical etching. Then for the $(Sn_{0.10}Sb_{0.90})_2Se_3$ crystal with higher Sn doping concentration, more obvious Sn-rich regions can be observed, as shown in Fig. 3.6c. This could be explained by phase separation, which is reasonable to occur, the minor Sn-rich phase solidifies first, and then is pushed to the grain boundaries upon freezing of the major phase. To further reveal the elemental composition of these Sn-rich regions, EDS analysis has been performed. Fig. 3.6d shows the EDS spectra recorded from two different positions (Point 1 in Fig. 3.56 and Point 2 in Fig. 3.6c), the atomic ratio of Sn : Sb : Se is 14.54 : 23.74 : 61.72 and 15.39 : 22.22 : 62.39 for Point 1 and Point 2, respectively. It is noted that the composition analysis of these Sn-rich regions performed on different $(Sn_xSb_{1-x})_2Se_3$ crystals show quite similar results, close to the ratio of 2 : 4 : 8 for $Sn_2Sb_4Se_8$, which is also consistent with the XRD results.

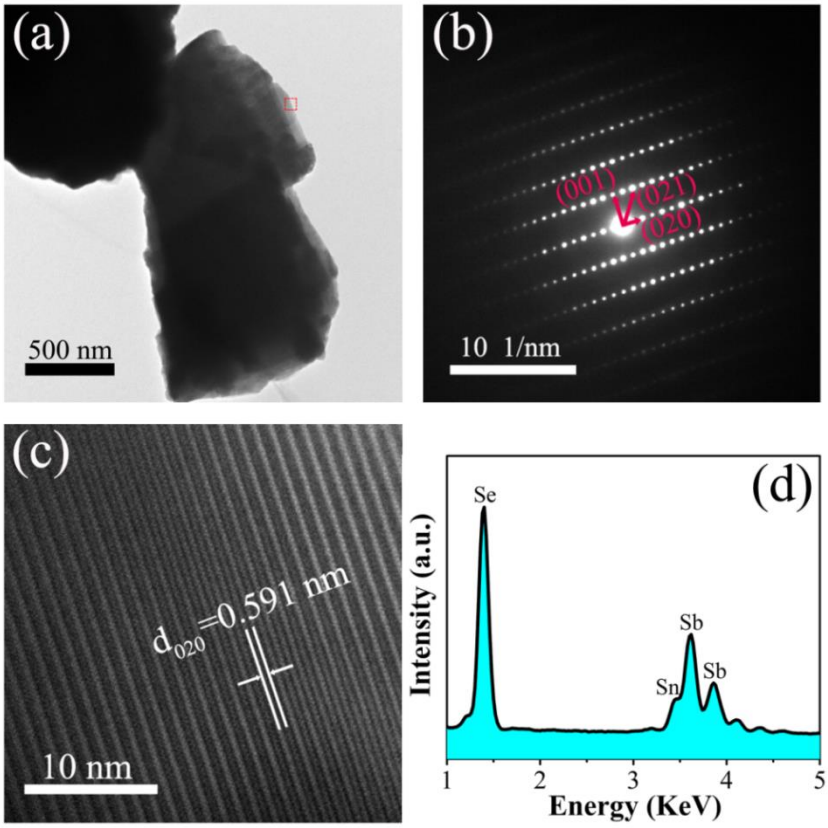

Fig. 3.7 (a) TEM image of the $(Sn_{0.10}Sb_{0.90})_2Se_3$ crystal. SAED pattern (b) and the corresponding HRTEM image (c) from the rectangle marked area in (a). (d) EDS spectrum

Fig. 3.7a presents the TEM image of an isolated particle milled from $(Sn_{0.10}Sb_{0.90})_2Se_3$ crystal. The selected area electron diffraction (SAED) pattern (Fig. 3.7b) from the red marked area (in Fig. 3.7a) is a periodic spot pattern, suggesting its highly crystalline nature. Fig. 3.7c shows the corresponding HRTEM image with obvious lattice fringes associated to the (020) planes

(*d*-spacing of 0.591 nm) of the orthorhombic phase Sb_2Se_3. Then the EDS spectrum (Fig. 3.7d) exhibits strong Sb and Se peaks as well as an observable Sn peak located at 3.44 eV, indicating the successful Sn doping in this crystal.

3.3.2 Electrical properties of $(Sn_xSb_{1-x})_2Se_3$ crystals

In this chapter, the Hall-effect measurements were used to study the influence of Sn doping on the electrical conductivity of Sb_2Se_3. The samples used for these measurements were finely polished disk-like samples. Fig. 3.8a shows the electrical resistivity of the as-synthesized $(Sn_xSb_{1-x})_2Se_3$ crystals with different x values. It can be seen that the pure Sb_2Se_3 exhibits an extremely high resistivity. With Sn doping, a significant decrease of resistivity is observed, and the decrease is almost exponential with the x value. The temperature dependence of the electrical conductivity (σ) in the temperature (T) range of 300 K-400 K has also been studied. As shown in Fig. 3.8b, the plots of ln σ versus 1/T indicate that the electrical conductivity increases with increasing temperature for all samples, confirming the semiconductor characteristics of these samples. Moreover, the conductivity exhibits single activation energy in the temperature range of measurement, according to the Arrhenius equation:

$$\sigma=\sigma_0\exp(-\Delta E/kT) \quad (3.1)$$

where σ_0 is the pre-exponential factor, $\triangle E$ is the activation energy and k is the Boltzmann constant [5]. Thus the thermal activation energy $\triangle E$ can be calculated from the slope, while the intercept on y-axis gives the σ_0 value. Then the bulk carrier density and the doping type were determined by Hall measurements. All the electrical parameters of the $(Sn_xSb_{1-x})_2Se_3$ crystals are summarized in Table 3.1.

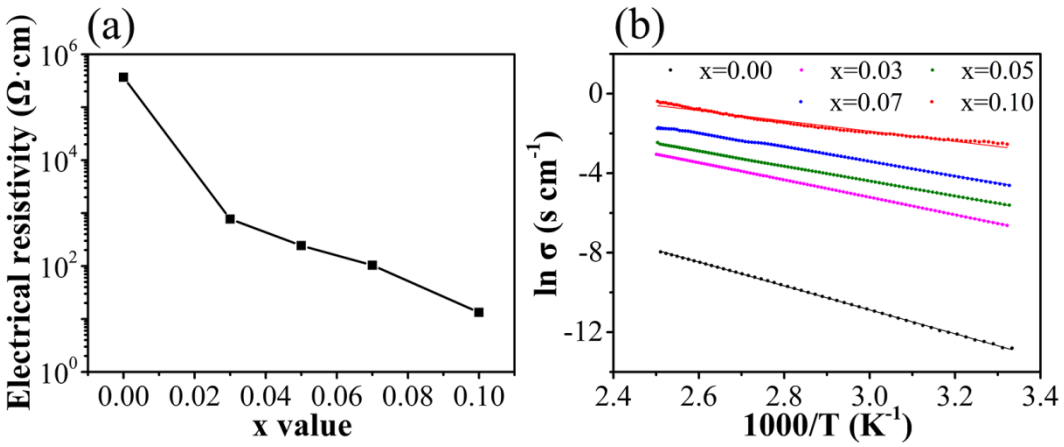

Fig. 3.8 (a) Electrical resistivity of $(Sn_xSb_{1-x})_2Se_3$ crystals with different x values. (b) Temperature dependent electrical conductivity (σ) of $(Sn_xSb_{1-x})_2Se_3$ crystals in the temperature (T) range 300 K-400 K

Table 3.1 Electrical conductivity (σ), bulk carrier density (n), pre-exponential factor (σ_0), activation energy (△E) and conduction type of $(Sn_xSb_{1-x})_2Se_3$ crystals

x value	σ ($s\ cm^{-1}$)	n (cm^{-3})	σ_0 ($s\ cm^{-1}$)	△E (eV)	Conduction type
0.00	2.71×10^{-6}	1.44×10^{11}	1.31×10^{3}	0.52	n
0.03	1.30×10^{-3}	1.52×10^{15}	2.65×10^{3}	0.38	p
0.05	4.12×10^{-3}	3.59×10^{15}	9.96×10^{2}	0.32	p
0.07	9.65×10^{-3}	6.90×10^{15}	1.49×10^{3}	0.30	p
0.10	7.50×10^{-2}	1.94×10^{16}	3.48×10^{2}	0.22	p

It is obvious that the room temperature electrical conductivity shows an increase with several orders of magnitude after Sn doping, accompanied by a synchronous increase of the bulk carrier density, which changes from 1.44×10^{11} cm^{-3} (x=0.00) to 1.94×10^{16} cm^{-3} (x=0.10). Importantly, such a great improvement is an important step for widening the applications of Sb_2Se_3. Since the activation energy varies inversely with the charge carrier density, Sn incorporation in this system should theoretically lead to a decrease of activation energy, which is consistent with the calculated △E values. The pre-exponential factor has a close relationship with the defect or impurities in the crystals, Sn doping into Sb_2Se_3 also creates compositional and configurational disorder, leading to an increase in the localized state density, which is an important factor for the change of σ_0 values. Table 3.1 also shows the conduction type of $(Sn_xSb_{1-x})_2Se_3$ crystals. Sn incorporation has been found to result in p-type behavior, suggesting Sn substitution at the Sb site. Sn possesses one fewer valence electron than Sb, thus replacing Sb with Sn constitutes the hole doping [6].

3.3.3 Photoconductive properties of $(Sn_xSb_{1-x})_2Se_3$ crystals

Photoconductivity is a well-known property of semiconductors which describes the electrical conductivity changes with the incident radiation. The photoconductive characteristics of the semiconducting $(Sn_xSb_{1-x})_2Se_3$ crystals are investigated here by using the classical 3-electrode photo-electro-chemical (PEC) measurements. It is noted that with this 3-electrode technique which measures the generated and separated electron-hole pairs on the surface, it can eliminate the influence of the bulk resistance of the sample, facilitating therefore the comparison between different samples.

Fig. 3.9 shows the current density versus voltage under chopped light using $(Sn_xSb_{1-x})_2Se_3$ (x=0.00, 0.03, 0.05, 0.07 and 0.10) as working electrode, respectively. It is obvious that both dark current and photocurrent density of pure Sb_2Se_3 are very weak, which can be explained by its intrinsic low conductivity and low carrier concentration. For Sn-doped crystals, a significant increase of current density is observed, and this increase is proportional to the Sn doping concentration. Up to x=0.10, the dark current density is increased approximately by 10 times (from −16 μA/cm^2 to −160 μA/cm^2 at a bias voltage of −0.6 V) and the photocurrent density is increased approximately by 14 times (from −18 μA/cm^2 to −250 μA/cm^2 at −0.6 V). This improvement can be considered as an important step to promote Sb_2Se_3-based semiconductors for applications in high performance photoelectric devices. It also shows that the Sn-doped Sb_2Se_3 crystals are identified as p-type semiconductors, due to their photocurrent density increase with a negative bias [7], which is confirmed by the Hall measurement results.

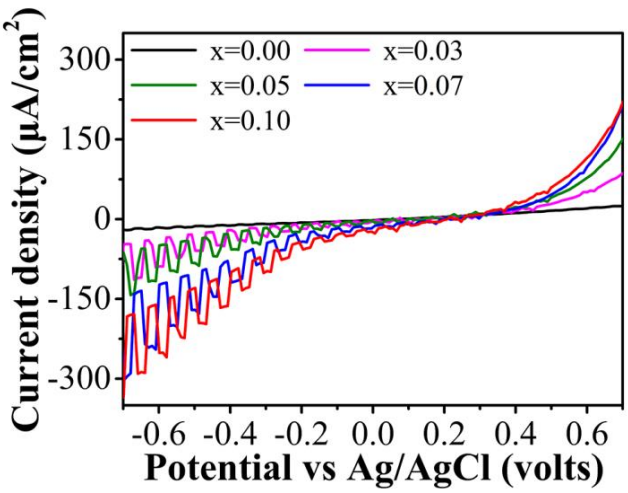

Fig. 3.9 Current-voltage characteristics using $(Sn_xSb_{1-x})_2Se_3$ crystals as working electrodes

Then the light intensity dependence of current density is also investigated and the results are shown in Fig. 3.10. Herein, using $(Sn_{0.10}Sb_{0.90})_2Se_3$ as an example, as shown in Fig. 3.10e, upon illumination, the current density is increased gradually with increasing light intensity. Additionally, current-voltage curves of the $(Sn_xSb_{1-x})_2Se_3$ at other x values (0.00, 0.03, 0.05 and 0.07) show similar phenomena. All the samples show that the photocurrent density strongly depends on the light intensity, which can be attributed to the change in photo-generated carriers. The corresponding photocurrent density as a function of light intensity is shown in Fig. 3.10f, and the dependence can be described by the power law：

$$J_{ph} = AP^{\theta} \quad (3.2)$$

where J_{ph} represents the photocurrent density; P is the power density of the incident light; A is a constant at a specific wavelength; and θ is an exponent [8]. The fitting curves showed that θ =0.27, 0.52, 0.65, 0.60 and 0.54 for x values of 0.00, 0.03, 0.05, 0.07 and 0.10, respectively. All these θ values are non-unity, indicating that some surface defects and carrier trapping at the localized states could result in a complex electron–hole non radiative recombination process [3].

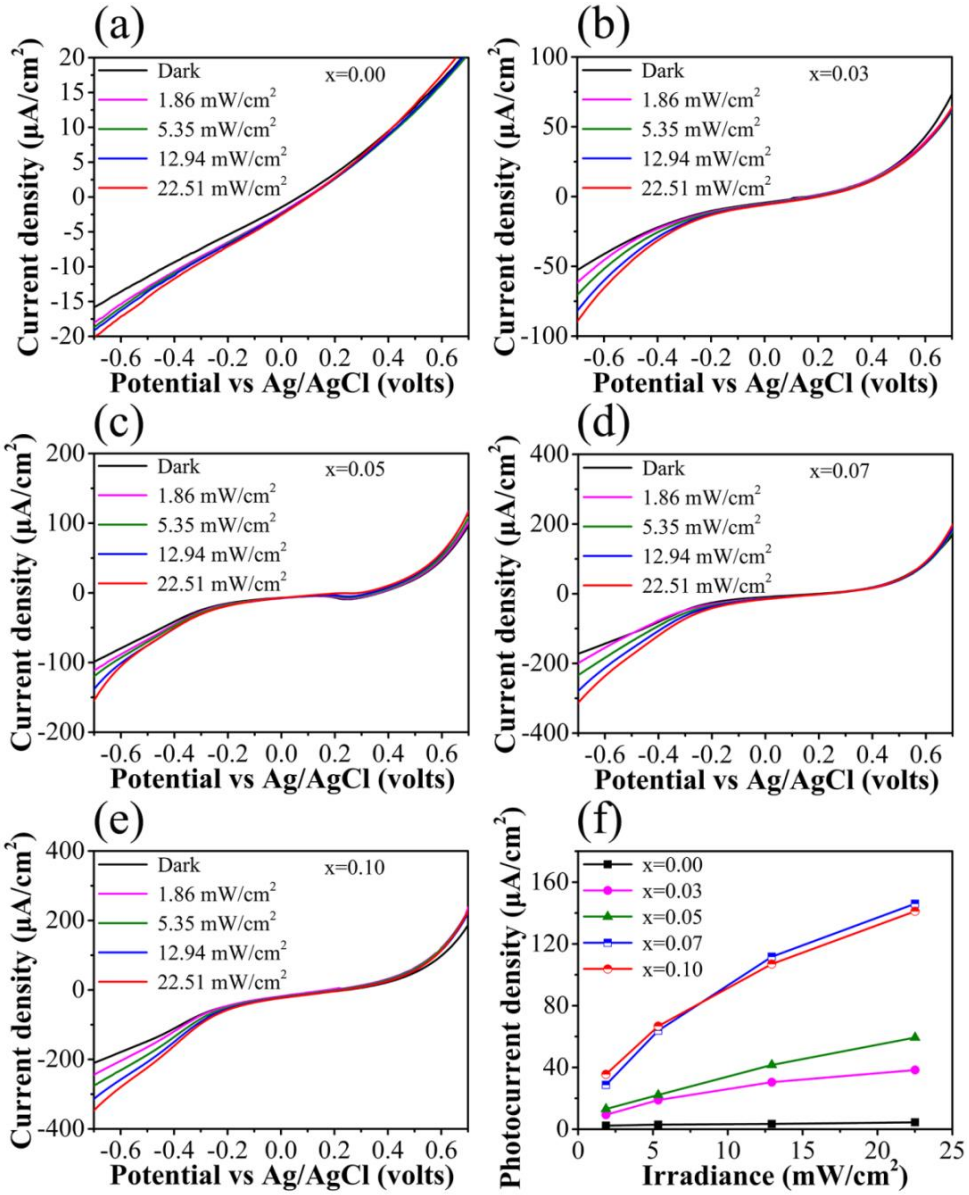

Fig. 3.10 (a-e) Dark current density and photocurrent densities at different power densities of the $(Sn_xSb_{1-x})_2Se_3$ crystals with Sn concentration x of 0.00, 0.03, 0.05, 0.07 and 0.10, respectively. (f) Photocurrent densities measured as a function of incident light density at a bias voltage of −0.7 V

To evaluate the stability and the response speed of the photocurrent, a chronoamperometry measurement has been performed. Fig. 3.11a and 3.11b show two plots of time-resolved PEC

response using Sb_2Se_3 and $(Sn_{0.10}Sb_{0.90})_2Se_3$ as working electrode, respectively. As shown in Fig. 3.11a, when the light is on, the current density rapidly increases from −10.75 μA/cm^2 (dark condition) to −12.25 μA/cm^2 (with 22.51 mW/cm^2 light illumination) and then sharply returns to its initial value as the light is turned off. This light response remains the same after multiple cycles, indicating the excellent reversibility and stability of this Sb_2Se_3 PEC electrode. Then a similar photoresponse can be seen for $(Sn_{0.10}Sb_{0.90})_2Se_3$, except with a larger photocurrent density in the latter case (Fig. 3.11b). When using $(Sn_{0.10}Sb_{0.90})_2Se_3$ crystal as working electrode, a huge photocurrent density spike, before arriving at the steady value, can also be observed, which is caused by the recombination with the presence of surface states [9].

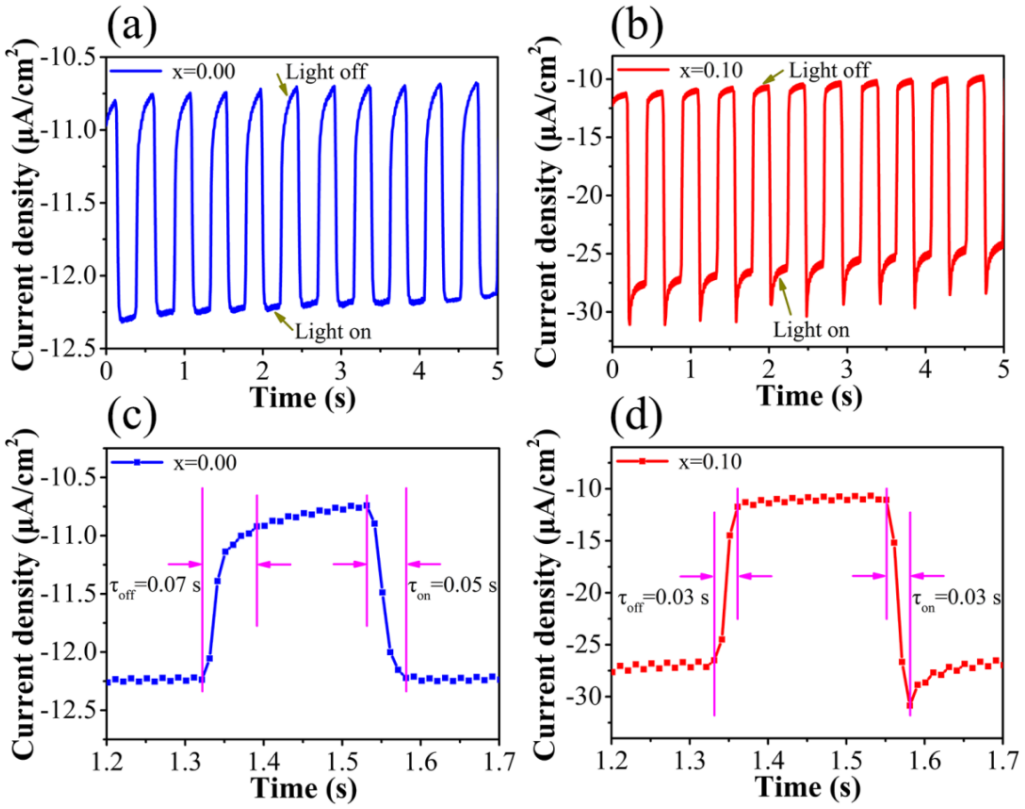

Fig. 3.11 Time-resolved PEC photoresponse by using Sb_2Se_3 (a) and $(Sn_{0.10}Sb_{0.90})_2Se_3$ (b) as working electrode, respectively. (c) Magnified plot of one response cycle in (a), and (d) one response cycle in (b), used to obtain the response time and the recovery time

To extract the exact response time, one of the response periods is magnified, as shown in Fig. 3.11c and d respectively. The response time (τ_{on}) and the recovery time (τ_{off}) of the Sb_2Se_3 working electrode are 0.05 s and 0.07 s respectively. For $(Sn_{0.10}Sb_{0.90})_2Se_3$, both two values show a decrease to 0.03 s, which can be attributed to the presence of much more surface dangling bonds. The high crystal quality and the preferential orientation are also important factors [10,11]. It is worth noting that these short response times are comparable to the very

good results of some reported high performance photodetectors [12], further conforming the high potential of Sn-doped Sb_2Se_3 crystals for application as excellent photoelectric devices.

The optical absorption spectrum is one of the most effective tools for understanding and/or engineering the band structures of semiconductor materials. It is known that a proper band gap of the semiconductor plays a crucial role in fabricating high performance photoelectric devices. In this work, optical absorption spectrum has been employed to characterize the as-synthesized $(Sn_xSb_{1-x})_2Se_3$ crystals. And the absorption data were calculated from diffuse reflectance data using Kubelka-Munk equations: $F(R)=\alpha/\Lambda=(1-R)^2/(2R)$, where R is the reflectance, α and Λ are the absorption and scattering coefficients, respectively [13]. As shown in Fig. 3.12a, the onset of the absorption of Sb_2Se_3 crystals starts near 1200 nm, and a shift toward longer wavelength is observed after Sn doping. The higher absorption efficiency for the doped crystals in the NIR range is interesting for broad spectrum application. Fig. 3.12b shows a plot of $[F(R)hv]^2$ versus energy (hv). giving a direct band gap of 1.17 eV for Sb_2Se_3 and close to 1.10 eV for the Sn-doped Sb_2Se_3 crystals. The dwindling band gap of the doped $(Sn_xSb_{1-x})_2Se_3$ crystals can be explained by the cooperation of the Burstein-Moss shift and the renormalization effect. This mechanism exists in narrow band gap semiconductors with specific doping level [14,15]. In fact, the band gap reduction phenomenon and the corresponding mechanism are consistent with the results and analysis of the Sn-doped Sb_2Se_3 nanorods, as shown in the last chapter, indicating the same principle for these two dopings. Finally, it is worth noting that the band gap of the $(Sn_xSb_{1-x})_2Se_3$ crystals is close to the best value for absorbing efficiently the solar spectrum, making them attractive candidates for photovoltaic application.

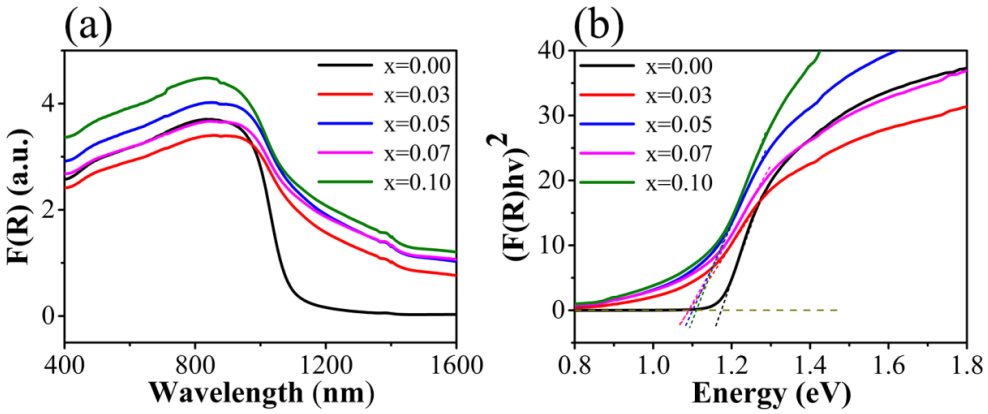

Fig. 3.12 (a) Optical absorption spectra (calculated from diffuse reflectance data) of the $(Sn_xSb_{1-x})_2Se_3$ crystals (x=0.00, 0.03, 0.05, 0.07 and 0.10) (b) A plot of $[F(R)hv]^2$ vs. energy, from which direct band gap was obtained

3.4 Conclusions

In this chapter, an effective high-temperature melting method has been used to synthesize high-quality and variably doped $(Sn_xSb_{1-x})_2Se_3$ crystals with dopant Sn ratio x ranging from 0.00 to 0.10. The successful doping is verified by XRD, XPS and EDS results. With increasing Sn doping concentration, $(Sn_xSb_{1-x})_2Se_3$ crystals exhibit an improvement of electrical conductivity with several orders of magnitude due to the much higher charge carrier concentration. The temperature dependent electrical conductivity displays a typical semiconductor characteristic and a decrease of activation energy is also confirmed with Sn incorporation. Sn-doped Sb_2Se_3 crystals are identified as p-type semiconductors according to the photoconductive characteristics. Notably, compared to pure Sb_2Se_3, the dark current density of a representative $(Sn_{0.10}Sb_{0.90})_2Se_3$ is increased approximately by 10 times and the photocurrent density by approximately 14 times. In addition, this material shows a short response/recovery time (0.03/0.03 s), reversible and stable photoresponse. Therefore, the Sn-doped Sb_2Se_3 crystals have optimal band gap (1.10 eV) which overlap well with the solar spectrum, excellent electrical conductivity and photoconductive properties. The synthesis technique is relatively simple and compatible with large-scale fabrication. These properties confirm the high application potential of Sn-doped Sb_2Se_3 as highly efficient photoelectric devices.

3.5 References

[1] Barpanda, P.; Ati, M.; Melot, B. C.; Rousse, G.; Chotard, J. N.; Doublet, M. L.; Sougrati, M. T.; Corr, S. A.; Jumas, J. C.; Tarascon, J. M., A 3.90 V iron-based fluorosulphate material for lithium-ion batteries crystallizing in the triplite structure. Nat Mater 2011, 10 (10), 772-779.

[2] Hu, C. H.; Chiang, M. H.; Hsieh, M. S.; Lin, W. T.; Fu, Y. S.; Guo, T. F., Phase formation, morphology evolution and tunable bandgap of $Sn_{1-x}Sb_xSe$ nanocrystals. CrystEngComm 2014, 16 (9), 1786.

[3] Liu, Y. Q.; Zhang, M.; Wang, F. X.; Pan, G. B., Facile microwave-assisted synthesis of uniform Sb2Se3 nanowires for high performance photodetectors. Journal of Materials Chemistry C 2014, 2 (2), 240-244.

[4] Guignard, M.; Nazabal, V.; Smektala, F.; Adam, J. L.; Bohnke, O.; Duverger, C.; Moréac, A.; Zeghlache, H.; Kudlinski, A.; Martinelli, G.; Quiquempois, Y., Chalcogenide Glasses Based on Germanium Disulfide for Second Harmonic Generation. Advanced Functional

Materials 2007, 17 (16), 3284-3294.

[5] Liu, X.; Zhang, D.; Li, H.; Li, L.; Yuan, H., A new 3-D open-framework Li-rich vanadoborate and its high ionic conductivity after transforming into glasses. Dalton Trans 2017, 46 (8), 2479-2484.

[6] Culp, S. R.; Simonson, J. W.; Poon, S. J.; Ponnambalam, V.; Edwards, J.; Tritt, T. M., (Zr,Hf)Co(Sb,Sn) half-Heusler phases as high-temperature (>700 ℃) p-type thermoelectric materials. Applied Physics Letters 2008, 93 (2), 022105.

[7] Liang, G. X.; Zheng, Z. H.; Fan, P.; Luo, J. T.; Hu, J. G.; Zhang, X. H.; Ma, H. L.; Fan, B.; Luo, Z. K.; Zhang, D. P., Thermally induced structural evolution and performance of Sb_2Se_3 films and nanorods prepared by an easy sputtering method. Solar Energy Materials and Solar Cells 2018, 174, 263-270.

[8] Zhang, H.; Zhang, X.; Liu, C.; Lee, S. T.; Jie, J., High-Responsivity, High-Detectivity, Ultrafast Topological Insulator Bi2Se3/Silicon Heterostructure Broadband Photodetectors. Acs Nano 2016, 10 (5), 5113-5122.

[9] Spray, R. L.; McDonald, K. J.; Choi, K.-S., Enhancing Photoresponse of Nanoparticulate α-Fe_2O_3 Electrodes by Surface Composition Tuning. The Journal of Physical Chemistry C 2011, 115 (8), 3497-3506.

[10] Choi, D.; Jang, Y.; Lee, J.; Jeong, G. H.; Whang, D.; Hwang, S. W.; Cho, K. S.; Kim, S. W., Diameter-Controlled and Surface-Modified Sb_2Se_3 Nanowires and Their Photodetector Performance. Scientific Reports 2014, 4, 6714.

[11] Zhang, K.; Luo, T.; Chen, H. R.; Lou, Z.; Shen, G. Z., Au-nanoparticles-decorated Sb_2S_3 nanowirebased flexible ultraviolet/visible photodetectors. Journal of Materials Chemistry C 2017, 5 (13), 3330-3335.

[12] Li, L.; Gu, L.; Lou, Z.; Fan, Z.; Shen, G., ZnO Quantum Dot Decorated Zn_2SnO_4 Nanowire Heterojunction Photodetectors with Drastic Performance Enhancement and Flexible Ultraviolet Image Sensors. Acs Nano 2017, 11 (4), 4067-4076.

[13] Vaughn, D. D.; Patel, R. J.; Hickner, M. A.; Schaak, R. E., Single-Crystal Colloidal Nanosheets of GeS and GeSe. Journal of the American Chemical Society 2010, 132 (43), 15170-15172.

[14] Walsh, A.; Da Silva, J. L. F.; Wei, S. H., Origins of band-gap renormalization in degenerately doped semiconductors. Physical Review B 2008, 78 (7).

[15] Gibbs, Z. M.; LaLonde, A.; Snyder, G. J., Optical band gap and the Burstein–Moss effect in iodine doped PbTe using diffuse reflectance infrared Fourier transform spectroscopy. New Journal of Physics 2013, 15 (7), 075020.

CHAPTER IV: SB2SE3-BASED QUASI-HOMOJUNCTION THIN FILM SOLAR CELLS

4.1 Introduction

Thin film solar cell is a relatively new concept of photovoltaic devices. They can be prepared by depositing single-layer, multi-layer photovoltaic thin films on glass, plastic or metal substrates. In recent years, compound thin film solar cells have become a hot research field in solar cells due to their advantages of low material consumption, low energy consumption, high temperature power generation performance and flexibility. Among them and in addition to silicon thin film solar cells, cadmium telluride (CdTe) and copper indium gallium selenide (CIGS) solar cells are two of the most representative thin film solar cells [1-3]. CdTe has excellent optoelectronic properties, the reported power conversion efficiency is more than 22% [4]. Moreover, the low-cost manufacturing makes it widely commercialized. However, the highly toxic Cd inhibits its large-scale applications. The highest power conversion efficiency of CIGS solar cells can reach 22.6% [4], which exceeds the efficiency record (20%) of polysilicon solar cells. However, the high cost of In and Ga, as well as the necessity of rigorous phase and composition control, make the fabrication process extremely complicated, thus obstructing its practical applications. The current research hotspot is the perovskite solar cells, which continuously refreshes the efficiency record thanks to its excellent optical and electrical properties. However, the toxicity of Pb and its intrinsic instability are tough issues that set barriers on its further commercialization.

Compared with the above-mentioned several compound thin film solar cells, the research on Sb_2Se_3 started late, but in recent years, the solar cell efficiency has steadily increased and still has a great space for further improvement. Firstly, Sb_2Se_3 is an inorganic compound semiconductor with orthorhombic crystal structure. It is composed of 1D $(Sb_4Se_6)_n$ nanoribbons stacking along a and b axes through van der Waals force. It possesses particularly excellent photoelectric properties. The band gap of Sb_2Se_3 is about 1.0-1.2 eV and according to the Shockley-Queisser theory, the theoretical solar conversion efficiency of a single-junction solar cell can reach up to 30% [5]. The absorption coefficient of bulk Sb_2Se_3 is larger than 10^5 cm^{-1} in ultraviolet and visible spectrum, allowing sufficient absorption of the solar spectrum within a 500 nm thin film. Secondly, Sb_2Se_3 thin film normally exhibits p-type conductivity. Its electron mobility is determined to be 15 $cm^2 \cdot V^{-1} s^{-1}$ and the hole mobility is 42 $cm^2 \cdot V^{-1} s^{-1}$. Moreover, its dielectric constant is relatively larger (~15), higher than CIGS (ε=13.6) and CdTe (ε=7.1), which leads to a lower exciton binding energy that implies an easier separation of electrons and holes upon photo-generation [5]. These intrinsic physical

properties ensure that Sb_2Se_3 can be used for fabricating high-efficiency solar cells. Finally, Sb_2Se_3 is a simple binary semiconductor and is composed of non-toxic and earth-abundant constituents. These features further strengthen its competitiveness as a new non-toxic absorber material for high-efficiency, low-cost photovoltaics.

The preparation of Sb_2Se_3 thin films plays a crucial role in the high performance solar cells. In the Chapter 1 (paragraph 1.4.3.2), a detailed introduction of thin film preparation methods, including chemical methods and physical methods has been clarified [6-10]. Among these methods, the widely used ones are liquid-phase preparation and thermal evaporation. For example, in 2014, Zhou et al. reported a hydrazine (N_2H_4) solution method to deposit Sb_2Se_3 thin film on classical TiO_2 buffer layer to build a heterojunction TiO_2/Sb_2Se_3 solar cell and the device achieved an efficiency of 2.26% [6]. Sb_2Se_3 has a melting point of 885 K and a very high vapor pressure, making it ideal for thermal evaporation. In 2015, Zhou et al. reported the rapid thermal evaporation process to prepare Sb_2Se_3 thin film and based on the structure of FTO/CdS/Sb_2Se_3/Au, device efficiency reached as high as 5.6% [11]. However, these two commonly used methods have their own shortcomings, which might affect the practical applications. For the former, the used organic solvents are generally toxic and the process is time-consuming. Moreover, the organic solvents are easy to introduce impurities, which will affect the purity of the thin films and the quality of the devices. For the latter process, the uniformity of the films is difficult to control, the stoichiometric ratio of different evaporation sources is easily deviated and the waste of raw materials is not negligible.

In this work, we firstly prepared uniform amorphous Sb_2Se_3-based thin films by Radio Frequency (RF) magnetron sputtering, and then the highly crystalline films were obtained with additional heat treatment in the same chamber. The whole process is carried out in a vacuum sputtering chamber, which can effectively avoid impurity contamination, and also ensure the unchanged chemical composition for the thin films compared to the original target. In addition, it is worth noting that the targets used for magnetron sputtering have variable composition, including Sb_2Se_3, $Sb_2Se_{3.3}$, $(Sn_{0.1}Sb_{0.9})_2Se_3$ and Sb_2 $(Se_{0.9}I_{0.1})_3$. Therefore, the prepared thin films can be considered as Sb_2Se_3-based thin films with tunable physical and chemical properties, which provide an important basis for the subsequent research on solar cells, especially for the construction of p-n junctions. In this chapter, the composition, structure, microstructure, optical properties and photo-electro-chemical performances of Sb_2Se_3-based thin films were investigated systematically. Finally, we successfully explored the possibility of making quasi-homojunction Sb_2Se_3 thin film solar cells.

4.2 Experimental section

4.2.1 Principle of magnetron sputtering deposition

In recent years, magnetron sputtering deposition technique has been developed rapidly with wide range of applications in many fields, such as metallization of semiconductor thin films, architectural glass surface coatings, reflective coatings on polymers, transparent conductive materials on glass or flexible substrates, mechanical wear-resistant coatings. With the increasing demand of high-quality functional films, the magnetron sputtering process is also constantly being improved. In many cases, it has unique advantages over other physical vapor deposition (PVD) processes.

Fig. 4.1 is a schematic representation of the magnetron sputtering deposition [12]. During the sputtering process, electrons collide with argon atoms when move to the substrate under the action of an electric field, causing the ionization of argon atoms to produce Ar^+ cations and new electrons. New electrons move toward the substrate, while Ar^+ ions are accelerated to fly to the cathode target under the action of the electric field. It bombards the target surface with high energy to induce sputtering. Among the sputtered particles, the neutral target atoms or molecules will be deposited on the substrate to form a thin film. However, the generated secondary electrons will drift in a specified direction with cycloid motion trajectory. If a toroidal magnetic field is applied, the electrons will make a circular motion with approximately cycloidal form on the surface of the target, which has a long motion path and is bound in the plasma region. This process will ionize a large amount of Ar atoms, which can bombard the target continually to achieve a high deposition rate. As the collisions increase, the secondary electrons will progressively lose its energy gradually leave away from the target surface and finally be directed on the substrate under the action of electric field. For different materials, magnetron sputtering has both Direct Current (DC) sputtering and Radio Frequency (RF) sputtering. DC sputtering requires that the target can transfer positive charges from ion bombardment to the close contacted cathode, thus it can only be used to sputter conductive materials. For insulating targets or non-metallic targets with poor electrical conductivity, RF sputtering is applied. In this work, considering the low electrical conductivity of Sb_2Se_3 semiconductor targets, RF magnetron sputtering was chosen for films deposition.

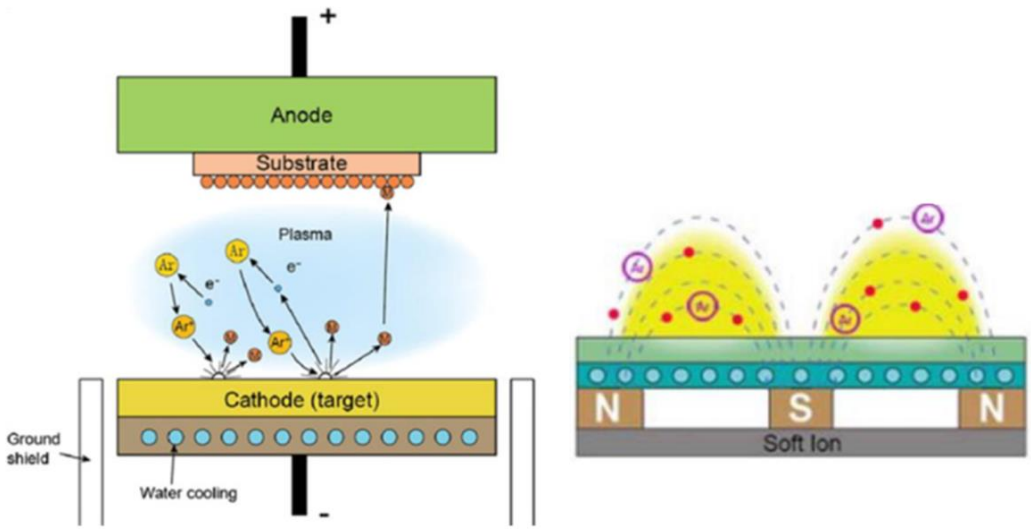

Fig. 4.1 Schematic representative of the magnetron sputtering system

4.2.2 Preparation of Sb_2Se_3-based target

Similar to the preparation process of the Sn-doped Sb_2Se_3 crystal in the last chapter, herein, high-temperature melting method was used to prepare targets for magnetron sputtering, including Sb_2Se_3, $Sb_2Se_{3.3}$, $(Sn_{0.1}Sb_{0.9})_2Se_3$ and $Sb_2(Se_{0.9}I_{0.1})_3$ four targets with different chemical compositions. The specific preparation process is shown in Fig. 4.2. Firstly, a mixture of 60 g raw materials for each single target was weighed according to its chemical composition and then was loaded into a fully cleaned silica tube of 50 mm internal diameter. A connected vacuum trap that was placed in liquid nitrogen was used to condense any volatile products and also to improve the vacuum. The silica tube was sealed under a typical vacuum of around 10^{-5} mbar and then was placed in a rocking furnace. The specific heat treatment procedure is shown in Fig. 4.2b. Within 10 hours, the mixture was heated from room temperature to 780 ℃, and kept in a rocking state for 10 hours to ensure complete melting and homogenization. Afterwards, the rocking was stopped and the furnace chamber was placed vertically to allow a slow cooling and crystallization process of the melt. After cooling down to room temperature, the bulk product was taken out and the surface was finely polished to obtain a magnetron sputtering target with a thickness of 3-4 mm and a diameter of 50 mm.

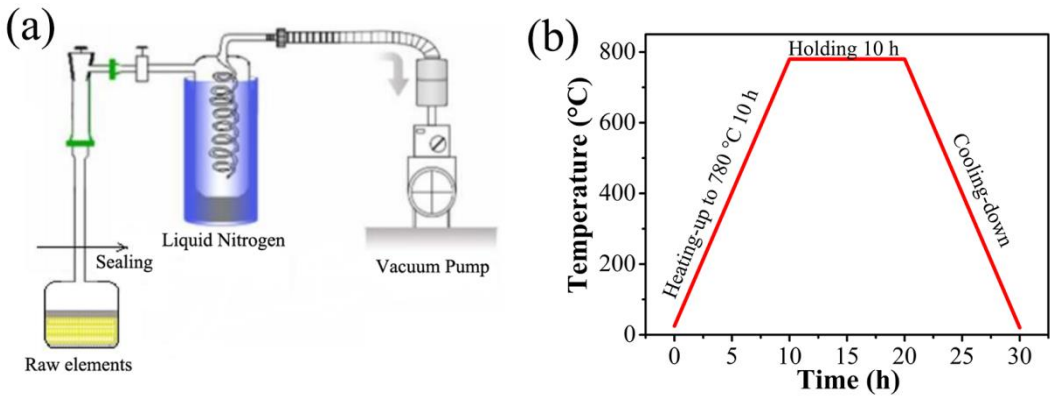

Fig. 4.2 Preparation process of the Sb_2Se_3-based targets: (a) Schematic of the evacuation process; (b) The heat treatment program

4.2.3 Preparation of Sb_2Se_3-based thin films

In 4.2.1, a detailed introduction of the principle of magnetron sputtering is presented. Among them, RF sputtering is a technology that uses a positive ion in the radio frequency discharge plasma to bombard a target and sputter its atoms to deposit on the substrate surface [13]. The process can generate a self-biasing effect, thereby achieving sputtering of the non-conducting target, which is suitable for the used Sb_2Se_3-based targets in this work. The deposition system is schematically illustrated in Fig. 4.3 [14], the used sputtering equipment is a Plassys MP600S with the possibility of using three confocal targets of 50 mm in diameter (only two targets are illustrated for the sake of clarity). The distance between target and substrate is 55 mm. Moreover, an important feature of the sputtering apparatus is that it is equipped with an optical monitoring system, as shown in Fig. 4.3. It can measure the reflectance of the substrate C at a certain wavelength in real time and feeds back the optical thickness of the as-deposited thin films. If the refractive index is known, the actual thickness of the thin film can be calculated. This method of optically monitoring film thickness has the advantages of real-time, simple and nondestructive control of the thin film. This optical system can also be used to observe the crystallization process. Specifically, the CD segment (Fig. 4.3) in the time-resolved reflectance curve represents the heat treatment process, with thin film changed from amorphous to crystalline, observable due to the sharp variation in reflectance.

Different from depositing on a high-temperature substrate that reported in the literature [10], herein, the magnetron sputtering deposition was firstly realized at low temperature (40 ℃) for the deposition of uniform amorphous thin film, and then the highly crystalline thin film was obtained with heat treatment after deposition. A thermal annealing system was installed to

heat the backside of the substrates. The deposition chamber is pumped to a residual pressure of less than 2×10^{-7} mbar before each deposition. All targets were etched by argon plasma for about 10 min to eliminate surface contamination. The flux of the Ar gas during sputtering was controlled at 10 sccm. In addition, according to the Thornton magnetron sputtering regional structure model [15], a relatively low deposition pressure of 5×10^{-3} mbar was used to ensure a high compactness. The RF sputtering power was fixed to 13 W and the obtained DC bias was typically between 80 and 95 volts. The deposition rate was about 5 nm/min.

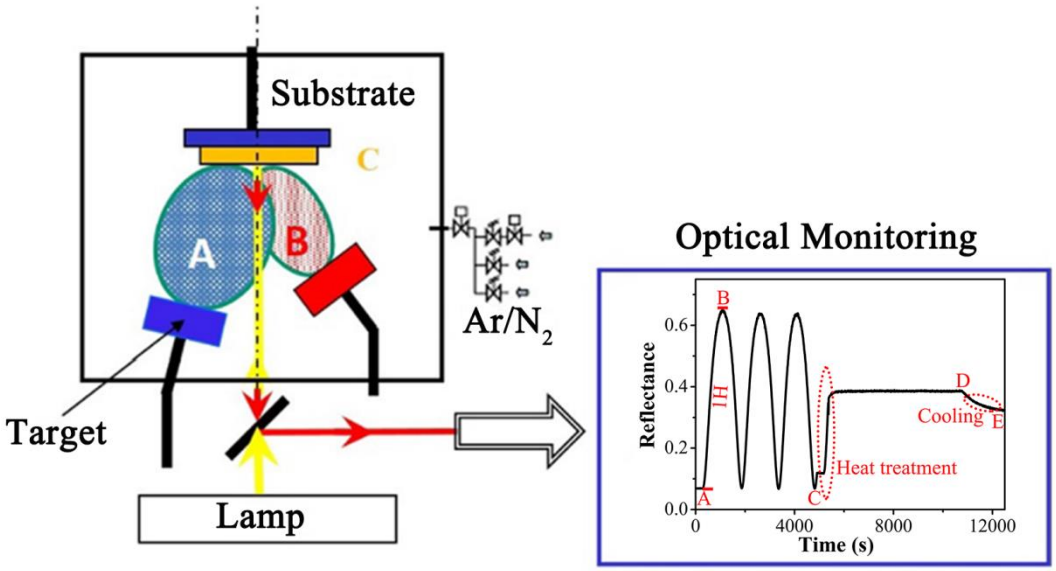

Fig. 4.3 Schematic illustration of the RF magnetron sputtering of Sb_2Se_3-based thin films, where A and B are the targets, the set-up is also equipped with an optical monitoring system

4.2.4 Preparation of Sb_2Se_3 quasi-homojunction thin film solar cells

Up to now, Sb_2Se_3-based thin film solar cells reported in the literature generally use semiconductors such as CdS [11], ZnO [16], TiO_2 [6] as buffer layers, and Sb_2Se_3 as p-type light absorbing layer to construct planar heterojunction thin film solar cells. In this work, for the first time, a novel quasi-homojunction Sb_2Se_3 thin film solar cell is constructed, based on the systematic study of Sb_2Se_3-based thin films, including pure Sb_2Se_3, non-stoichiometric $Sb_2Se_{3.3}$, doped $(Sn_{0.1}Sb_{0.9})_2Se_3$ and $Sb_2(Se_{0.9}I_{0.1})_3$ thin films. The device does not require liquid-phase deposition of the buffer layer. The entire thin film deposition process can be completed by full vacuum magnetron sputtering, which not only simplifies the process, but also effectively avoids the use of toxic organic solvents and the introduction of impurities. Fig. 4.4 is a schematic illustration of the quasi-homojunction Sb_2Se_3 thin film solar cell, namely Glass/ITO/$Sb_2(Se_{0.9}I_{0.1})_3$/Sb_2Se_3/Au. The commercial ITO-coated soda lime glass is selected

as device substrate, wherein the ITO surface resistivity is 30 Ω, the area is 2 × 2 cm, and the glass thickness is 1 mm. Prior to sputtering, the substrate was ultrasonically cleaned in a detergent, acetone, isopropanol, ethanol solution for 20 min, respectively. After being dried, it was used for further Sb_2Se_3-based thin films magnetron sputtering deposition as described in 4.2.3. Finally, two gold contacts (2mm diameter) were deposited through a physical mask with a LEICA DC Sputtering system, after that, the obtained thin film solar cell was directly used for device performance measurements.

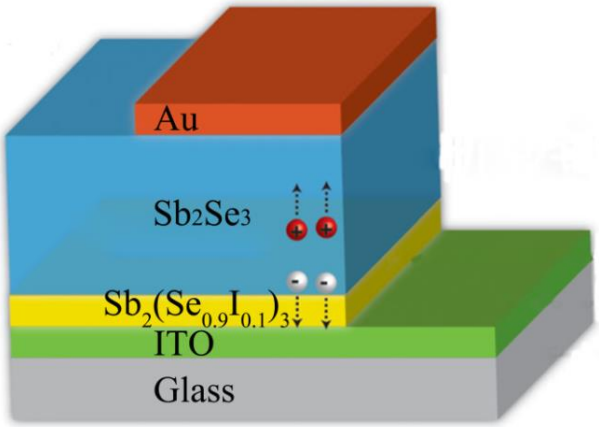

Fig. 4.4 Schematic configuration of the Sb_2Se_3 quasi-homojunction thin film solar cell

4.2.5 Characterization

(i) X-ray diffraction (XRD) analysis was carried out on a PANalytical's X-ray diffractometer with a step width of 0.02 °and a counting duration of 0.13 s/step.

(ii) Scanning electron microscope (SEM) images of the Sb_2Se_3-based thin films and the corresponding Energy Dispersive Spectrometer (EDS) elemental mappings were obtained from a JEOL JSM-7100F thermal field emission electron microscope equipped with an EDAX instrument.

(iii) The optical properties of the Sb_2Se_3-based thin films, including reflectance, transmittance, and optical band gap, were measured and analyzed using a PerkinElmer LAMBDA 1050 UV/Vis/NIR spectrophotometer with a dual beam, dual monochromator. Then the band gap of the as-prepared thin films can be calculated by:

$$\alpha=\frac{1}{d}\ln\left(\frac{1-R(\lambda)}{T(\lambda)}\right) \quad (4.1)$$

$$\alpha h\nu=C(h\nu-E_g)^n \quad (4.2)$$

where α is the absorption coefficient, d is thickness, R and T are the reflectance and transmittance respectively [17]. The latter is a typical Tauc formula, where C is a constant, h

is the Planck's constant, v is the photon frequency, n is an index, and n = 0.5 when the sample is a direct bandgap semiconductor, n = 2 when the sample is an indirect bandgap semiconductor [18]. Then the band gap E_g can be determined by extrapolating the linear part of the spectrum to zero.

(iv) Photo-electro-chemical (PEC) measurements. To characterize the photoelectric performance of the Sb_2Se_3-based thin films, the PEC measurements have been carried out by using the classical 3-electrode method, where Ag/AgCl in saturated KCl was used as the reference electrode, Pt-wire as the counter electrode and our sample as the working electrode. Additionally, to prepare the thin film working electrode, the ITO-coated soda lime glass (surface size 2 × 2 cm) was used as the substrate for magnetron sputtering, and a physical mask with an exposed surface diameter of 1.5 cm was used during the deposition. After that, silver paint was applied on the ITO surface, which was connected with a copper wire, and then all the areas were covered with insulating tape to be isolated from the electrolyte during the PEC test. The specific test procedure was identic with the PEC test performed on Sb_2Se_3 bulk crystal.

(v) The conductive type measurement. The conductive type of the as-prepared thin films was measured with a Semilab PN tester PN-100 (Fig. 4.5a). A semiconductor surface covered by a thin layer oxide is typically in depletion conditions regardless of its type. As a consequence the polarity of the surface barrier is characteristic of the conductivity type of the sample under test. Surface barrier polarity can be detected in a non-contact way by measuring the surface photovoltage. During such measurement, a chopped laser light is applied: by the high intensity illumination, excess carriers are generated and their presence decreases the surface barrier, i.e. flat band condition is approached. The barrier change due to the illumination is capacitively detected by a probe. Conductivity type is determined by the polarity of the surface barrier change due to illumination. The above working principle is also illustrated in Fig. 4.5b [18].

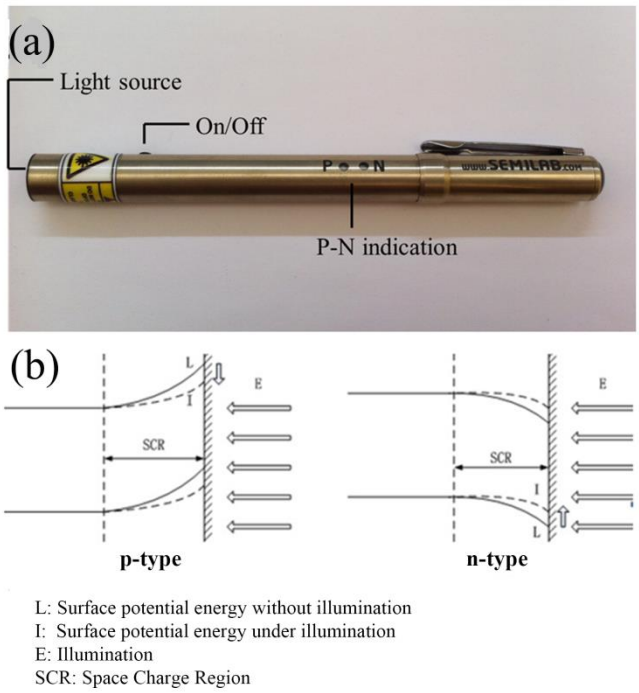

Fig. 4.5 (a) Photograph of the PN tester; (b) Schematic of the working principle

(vi) Thin film solar cells performance measurements. Key performance indicators for solar cells include short circuit current density (J_{SC}), open circuit voltage (V_{OC}), fill factor (FF), power conversion efficiency (η) and external quantum efficiency (EQE). The measurements mainly include current density-voltage (J-V) measurement and wavelength-dependent EQE measurement. In the J-V measurement, two different light sources were used. One was a PGSTAT101 (Metrohm AUTOLAB) test system using fiber optic lamp (MI-150 EDMUND), equipped with a 150 W tungsten halogen lamp with continuously adjustable light intensity, and the intensity is calibrated with a UNO power meter. Another J-V measurement was carried out by Professor L. Le Brizoual, under AM 1.5G light illumination from a 3 A solar simulator with intensity calibrated to 86 mW/cm^2 by using a Si reference cell, and the data was recorded using a multimeter (Keithley 2400). The power conversion efficiency (η) can be calculated by:

$$\eta=\frac{P_{max}}{P_{in}}=\frac{V_{OC}\times J_{SC}\times FF}{P_{in}} \tag{2.5}$$

where P_{max} is the maximum output power and P_{in} incident illumination power [19].

Finally, a measurement system built at the University of Nantes, France, was used by Professor N. Barreau to measure the EQE of the thin film solar cells. The xenon lamp and a monochromator with dual beam setting were used with a reference cell. The specific test device is shown in Fig. 4.6.

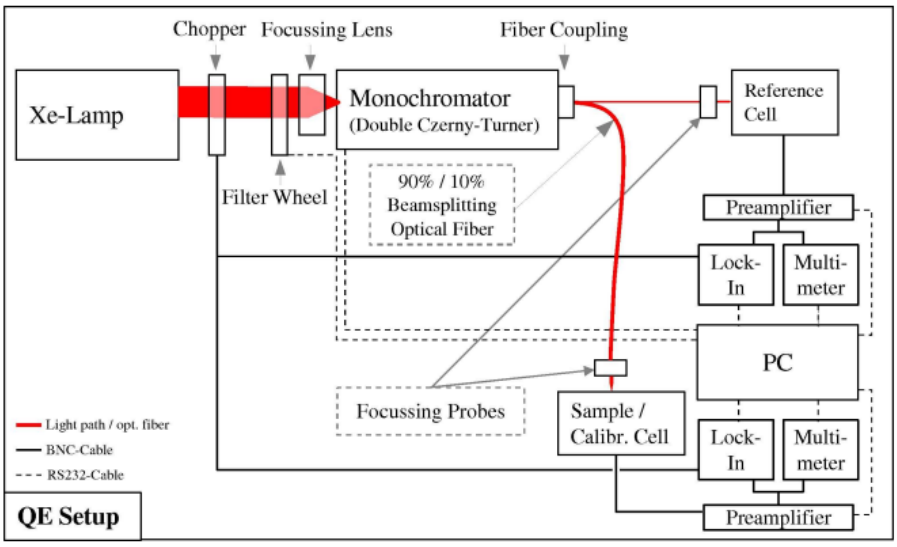

Fig. 4.6 Schematic overview of the setup for external quantum efficiency measurement

4.3 Results and discussion

4.3.1 Composition analysis and surface morphology of Sb_2Se_3-based targets

Fig 4.7 shows the XRD patterns of the as-prepared four targets with different chemical composition, namely Sb_2Se_3, $Sb_2Se_{3.3}$, $(Sn_{0.1}Sb_{0.9})_2Se_3$, and $Sb_2(Se_{0.9}I_{0.1})_3$ and respectively labeled as T1, T2, T3, and T4. It can be seen that all the diffraction peaks of T1 are matched well with the orthorhombic phase of Sb_2Se_3 with the JCPDS standard card (No. 15-0861), and no diffraction peak corresponding to the detrimental second phase can be detected. Compared with T1, in addition to the diffraction peaks of Sb_2Se_3, an observable diffraction peak of Se exists in T2, which corresponds to the excess of Se, consistent with the Se-rich Sb_2Se_3 target. Excess of Se is for compensating possible Se losses during the thin film deposition and the post high-temperature heat treatment. T3 and T4 are Sn and I doped Sb_2Se_3 targets respectively. The objective is mainly to improve the electrical conductivity of Sb_2Se_3 by doping. The XRD result of T3 is consistent with that of the Sn-doped Sb_2Se_3 crystals presented in chapter III. T4 is a $Sb_2(Se_{0.9}I_{0.1})_3$ target, the XRD pattern shows a mixed of the main crystalline phase Sb_2Se_3 and also a second phase SbSeI, which is closely related to the target preparation process. Except for the substitution of Se by I in the Sb_2Se_3 lattice, during the slow cooling process, some Se still have enough thermodynamic energy to form the second phase SbSeI. Such mechanism has been observed in the previous research on I-doped glass-ceramic containing Sb_2Se_3 [20].

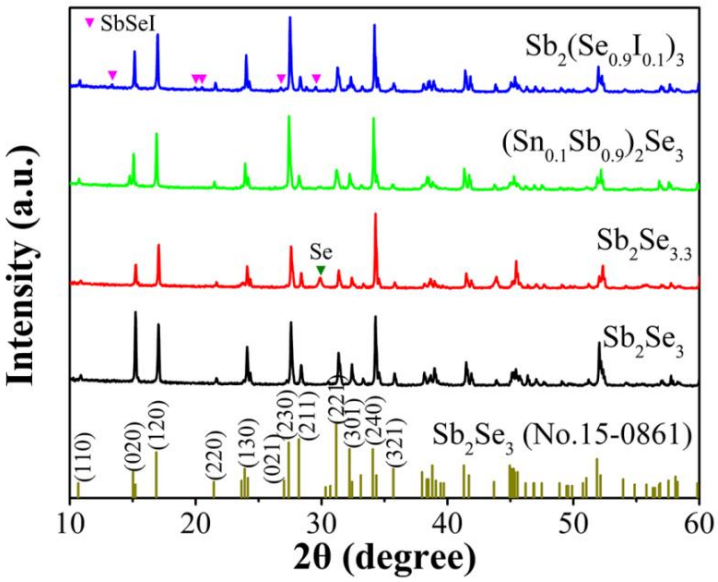

Fig. 4.7 XRD patterns of Sb_2Se_3-based targets

Fig. 4.8 shows the surface morphology of the polished Sb_2Se_3-based targets. All the targets present approximately flat and smooth surface, and the existence of some cracks and holes could be attributed to the high vapor pressure of the constitutes. However, on the whole, the as-prepared targets meet the requirements for using in magnetron sputtering deposition.

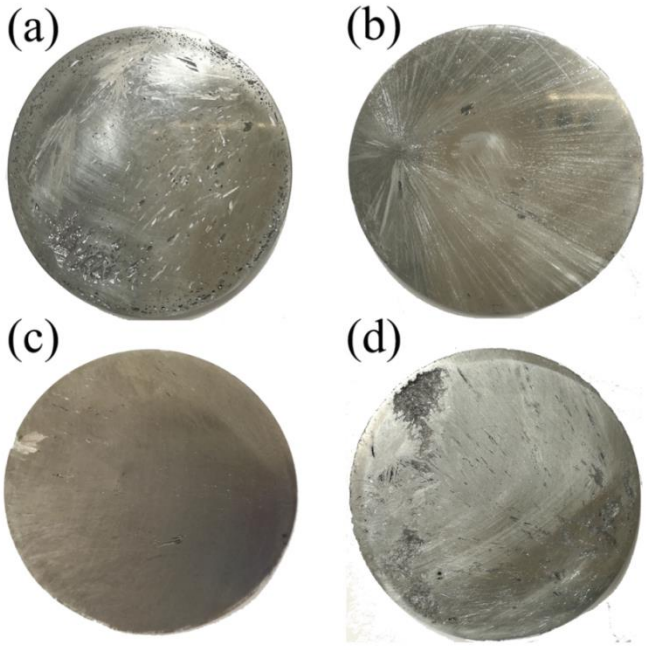

Fig. 4.8 Surface morphology of Sb_2Se_3-based targets

4.3.2 Composition analysis and surface morphology of Sb_2Se_3-based thin films

Fig. 4.9 shows the XRD pattern of the Sb_2Se_3 thin films using T1 as the sputtering target and

BK7 glass as the substrate. No diffraction peaks correspond to the crystalline phase can be observed for the as-deposited thin film, and the broad peak (20 ° to 40 °) is attributed to the amorphous Sb_2Se_3 due to the low mobility of Sb and Se atoms during the deposition with the substrate at 40 ℃. After that, the thin film was annealed at four different temperatures of 250 ℃, 300 ℃, 350 ℃ and 400 ℃. As shown in Fig. 4.9, the XRD patterns of these heated thin films exhibit prominent peaks in agreement with the JCPDS standard card (No. 15-0861) of the orthorhombic phase of Sb_2Se_3. No diffraction peak corresponding to the detrimental Se or Sb_2O_3 can be detected. The sharp diffraction peaks further indicate the high crystalline nature. The preferential crystallographic orientation is [120] for the crystalline thin films. It is known that the preferential growth direction of the thin films on the substrate is highly important to the migration of photo-generated charge carriers in the thin films and to the recombination loss at the grain boundaries, which will greatly affect the device efficiency [11].

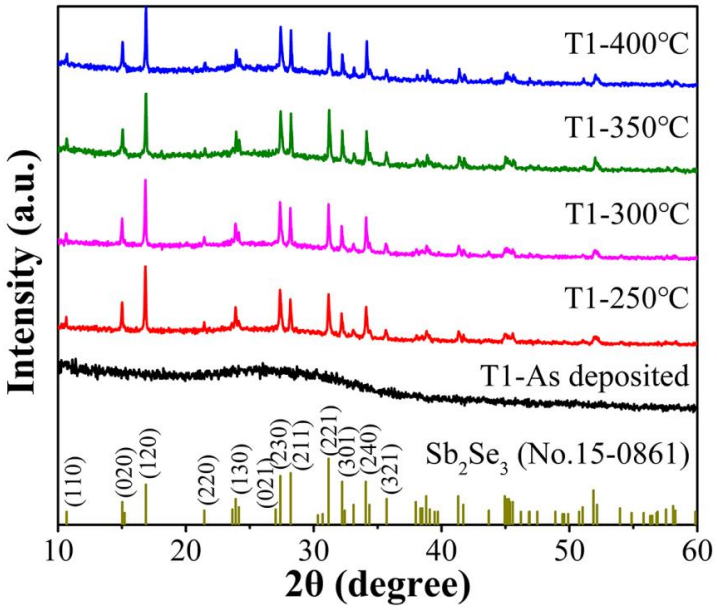

Fig. 4.9 XRD patterns of Sb_2Se_3 thin films with different heat treatment temperatures

Fig. 4.10 shows the SEM image of the Sb_2Se_3 thin films after heat treatment at different temperatures. For the as-deposited amorphous thin film, no obvious crystal grains can be observed, which is consistent with the XRD results. Various small holes are observable, resulting in low density of the thin film. After heat treatment at 250 ℃, as shown in Fig. 4.10b, large crystal clusters begin to appear, and the surface of the thin film became rough, indicating the start of crystal growth, which is also consistent with the XRD results. When the heat treatment temperature is increased to 300 ℃, the crystal grains become more obvious, and the clear grain boundaries are also observed. And then the temperature is further increased, which

leads to a more dense crystalline thin film, accompanied by further growth of some grains. This phenomenon can be explained by the thermally induced coalescence of small grains with high surface energy, which is advantageous for suppressing or reducing the recombination loss of photo-generated carriers at the grain boundaries, thereby improving the performance of the photovoltaic devices. However, if the temperature is too high, as shown in Fig. 4.10e, for the film heated at 400 ℃, the grains become thicker and the surface of the thin film become rough again. And some grain-melting/sintering regions appear, which can be attributed to a king of thermal etching at high temperature. These results indicate that the heat treatment temperature directly affects the microscopic morphology of the thin films. This work provides important guideline for further controlling the morphology and the performance of the thin films in solar cells. Finally, Fig. 4.10f is a cross-sectional SEM image of the thin film heated at 350 ℃. The thin film is in close contact with the glass substrate and has a thickness of 400 nm, which is consistent with the thickness controlled by the optical monitoring system.

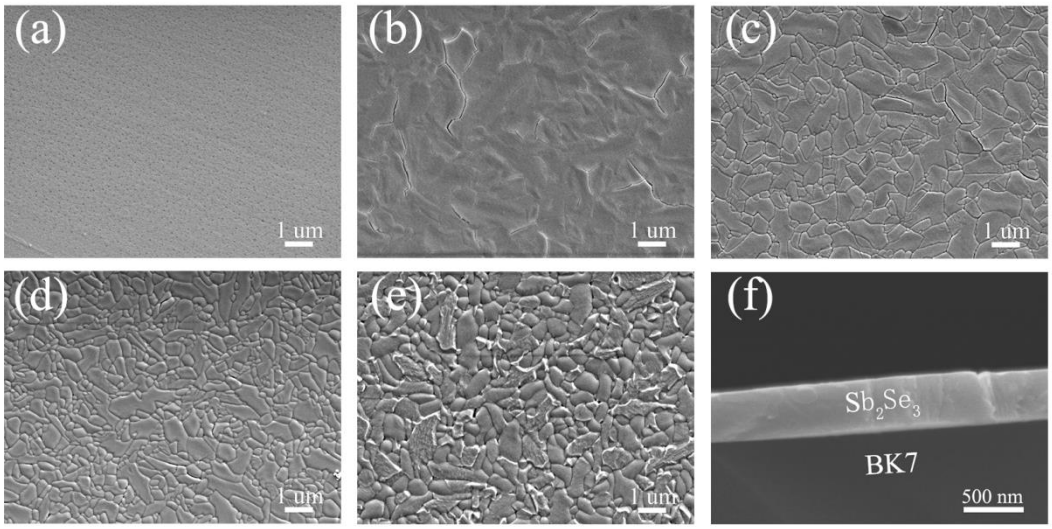

Fig. 4.10 SEM images of Sb_2Se_3 thin films at different heat treatment temperatures: (a) As-deposited; (b) 250 ℃; (c) 300 ℃; (d) 350 ℃; (e) 400 ℃; (f) Cross-sectional SEM image of the thin film heated at 350 ℃

Fig. 4.11 shows the XRD patterns of the $Sb_2Se_{3.3}$ thin films using T2 ($Sb_2Se_{3.3}$) as the sputtering target and BK7 glass as the substrate. Similar to the thin films sputtered by target T1, the as-deposited thin film is amorphous, after heat treatment above 250 ℃, the crystalline thin films can be obtained, and all diffraction peaks match well with the orthorhombic phase of Sb_2Se_3. It is worth noting that, unlike the XRD pattern of the corresponding target, no diffraction peak corresponding to excess Se is observed in the crystalline thin film (2θ=29.9°), indicating the loss of some Se possibly during the deposition and post heat treatment process

because of its high vapor pressure. The preferential orientation of the $Sb_2Se_{3.3}$ crystalline thin films is also [120], and as the heat treatment temperature increases, the relative intensity of the (221) peak gradually increases, indicating that the crystal grains start to grow in the vertical direction based from the substrate.

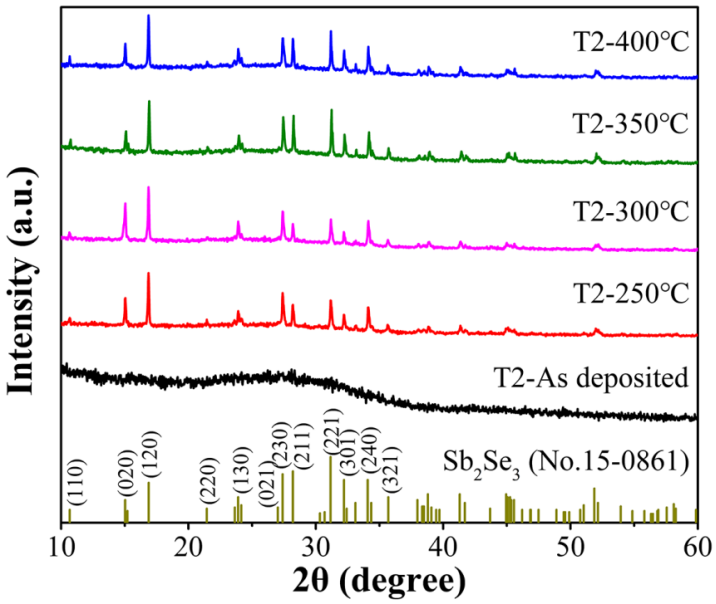

Fig. 4.11 XRD patterns of thin films with $Sb_2Se_{3.3}$ as the target and different heat treatment temperatures

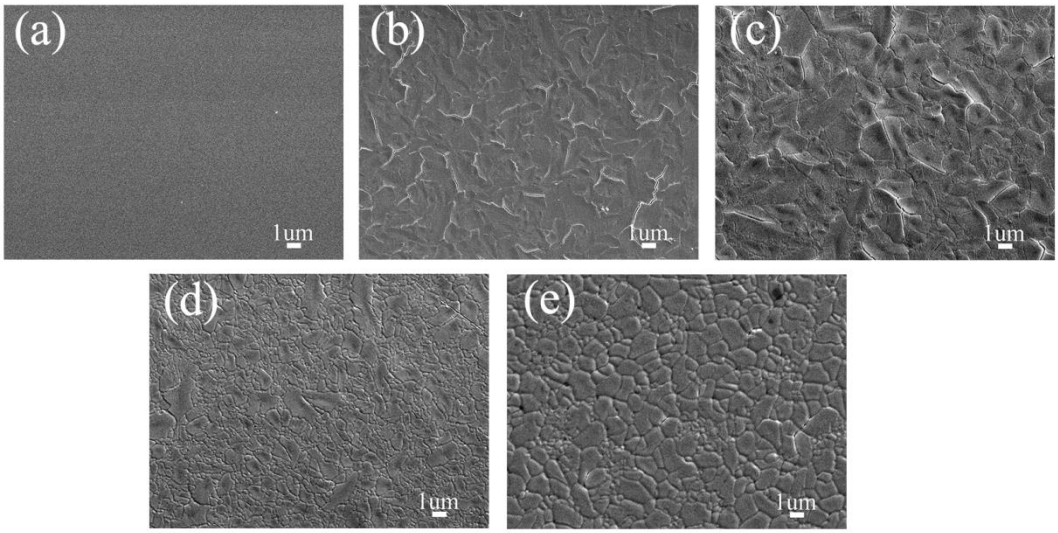

Fig. 4.12 SEM images of $Sb_2Se_{3.3}$ thin films at different heat treatment temperatures: (a) As-deposited; (b) 250 ℃; (c) 300 ℃; (d) 350 ℃; (e) 400 ℃

Similar to the micro-morphology evolution of the Sb_2Se_3 thin films with heat treatment temperature, Fig. 4.12 shows the $Sb_2Se_{3.3}$ thin films change from amorphous to crystalline

state, from the amorphous grain clusters with rough surface to the crystalline grains with flat surface and clear grain boundary. However, a small difference of the changing rate with the heat treatment temperature can be observed. For example, the morphology of $Sb_2Se_{3.3}$ thin film heated at 300 ℃ is close to that of Sb_2Se_3 thin film heated at 250 ℃, further indicating that the film composition is also a key factor affecting the microstructure of the thin film.

Fig. 4.13 shows XRD pattern of the thin films obtained by using T3 ($(Sn_{0.1}Sb_{0.9})_2Se_3$) as sputtering target and with heat treatment at different temperatures. The as-deposited thin film is also amorphous, and then single-crystalline phase of orthorhombic Sb_2Se_3 thin films could be obtained by high-temperature heat treatment. Compared with the Sb_2Se_3 crystalline thin films, the biggest difference is that the $(Sn_{0.1}Sb_{0.9})_2Se_3$ thin film heated at 250 ℃ is amorphous, indicating that Sn doped into Sb_2Se_3 lattice affects the crystallization activation energy, thereby increasing the crystallization temperature of the thin film. Similar phenomena have also been observed in the study of Si-doped Sb_2Te_3 thin films and N-doped $Ge_2Sb_2Te_5$ thin films [21, 22].

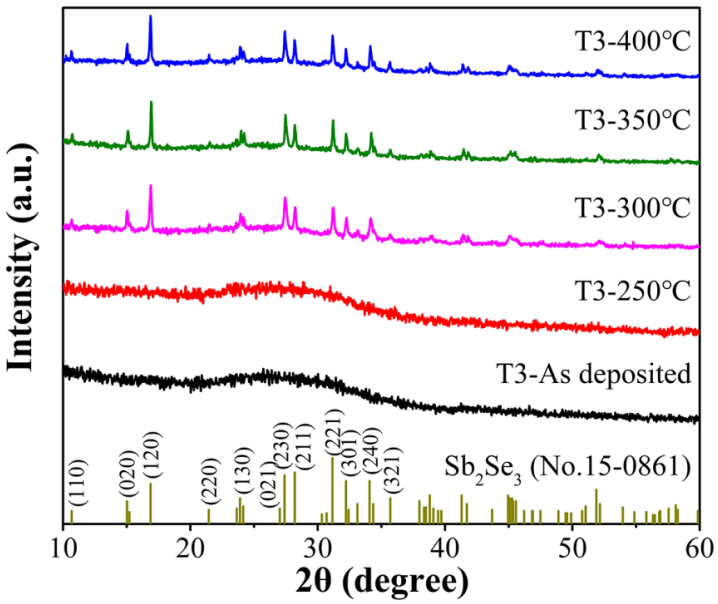

Fig. 4.13 XRD patterns of $(Sn_{0.1}Sb_{0.9})_2Se_3$ thin films at different heat treatment temperatures

The SEM images reveal the surface morphology of the amorphous thin film and crystalline thin films of $(Sn_{0.1}Sb_{0.9})_2Se_3$ (Fig. 4.14). Fig. 4.14a and 4.14b show no obvious crystal grains, indicating the amorphous nature, which is consistent with the XRD results. When the heat treatment temperature is increased to 300 ℃, grain clusters begin to appear on the surface (Fig. 4.14c). With increased the heat treatment temperature, the grain profile become clearer.

Compared with the Sb_2Se_3 crystalline thin film, the grain size is significantly reduced from about 1 um to about 200 nm. This indicates that the doping atoms of Sn inhibit the growth of Sb_2Se_3 grains. In fact, as it will be discussed later, the impurity Sn atoms can be segregated at the grain boundaries, and space charge region will then be established. This will reduce the mobility of the grain boundaries, therefore slowing down the grow up of the grains. This phenomenon is ubiquitous in crystal doping and is called "solute resistance to inhibit grain growth" [23].

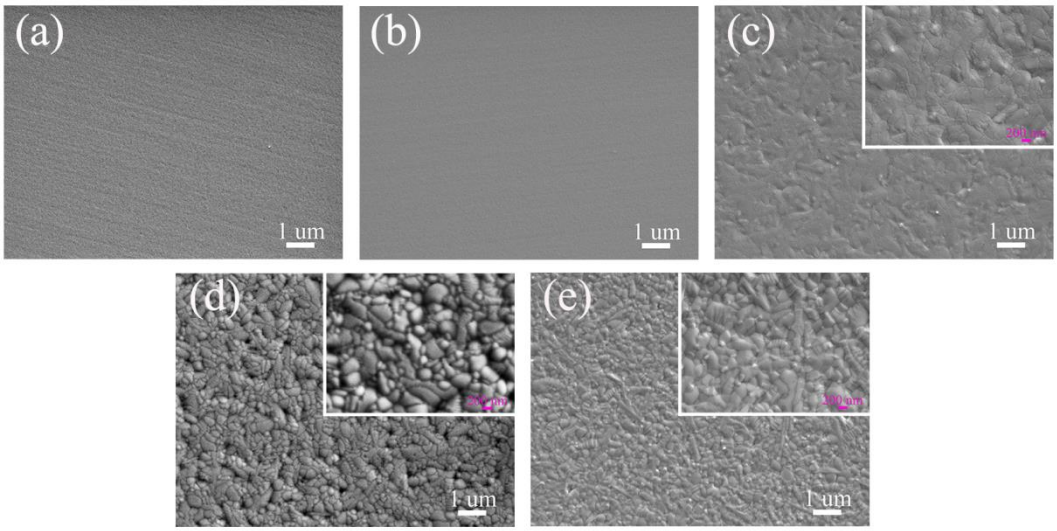

Fig. 4.14 SEM images of $(Sn_{0.1}Sb_{0.9})_2Se_3$ thin films at different heat treatment temperatures: (a) As-deposited; (b) 250 ℃; (c) 300 ℃; (d) 350 ℃; (e) 400 ℃

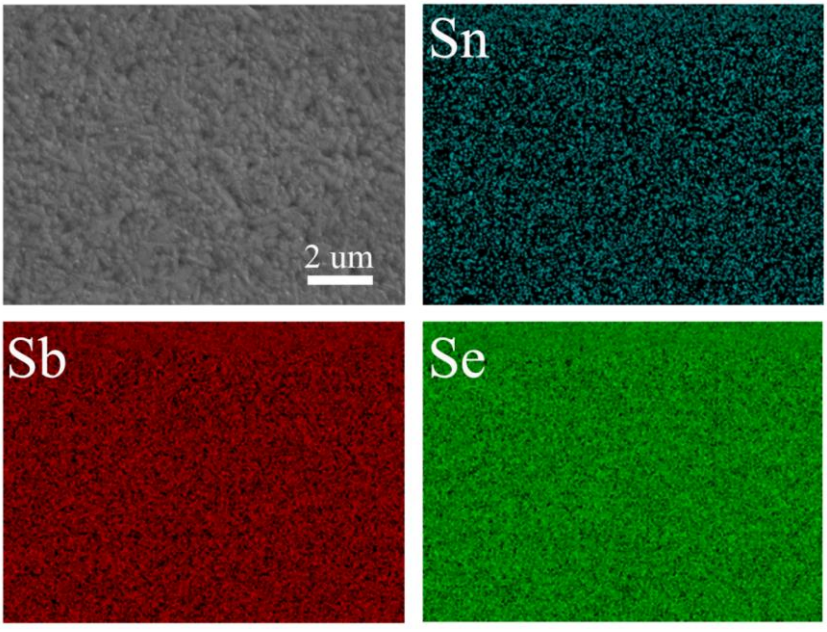

Fig. 4.15 SEM image of $(Sn_{0.1}Sb_{0.9})_2Se_3$ thin film post-heated at 350 ℃ and the corresponding EDS mapping images of Sn, Sb and Se

In order to deeply analyze the microstructure of $(Sn_{0.1}Sb_{0.9})_2Se_3$ crystalline thin film, EDS elemental analysis was performed, Fig. 4.15 shows the EDS mapping images of the thin film with heat treatment of 350 ℃. It can be seen that all the elements are uniformly distributed, further indicating that Sn is successfully doped into the Sb_2Se_3 crystal.

Fig. 4.16 shows XRD pattern of the thin films obtained by using T4, $Sb_2(Se_{0.9}I_{0.1})_3$, as sputtering target and with heat treatment at different temperatures. The as-deposited thin film is amorphous, similar to the above results. However, the diffraction peaks intensity of the crystalline thin films show an obvious difference. Firstly, the diffraction peaks can be indexed to the orthorhombic phase of Sb_2Se_3, and unlike its target (T4), no peak corresponding to SbSeI impurity phase can be observed, indicating that the thin films probably contain less content of I compared to its target. Moreover, I doping can significantly change the preferential orientation of the thin film, that is, from the original [120] orientation to the [020] orientation. As the heat treatment temperature is gradually increased, the (020) peak intensity get stronger accordingly. This can be explained that I doping into the Sb_2Se_3 lattice affects the surface tension and surface energy of some crystal planes, therefore changing the preferential growth direction of the crystal [24].

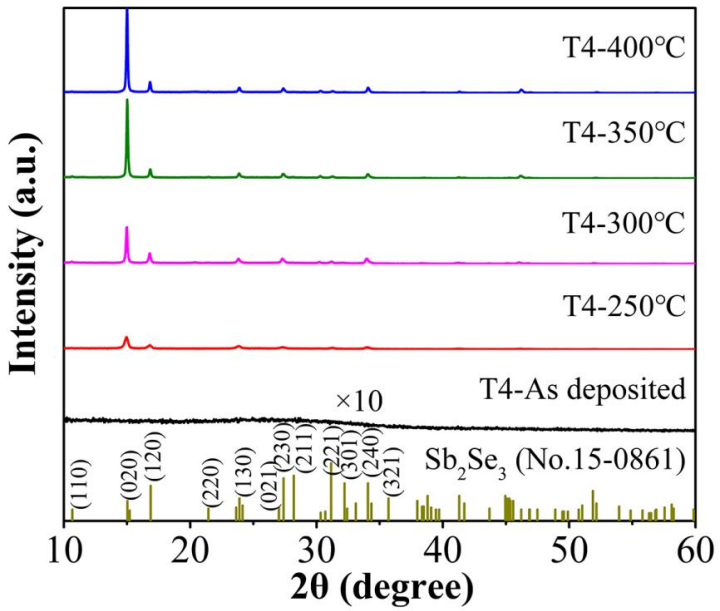

Fig. 4.16 XRD patterns of $Sb_2(Se_{0.9}I_{0.1})_3$ thin films at different heat treatment temperatures

The corresponding SEM images of the $Sb_2(Se_{0.9}I_{0.1})_3$ thin films are shown in Fig. 4.17, where the amorphous thin film is similar to the above results for other compositions. Then the thin films with heat treatment at 250 ℃ and 300 ℃ consist of dense fine grains, as shown in 4.17b

and 4.17c. When the heat treatment temperature is increased to 350 ℃ or 400 ℃, on one hand, the higher temperature facilitates the growth of the grains, on the other hand, it can create porous thin films with low density, shown in Fig. 4.17d and 4.17e. This is attributed to the high saturated vapor pressure of I, which might easily escape from the thin films at high temperatures.

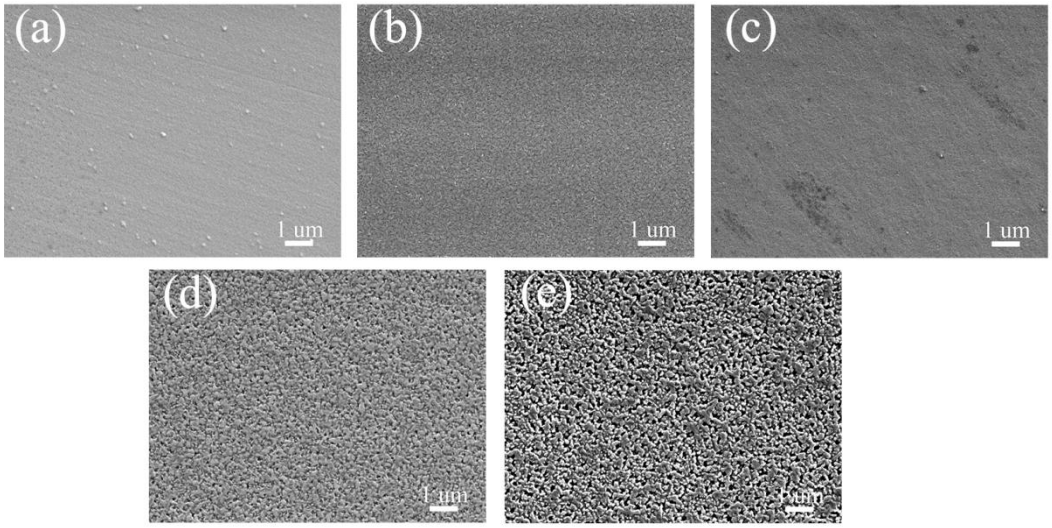

Fig. 4.17 SEM images of $Sb_2(Se_{0.9}I_{0.1})_3$ thin films at different heat treatment temperatures: (a) As-deposited; (b) 250 ℃; (c) 300 ℃; (d) 350 ℃; (e) 400 ℃

Finally, the crystalline quality and the actual elemental composition obtained from SEM-coupled EDS of all the Sb_2Se_3-based thin films are summarized in Table 4.1, where the results are consistent with the above analysis.

Table 4.1 Summary of crystalline quality and elemental composition of the Sb_2Se_3-based thin films

Film composition	Heat treatment	Crystallization	EDS at%
Sb_2Se_3	--	Amorphous	Sb=34.4 Se=65.6
Sb_2Se_3	250 ℃	Crystalline	Sb=36.5 Se=63.5
Sb_2Se_3	300 ℃	Crystalline	Sb=36.9 Se=63.1
Sb_2Se_3	350 ℃	Crystalline	Sb=37.7 Se=62.3
Sb_2Se_3	400 ℃	Crystalline	Sb=37.4 Se=61.6
$Sb_2Se_{3.3}$	--	Amorphous	Sb=34.0 Se=66.0
$Sb_2Se_{3.3}$	250 ℃	Crystalline	Sb=33.9 Se=66.1
$Sb_2Se_{3.3}$	300 ℃	Crystalline	Sb=34.4 Se=65.6
$Sb_2Se_{3.3}$	350 ℃	Crystalline	Sb=35.5 Se=64.5
$Sb_2Se_{3.3}$	400 ℃	Crystalline	Sb=35.2 Se=64.8

$(Sn_{0.1}Sb_{0.9})_2Se_3$	--	Amorphous	Sn=2.5 Sb=32.6 Se=64.9
$(Sn_{0.1}Sb_{0.9})_2Se_3$	250 ℃	Amorphous	Sn=2.0 Sb=33.8 Se=64.2
$(Sn_{0.1}Sb_{0.9})_2Se_3$	300 ℃	Crystalline	Sn=2.4 Sb=33.3 Se=64.3
$(Sn_{0.1}Sb_{0.9})_2Se_3$	350 ℃	Crystalline	Sn=2.3 Sb=33.8 Se=63.9
$(Sn_{0.1}Sb_{0.9})_2Se_3$	400 ℃	Crystalline	Sn=2.5 Sb=34.3 Se=63.2
$Sb_2(Se_{0.9}I_{0.1})_3$	--	Amorphous	Sb=35.2 Se=61.4 I=3.4
$Sb_2(Se_{0.9}I_{0.1})_3$	250 ℃	Crystalline	Sb=34.5 Se=62.1 I=3.4
$Sb_2(Se_{0.9}I_{0.1})_3$	300 ℃	Crystalline	Sb=35.1 Se=61.9 I=3.0
$Sb_2(Se_{0.9}I_{0.1})_3$	350 ℃	Crystalline	Sb=34.2 Se=64.2 I=1.6
$Sb_2(Se_{0.9}I_{0.1})_3$	400 ℃	Crystalline	Sb=34.7 Se=64.1 I=1.2

4.3.3 Optical properties of the Sb_2Se_3-based thin films

Reflectance and transmittance are important optical properties of thin films and thin film devices. Herein, UV/Vis/NIR spectrophotometer was used to obtain the reflection and transmission spectra of the Sb_2Se_3-based thin films. Then the optical band gap of these thin films can be obtained through some calculations, which can provide important guidance for further understanding and engineering the band structure of the semiconductor materials and also the photoelectric devices.

Fig. 4.18a-c shows respectively the reflection spectra, back side reflection spectra and transmission spectra of the Sb_2Se_3 thin films. The used substrate was BK7 glass. All the three spectra show a significant difference in reflectance or transmittance between the as-deposited amorphous thin film and the crystalline thin films with heat treatment at different temperatures. As shown in Fig. 4.18a, the reflectance of the amorphous thin film is lower than that of the crystalline thin films in the short wavelength absorption region, which can be attributed to in the lower refractive index of the amorphous thin film. After heat treatment at 250 ℃, the thin film begin to crystallize, and the atomic arrangement changed from disorder to order. Therefore, the reflectance is significantly improved. With further increased heat treatment temperature to 300 ℃, the thin film crystallizes more thoroughly, thus the reflectance of thin film is further increased. However, if the heat treatment temperature is continuously increased, especially when it reaches 400 ℃, an obvious decrease of the reflectance can be observed. The dominant factor in this situation is the roughness of the thin films, because the high temperature heat treatment increases the roughness of the thin film, which is proved by the SEM results. Therefore, the factors affecting the reflectance of the Sb_2Se_3 thin films are mainly the crystallinity and the roughness of the thin films. The back

side reflection spectra show a similar trend, implying the homogeneous feature of the Sb_2Se_3 thin films. The overall lower reflectance value is caused by the BK7 glass substrate.

According to the transmission spectra (Fig. 4.18c), the short wavelength cut-off edge of the amorphous thin film is 665 nm, and then it shifts to a longer wavelength at about 890 nm for the crystalline thin films. This is also closely related to the structure and the structural disorder of the amorphous thin film increases the band gap energy, leading to a blue shift of the cut-off edge [25]. In order to specifically characterize the band gap of the thin films, the corresponding calculation has been performed. The results are shown in Fig. 4.18d, and they are consistent with the above analysis.

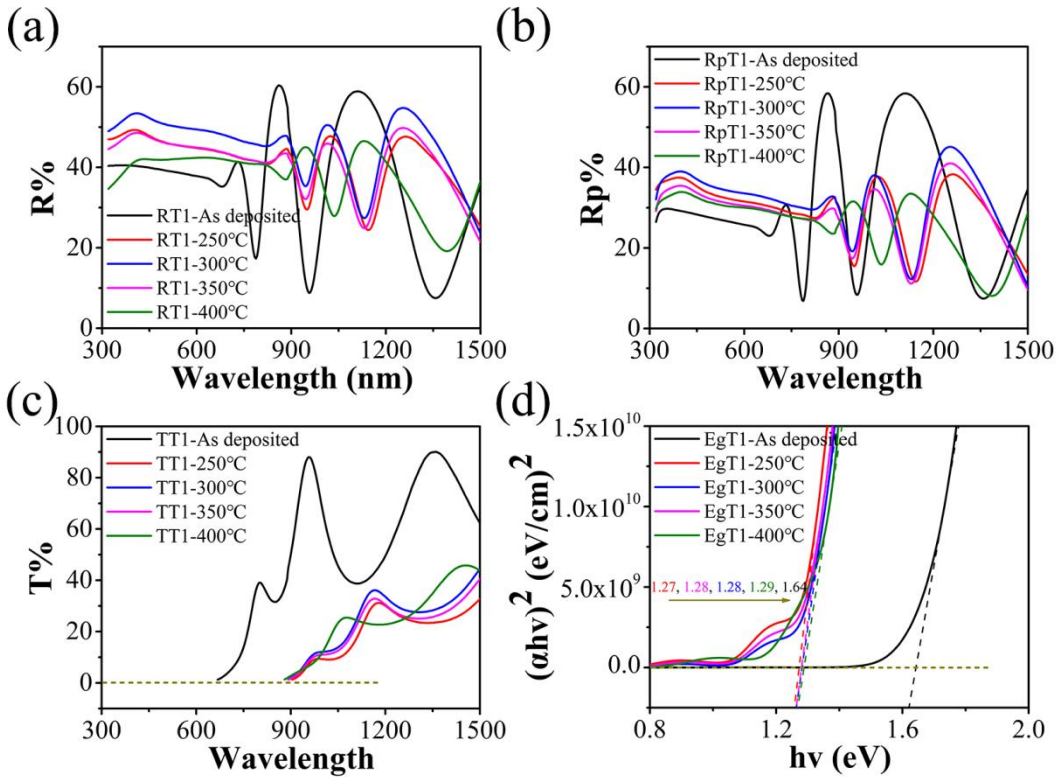

Fig. 4.18 Optical characterization of the Sb_2Se_3 thin films as a function of wavelength and with different temperature of heat treatment. (a) Reflection spectra; (b) Back side reflection spectra, (c) Transmission spectra and (d) Plot of $(\alpha h\upsilon)^2$ vs. hv, from which direct band gap is obtained

Fig. 4.19 shows the reflection, transmission spectra and the band gap of the $Sb_2Se_{3.3}$ amorphous thin film and the corresponding crystalline thin films. Compared with Sb_2Se_3 thin films, very similar change mechanism in reflection and in transmission spectra can be observed. Moreover, though they have different nominal chemical composition, the calculated band gap is very close, implying a small variation in the crystal structure. Furthermore, it is worth noting that the band gap for the crystalline thin film is about 1.28 eV, which is close to

the best value for absorbing efficiently the solar spectrum, making them attractive candidates for photovoltaic application.

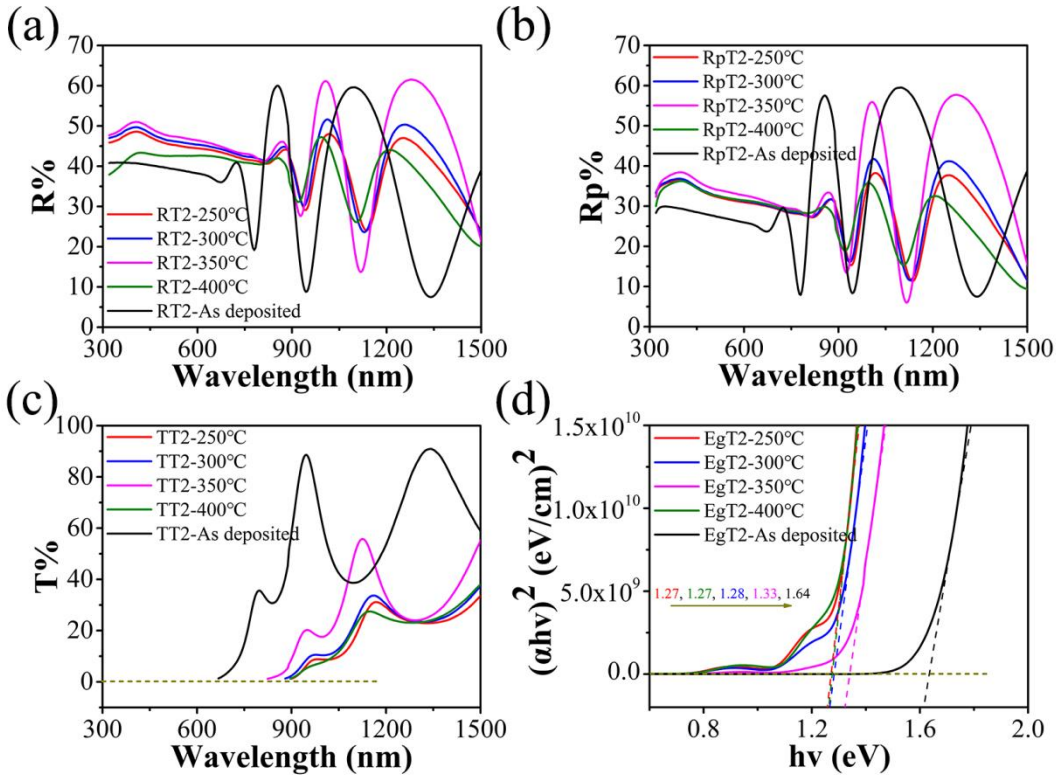

Fig. 4.19 Optical characterization of the $Sb_2Se_{3.3}$ thin films as a function of wavelength and with different temperature of heat treatment. (a) Reflection spectra; (b) Back side reflection spectra; (c) Transmission spectra and (d) Plot of $(\alpha h\upsilon)^2$ vs. hv, from which direct band gap is obtained

Similarly, Fig. 4.20 shows the reflection, transmission spectra and the band gap of the $(Sn_{0.1}Sb_{0.9})_2Se_3$ thin films. Compared with Sb_2Se_3, the biggest difference is that the reflectance and transmittance of the $(Sn_{0.1}Sb_{0.9})_2Se_3$ thin film with heat treatment at 250 ℃ show the same parameters of its amorphous thin film, further indicating the amorphous nature. This result is consistent with the XRD and SEM results. The band gap of the $(Sn_{0.1}Sb_{0.9})_2Se_3$ crystalline thin film is slightly reduced, compared with the amorphous film. Such phenomena have been observed and discussed in both Sn-doped Sb_2Se_3 nanorods and Sn-doped Sb_2Se_3 bulk crystals. The mechanism can be explained with the cooperation of the Burstein-Moss shift and the renormalization effect [26].

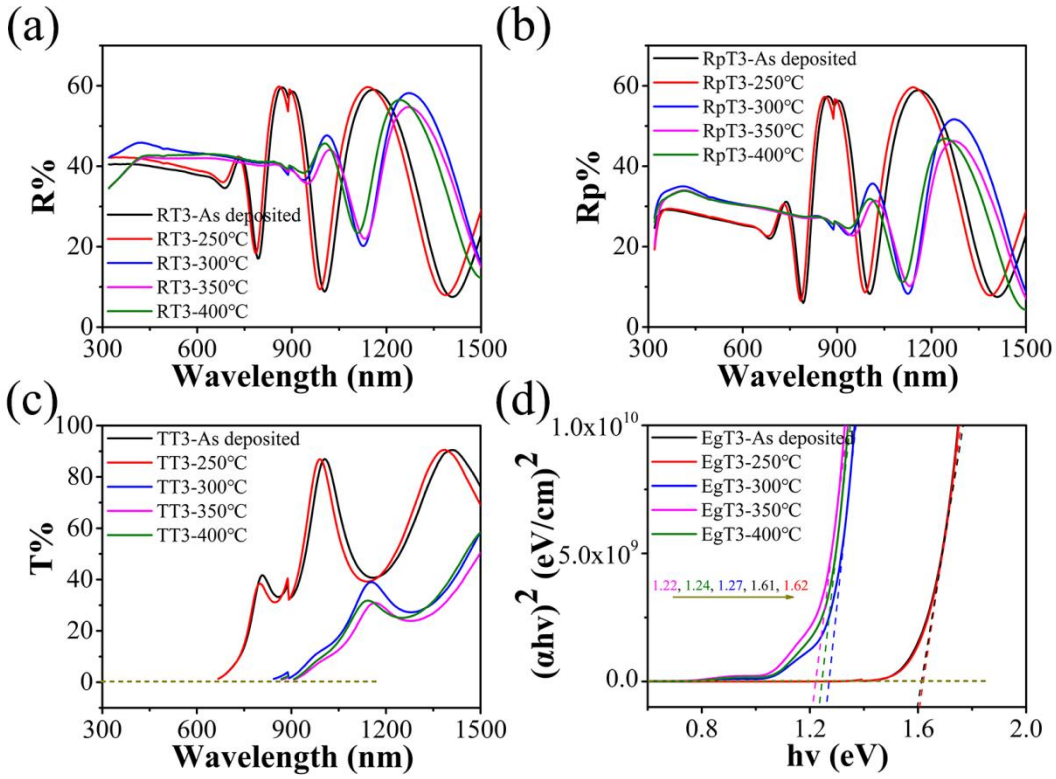

Fig. 4.20 Optical characterization of the $(Sn_{0.1}Sb_{0.9})_2Se_3$ thin films as a function of wavelength and with different temperature of heat treatment. (a) Reflection spectra; (b) Back side reflection spectra; (c) Transmission spectra and (d) Plot of $(\alpha h\upsilon)^2$ vs. hv, from which direct band gap is obtained

Finally, for the $Sb_2(Se_{0.9}I_{0.1})_3$ thin films, as shown in Fig. 4.21a, the reflectance of the thin film is also synergistically affected by its order/disorder and roughness. Notably, the thin film with heat treatment at 400 ℃ exhibits an abnormal phenomenon, which can be attributed to the loss of iodine at high temperature. This is consistent with the porous thin film observed by SEM. The transmission spectra (Fig. 4.21c) show that the short wavelength cut-off edge of the amorphous thin film is 660 nm, and is close to that of the Sb_2Se_3 amorphous thin film. Then the short wavelength cut-off edge of the $Sb_2(Se_{0.9}I_{0.1})_3$ thin film heated at 300 ℃ is 800 nm, which shows a significant blue shift compared with the Sb_2Se_3 thin film heated at the same temperature. The calculated band gap is shown in Fig. 4.21d. Under the crystalline state, iodine doping will significantly increase the band gap of Sb_2Se_3. According to the previous research on I-doped Sb_2Se_3 semiconductors, the dopant I can replace the lattice position of Se and play a strong electron donor role [14, 20]. The doped semiconductor is mainly represented by n-type semiconductor and also with an enlarged band gap width.

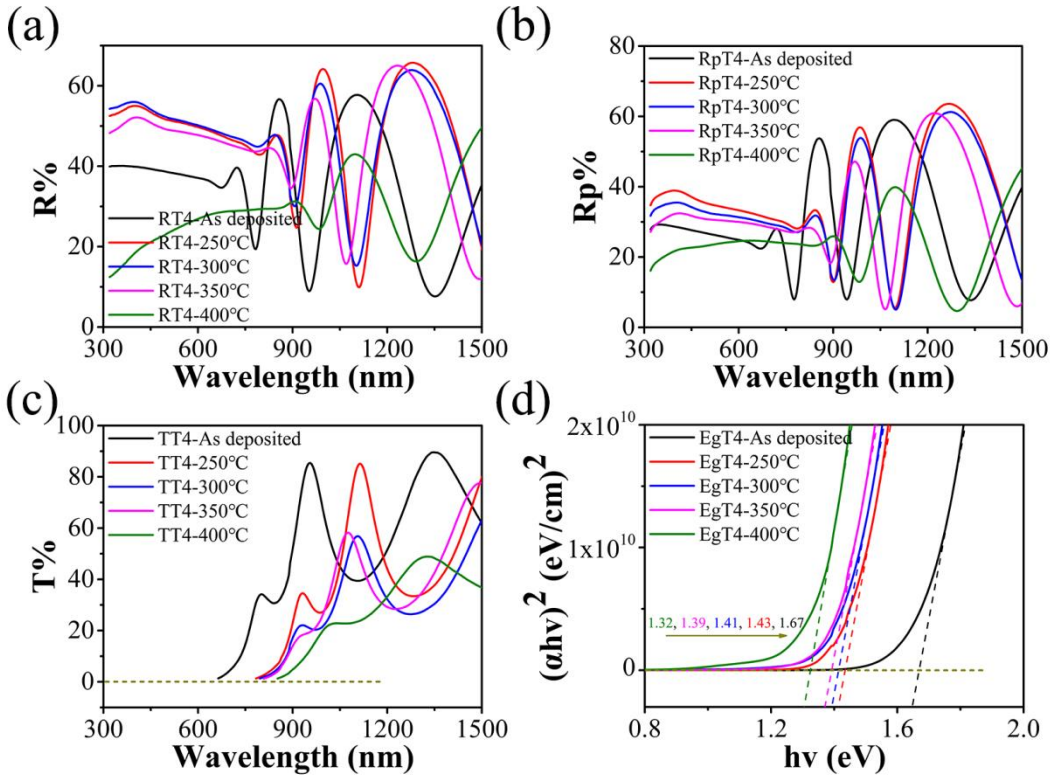

Fig. 4.21 Optical characterization of the $(Sn_{0.1}Sb_{0.9})_2Se_3$ thin films as a function of wavelength and with different temperature of heat treatment. (a) Reflection spectra; (b) Back side reflection spectra; (c) Transmission spectra and (d) Plot of $(\alpha h\upsilon)^2$ vs. hv, from which direct band gap is obtained

The conductive type of the as-prepared thin films was measured with a Semilab PN tester PN-100. Finally, the band gap and the p/n type information (No information represents weak p/n type) of the thin films are summarized in Table 4.2. It can be seen that for the Sb_2Se_3 and $Sb_2Se_{3.3}$ thin films, the amorphous state and the low-temperature heat treatment result in p-type thin films. $(Sn_{0.1}Sb_{0.9})_2Se_3$ is a p-type semiconductor. However, the conductive type cannot be detected for the thin films with high-temperature heat treatment. This can be attributed to its high electrical conductivity and the photo-generated carriers under illumination are small compared to the intrinsic carrier concentration. Therefore, it is difficult to judge the polarity of the surface photovoltage and also the conductive type. The $Sb_2(Se_{0.9}I_{0.1})_3$ crystalline thin films show n-type behaviors, which is consistent with the above analysis.

Table 4.2 A summarize of optical band gap and p/n type of Sb_2Se_3-based thin films

Film composition	Heat treatment (℃)	Band gap (eV)	p/n type
Sb_2Se_3	--	1.64	p
Sb_2Se_3	250	1.27	p
Sb_2Se_3	300	1.28	p
Sb_2Se_3	350	1.28	n
Sb_2Se_3	400	1.29	n
$Sb_2Se_{3.3}$	--	1.64	p
$Sb_2Se_{3.3}$	250	1.27	p
$Sb_2Se_{3.3}$	300	1.28	p
$Sb_2Se_{3.3}$	350	1.33	p
$Sb_2Se_{3.3}$	400	1.27	n
$(Sn_{0.1}Sb_{0.9})_2Se_3$	--	1.61	p
$(Sn_{0.1}Sb_{0.9})_2Se_3$	250	1.62	p
$(Sn_{0.1}Sb_{0.9})_2Se_3$	300	1.27	p
$(Sn_{0.1}Sb_{0.9})_2Se_3$	350	1.22	No information
$(Sn_{0.1}Sb_{0.9})_2Se_3$	400	1.24	No information
$Sb_2(Se_{0.9}I_{0.1})_3$	--	1.67	No information
$Sb_2(Se_{0.9}I_{0.1})_3$	250	1.43	n
$Sb_2(Se_{0.9}I_{0.1})_3$	300	1.41	n
$Sb_2(Se_{0.9}I_{0.1})_3$	350	1.39	n
$Sb_2(Se_{0.9}I_{0.1})_3$	400	1.32	n

4.3.4 Photo-electro-chemical performance of the Sb_2Se_3-based thin films

The photo-electro-chemical (PEC) characterization of the Sb_2Se_3-based thin films was carried out by using the classical 3-electrode method. Fig. 4.22 shows the current density versus voltage under chopped light using Sb_2Se_3 or $Sb_2Se_{3.3}$ or $(Sn_{0.1}Sb_{0.9})_2Se_3$ or $Sb_2(Se_{0.9}I_{0.1})_3$ thin films as working electrodes, respectively. A white light tungsten halogen lamp with light intensity of 25 mW/cm^2 was used as the light source, and the chopped light was obtained through a mechanical chopper.

As shown in Fig. 4.22a1, the Sb_2Se_3 amorphous thin film can produce a photocurrent of 170 μA/cm^2 at −0.7 V, which is significantly improved compared with the photocurrent generated by using Sb_2Se_3 bulk crystal as working electrode (Fig. 3.9, Chapter 6), indicating that the

thin film working electrode surface is highly reactive. This is closely related to the process of magnetron sputtering, which can create some slight composition deviation from the stoichiometry, leading to a significant increase of charge carrier concentration. In addition, it also shows the current density increases with a negative bias, indicating that the amorphous thin film exhibits p-type conductivity, which is consistent with the information given by the PN tester. For the Sb_2Se_3 crystalline thin film, when the heat treatment temperature is 250 ℃, the thin film is still p-type, and the photocurrent does not change significantly. However, when the heat treatment temperature is increased to 350 ℃, the high crystallinity would probably lead to higher conductivity (higher charge carrier concentration) and the corresponding photocurrent increase from 170 μA/cm^2 to 370 μA/cm^2 (+0.7 V). Moreover, it is worth noting that the thin film changes from p-type to n-type, indicating that the heat treatment temperature has an important influence on the conductive type. This is closely related to the loss of Se at high temperature, and similar phenomenon has been previously reported [10]. It also shows that the p/n type can be adjusted by adjusting the heat treatment temperature, which is of great significance in the structural design of thin film solar cells. For the $Sb_2Se_{3.3}$ thin films, as shown in Fig. 4.22b1-b3, the PEC performance is similar to the Sb_2Se_3 thin films, in addition to a slight difference in the photocurrent density.

Then for the $(Sn_{0.1}Sb_{0.9})_2Se_3$ thin films (Fig. 4.22c1-c3), both the amorphous and crystalline thin films show p-type, in consistence with the results of Sn-doped Sb_2Se_3 crystals. However, unlike the enhanced photoconductivity observed for the doped bulk crystals, no improvement of photocurrent can be observed for the $(Sn_{0.1}Sb_{0.9})_2Se_3$ thin films. This indicates that the content of Sn in the thin film is different from the doping concentration in bulk crystals, therefore the required Sn doping level and the corresponding magnetron sputtering process is still facing challenges and needs further exploration.

Finally, Fig. 4.22d1-d3 shows the current density versus voltage of the $Sb_2(Se_{0.9}I_{0.1})_3$ amorphous and crystalline thin films. All these thin films present n-type characteristics, indicating that I doping leads to electron conduction. Moreover, the amorphous thin film, the crystalline thin films with heat treatment at 250 ℃ and 350 ℃ produces a photocurrent of respectively 175 μA/cm^2, 265 μA/cm^2 and 770 μA/cm^2 at 0.7 V. Compared with the Sb_2Se_3 thin films, the current density has been increased, implying superior photoelectric properties. Therefore, the $Sb_2(Se_{0.9}I_{0.1})_3$ crystalline thin film is preferred in the subsequent study of Sb_2Se_3 quasi-homojunction thin film solar cells.

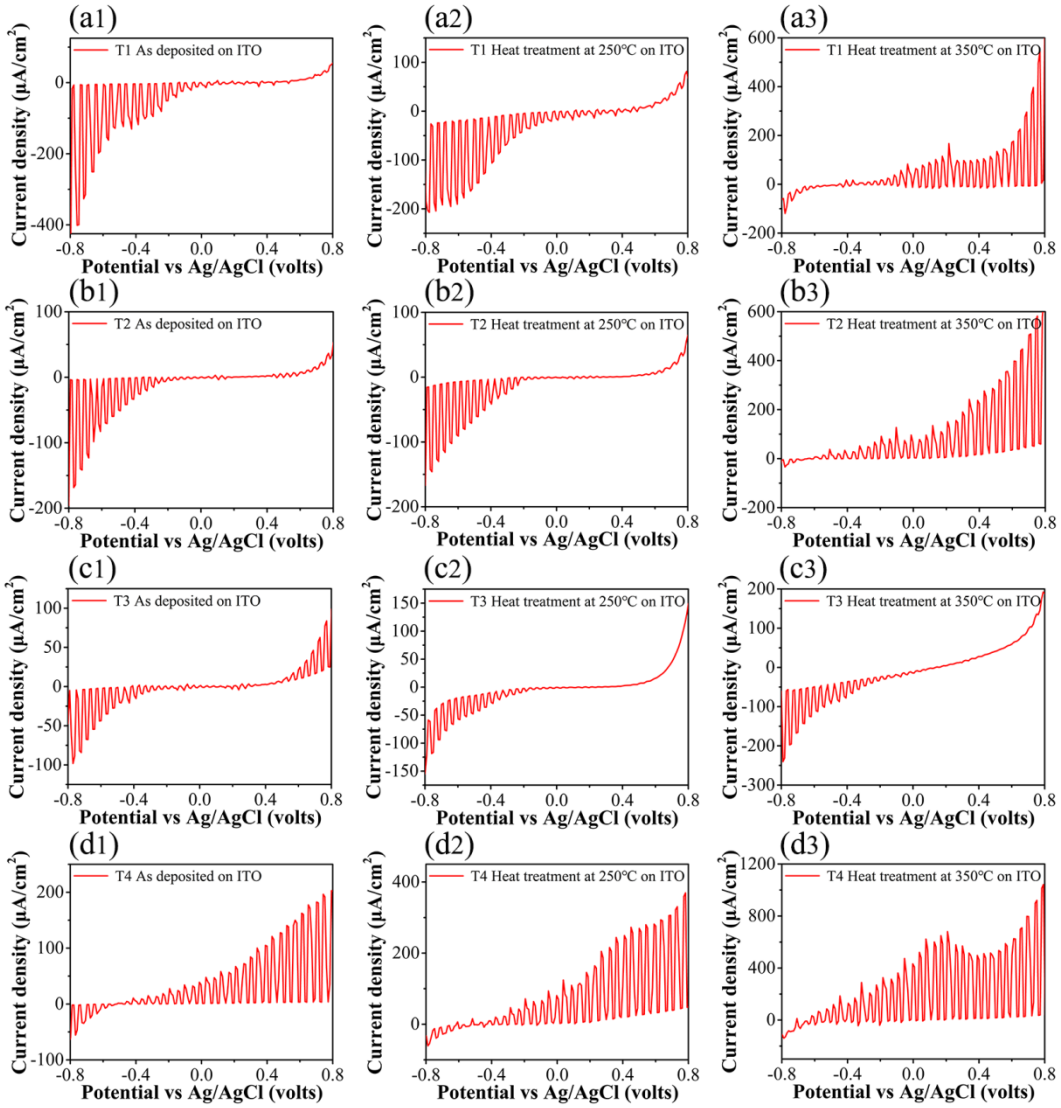

Fig. 4.24 Current density versus voltage curves obtained by using as-deposited and post-annealed Sb_2Se_3-based thin films as working electrodes: a1-a3 for Sb_2Se_3 thin films, b1-b3 for $Sb_2Se_{3.3}$ thin films; c1-c3 for $(Sn_{0.1}Sb_{0.9})_2Se_3$ thin films; d1-d3 for $Sb_2(Se_{0.9}I_{0.1})_3$ thin films

To evaluate the stability and the response speed of the photocurrent, a chronoamperometry measurement has been performed. Fig. 4.23a and 4.23b represent the time-resolved PEC response curves using respectively Sb_2Se_3 crystalline thin film and $Sb_2(Se_{0.9}I_{0.1})_3$ crystalline thin film (heated at 350 ℃) as working electrode. As shown in Fig. 4.23a, when the light is on, the current density rapidly increases from 28 μA/cm^2 (dark condition) to 202 μA/cm^2 (under 25 mW/cm^2 light illumination), and then sharply returns to its initial value as the light is turned off. This light response remains the same after multiple cycles, indicating the excellent reversibility and stability of this Sb_2Se_3 thin film PEC electrode. Then a similar photoresponse can be seen for $Sb_2(Se_{0.9}I_{0.1})_3$ thin film, except with a larger photocurrent density in the latter case (Fig. 4.23b). To extract the exact response time, one of the response periods is magnified,

as shown respectively in Fig. 4.23c and 4.23d. Under closer examination, the response time (τ_{on}) and the recovery time (τ_{off}) of these two working electrodes are 0.03 s. It is worth noting that such a short response time is closely related to the high-quality of the thin film, which is manifested in terms of phase purity, big grain size and absence of visible defects, which is also a prerequisite for the high performance thin film solar cells.

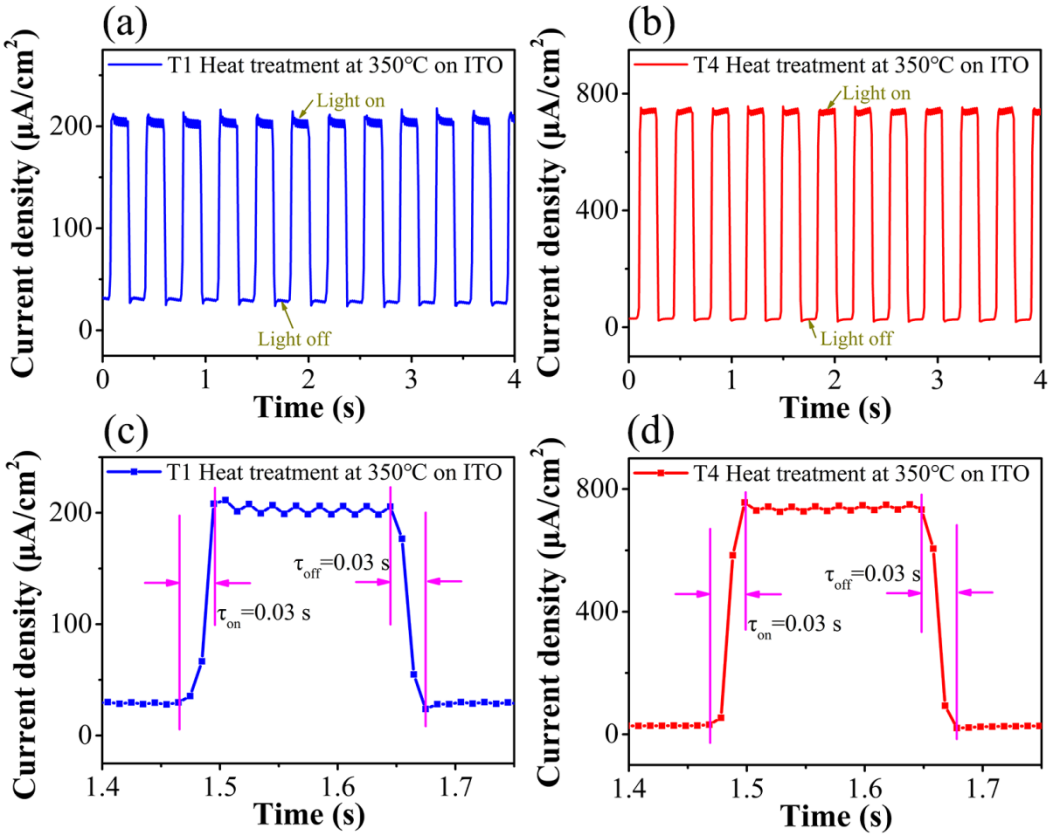

Fig. 4.23 Time-resolved PEC photoresponse by using respectively crystalline Sb_2Se_3 thin film (a) and crystalline $Sb_2(Se_{0.9}I_{0.1})_3$ thin film (b) as working electrode. (c) Magnified plot of one response cycle in (a), and (d) one response cycle in (b), used to obtain the response time and the recovery time

4.3.5 Sb_2Se_3 quasi-homojunction thin film solar cells

Based on the systematic study of Sb_2Se_3-based thin films, we have tried for the first time, to construct a quasi-homojunction Sb_2Se_3 thin film solar cell. The cell structure does not require liquid-phase deposition of buffer layers such as CdS and TiO_2. The whole deposition process can be completed through a full vacuum magnetron sputtering. Moreover, the two thin film layers forming the homojunction have large absorption coefficient, which can effectively improve the solar energy absorption efficiency.

The first solar cell structure is designed to be ITO/$Sb_2(Se_{0.9}I_{0.1})_3$/Sb_2Se_3/Au, in which the

thickness of $Sb_2(Se_{0.9}I_{0.1})_3$ layer is controlled to be 70 nm, and the thickness of Sb_2Se_3 is 400 nm. The thin films were heat treated at 250 ℃ and the device area (2 mm in diameter) was defined by the size of the gold electrodes. An AM 1.5G solar simulator with intensity of 86 mW/cm^2 and a 150 W tungsten halogen lamp with light intensity of 25 mW/cm^2 were used as the light source. Fig. 4.24 shows the corresponding current density-voltage (J-V) curves. The dark current of the device has obvious rectification characteristics, indicating the existence of p-n junction structure at the interface $Sb_2(Se_{0.9}I_{0.1})_3/Sb_2Se_3$. According to the above analysis, the 1st thin film is n-type and the 2nd is p-type. Specifically, under the simulated AM1.5G solar irradiation, the device shows a short-circuit current density (J_{SC}) of 7.62 mA/cm^2, an open circuit voltage (V_{OC}) of 0.28 V, and a fill factor (FF) of 44.06%, thus achieving a power conversion efficiency of 1.09%. As a comparison and also a reference standard for later testing, the same device was illuminated under a 25 mW/cm^2 tungsten halogen lamp, a V_{OC} of 0.30 V and J_{SC} of 15.04 mA/cm^2 have been obtained. The light from the tungsten lamp was delivered onto the solar cells through a flexible optical fiber bundle. The specter of these two light sources is very different. Obviously, the light from the fibred tungsten lamp correspond much better to the response curve of this solar cell.

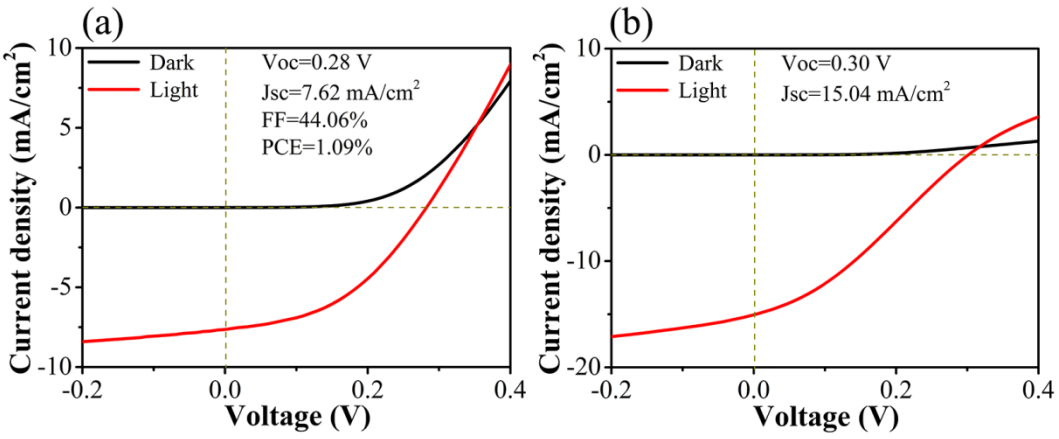

Fig. 4.24 J-V curves of the $Sb_2(Se_{0.9}I_{0.1})_3/Sb_2Se_3$ thin film solar cell: (a) Under simulated AM1.5G illumination with intensity calibrated to 86 mW/cm^2; (b) Under tungsten halogen lamp illumination with light intensity of 25 mW/cm^2

Next, we have studied the effect of heat treatment temperature on the performance of the $Sb_2(Se_{0.9}I_{0.1})_3/Sb_2Se_3$ thin film solar cells. Fig. 4.25 shows the J-V curves of the devices obtained by heat treatment at 235 ℃, 250 ℃ and 265 ℃, respectively. The used light source was tungsten halogen lamp (25 mW/cm^2). It can be seen that when the temperature is low (235 ℃), the J_{SC} is small due to the poor crystalline quality of the thin films. However, if the

temperature is too high, the film density can be negatively affected, especially the very thin n-type layer of $Sb_2(Se_{0.9}I_{0.1})_3$ will become porous, resulting in the decrease of junction quality, thereby reducing the J_{SC} and V_{OC} of the device.

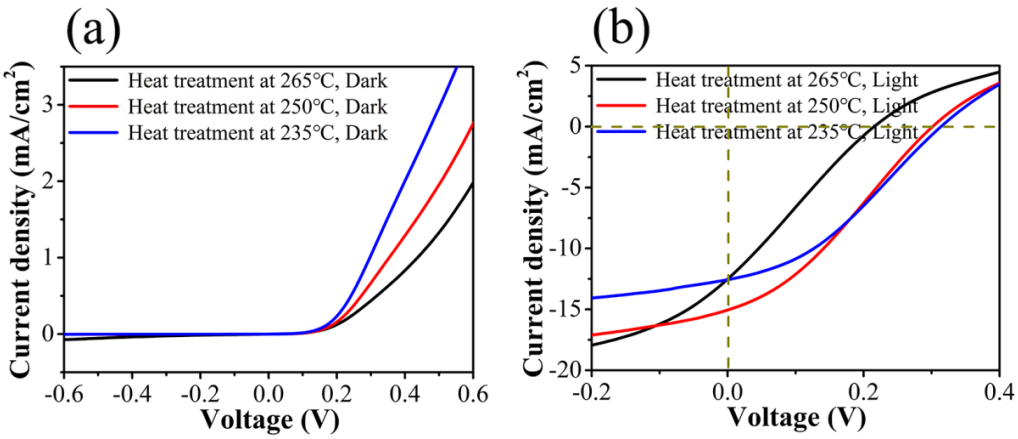

Fig. 4.25 J-V curves of the $Sb_2(Se_{0.9}I_{0.1})_3/Sb_2Se_3$ thin film solar cells with different heat treatment temperatures: (a) In the dark; (b) Under tungsten halogen lamp illumination with light intensity of 25 mW/cm^2

The thickness of the absorbing layer has an important influence on the efficiency of the solar cell, because it needs certain thickness to ensure an effective absorption of sunlight. However, if the film is too thick, the resulting series resistance of the device will be increased, leading to a decrease in power conversion efficiency [27]. For the Sb_2Se_3 quasi-homojunction thin film solar cell, due to the intrinsic high resistivity of Sb_2Se_3, J_{SC} can be significantly reduced with a layer. Therefore, the thickness of the Sb_2Se_3 layer was modified and its influence on the device efficiency was investigated as shown in Fig. 4.26. H is the thickness of the films determined by the optical monitoring system measuring the reflectance, and is approximately 70 nm in this situation. Under the irradiation of 25 mW/cm^2 tungsten halogen lamp, when the thickness of Sb_2Se_3 layer is 3H, 4H and 5H, the obtained J_{SC} is respectively 12.04 mA/cm^2, 21.23 mA/cm^2 and 21.80 mA/cm^2, the V_{OC} is respectively 0.31 V, 0.33 V and 0.28 V. Therefore, for the $Sb_2(Se_{0.9}I_{0.1})_3/Sb_2Se_3$ thin film solar cells, the optimal thickness is 70 nm/280 nm and the heat treatment temperature is 250 ℃. Through the above optimization, the corresponding power conversion efficiency can be improved to about 1.7%, of course measured with a normalized solar simulator.

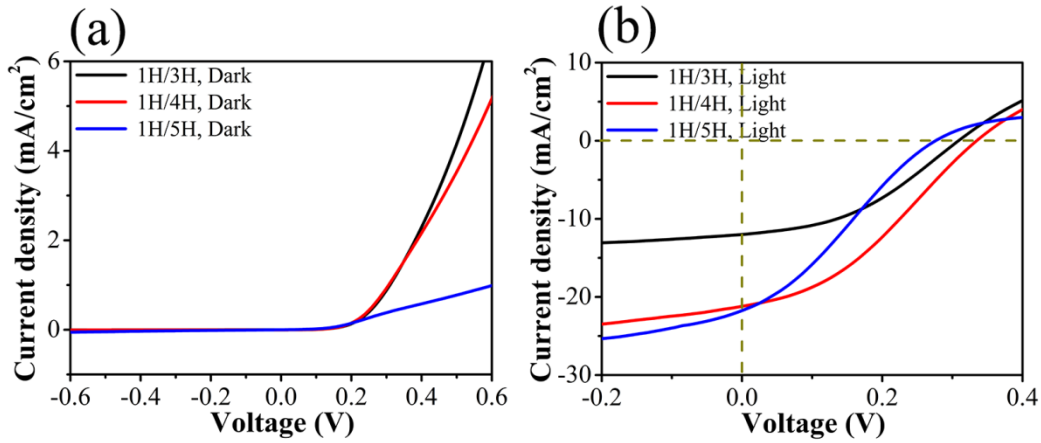

Fig. 4.26 J-V curves of the $Sb_2(Se_{0.9}I_{0.1})_3/Sb_2Se_3$ thin film solar cells with different film thickness: (a) In the dark; (b) Under tungsten halogen lamp illumination with light intensity of 25 mW/cm^2

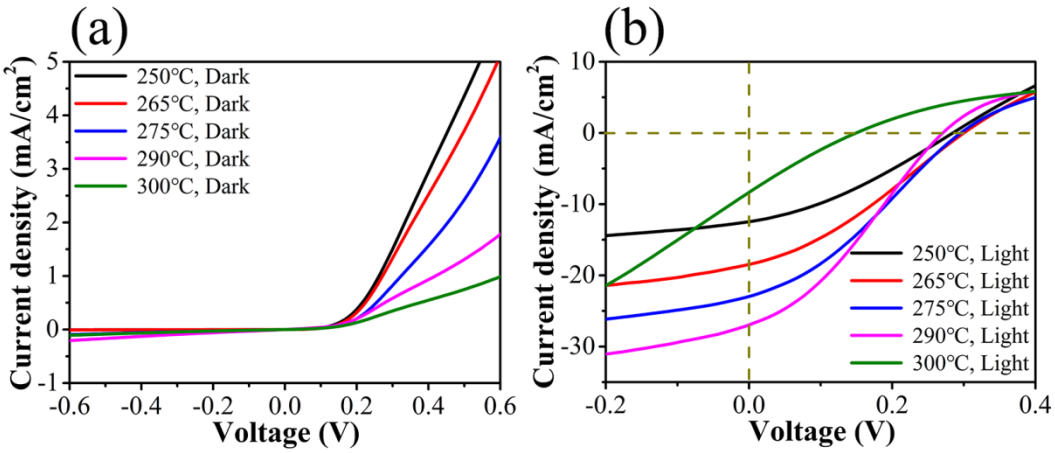

Fig. 4.27 J-V curves of the $Sb_2(Se_{0.9}I_{0.1})_3/Sb_2Se_{3.3}$ thin film solar cells with different heat treatment temperatures: (a) In the dark; (b) Under tungsten halogen lamp illumination with light intensity of 25 mW/cm^2

According to the analysis of the PEC performance of the thin films, the solar cell structure of ITO/$Sb_2(Se_{0.9}I_{0.1})_3/Sb_2Se_{3.3}$/Au was chosen for further investigation. The thin film thickness was kept unchanged at 70 nm/280 nm, while studying the effect of heat treatment temperature on the device performance. Fig. 4.27a demonstrates the existence of p-n junction structure in the quasi-homojunction $Sb_2(Se_{0.9}I_{0.1})_3/Sb_2Se_{3.3}$ thin film solar cells. Fig. 4.27b shows the J-V curves under tungsten halogen lamp illumination. When the heat treatment temperature is increased from 250 ℃ to 290 ℃, the J_{SC} is gradually increased from 12.51 mA/cm^2 to 26.94 mA/cm^2. The V_{OC} shows no obvious variation and is about 0.30 V. If the heat treatment temperature is further increased, the device performance will be significantly reduced. Compared with the $Sb_2(Se_{0.9}I_{0.1})_3/Sb_2Se_3$ thin film solar cells, the biggest advantage of this device structure is that the J_{SC} can be improved by increasing the heat treatment temperature,

and this is consistent with the SEM observation of the thin films, indicating that a dense $Sb_2Se_{3.3}$ crystalline thin film can be obtained at higher heat treatment temperature.

Although the J_{SC} of the $Sb_2(Se_{0.9}I_{0.1})_3/Sb_2Se_{3.3}$ thin film solar cells has been greatly improved with the increase of heat treatment temperature, it is still limited by the high resistivity of the $Sb_2Se_{3.3}$ thin films. The induced high series resistance will limit further improvement of conversion efficiency. In this work, a new concept for solving this issue was tested by constructing the ITO/$Sb_2Se_{3.3}$/$Sb_2(Se_{0.9}I_{0.1})_3$/Au solar cell structure. Thus the n-type $Sb_2(Se_{0.9}I_{0.1})_3$ thin film with higher electrical conductivity can be used as the thicker absorption layer. During the sputtering process, the thickness of the $Sb_2Se_{3.3}$ thin film was maintained at 70 nm (1H), and the thickness of $Sb_2(Se_{0.9}I_{0.1})_3$ was changed while the heat treatment temperature was kept 290 ℃. The J-V curves in the dark indicate the existence of high-quality p-n junction inside the device structure (Fig. 4.28a) with low dark current density. Fig. 4.28b is the J-V curves of the devices under the illumination of 25 mW/cm^2 tungsten halogen lamp. When the thickness of $Sb_2(Se_{0.9}I_{0.1})_3$ thin film is 4H, 5H and 6H, the short-circuit current density J_{SC} is respectively 39.75 mA/cm^2, 47.40 mA/cm^2 and 37.42 mA/cm^2, the open-circuit voltage V_{OC} is respectively 0.39 V, 0.41 V and 0.36 V. Importantly, the obtained J_{SC} is significantly increased, which can be attributed to the higher electrical conductivity of the light absorbing layer of $Sb_2(Se_{0.9}I_{0.1})_3$. Specifically, the series resistance is reduced, the effective collection of photo-generated carriers is increased. The thickness of the light absorbing layer can also be appropriately increased to enhance the light absorption for this solar cell structure. Pulished results demonstrated that interfacial recombination is the main recombination mechanism of Sb_2Se_3-based solar cells, herein, the improvement of V_{OC} may bring a positive effect for the reduction of interface defect density [27,28].

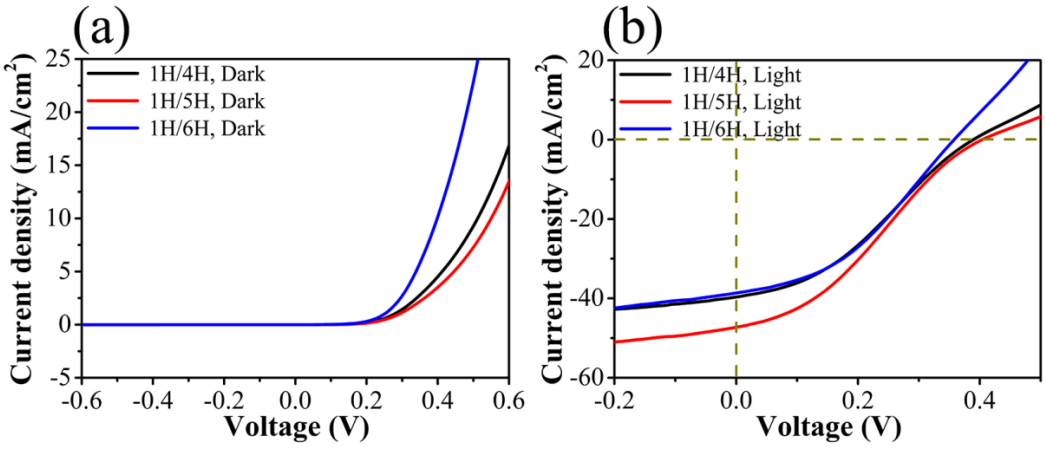

Fig. 4.28 J-V curves of the $Sb_2Se_{3.3}/Sb_2(Se_{0.9}I_{0.1})_3$ thin film solar cells with different film thickness: (a) In the dark; (b) Under tungsten halogen lamp illumination with light intensity of 25 mW/cm^2

Finally, the optimal device, namely ITO/$Sb_2Se_{3.3}$ (1H)/$Sb_2(Se_{0.9}I_{0.1})_3$ (5H)/Au thin film solar cells has been chosen for efficiency measurements, the results are shown in Fig. 4.29. The J-V curves were obtained under simulated AM 1.5G (86 mW/cm^2) solar illumination, no obvious hysteresis between forward (J_{SC} to V_{OC}) and reverse (V_{OC} to J_{SC}) scans was observed in our device (Fig. 4.29a). This hysteresis-free behavior can be attributed to the high-quality thin film materials and device structure [9]. The device has a J_{SC} of 17.82 mA/cm^2, V_{OC} of 0.32 V, and FF of 37.88%, resulting in a power conversion efficiency of 2.65%. According to the literatures, the highest conversion efficiency of the currently reported Sb_2Se_3 thin film solar cell is 6.84% [29], and its device structure is FTO/CdS/Sb_2Se_3/CZ-TA (hole transport layer)/Au, the corresponding J_{SC} of 28.4 mA/cm^2, V_{OC} of 0.42 mV and FF of 57.1% were obtained under AM 1.5G (100 mW/cm^2) illumination. Our preliminary results on quasi-homojunction thin film solar cells are highly encouraging, with the quasi-homojunction structure, which certainly need to be optimized. Fig. 4.29b shows the external quantum efficiency (EQE) curve of the device. The EQE value is lower than 50% over the whole working spectrum, indicating the existence of abundant interface defects in the $Sb_2Se_{3.3}$/$Sb_2(Se_{0.9}I_{0.1})_3$ thin films, resulting in severe recombination loss of the photo-generated carriers. The EQE can also be further improved by surface passivation and the improvement of the internal junction quality [10,30]. Moreover, compared to the state-of-art Sb_2Se_3 thin film solar cells, our quasi-homojunction solar cells have significantly higher EQE in the short wavelength range due to the absence of parasitic absorption of those buffer layers [11,16]. In summary, although the research on Sb_2Se_3 quasi-homojunction thin film solar cells has just been started, it has already an interesting power conversion efficiency.

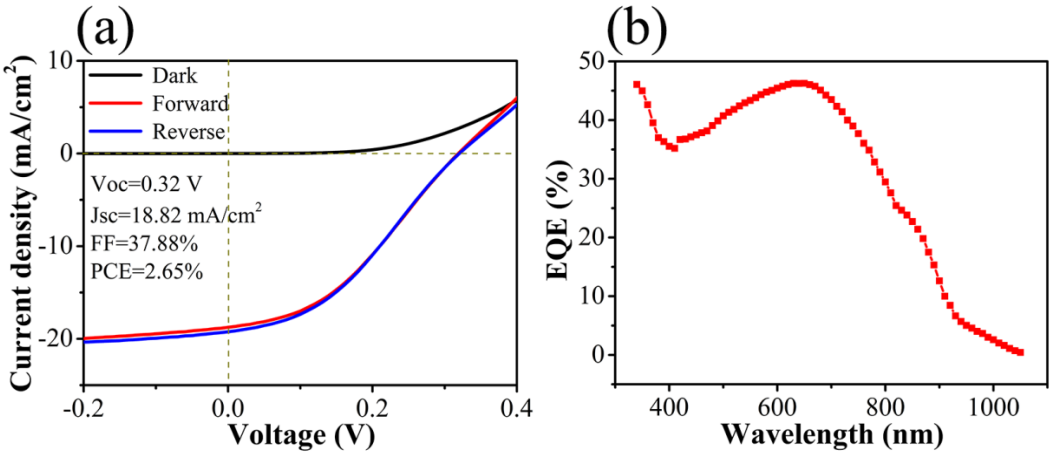

Fig. 4.29 Forward and reversed J-V curves of the $Sb_2Se_{3.3}$/$Sb_2(Se_{0.9}I_{0.1})_3$ thin film solar cell performance in the dark and under 86 mW/cm^2 simulated AM1.5G solar irradiation; (b) External quantum efficiency

4.4 Conclusions

In this chapter, four Sb_2Se_3-based targets with the chemical composition of Sb_2Se_3, $Sb_2Se_{3.3}$, $(Sn_{0.1}Sb_{0.9})_2Se_3$ and $Sb_2(Se_{0.9}I_{0.1})_3$ were successfully prepared by using the high-temperature melting. Then the corresponding thin films were deposited by using RF magnetron sputtering. The as-deposited thin film showed amorphous nature and after a heat treatment at a certain temperature, highly crystallized thin films composed of large crystal grains were obtained. The optical properties of the thin films were systematically investigated. The crystallinity and the roughness of the films were the main factors that affecting their quality. The band gap of the Sb_2Se_3 amorphous thin film was measured to be 1.64 eV, then turned to 1.28 eV for the crystalline thin film probably due to the loss of Se during the heated treatment. The band gap can be tuned by modifying the stoichiometry of the film or through doping by Sn for example. The heat treatment temperature can determine the p/n type of the Sb_2Se_3 and $Sb_2Se_{3.3}$ thin films with a transformation from p type to n type with increasing temperature. Differently, all the $(Sn_{0.1}Sb_{0.9})_2Se_3$ thin films were p type and all the $Sb_2(Se_{0.9}I_{0.1})_3$ thin films were n type. The PEC measurements indicated that the Sb_2Se_3-based thin films showed long-term stability. Accordingly, a novel quasi-homojunction Sb_2Se_3 based thin film solar cell was firstly fabricated. The existence of p-n junction inside the device structure has been demonstrated. The thickness and the heat treatment temperature of the films have a critical influence on the device performance. Preliminary results show a highly encouraging power conversion efficiency of 2.65% for our device, demonstrating the great potential these thin film solar cells.

4.5 References

[1] Jackson, P.; Wuerz, R.; Hariskos, D.; Lotter, E.; Witte, W.; Powalla, M., Effects of heavy alkali elements in Cu(In,Ga)Se_2 solar cells with efficiencies up to 22.6%. physica status solidi (RRL) - Rapid Research Letters 2016, 10 (8), 583-586.

[2] Green, M. A.; Hishikawa, Y.; Warta, W.; Dunlop, E. D.; Levi, D. H.; Hohl-Ebinger, J.; Ho-Baillie, A. W. H., Solar cell efficiency tables (version 50). Progress in Photovoltaics: Research and Applications 2017, 25 (7), 668-676.

[3] Lamb, D. A.; Underwood, C. I.; Barrioz, V.; Gwilliam, R.; Hall, J.; Baker, M. A.; Irvine, S. J. C., Proton irradiation of CdTe thin film photovoltaics deposited on cerium-doped space glass. Progress in Photovoltaics 2017, 25 (12), 1059-1067.

[4] https://en.wikipedia.org/wiki/Solar_cell_efficiency.

[5] Zeng, K.; Xue, D. J.; Tang, J., Antimony selenide thin-film solar cells. Semiconductor

Science and Technology 2016, 31 (6).

[6] Zhou, Y.; Leng, M. Y.; Xia, Z.; Zhong, J.; Song, H. B.; Liu, X. S.; Yang, B.; Zhang, J. P.; Chen, J.; Zhou, K. H.; Han, J. B.; Cheng, Y. B.; Tang, J., Solution-Processed Antimony Selenide Heterojunction Solar Cells. Advanced Energy Materials 2014, 4 (8).

[7] Xia, Z.; Zhong, J.; Leng, M.; Hu, L.; Xue, D. J.; Yang, B.; Zhou, Y.; Liu, X.; Qin, S.; Cheng, Y. B.; Tang, J., Generalized Water-Processed Metal Chalcogenide Complexes: Synthesis and Applications. Chemistry of Materials 2015, 27 (23), 8048-8057.

[8] Luo, M.; Leng, M. Y.; Liu, X. S.; Chen, J.; Chen, C.; Qin, S. K.; Tang, J., Thermal evaporation and characterization of superstrate CdS/Sb_2Se_3 solar cells. Applied Physics Letters 2014, 104 (17).

[9] Leng, M. Y.; Luo, M.; Chen, C.; Qin, S. K.; Chen, J.; Zhong, J.; Tang, J., Selenization of Sb_2Se_3 absorber layer: An efficient step to improve device performance of CdS/Sb_2Se_3 solar cells. Applied Physics Letters 2014, 105 (8).

[10] Liang, G. X.; Zheng, Z. H.; Fan, P.; Luo, J. T.; Hu, J. G.; Zhang, X. H.; Ma, H. L.; Fan, B.; Luo, Z. K.; Zhang, D. P., Thermally induced structural evolution and performance of Sb_2Se_3 films and nanorods prepared by an easy sputtering method. Solar Energy Materials and Solar Cells 2018, 174, 263-270.

[11] Zhou, Y.; Wang, L.; Chen, S. Y.; Qin, S. K.; Liu, X. S.; Chen, J.; Xue, D. J.; Luo, M.; Cao, Y. Z.; Cheng, Y. B.; Sargent, E. H.; Tang, J., Thin-film Sb_2Se_3 photovoltaics with oriented one-dimensional ribbons and benign grain boundaries. Nature Photonics 2015, 9 (6), 409-415.

[12] http://www.directvacuum.com/pdf/what_is_sputtering.pdf

[13] Fumagalli, F.; Mart ŕRujas, J.; Di Fonzo, F., Room temperature deposition of high figure of merit Al-doped zinc oxide by pulsed-direct current magnetron sputtering: Influence of energetic negative ion bombardment on film's optoelectronic properties. Thin Solid Films 2014, 569, 44-51.

[14] Zhang, X. H.; Korolkov, I.; Fan, B.; Cathelinaud, M.; Ma, H. L.; Adam, J. L.; Merdrignac, O.; Calvez, L.; Lhermite, H.; Le Brizoual, L.; Pasquinelli, M.; Simon, J. J., Chalcogenide glass-ceramic with self-organized heterojunctions: application to photovoltaic solar cells. Epj Photovoltaics 2018, 9.

[15] Meese, W. J.; Lu, T. M., Scaling behavior of columnar structure during physical vapor deposition. Journal of Applied Physics 2018, 123 (7), 075302.

[16] Wang, L.; Li, D.-B.; Li, K.; Chen, C.; Deng, H.-X.; Gao, L.; Zhao, Y.; Jiang, F.; Li, L.; Huang, F.; He, Y.; Song, H.; Niu, G.; Tang, J., Stable 6%-efficient Sb_2Se_3 solar cells with a ZnO buffer layer. Nature Energy 2017, 2, 17046.

[17] Choi, B. G.; Kim, I. H.; Kim, D. H.; Lee, K. S.; Lee, T. S.; Cheong, B.; Baik, Y. J.; Kim, W. M., Electrical, optical and structural properties of transparent and conducting ZnO thin films doped with Al and F by rf magnetron sputter. Journal of the European Ceramic Society 2005, 25 (12), 2161-2165.

[18] http://cdmd.cnki.com.cn/Article/CDMD-10335-1017040361.htm

[19] Sanjay, P.; Deepa, K.; Madhavan, J.; Senthil, S., Optical, spectral and photovoltaic characterization of natural dyes extracted from leaves of Peltophorum pterocarpum and Acalypha amentacea used as sensitizers for ZnO based dye sensitized solar cells. Optical Materials 2018, 83, 192-199.

[20] Zhang, X. H.; Xu, Y.; Shen, Q. H.; Fan, B.; Qiao, X. S.; Fan, X. P.; Yang, H.; Luo, Q.; Calvez, L.; Ma, H. L.; Cathelinaud, M.; Simond, J. J., Enhancement of charge photo-generation and transport via an internal network of Sb_2Se_3/Cu_2GeSe_3 heterojunctions. Journal of Materials Chemistry A 2014, 2 (40), 17099-17106.

[21] Li, X.; Rao, F.; Song, Z.; Ren, K.; Liu, W.; Sun, Z., Experimental and theoretical study of silicon-doped Sb_2Te_3 thin films: Structure and phase stability. Applied Surface Science 2011, 257 (10), 4566-4568.

[22] Chia Tan, C.; Shi, L.; Zhao, R.; Guo, Q.; Li, Y.; Yang, Y.; Chong Chong, T.; Malen, J. A.; Ong, W.-L.; Schlesinger, T. E.; Bain, J. A., Compositionally matched nitrogen-doped $Ge_2Sb_2Te_5/Ge_2Sb_2Te_5$ superlattice-like structures for phase change random access memory. Applied Physics Letters 2013, 103 (13), 133507.

[23] Boonlakhorn, J.; Thongbai, P.; Putasaeng, B.; Yamwong, T.; Maensiri, S., Very high-performance dielectric properties of $Ca_{1-3x}/2Yb_xCu_3Ti_4O_{12}$ ceramics. Journal of Alloys and Compounds 2014, 612, 103-109.

[24] Ye, M.; Sun, Q.; Chen, X.; Jiang, Z.; Wang, F., Effect of Nb doping on preferential orientation, phase transformation behavior and electrical properties of $PbZrO_3$ thin films. Journal of Alloys and Compounds 2012, 541, 99-103.

[25] Abdolahzadeh Ziabari, A.; Ghodsi, F. E., Influence of Cu doping and post-heat treatment on the microstructure, optical properties and photoluminescence features of sol–gel derived nanostructured CdS thin films. Journal of Luminescence 2013, 141, 121-129.

[26] Walsh, A.; Da Silva, J. L. F.; Wei, S. H., Origins of band-gap renormalization in degenerately doped semiconductors. Physical Review B 2008, 78 (7).

[27] Liu, X. S.; Chen, C.; Wang, L.; Zhong, J.; Luo, M.; Chen, J.; Xue, D. J.; Li, D. B.; Zhou, Y.; Tang, J., Improving the performance of Sb_2Se_3 thin film solar cells over 4% by controlled addition of oxygen during film deposition. Progress in Photovoltaics 2015, 23 (12), 1828-

1836.

[28] Liu, X.; Xiao, X.; Yang, Y.; Xue, D. J.; Li, D. B.; Chen, C.; Lu, S.; Gao, L.; He, Y.; Beard, M. C.; Wang, G.; Chen, S.; Tang, J., Enhanced Sb_2Se_3 solar cell performance through theory-guided defect control. Progress in Photovoltaics: Research and Applications 2017.

[29] Li, D. B.; Yin, X.; Grice, C. R.; Guan, L.; Song, Z.; Wang, C.; Chen, C.; Li, K.; Cimaroli, A. J.; Awni, R. A.; Zhao, D.; Song, H.; Tang, W.; Yan, Y.; Tang, J., Stable and efficient CdS/Sb_2Se_3 solar cells prepared by scalable close space sublimation. Nano Energy 2018, 49, 346-353.

[30] Xue, D. J.; Liu, S. C.; Dai, C. M.; Chen, S.; He, C.; Zhao, L.; Hu, J. S.; Wan, L. J., GeSe Thin-Film Solar Cells Fabricated by Self-Regulated Rapid Thermal Sublimation. Journal of the American Chemical Society 2017, 139 (2), 958-965.

CHAPTER V: SYNTHESIS OF γ-IN2SE3 NANOFLOWERS FOR HIGH PERFORMANCE γ-IN2SE3/SI HETEROJUNCTION PHOTODIODE

5.1 Introduction

The III–VI binary semiconductors have drawn tremendous research attention in recent years due to their highly interesting electrical and optical properties as well as their potential applications in electronic and optoelectronic devices. Various types of high-performance devices, such as solar cells, photodetectors, and transistors have been reported [1-5]. Among these semiconductors, indium selenide is an important layered semiconductor with an optimum direct band gap, efficient visible-light absorption and phase-change memory effect. These properties make it a promising candidate for various important applications in diverse areas such as solar energy conversion, thermoelectric power generation, random access memories, photodetectors and optoelectronics in the visible region [6-10].

Owing to the mismatch of valence electron numbers, indium selenides contain various complex compounds with different stoichiometric ratios, such as InSe, In_2Se_3, In_3Se_4, In_4Se_3 and In_6Se_7 [11]. With the same stoichiometric ratio, different phases and crystal structures may coexist, such as, α, β, γ, κ and δ phases in the case of In_2Se_3 [11,12]. In_2Se_3 has emerged as one of the most promising materials for visible photodetection due to its direct and narrow band gap, high absorption coefficient in the visible range, and high sensitivity [3,4,6,13]. Despite their huge potential, the difficulties associated to the solution based synthesis of single phase indium selenide nanomaterials cannot be ignored because various indium selenides can thermodynamically coexist in the same reaction system [14]. Up to now, several In_2Se_3 nanostructures with different morphologies have been synthesized using ambient pressure and also hydrothermal/solvothermal methods. Li et al. presented an ambient pressure organic solution phase synthesis of amorphous In_2Se_3 nanoparticles, flower-like shaped β-In_2Se_3 nanocrystals, and two-dimensional β-In_2Se_3 nanosheets [15]. Wei et al. reported the synthesis of porous γ-In_2Se_3 tetragons with a two-step hydrothermal process [10]. Shi et al. demonstrated the solvothermal synthesis of α-In_2Se_3 flowerlike nanostructures assembled by nanosheets in oleic acid [16]. Colloidal synthesis, due to its ambient pressure condition and open operation system, is a safe, facile and scalable preparation method [17,18]. However, the synthesis of In_2Se_3 by colloidal routes is rarely reported. In this work, we report an effective colloidal process involving hot-injection method for the synthesis of high-quality flowerlike γ-In_2Se_3 nanostructures consisted of two-dimensional (2D) nanosheets.

Silicon is a versatility substrate for optoelectronic applications, and combining In_2Se_3 with the mature Si technology will open up a new and feasible scenario for the development of

innovative optoelectronic device such as high performance photodetectors. The state-of-the-art photodetection technology is focused on multispectral (broadband or dual band) photodetectors for various applications, such as discrimination of objects, imaging under varying atmospheric conditions, sensing and optical communications [19,20]. However, most of the high performance broadband photodetectors do not perform zero bias operation, which therefore makes them mostly uneconomical in the modern day scenario [20,21]. Herein, for the first time, we present an efficient heterojunction photodiode formed by γ-In_2Se_3 nanoflower film and Si substrate, which is self-powered and demonstrates a remarkable responsivity and detectivity in a wide range of wavelengths.

5.2 Experimental section

5.2.1 Raw materials

Indium chloride (Aladdin, 99.9%), Selenium dioxide (Aladdin, 99%), 1-Hexadecylamine (Aladdin, 90%), 1-Octadecene (Aladdin, 90%) and Oleic acid (Aladdin, AR). Chloroform and Isopropyl alcohol were used for the synthesis without further purification.

5.2.2 Synthesis of γ-In_2Se_3 nanoflowers

For the synthesis of γ-In_2Se_3 nanoflowers, at first, 8 mmol selenium dioxide and 10 ml 1-octadecene were added into a 25 mL three-neck flask and heated up to 200 ℃ for several hours with continous stirring under argon atmosphere until the selenium dioxide was completely dissolved, forming a 0.8 M selenium precursor solution. To prepare indium precursor solution, 1 mmol indium chloride, 8 mmol 1-hexadecylamine, 15 ml 1-octadecene, and 6 ml oleic acid were degassed at room temperature and then heated at 220 ℃ for 30 min, forming a transparent yellow solution. Subsequently, 8 ml 0.8 M selenium precursor solution was rapidly injected into the yellow indium precursor solution which was heated up to 240 ℃ beforehand. The mixture was stirred for 10 min and then cooled down to room temperature. The obtained solid γ-In_2Se_3 nanoflowers were collected by centrifugation, washed with chloroform and isopropyl alcohol for several times, and finally dried at 60 ℃ under vacuum.

5.2.3 Fabrication of the γ-In_2Se_3/Si heterojunction photodiode

The as-synthesized γ-In_2Se_3 nanoflowers were repeatedly purified by washing and then ultrasonically dispersed in chloroform. The γ-In_2Se_3 film was formed by spin-coating the

dispersion solution on a pre-cleaned square Si window (500 μm × 500 μm, which was exposed from SiO_2/Si substrate by lithography). To perform the photocurrent measurements, the γ-In_2Se_3 nanoflower film was dried by vacuum-annealing at 40 ℃ for 30 min and it fully covered the Si window. The top electrode Cr/Au (5 nm/60 nm) was prepared by lithography and e-beam evaporation with a lift-off process. In:Ga was pasted on the Si substrate as back electrode to form Ohmic contact with n-Si.

5.2.4 Characterization

X-ray diffraction (XRD) analysis was carried out on PANalytical B.V. Empyrean 200895 x-ray diffractometer with Cu Kα radiation (λ = 1.54 Å) at a scan speed of 2.00 deg/min. A Hitachi S-4800 field emission scanning electron microscope (SEM) was used to observe the morphology of the γ-In_2Se_3 nanoflowers. Transmission electron microscopy (TEM) and selected area electron diffraction (SAED) images were obtained from a FEI Tecnai G2F20 field emission transmission electron microscope operating at an acceleration voltage of 200 kV. Samples were prepared by placing a drop of a dilute chloroform dispersion of the nanoflowers on the surface of a copper grid. Energy dispersive spectroscopy (EDS) analysis has been performed with an EDAX instrument. The optical absorption spectra of the γ-In_2Se_3 nanoflowers were taken from a SHIMADZU UV-3150 spectrophotometer and the valence band was analyzed by x-ray photoelectron spectroscopy (XPS, ESCALAB). The photoresponse performance of the γ-In_2Se_3/Si heterojunction photodiode was recorded using a Keithley 2450 SCS and SUSS PM8 probe station in a clean and shielded box at room temperature. A xenon lamp equipped with a monochromator was used as the light source for the photocurrent measurements. To investigate the time-resolved photoresponse characteristics, a 808 nm laser source with controllable light intensities was used.

5.3 Results and discussion

5.3.1 Preparation and characterization of γ-In_2Se_3 nanoflowers

Fig. 5.1a shows the XRD pattern of the as-synthesized γ-In_2Se_3 nanoflowers, which exhibits prominent peaks in agreement with the JCPDS standard card (89-0658) of the hexagonal structure and γ crystalline phase of In_2Se_3 without any second phase, indicating the absence of any detectable impurity such as InSe, In_3Se_4, In_4Se_3 or Se. The SEM image (Fig. 5.1b) shows the flowerlike microspheres with narrow-distributed diameter in the range of 0.8-1.2 μm. Those flowerlike microspheres are built of 2D nanosheets (with thickness of about 20 nm)

connected with each other to form the hierarchical 3-dimensional (3D) nanoflowers. Fig. 5.1c presents the TEM image of an isolated nanoflower with a diameter of 1.2 μm. From the selected area electron diffraction (SAED) pattern (inset in Fig. 5.1c), a microsphere is indexed as a polycrystalline structure, which can be attributed to the different orientation of the nanosheets.

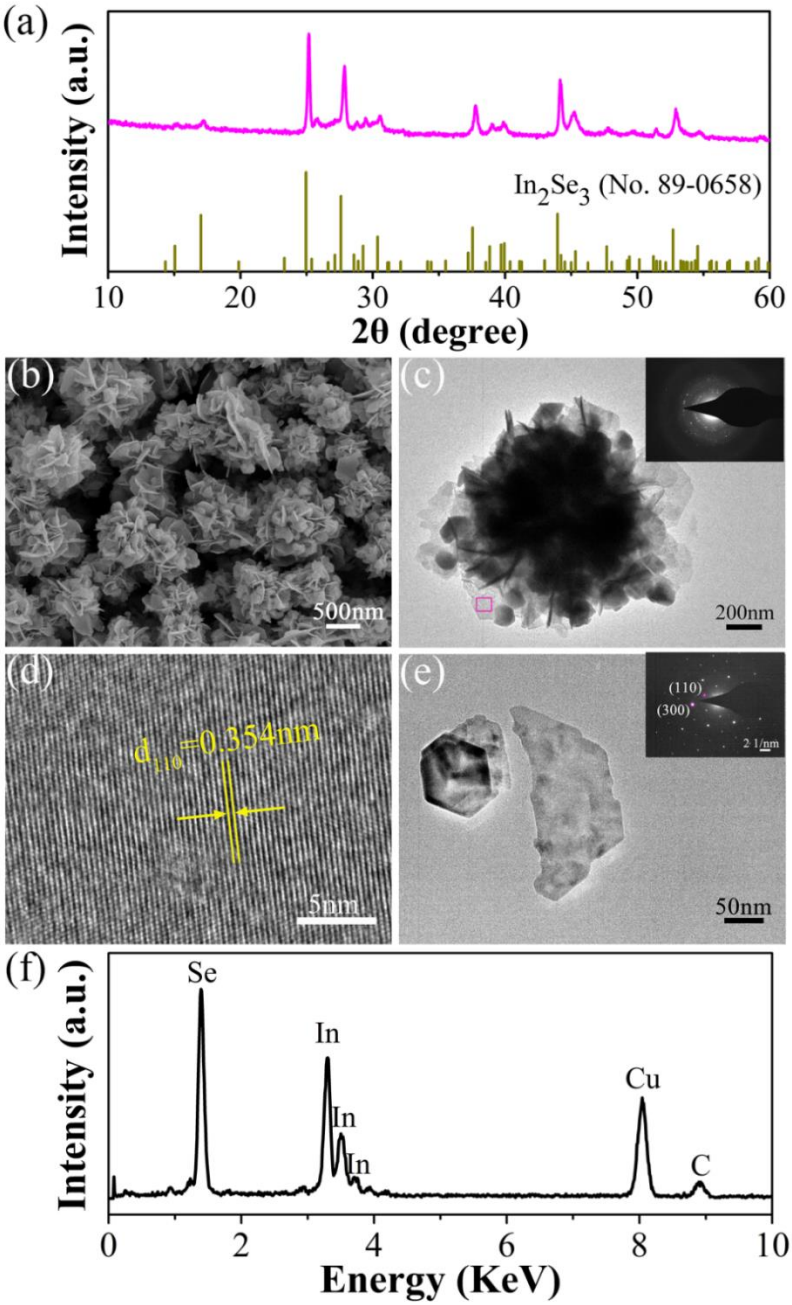

Fig. 5.1 Crystalline phase and morphological characterization of the γ-In_2Se_3 nanoflowers: (a) XRD pattern. (b) SEM image. (c) TEM image, the inset shows the corresponding SAED pattern. (d) HRTEM image from the pink marked area in (c). (e) TEM image of separated nanosheets from the nanoflower, the inset shows the SAED pattern of the right single nanosheet in (e). (f) EDX spectrum

The high-resolution TEM (HRTEM) image reveals highly crystalline nature of the nanosheets associated with the (110) crystalline plane of γ-In_2Se_3 (d-spacing of 0.354 nm) (Fig. 5.1d). Fig. 5.1e shows the TEM image of several typical nanosheets separated from the nanoflowers. The corresponding SAED pattern (inset in Fig. 5.1e) provides additional insight into the structure of the hexagonal γ-In_2Se_3, which is consistent with the results displayed in the XRD pattern. EDS (Fig. 5.1f) of a single nanoflower exhibits strong In and Se peaks, where the atomic ratio of In and Se is close to the 2:3 stoichiometry, as expected.

To reveal the growth process of the flowerlike structure in more detail, time-dependent and temperature-dependent experiments were performed and the corresponding products were examined by SEM. In this work, the synthesis involes the injection of selenium precursor into the indium precursor solution. Immediately after the injection, the color of the mixed solution turned from yellow to brown, indicating the formation of In_2Se_3 species. Serial aliquots were taken at 10 s intervals for monitoring the kinetics of nanoflower formation, and the resulting solid products were purified and observed with SEM, as shown in Fig. 5.2. In the initial stage, depicted in Fig. 5.2a (1 s), the sample is consisted of many nanosheets with relatively small size, and the nanosheets are not planar sheets but helicoids. By increasing the reaction time, the size and thickness of the nanosheets increased simultaneously. At this stage, the nanosheets are connected with each other to form the hierarchical 3D flowerlike nanostructures. Finally, homogeneous nanoflowers with diameters of ~600 nm are obtained after 30 s reaction (Fig. 5.2d). Then compared to other solution phase synthesis of flowerlike In_2Se_3 nanostructures, the most interesting feature of this method is that the reaction time can be less than 30 s for obtaining uniform products. This feature has a close relationship with the nucleation process and the growth kinetics. The detailed working mechanism of the hot-injection method has been discussed in Chapter II.

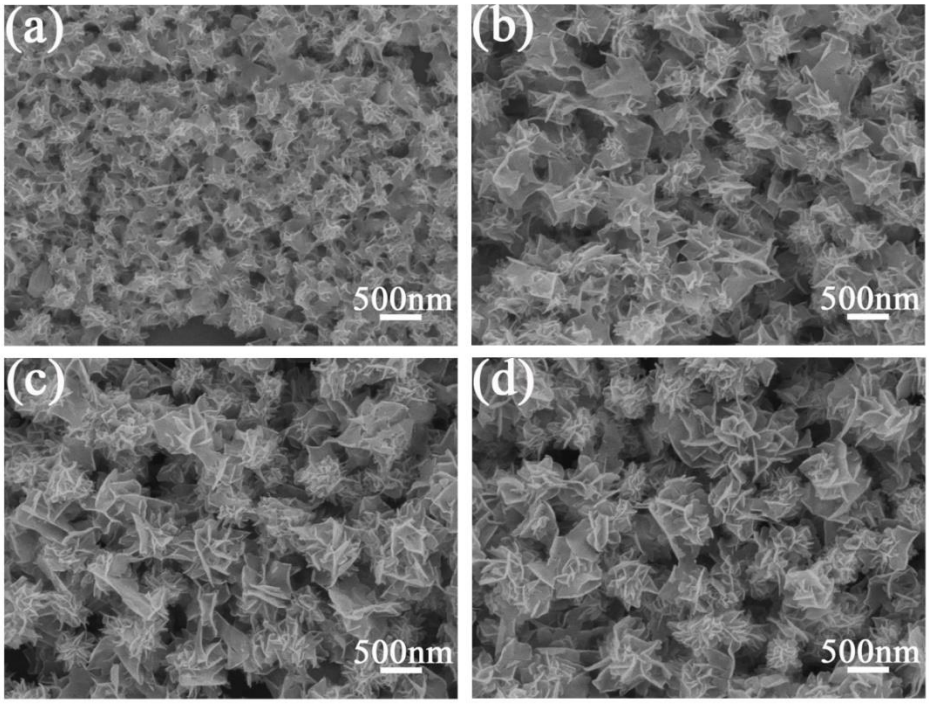

Fig. 5.2 SEM images of theγ-In_2Se_3 nanoflowers synthesized at 240 ℃ with different reaction time: (a) 1 s; (b) 10 s; (c) 20 s and (d) 30 s

The temperature-dependent studies for the formation of γ-In_2Se_3 nanoflowers were also carried out by XRD and SEM analysis (Fig. 5.3). Fig. 5.3a is the XRD patterns of the products collected at the temperature of 180 ℃, 210 ℃, 270 ℃ for 10 min respectively. Fig. 5.3b shows the SEM image of the sample synthesized at 180 ℃, and many flowerlike microspheres with thinner nanosheets can be seen. The corresponding XRD pattern with lower diffraction intensity indicates that the crystallinity is comparatively poor at this temperature. Then the diffraction peaks intensity of the hexagonal γ-In_2Se_3 gets stronger with increasing temperature, indicating a better crystallinity. At 210 ℃, the nucleation and growth rate were accelerated compared to the synthesis at 180 ℃ and the well-known Ostwald ripening leads to the appearance of flowerlike products with thicker nanosheets (Fig. 5.3c). It has been reported that the driving force for the formation of sheet-like shape could be derived from the inherent crystal structure of In_2Se_3. And the rate of In_2Se_3 crystal growth along the top–bottom crystalline plane should be much faster than that along the c-axis [16]. With temperature rises, solution medium met the thermodynamic and kinetic condition for preferential 2D growth. Then the flower-like shaped microspheres are formed by aggregating the 2D nanosheets with different oriented directions. However, with the temperature rises to 270 ℃, the nucleation occurs too rapidly due to the high temperature, and the precursor concentration is consumed with then decreased crystal growth rate, which inhibits the

preferential 2D growth, resulting in the formation of ellipsoid-like nanosheets (Fig. 5.3d).

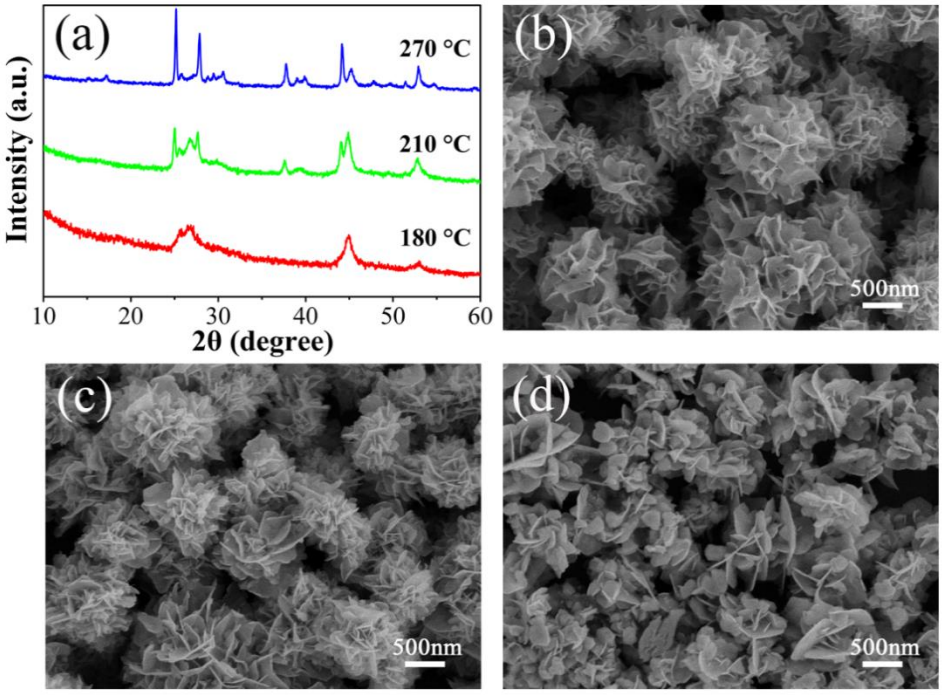

Fig. 5.3 (a) XRD patterns of the γ-In_2Se_3 nanoflowers synthesized for 10 min at different temperatures. SEM images of the γ-In_2Se_3 nanoflowers synthesized for 10 min at (b) 180 ℃, (c) 210 ℃, and (d) 270 ℃

To reveal the growth process of the flowerlike nanostructures more in detail and to further understand the preferential 2D growth, a series of intermediate products were collected during the heating-up process after the precursor injection at 180 ℃. The SEM images of the products are shown in Fig. 5.4. Different from the reaction at 240 ℃, in the initial stage, no obvious color change was observed of the mixed solution within 2 min due to the low temperature after injection. Fig. 5.4a shows that the obtained products are sphere-shaped particles with an average diameter of about 500 nm after 2 min reaction. Then some irregular nanosheets appear on the surface of the spheres (Fig. 5.4b). By increasing the reaction time, the flower-like nanostructure is formed and it coexists with the spheres, showing a favorable solution condition for preferential 2D growth. Then the continuous growth of γ-In_2Se_3 and the continuous depletion of the spheres as sacrificial template lead finally to the formation of complete flowerlike γ-In_2Se_3 nanostructures. In this stage with higher temperatures, the thermodynamic and kinetic condition for preferential 2D growth is further enhanced for extending selective epitaxial growth, leading to increased diameter of the nanoflowers and to slightly thicker nanosheets. Finally, as shown in Fig. 5.4f, nearly no original sphere can be

observed, and the as-synthesized flowerlike nanostructures become more uniform in cluster size with average diameter of 800 nm.

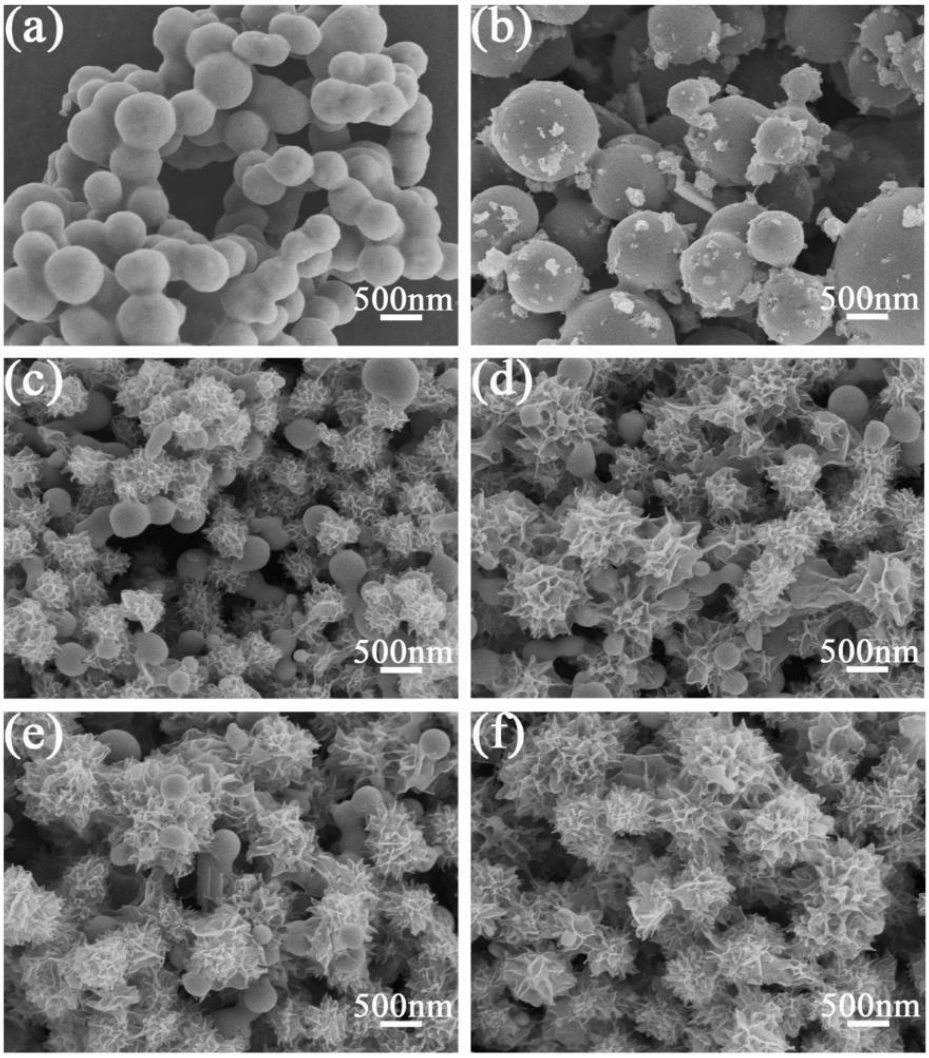

Fig. 5.4 SEM images of the γ-In_2Se_3 crystals synthesized at 180 ℃ for (a) 2.0 min, (b) 2.5 min, (c) 3.0 min, (d) 3.5 min, (e) 4.0 min, and (f) 4.5 min

5.3.2 Performance of the γ-In_2Se_3/Si heterojunction photodiode

In this work, optical absorption spectrum has also been employed to investigate the optical properties of the as-synthesized γ-In_2Se_3 nanoflowers. Herein, the absorption (α/Λ) is calculated from the reflectance data using Kubelka-Munk equations: $F(R)=\alpha/\Lambda=(1-R)^2/(2R)$, where R is the reflectance, α and Λ are the absorption and scattering coefficients, respectively [22]. As shown in Fig. 5.5a, the onset of the absorption of γ-In_2Se_3 starts from about 900 nm. A plot of $[F(R)hv]^2$ versus energy (hv) yields a direct band gap of 1.78 eV (inset in Fig. 5.5a), which is very close to the reported value (1.8 eV) of γ-In_2Se_3 [23]. The valence band of γ-

In_2Se_3 film was measured by XPS (Fig. 5.5b), using a linear extrapolation method to determine the valence band maximum, which is about 0.46 eV. Considering the band gap obtained from the optical absorption spectrum, the γ-In_2Se_3 film shows p-type photoconductive characteristics, which is consistent with the previous results [24].

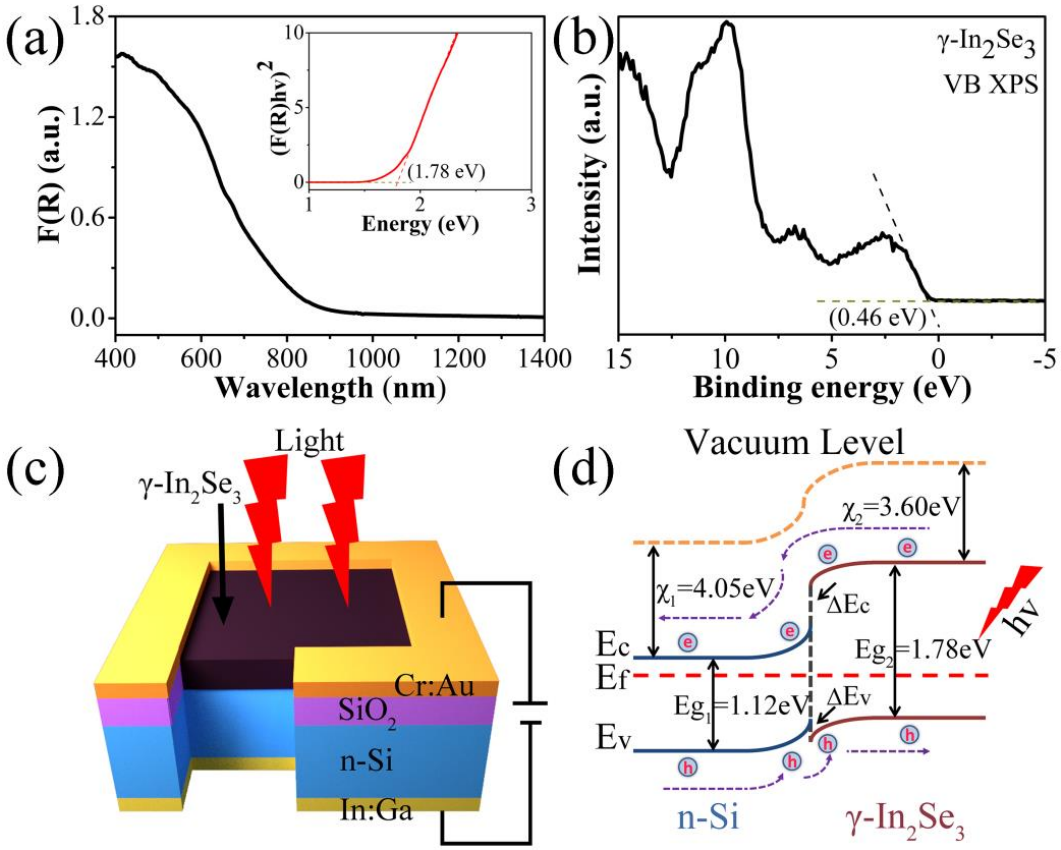

Fig. 5.5 (a) Optical absorption spectrum of γ-In_2Se_3 nanoflowers. Inset: A plot of $[F(R)hv]^2$ vs. photon energy, used to obtain the direct band gap. (b) Valence-band XPS spectrum of γ-In_2Se_3 nanoflowers. (c) Schematic diagram of the γ-In_2Se_3/Si heterojunction photodiode. (d) Energy-band diagram of the heterojunction photodiode showing the photogenerated carriers transfer process under light illumination. E_c, E_f and E_v denote the conduction band minimum, fermi energy level and valence band maximum, respectively. χ_1 and χ_2 are the electron affinity of n-Si and γ-In_2Se_3, respectively, hv represents incident light photon energy

Based on the controllable synthesis of γ-In_2Se_3 nanoflowers and its excellent photoelectric properties, we have tried to fabricate γ-In_2Se_3/Si heterojunction photodiode and systematically studied the device performance. A schematic illustration of this photodiode used for photoresponse measurements is presented in Fig. 5.5c. The top view and cross-sectional view SEM images of the as-fabricated device (Fig. 5.6) clearly show that γ-In_2Se_3 nanoflower film is closely contact with Si substrate, forming a heterojunction with high surface area. The

energy band diagram of the heterojunction photodiode is shown in Fig. 5.5d. Here, Eg_1 is the band gap of n-Si (1.12 eV) and Eg_2 is the band gap of γ-In_2Se_3 (1.78 eV). According to the previous reports, the electron affinity for Si and γ-In_2Se_3 is 4.05 eV and 3.60 eV [25,26], thus producing conduction and valence band offsets of 0.45 eV and 0.21 eV, respectively. For the heterojunction structure, a depletion region is formed on both Si and γ-In_2Se_3 sides by carrier diffusion, leading to the creation of a built-in electric field at the γ-In_2Se_3/Si interface. When the incident light is absorbed, holes (h) and electrons (e) are generated and driven toward γ-In_2Se_3 and n-Si, respectively, by the built-in electric field, generating photocurrent in the heterojunction photodiode.

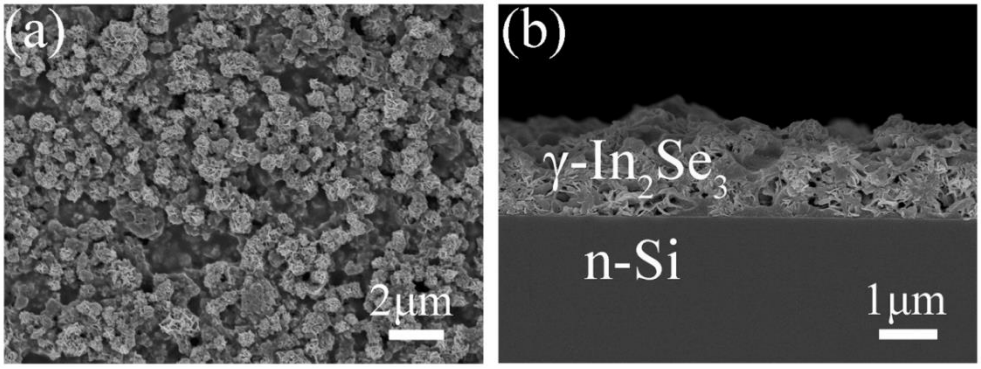

Fig. 5.6 (a) Top view and (b) cross-sectional view SEM images of the as-fabricated γ-In_2Se_3/Si heterojunction photodiode

Fig. 5.7a-c shows the I-V curves of the γ-In_2Se_3/Si heterojunction device under dark, and illumination with different light intensities using xenon lamp of 380 nm, 680 nm and 880 nm as illumination sources. The results clearly exhibit a rectifying characteristic and also demonstrate that the γ-In_2Se_3/Si heterojunction behaves as a well-defined photodiode. As shown in the I-V curves, the dark current is low (about −0.75 nA) at reverse bias. Upon the illumination, a significant increase of current in the reverse bias region is observed. The photoresponse was tested under various light intensities for all the three light sources. It is obvious that the photocurrent strongly depends on the light intensity, and increases significantly with increasing light intensity at reverse bias region. It can be attributed to the change in photo-generated carriers, revealing the high sensitivity of the device ranging from UV to NIR light. The corresponding photocurrent as a function of light intensity is shown in Fig. 5.7d. The photocurrent is nearly linear to the light power densities and the dependence can be described by the power law：

$$I_{ph} = AP^{\theta} \quad (5.1)$$

where I_{ph} represents the photocurrent ($I_{illumination}$-I_{dark}); A is a constant at a specific wavelength; P is the power density of the incident light; and θ is an exponent [27]. The fitting curves showed that θ = 1.08, 0.90, and 0.87 for the wavelengths of 380 nm, 680 nm and 880 nm, respectively. Note that the factor θ is close to one, revealing low trap states in the γ-In_2Se_3/Si heterojunction. Then the recombination rate of photo-generated carriers is proportional to the excess of charge carriers by the following formula:

$$d\Delta n/dt=g_n-\Delta n/\tau_n \quad (5.2)$$

where g_n is the generation rate of charge carriers, Δn is the concentration of electrons (or holes) created by photoexcitation, and τ_n is the time constant of charge carriers [27]. Assuming g_n and τ_n are independent of Δn, then the carrier recombination rate will decrease with increasing light intensity (increasing carrier concentration).

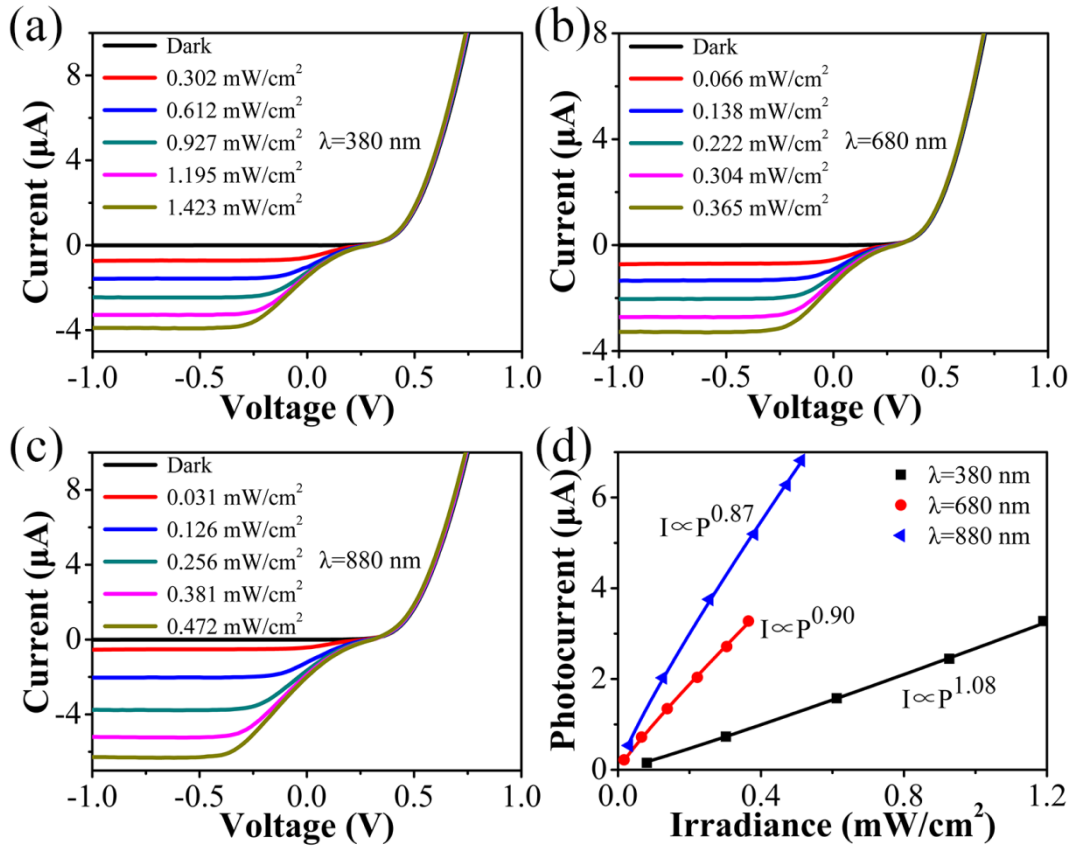

Fig. 5.7 (a) Photoelectric properties of the γ-In_2Se_3/Si heterojunction photodiode under dark and illumination with different light intensities at various wavelengths. (a) 380 nm, (b) 680 nm and (c) 880 nm. (d) Relationships between the photocurrent and the light intensity at a bias of −1 V

Fig. 5.7d also shows that the photocurrent is relatively small and increased more slowly with the increasing light intensity at the wavelength of 380 nm. In contrast, the photocurrent from 880 nm light illumination increases much more rapidly. This difference can be explained as

follows: Firstly, at the same optical power density, the number of photons is more than two times higher at 880 nm than at 380 nm. Secondly, the reflection loss at 380 nm is also much higher than that at 880 nm due to the difference of refractive index.

A useful figure of merit for the photodiode is the responsivity (R_{res}), which can be calculated from:

$$R_{res}=I_{ph}/I_{irr}A \quad (5.3)$$

where I_{ph} is the photocurrent, I_{irr} is the irradiance of the incident light, and A is the effective device area (2.5×10^{-3} cm^2 for this device) [6]. Light intensity-dependent responsivity of the γ-In_2Se_3/Si heterojunction photodiode (Fig. 5.8) further confirms a higher R_{res} value under light illumination of 880 nm.

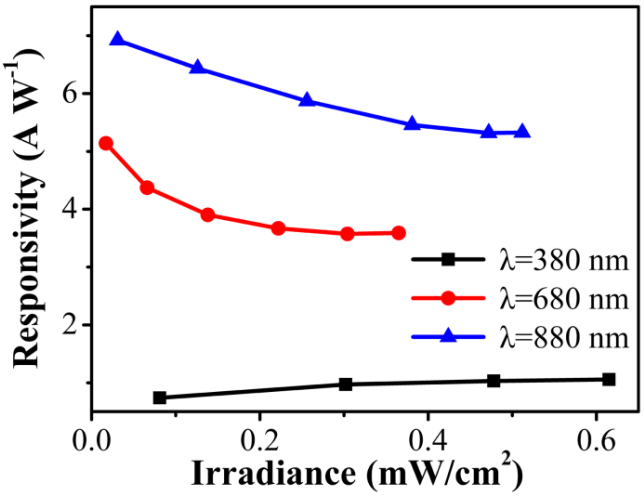

Fig. 5.8 Light intensity-dependent responsivity of the γ-In_2Se_3/Si heterojunction photodiode at different wavelengths

To further investigate the photoresponse characteristics, a plot of time-resolved photoresponse under illumination of 808 nm laser source with reverse bias of 0 V and −1 V is shown in Fig. 5.9a. The results show that the heterostructure device can function as a self-driven photodetector operating at zero bias voltage, thus allowing low on-chip power consumption. When the applied voltage is −1 V (with an incident light density of 0.05 mW cm^{-2}), the current dramatically increases from −1 nA (OFF state, dark condition) to −1570 nA (ON state, light illumination). The switching "ON/OFF" ratio is as high as 1570, comparable to the state-of-the-art results reported previously. The response remains the same after multiple cycles, demonstrating the excellent stability of the γ-In_2Se_3/Si heterojunction photodiode. Furthermore, the response speed of the device was investigated by monitoring the variation of photocurrent under the modulated incident light (808 nm) using an oscilloscope. The

modulated light with different frequencies was generated by a mechanical chopper. The schematic diagram of the measurement is illustrated in Fig. 5.9b. Fig. 5.9c shows the representative time response characteristics of the heterojunction photodiode at the frequency of 1 kHz (applied reverse bias of −1 V), implying the potential for high frequency photodetection. To extract the exact response time, one of the response periods in Fig. 5.9c is magnified, as shown in Fig. 5.9d. In this time domain, the speed of a photodetector is often characterized by the response time (τ_{res}, the time interval for the response to rise from 10% to 90% of its peak value) and the recovery time (τ_{rec}, the time interval for the response to decay from 90% to 10% of its peak value). In our work, a short response time (175 μs) and recovery time (226 μs) were observed, which are also comparable to the previously reported excellent results [28].

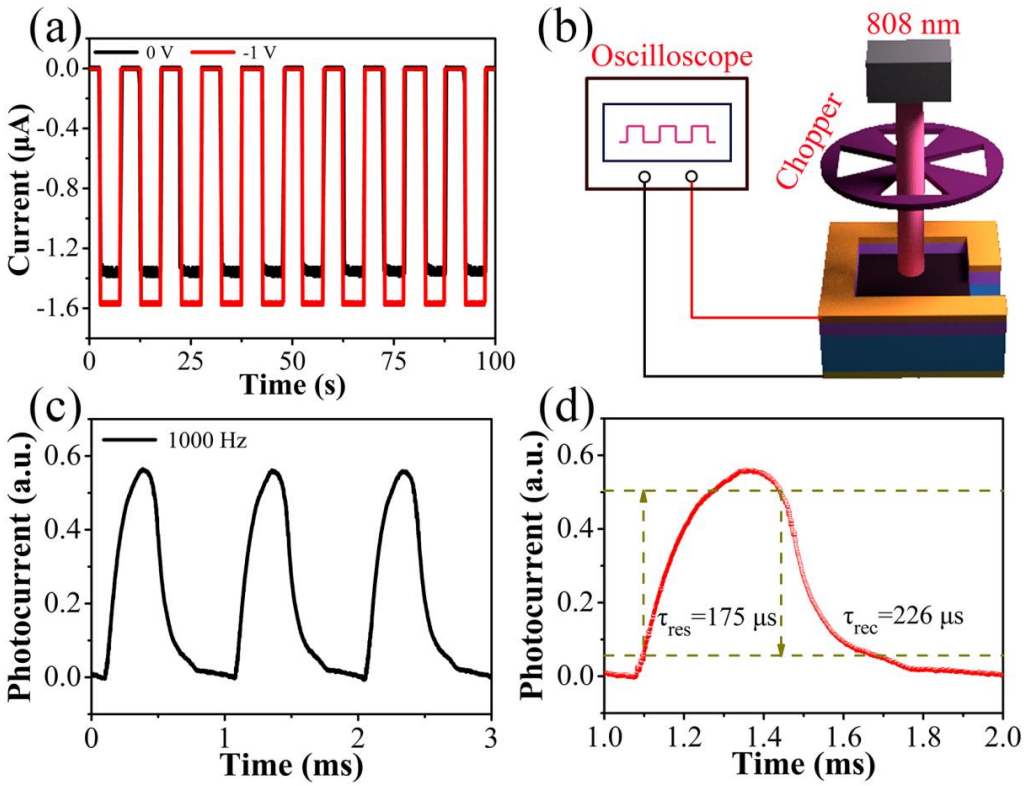

Fig. 5.9 Photoresponse of the γ-In_2Se_3/Si heterojunction photodiode. (a) Time-resolved photoresponse at the bias voltage of 0 V and −1 V under 808 nm light illumination. (b) Schematic illustration of the measurement configuration for photoresponse speed measurement. (c) Representative photoresponse of the heterojunction photodiode under 808 nm light illumination with the modulated chopper frequency of 1000 Hz. (d) Magnified plot of one response cycle in (c), used to obtain the response time and the recovery time

To clearly show the selective spectral response of the heterojunction photodiode,

photodetection at the monochromatic wavelength in range from UV to IR was investigated. Fig. 5.10a shows the wavelength-dependent responsivity (R_{res}) in the wavelength region of 300~1100 nm under a reverse bias of −1 V. The calculated R_{res} rises from 300 nm to 820 nm, and reaches the highest value of 5.67 A W^{-1} at 820 nm. The detectivity decrease after 820 nm can be attributed to the decreasing absorption of the γ-In_2Se_3. Importantly, the R_{res} of the γ-In_2Se_3/Si heterojunction photodiode is much higher than that of the commercial Si-based p-n or Schottky junction photodetectors, which usually have a smaller peak value of ~0.8 A W^{-1} [27,29]. Moreover, it is obvious that the broad spectral response of our heterojunction photodiode makes it useful for multispectral applications.

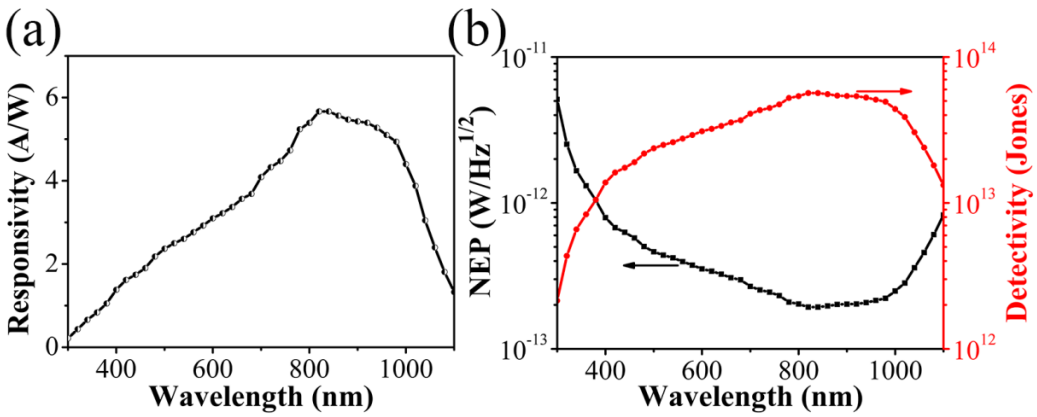

Fig. 5.10 Wavelength-dependence of (a) responsivity, and (b) noise equivalent power (NEP) and detectivity (D*) of the γ-In_2Se_3/Si heterojunction photodiode at a reverse bias of −1 V

To further characterize the performance of this heterojunction photodiode, noise equivalent power (NEP), i.e., NEP=S_I/R_{res}, where S_I is the root mean square (RMS) dark noise density, was measured within a specified bandwidth (commonly 1 Hz) [30]. To obtain S_I, a large sequence of current fluctuations (I_{noise}) was measured with 0.5 s integration time (corresponding to a bandwidth of 1 Hz), while keeping the photodiode in dark. The RMS noise density was then calculated as $S_I=(\langle I^2_{noise}\rangle/1Hz)^{1/2}$. Fig. 5.10b shows the NEP across the working spectrum in this study. It was found that the NEP of our photodiode can reach 1.93×10^{-13} W/$Hz^{1/2}$ at 820 nm, implying that even a very weak incident light can be detected above the noise level. The spectral detectivity (D*) curve under the bias of −1 V is also presented in the Fig. 5.10b. The D* is given by the following equation:

$$D^*=R_{res}/(2qJ_d)^{1/2} \quad (5.4)$$

where R_{res} is the responsivity of the photodiode, q is the fundamental unit of charge and J_d is the dark current [27]. The calculated peak D* value is 5.66×10^{13} Jones (Jones = cm $Hz^{1/2}$ W^{-1}) at 820 nm, which is much higher than that of other Si-based heterojunction photodiodes

[27,28,31-33], confirming the excellent detection performance of this γ-In_2Se_3/Si heterojunction photodiode.

Table 5.1 summarizes the key parameters of our γ-In_2Se_3/Si heterojunction photodiode, compared to various Si-based heterojunction photodiodes reported in the literature. The performance of our devices is comparable to that of the previously reported state-of-the-art devices. Such results can be attributed to the following reasons: (i) The direct and narrow band gap, as well as a high absorption coefficient and high sensitivity make γ-In_2Se_3 an excellent material for photo-detection. (ii) The high crystalline quality of the γ-In_2Se_3 film minimizes the defect density and grain boundary recombination, thus facilitating the carriers transport in the film. (iii) The flower-like morphology of γ-In_2Se_3 with high surface area benefits from the built-in electric field near the γ-In_2Se_3/Si interface, leading to enhanced photoelectrical performance. Other non-Si heterojunction based nano-photodetectors, consisting of various nanomaterials, have also been reported in the literature [35,36]. Most of them are resistors and based on the intrinsic photoconductivity of nanomaterials. The device structure and current-generation mechanism are really different from the p-n heterojunction photodiode in this work. However, in terms of photodetector performance, such nano-photodetectors usually show higher responsivity but slower response speed. The issue of balancing all key parameters seems to be crucial for the future device optimization.

Table 5.1 Comparison of key parameters between this work and various Si-based heterojunction photodiodes

Photodiodes	Wavelength (nm)	Responsivity ($A\,W^{-1}$)	Detectivity (Jones)	τ_{res}/τ_{rec} (μs)	Ref.
γ-In_2Se_3/Si	820/808	5.67	5.66×10^{13}	175/226	This work
ZnO/Si	442	1.02	-	10^4/-	34
CuO/Si	532	1.05×10^{-4}	1.00×10^{9}	60/80	28
MoS_2/Si	650	11.90	2.10×10^{10}	31/72	31
Bi_2Se_3/Si	808	24.28	4.39×10^{12}	2.5/5.5	27
Bi_2Te_3/Si	635	1.00	2.50×10^{11}	$10^5/10^5$	32
graphene/Si	890	0.73	4.08×10^{13}	320/750	29

5.4 Conclusions

An effective colloidal process involving the hot-injection method has been developed to synthesize uniform crystalline γ-In_2Se_3 nanoflowers, which consist of 20 nm thick two-dimensional nanosheets. The band gap of the as-synthesized γ-In_2Se_3 nanoflowers was experimentally determined to be 1.78 eV, showing p-type conduction. A heterojunction photodiode formed by n-Si and γ-In_2Se_3 nanoflower film has been fabricated. The p-n heterojunction photodiodes not only exhibited excellent rectification characteristics in the dark, but also showed remarkable photoresponse with an "ON/OFF" ratio as high as 1570, short response/recovery times (175/226 μs) and long-term durability. Under visible and near-infrared light illumination, the device displayed high responsivity and detectivity, which is attributed to the high surface area and built-in electric field at the γ-In_2Se_3/Si interface. Therefore, this broadband photodiode, with its features of easy fabrication and high performance, has significant application potential in the fields of environmental sensing, optical switching, and optoelectronic integrated circuits.

5.5 References

[1] Chandiran, A. K.; Tetreault, N.; Humphry-Baker, R.; Kessler, F.; Baranoff, E.; Yi, C.; Nazeeruddin, M. K.; Gratzel, M., Subnanometer Ga_2O_3 tunnelling layer by atomic layer deposition to achieve 1.1 V open-circuit potential in dye-sensitized solar cells. Nano Letters 2012, 12 (8), 3941-3947.

[2] Chen, X.; Liu, K.; Zhang, Z.; Wang, C.; Li, B.; Zhao, H.; Zhao, D.; Shen, D., Self-Powered Solar-Blind Photodetector with Fast Response Based on Au/beta-Ga_2O_3 Nanowires Array Film Schottky Junction. ACS Appl Mater Interfaces 2016, 8 (6), 4185-4191.

[3] Zhai, T. Y.; Fang, X. S.; Liao, M. Y.; Xu, X. J.; Li, L.; Liu, B. D.; Koide, Y.; Ma, Y.; Yao, J. N.; Bando, Y.; Golberg, D., Fabrication of High-Quality In_2Se_3 Nanowire Arrays toward High-Performance Visible-Light Photodetectors. Acs Nano 2010, 4 (3), 1596-1602.

[4] Island, J. O.; Blanter, S. I.; Buscema, M.; van der Zant, H. S.; Castellanos-Gomez, A., Gate Controlled Photocurrent Generation Mechanisms in High-Gain $In_{(2)}Se_{(3)}$ Phototransistors. Nano Letters 2015, 15 (12), 7853-7858.

[5] Nayak, P. K.; Hedhili, M. N.; Cha, D.; Alshareef, H. N., High performance In_2O_3 thin film transistors using chemically derived aluminum oxide dielectric. Applied Physics Letters 2013, 103 (3), 033518.

[6] Jacobs-Gedrim, R. B.; Shanmugam, M.; Jain, N.; Durcan, C. A.; Murphy, M. T.; Murray, T.

M.; Matyi, R. J.; Moore, R. L.; Yu, B., Extraordinary Photoresponse in Two-Dimensional In_2Se_3 Nanosheets. Acs Nano 2014, 8 (1), 514-521.

[7] Zhai, T.; Ma, Y.; Li, L.; Fang, X.; Liao, M.; Koide, Y.; Yao, J.; Bando, Y.; Golberg, D., Morphology-tunable In_2Se_3 nanostructures with enhanced electrical and photoelectrical performances via sulfur doping. Journal of Materials Chemistry 2010, 20 (32), 6630.

[8] Peng, H. L.; Xie, C.; Schoen, D. T.; Cui, Y., Large anisotropy of electrical properties in layer-structured In_2Se_3 nanowires. Nano Lett 2008, 8 (5), 1511-1516.

[9] Kang, D.; Rim, T.; Baek, C. K.; Meyyappan, M.; Lee, J. S., Investigation of electromigration in In_2Se_3 nanowire for phase change memory devices. Applied Physics Letters 2013, 103 (23), 233504.

[10] Wei, D.; Lin, Z.; Cui, Z.; Su, S.; Zhang, D.; Cao, M.; Hu, C., Two-step fabrication of a porous gamma-In_2Se_3 tetragonal photocatalyst for water splitting. Chemical Communications 2013, 49 (83), 9609-9611.

[11] Han, G.; Chen, Z. G.; Drennan, J.; Zou, J., Indium selenides: structural characteristics, synthesis and their thermoelectric performances. Small 2014, 10 (14), 2747-2765.

[12] Li, Y.; Gao, J.; Li, Q. L.; Peng, M. F.; Sun, X. H.; Li, Y. Y.; Yuan, G.; Wen, W.; Meyyappan, M., Thermal phase transformation of In_2Se_3 nanowires studied by in situ synchrotron radiation X-ray diffraction. Journal of Materials Chemistry 2011, 21 (19), 6944-6947.

[13] Kang, D.; Rim, T.; Baek, C. K.; Meyyappan, M.; Lee, J. S., Thermally Phase-Transformed In_2Se_3 Nanowires for Highly Sensitive Photodetectors. Small 2014, 10 (18), 3795-3802.

[14] Tan, X.; Zhou, J.; Yang, Q., Ascorbic acid-assisted solvothermal growth of γ-In_2Se_3 hierarchical flowerlike architectures. CrystEngComm 2011, 13 (7), 2792.

[15] Li, T.; Wang, J.; Lai, J.; Zheng, X.; Liu, W.; Ji, J.; Liu, H.; Jin, Z., Multi-morphological growth of nano-structured In_2Se_3 by ambient pressure triethylene glycol based solution syntheses. Journal of Alloys and Compounds 2015, 646, 603-611.

[16] Shi, W. D.; Yu, S.; Liu, P.; Fan, W. Q.; Luo, H.; Song, S. Y., Near-infrared photoluminescent flowerlike alpha-In_2Se_3 nanostructures from a solvothermal treatment. Chemical Engineering Journal 2013, 225, 474-480.

[17] Razgoniaeva, N.; Acharya, A.; Sharma, N.; Adhikari, P.; Shaughnessy, M.; Moroz, P.; Khon, D.; Zamkov, M., Measuring the Time-Dependent Monomer Concentration during the Hot-Injection Synthesis of Colloidal Nanocrystals. Chemistry of Materials 2015, 27 (17), 6102-6108.

[18] Jeong, S.; Yoo, D.; Jang, J. T.; Kim, M.; Cheon, J., Well-Defined Colloidal 2-D Layered Transition-Metal Chalcogenide Nanocrystals via Generalized Synthetic Protocols. J Am Chem Soc 2012, 134 (44), 18233-18236.

[19] Ariyawansa, G.; Apalkov, V.; Perera, A. G. U.; Matsik, S. G.; Huang, G.; Bhattacharya, P., Bias-selectable tricolor tunneling quantum dot infrared photodetector for atmospheric windows. Applied Physics Letters 2008, 92 (11), 111104.

[20] Sarkar, S.; Basak, D., Self Powered Highly Enhanced Dual Wavelength ZnO@CdS Core-Shell Nanorod Arrays Photodetector: An Intelligent Pair. ACS Appl Mater Interfaces 2015, 7 (30), 16322-16329.

[21] Bera, A.; Das Mahapatra, A.; Mondal, S.; Basak, D., Sb_2S_3/Spiro-OMeTAD Inorganic-Organic Hybrid p-n Junction Diode for High Performance Self-Powered Photodetector. ACS Appl Mater Interfaces 2016, 8 (50), 34506-34512.

[22] Vaughn, D. D.; Patel, R. J.; Hickner, M. A.; Schaak, R. E., Single-Crystal Colloidal Nanosheets of GeS and GeSe. Journal of the American Chemical Society 2010, 132 (43), 15170-15172.

[23] Sreekumar, R.; Jayakrishnan, R.; Sudha Kartha, C.; Vijayakumar, K. P., Anomalous photoconductivity in gamma In_2Se_3. Journal of Applied Physics 2006, 100 (3), 033707.

[24] Bernede, J. C.; Marsillac, S., Band alignment at the interface of a SnO_2/gamma-In_2Se_3 heterojunction. Materials Research Bulletin 1997, 32 (9), 1193-1200.

[25] Li, Y.; Xu, C. Y.; Wang, J. Y.; Zhen, L., Photodiode-like behavior and excellent photoresponse of vertical Si/monolayer MoS_2 heterostructures. Scientific Reports 2014, 4, 7186.

[26] Drapak, S. I.; Kovalyuk, Z. D.; Netyaga, V. V.; Orletskii, V. B., On the mechanisms of current transfer in n-In_2Se_3-p-GaSe heterostructures. Technical Physics Letters 2002, 28 (9), 707-710.

[27] Zhang, H.; Zhang, X.; Liu, C.; Lee, S. T.; Jie, J., High-Responsivity, High-Detectivity, Ultrafast Topological Insulator Bi_2Se_3/Silicon Heterostructure Broadband Photodetectors. Acs Nano 2016, 10 (5), 5113-5122.

[28] Hong, Q.; Cao, Y.; Xu, J.; Lu, H.; He, J.; Sun, J. L., Self-powered ultrafast broadband photodetector based on p-n heterojunctions of CuO/Si nanowire array. ACS Appl Mater Interfaces 2014, 6 (23), 20887-20894.

[29] Wang, X.; Cheng, Z.; Xu, K.; Tsang, H. K.; Xu, J. B., High-responsivity graphene/silicon-heterostructure waveguide photodetectors. Nature Photonics 2013, 7 (11), 888-891.

[30] An, X.; Liu, F.; Jung, Y. J.; Kar, S., Tunable graphene-silicon heterojunctions for ultrasensitive photodetection. Nano Letters 2013, 13 (3), 909-916.

[31] Zhang, Y.; Yu, Y.; Mi, L.; Wang, H.; Zhu, Z.; Wu, Q.; Zhang, Y.; Jiang, Y., In Situ Fabrication of Vertical Multilayered MoS_2/Si Homotype Heterojunction for High-Speed Visible-Near-Infrared Photodetectors. Small 2016, 12 (8), 1062-1071.

[32] Yao, J.; Shao, J.; Wang, Y.; Zhao, Z.; Yang, G., Ultra-broadband and high response of the Bi_2Te_3-Si heterojunction and its application as a photodetector at room temperature in harsh working environments. Nanoscale 2015, 7 (29), 12535-12541.

[33] Li, X. M.; Zhu, M.; Du, M. D.; Lv, Z.; Zhang, L.; Li, Y. C.; Yang, Y.; Yang, T. T.; Li, X.; Wang, K. L.; Zhu, H. W.; Fang, Y., High Detectivity Graphene-Silicon Heterojunction Photodetector. Small 2016, 12 (5), 595-601.

[34] Pradel, K. C.; Jevasuwan, W.; Suwardy, J.; Bando, Y.; Fukata, N.; Wang, Z. L., Solution derived p-ZnO/n-Si nanowire heterojunctions for photodetection. Chemical Physics Letters 2016, 658, 158-161.

[35] Zhai, T.; Li, L.; Wang, X.; Fang, X.; Bando, Y.; Golberg, D., Recent Developments in One-Dimensional Inorganic Nanostructures for Photodetectors. Advanced Functional Materials 2010, 20 (24), 4233-4248.

[36] Guo, P.; Xu, J.; Gong, K.; Shen, X.; Lu, Y.; Qiu, Y.; Xu, J.; Zou, Z.; Wang, C.; Yan, H.; Luo, Y.; Pan, A.; Zhang, H.; Ho, J. C.; Yu, K. M., On-Nanowire Axial Heterojunction Design for High-Performance Photodetectors. Acs Nano 2016, 10 (9), 8474-8481.

GENERAL CONCLUSIONS

During the last half century, semiconductor technology has achieved rapid development as the core of modern high technology. Various new materials and functional devices based on semiconductor technology affect all aspects of our life. It is known that the fundamental research and application of semiconductor materials are the basis for developing semiconductor technology, which is also an important source of motivation for numerous scientific researchers. In this dissertation, two different selenide semiconductors with excellent properties are selected as our research targets, including controllable preparation of materials and exploration of applications as high performance photoelectric functional devices. The most significant results are as follows:

The high-quality Sb_2Se_3 nanorods were successfully synthesized by a hot-injection method. The reaction temperature, reaction time and the nature of the surfactants show important impact on the morphology and structure of the nanorods. The intrinsic resistivity of Sb_2Se_3 is as high as 10^6 Ω·m, which greatly limits its practical applications. To overcome this challenge, two effective approaches have been developed. One was the formation of composites with a conductive second phase and the hybrid nanorods with $Sb_2Se_3/AgSbSe_2$ heterojunction structure have been prepared accordingly. This interconnected heterojunction structure can significantly improve the electrical conductivity of the Sb_2Se_3 nanorods. The other approach was doping, where Sn was chosen as a dopant. With increasing Sn^{4+} doping concentration, the obtained $(Sn_xSb_{1-x})_2Se_3$ nanorods exhibit an improvement of electrical conductivity with several orders of magnitude due to the much higher carrier concentration. Finally, the as-synthesized Sb_2Se_3 nanorods, hybrid nanorods with the $Sb_2Se_3/AgSbSe_2$ heterojunction structure and $(Sn_xSb_{1-x})_2Se_3$ nanorods were all used for fabricating prototype photodetectors. The results show that the $Sb_2Se_3/AgSbSe_2$ heterojunction nanorod film photodetector has a remarkable response to visible light and the responsivity is about 4.2 times higher than that of the undoped Sb_2Se_3 nanorod film photodetector. Then the $(Sn_xSb_{1-x})_2Se_3$ nanorod film photodetector also exhibits remarkable responsivity and detectivity over a wide spectral range from ultraviolet to near-infrared. Overall, the Sb_2Se_3 nanorods with enhanced electrical conductivity show great application potential as highly efficient photodetectors.

$(Sn_xSb_{1-x})_2Se_3$ (x=0.00, 0.03, 0.05, 0.07, 0.10) polycrystalline semiconductors were successfully prepared by using an effective high-temperature melting process. The $(Sn_xSb_{1-}$

$_x)_2Se_3$ bulk crystal surface with appropriate chemical etching clearly show micron-sized grains. With increasing Sn doping concentration, $(Sn_xSb_{1-x})_2Se_3$ crystals also exhibit a great improvement of electrical conductivity with several orders of magnitude due to the much higher charge carrier concentration. The PEC measurements by using $(Sn_xSb_{1-x})_2Se_3$ crystals as working electrode show clear photoelectric response and the crystals are identified as p-type semiconductors. Compared to pure Sb_2Se_3, the dark current density of a representative $(Sn_{0.10}Sb_{0.90})_2Se_3$ is increased approximately by 10 times and the photocurrent density by approximately 14 times. In addition, this material shows a short response/recovery time (0.03/0.03 s), reversible and stable photoresponse. Therefore, the Sn-doped Sb_2Se_3 crystals can have an optimal band gap (1.10 eV) which overlap well with the solar spectrum with excellent electrical conductivity and photoconductive properties. The synthesis technique is relatively simple and compatible with large-scale fabrication. These properties confirm the high application potential of Sn-doped Sb_2Se_3 for highly efficient photoelectric devices.

Four Sb_2Se_3-based targets with the chemical composition of Sb_2Se_3, $Sb_2Se_{3.3}$, $(Sn_{0.1}Sb_{0.9})_2Se_3$ and $Sb_2(Se_{0.9}I_{0.1})_3$ have been successfully prepared by high-temperature melting. Then the thin films were deposited by using RF magnetron sputtering. The as-deposited thin film showed amorphous nature and after a heat treatment at an appropriate temperature, a high crystalline thin film composed of large crystal grains was obtained. The optical properties of the thin films were investigated systematically. It has been found that the crystallinity and the roughness were the main factors affecting the reflectance of the thin films. The band gap of the Sb_2Se_3 amorphous film was 1.64 eV, then turned to 1.28 eV for the crystalline film. The heat treatment temperature play an important role for determining the p/n type of the Sb_2Se_3 and $Sb_2Se_{3.3}$ thin films with a transformation from p type to n type with increasing temperature. Differently, all the $(Sn_{0.1}Sb_{0.9})_2Se_3$ thin films show p-type behavior and all the $Sb_2(Se_{0.9}I_{0.1})_3$ thin films are n-type. The PEC measurements indicate that Sb_2Se_3-based thin films have relatively high photoelectric response, as well as fast response and long-term stability. Accordingly, a novel quasi-homojunction Sb_2Se_3 thin film solar cell was fabricated for the first time. The existence of p-n junction inside the device structure has been demonstrated. The thickness and the heat treatment temperature have a close relationship with the device performance. The highest conversion efficiency obtained in our work reaches already a highly interesting 2.65%.

An effective hot-injection method has also been developed for synthesizing uniform γ-In_2Se_3 nanoflowers with single crystal phase. The systematic studies on the reaction time and

reaction temperature reveal the growth mechanism of γ-In_2Se_3 nanoflowers. Afterwards, an effective heterojunction photodiode formed by n-Si and γ-In_2Se_3 nanoflower film was fabricated for the first time. It is self-powered, with a very short response/recovery time (175/226 μs) and long-term durability, and it also displays a high responsivity and detectivity in a wide range of wavelength. These excellent properties indicate that the γ-In_2Se_3/Si heterojunction photodiode is very promising to be used as highly efficient photodetector.

PUBLICATION LIST

[1] **Shuo Chen**, Xvsheng Qiao, Fengxia Wang, Qun Luo, Xianghua Zhang, Xia Wan, Yang Xu, Xianping Fan, Facile synthesis of hybrid nanorods with the $Sb_2Se_3/AgSbSe_2$ heterojunction structure for high performance photodetectors, *Nanoscale*, 2016, 8, 2277-2283.

[2] **Shuo Chen**, Xuemei Liu, Xvsheng Qiao, Xia Wan, Khurram Shehzad, Xianghua Zhang, Yang Xu, Xianping Fan, Facile Synthesis of γ-In_2Se_3 Nanoflowers toward High Performance Self-Powered Broadband γ-In_2Se_3/Si Heterojunction Photodiode, *Small*, 2017, 1604033.

[3] **Shuo Chen**, Xvsheng Qiao, Zhuanghao Zheng, Michel Cathelinaud, Hongli Ma, Xianping Fan, Xianghua Zhang, Enhanced electrical conductivity and photoconductive properties of Sn-doped Sb_2Se_3 crystals, *Journal of Materials Chemistry C*, 2018, 6, 6465-6470.

[4] **Shuo Chen**, Khurram Shehzad, Xvsheng Qiao, Wei Li, Xuemei Liu, Xue Luo, Yuting Zhang, Xianghua Zhang, Yang Xu, Xianping Fan, High Performance Broadband Photodetector based on Doped $(Sn_xSb_{1-x})_2Se_3$ Nanorods with Enhanced Electrical Conductivity, *Journal of Materials Chemistry C*, 2018, DOI: 10.1039/C8TC03834A.

[5] **Shuo Chen**, Michel Cathelinaud, Xvsheng Qiao, Zhuanghao Zheng, Hongli Ma, Xianping Fan, Xianghua Zhang, Magnetron sputtered quasi-homojunction Sb_2Se_3 thin film solar cells, (Manuscript in preparation).

UNIVERSITE MATIERE BRETAGNE MOLECULES LOIRE ET MATERIAUX

UNIVERSITÉ DE RENNES 1

Titre : **Préparation et caractérisation de semi-conducteurs à base de séléniures pour applications photoélectriques**

Mots clés : semi-conducteur de séléniures, hétérojonction, dopage, photodétecteurs, cellules solaires

Résumé : Dans cette thèse, deux semi-conducteurs en séléniure ayant d'excellentes propriétés ont été étudiés afin de développer des matériaux performants pour des applications photoélectriques.

Tout d'abord, les nanorodes de Sb_2Se_3 ont été synthétisés en utilisant une méthode d'injection à chaud, et le plus grand défi associé à la faible conductivité de Sb_2Se_3 a été relevé en formant des hétérojonctions et/ou par un dopage. Les nanorodes de Sb_2Se_3 à conductivité électrique nettement améliorée ont été utilisés pour fabriquer des photo-détecteurs prototypes, qui présentent un grand potentiel d'application grâce à leur grande efficacité.

Le Sb_2Se_3 dopés au Sn a été préparé en utilisant un procédé de fusion à haute température. Avec l'augmentation de la concentration en Sn, les cristaux $(Sn_xSb_{1-x})_2Se_3$ présentent également une grande amélioration de la conductivité et des propriétés photoconductrices.

Quatre cibles à base de Sb_2Se_3 avec la composition chimique de Sb_2Se_3, $Sb_2Se_{3.3}$, $(Sn_{0.1}Sb_{0.9})_2Se_3$ et $Sb_2(Se_{0.9}I_{0.1})_3$ ont été préparées et les couches minces ont été déposées en utilisant la pulvérisation cathodique. Une étude systématique de la cristallinité, de la morphologie de surface, des propriétés optiques, du type de conduction (p ou n) et des performances photo-électro-chimique des couches minces a été réalisée. Une nouvelle cellule solaire à couches minces de Sb_2Se_3 avec une quasi-homojonction a été fabriquée pour la première fois et le rendement de conversion atteint déjà un taux très intéressant de 2,65%.

Une méthode efficace d'injection à chaud a également été développée pour la synthèse de nano-fleurs uniformes de γ-In_2Se_3. Une photodiode à hétérojonction formée en déposant une couche mince de nanoflower γ-In_2Se_3, du type p, sur un substrat en Si de type n, a été fabriquée pour la première fois. Il a été démontré que ce photo-détecteur peut être autoalimenté avec d'excellentes performances, notamment une réponse rapide et une sensibilité à large bande.

UNIVERSITE MATIERE BRETAGNE MOLECULES LOIRE ET MATERIAUX

UNIVERSITÉ DE RENNES 1

Titre : **Preparation and characterization of selenide semiconductors for photoelectric applications**

Keywords : selenide semiconductor, heterojunction, doping, photodetectors, solar cells

Abstract : In this dissertation, two different selenide semiconductors with excellent properties have been studied in order to develop high performance materials and devices for photoelectric applications.

Firstly, Sb_2Se_3 nanorods were synthesized via hot-injection method, and the biggest challenge of low conductivity of Sb_2Se_3 nanorods has been overcome successfully by forming heterojunction and/or doping. The Sb_2Se_3 nanorods with enhanced electrical conductivity were used for fabricating prototype photodetectors, which show great application potential as highly efficient photodetectors.

The Sn-doped Sb_2Se_3 crystals were successfully prepared by using high-temperature melting process. With increasing Sn doping concentration, the $(Sn_xSb_{1-x})_2Se_3$ crystals also exhibit a great improvement of conductivity and photoconductive properties.

Four Sb_2Se_3-based targets with the chemical composition of Sb_2Se_3, $Sb_2Se_{3.3}$, $(Sn_{0.1}Sb_{0.9})_2Se_3$ and $Sb_2(Se_{0.9}I_{0.1})_3$ have been successfully prepared by using high-temperature melting technique. Then thin films have been deposited by using RF magnetron-assisted sputtering. A systematic investigation of the crystallinity, surface morphology, optical properties, p/n type and photo-electro-chemical performance of the thin films has been performed. A novel quasi-homojunction Sb_2Se_3 thin film solar cells was fabricated for the first time and the highest conversion efficiency obtained in our work reaches already a highly interesting 2.65%.

An effective hot-injection method has also been developed for synthesizing uniform γ-In_2Se_3 nanoflowers. An efficient heterojunction photodiode formed by n-type Si substrate and p-type γ-In_2Se_3 nanoflower film was fabricated for the first time. It has been demonstrated that this photodetector can be self-powered with excellent performance including fast response and broadband sensibility.